RICE UNIVERSITY

Multiphysics model of a cardiac myocyte: A voltage-clamp study

by

Abhilash Krishna

A Thesis Submitted
in Partial Fulfillment of the
Requirements for the Degree

Doctor of Philosophy

Approved, Thesis Committee:

John W Clark Jr., Chair
Professor of Electrical and Computer
Engineering and Bioengineering

Joseph R. Cavallaro
Professor of Electrical and Computer
Engineering and Computer Science

Andrew J. Dick
Assistant Professor of Mechanical
Engineering and Materials Science

Houston, Texas

August, 2012

ABSTRACT

Multiphysics model of a cardiac myocyte:
A voltage-clamp study

by

Abhilash Krishna

We develop a composite multiphysics model of excitation-contraction coupling for a rat ventricular myocyte under voltage clamp (VC) conditions to: (1) probe mechanisms underlying the response to Ca^{2+}-perturbation; (2) investigate the factors influencing its electromechanical response; and (3) examine its rate-dependent behavior (particularly the force-frequency response (FFR)). Motivation for the study was to pinpoint key control variables influencing calcium-induced calcium-release (CICR) and examine its role in the context of a physiological control system regulating cytosolic Ca^{2+} concentration and hence the cardiac contractile response.

Our cell model consists of an electrical-equivalent model for the cell membrane and a fluid-compartment model describing the flux of ionic species between the extracellular and several intracellular compartments. The model incorporates frequency-dependent calmodulin (CaM) mediated spatially heterogenous interaction of calcineurin (CaN) and Ca^{2+}/calmodulin-dependent protein kinase-II (CaMKII) with their principal targets and accounts for rate-dependent, cyclic adenosine monophosphate (cAMP)-mediated up-regulation. We also incorporate a biophysical model for cardiac contractile mechanics to study the factors influencing force response.

The model reproduces measured VC data published by several laboratories, and

generates graded Ca^{2+}-release with high Ca^{2+} gain by achieving negative feedback control and Ca^{2+}-homeostasis. We examine the dependence of cellular contractile response on: (1) the amount of activator Ca^{2+} available; (2) the type of mechanical load applied; (3) temperature (22 to 38°C); and (4) myofilament Ca^{2+} sensitivity. We demonstrate contraction-relaxation coupling over a wide range of physiological perturbations. Our model reproduces positive peak FFR observed in rat ventricular myocytes and provides quantitative insight into the underlying rate-dependence of CICR.

The role of Ca^{2+} regulating mechanisms are examined in handling induced Ca^{2+}-perturbations using a rigorous cellular Ca^{2+} balance. Extensive testing of the composite model elucidates the importance of various direct and indirect modulatory influences on the cellular twitch-response with wide agreement with measured data on all accounts. We identify cAMP-mediated stimulation, and rate-dependent CaMKII-mediated up-regulation of Ca^{2+}-trigger current ($I_{Ca,L}$) as the key mechanisms underlying the aforementioned positive FFR. Our model provides biophysically-based explanations of phenomena associated with CICR and provides mechanistic insights into whole-cell responses to a wide variety of testing approaches used in studies of cardiac myofilament contractility.

Dedicated to

my parents, Kuruvail Malathi Devi and Chodon Chatoth Gopal Krishna

Acknowledgments

Foremost, I am extremely grateful for the mentorship of my adviser, Dr. John W. Clark. I am thankful for the opportunity he gave me to utilize and hone my skills in systems engineering while exploring my computational interests. I could not have accomplished this challenging undertaking without Dr. Clark's support and confidence. I admire his scientific insight, integrity and willingness to give honest criticism and advice. Because of Dr. Clark's support, the years I have spent at Rice have been rich both intellectually and in a much broader sense.

I am indebted to our collaborator Dr. Miguel Valderrábano who periodically took the time to discuss the progress and direction of my project while constantly ensuring the clinical relevance of my work. I have benefitted greatly from his generosity, scientific advice, and mentorship. I am thankful to Dr. Philip T. Palade who over the years took time to meticulously critique my work with incredible patience. Dr. Palade's insights into cardiac electrophysiology have always proved to be invaluable. His influence on my thesis is unmistakable. I thank Dr. Liang Sun who generously contributed his time and resources at the early stage of the project and also for sharing his motivating experiences as a graduate student.

I would like to thank my thesis proposal and defense committee members Dr. Lin Zhong, Dr. Joseph R. Cavallaro and Dr. Andrew Dick for their time and critical review of my work.

I am indebted to Deepa Ramachandran for her constructive inputs during the course of my work. I thank Deepa for her unmatched support through all the ups and downs. Thanks to Deepa, the years I spent at Rice will remain an indelible experience.

I am particularly thankful to Dr. Matthias Heinkenschloss for always being willing to share his expertise in computational numerical analysis and for his genuine interest in my research. I have benefited from conversations and interactions with innumerable others. This list is woefully incomplete, but I would like to thank Dr. Beatrice M. Riviere, Dr. Tim Warburton, Dr. Fathi Ghorbel, Dr. Michael W. Deem, Dr. Ka-Yiu San, Dr. Erzsébet Merényi, Dr. Osama R. Mawlawi and Dr. C. Sidney Burrus. I have also benefited from interaction with fellow students in the Department of Electrical and Computer Engineering, Bioengineering, Computational and Applied Mathematics and other programs at Rice.

I express my deep sense of gratitude to my wife Kishori who has always believed in my academic abilities and has been extremely generous with her patience and time ensuring that my work is never interrupted. I thank my parents for the lifelong, selfless struggle they endured to give me a great education. My parents helped me develop an enthusiasm for many of the activities that have enriched my life at Rice, including art, music, cooking and sports. I express my heartfelt gratitude to my grandparents K. Janaki Devi and late C. C. Madhavan Nambiar for their unconditional love and encouragement. I cannot begin to thank my sister Preethi and my brother Rahul for being my greatest fans and for always rooting for me. I would also like to thank my brothers-in-law Sanjeev and Sricharan for sharing this experience with me. I am very thankful to my father and mother-in-law for their support. Finally, I thank my lovely son Vedanth for his contagious smile and for making my last eight months at Rice very exciting.

I express my sincere gratitude to all my friends for all the different ways they show their love, support and concern. I would like to particularly thank Theja and Vishnu for sharing their computational resources at times when I needed it the most, undoubtedly contributing to timely progress of my work.

I also appreciate funding from Methodist Hospital Research Institute.

Contents

Illustrations

Tables

Chapter 1

Introduction

The heart's pumping action depends on the rhythmic, coordinated contraction of the ventricles and the proper functioning of the valves. Each mechanical heartbeat is triggered by an action potential which originates from a rhythmic, pacemaker cell within the heart. The impulse is then conducted rapidly throughout the organ in order to produce coordinated contraction. Disturbances in the heart's electrical activity may cause significant abnormalities in its mechanical function, and are the basis of much cardiac morbidity and mortality. In fact, malfunction of the heart's electrical behavior is the principal cause of sudden cardiac death. One way to characterize this electrical activity is via the electrocardiogram (ECG), which measures the integrated electrical activity of the heart by means of electrodes placed on the surface of the body. Although, an important tool in cardiac research, the ECG itself does not provide insight into the quantitative mechanisms responsible for preserving intact electrical activity in the heart. To better understand these fundamental mechanisms, it is necessary to focus on sub-cellular biophysical processes in individual cardiac cells. This chapter will discuss cardiac electrophysiology leading to a description of the genesis of cardiac contraction beginning at the cellular level.

1.1 Electrophysiology of Myocardial Cells

Living cells are enclosed by a cell membrane or sarcolemma, which separates the outside or extracellular space from the inside of the cell, known as the intracellular space. The cell membrane controls what enters or leaves the cell. Embedded in the cell membrane are proteins known as ion channels which allow certain types of ions, such as Na^+, K^+, Ca^{2+}, and Cl^-, to pass through the cell membrane. Because the phospholipid bilayer, of which the cell membrane is composed, separates charge, an electrical potential develops across the cell membrane as a result of the movement of the ions. This membrane potential can regulate the conductance of some ion channels, so that these ion channels open and close both with time and voltage. Ions are driven through these ion channels as a result of ion concentration gradients and electric potential differences across the cell membrane.

Normally, the membrane potential is at a steady state called the resting potential, and the cell is said to be quiescent. At this rest state, the membrane potential is negative inside the cell relative to the outside. In an excitable cell, the opening and closing of ion channels can lead to a sequence of changes in the membrane currents which can result in a fast spike in the membrane potential, known as an action potential. An action potential can occur when an excitatory stimulus (a brief inward current pulse) depolarizes (increases) the membrane potential past a certain threshold voltage.

1.1.1 The Cardiac Action Potential

Cardiac transmembrane potentials may be recorded by means of microelectrodes. A typical resting potential in a ventricular muscle fiber is -80 to-90 millivolts with respect to surrounding extracellular fluid, similar to that found in nerve and skeletal

muscle. The shape of the cardiac action potential, however, is quite distinctive primarily because of its long duration. A typical action potential from a mid-cardial rat ventricular cell is diagrammed in Fig. 1.1. Its total duration may be 50-80 milliseconds (epicardial cells have shorter action potential duration (APD) while endocardial cells have longer APD), and it consists of 5 distinct phases. The initial rapid upstroke (phase 0) from the resting potential to a positive value of about +20 millivolts is similar to the spikes of other cells. Early repolarization (phase 1) brings the potential down to a plateau level (not prominent in midcardial rat ventricular myocytes) over 2 to 3 milliseconds. The plateau itself (phase 2) follows, and accounts for most of the action potential duration. Repolarization (phase 3) brings the potential back to the resting level. The period between action potentials (phase 4) is stable except in cells which have the property of autorhythmicity, the ability to spontaneously generate propagated action potentials, and function as pacemaker cells. A cardiac action potential, once started in a cell, propagates by local current spread as in other excitable cells.

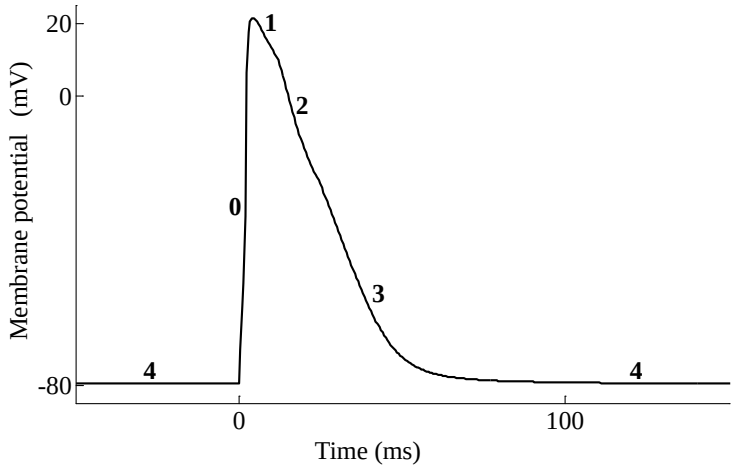

Figure 1.1 : A typical action potential from a rat ventricular myocardial cell.

1.1.2 The Ionic Basis for Cellular Potentials

The ionic basis for the cardiac action potential has features which are similar to those of nerve and skeletal muscle [2], but there are important differences as well [3]. Cardiac cells maintain gradients of various ions across their membranes by energy-requiring pumps. The cell membrane is semi-permeable, and contains a number of functionally independent channels through which different ions flow. Fig. 1.2 is a circuit representation of a cell membrane showing channels for multiple ionic species configured in parallel. Each channel has a specific ionic conductance (which may vary with membrane potential or time) and an equilibrium potential for the relevant ion. The membrane capacitance is represented by C_m. The total current density flowing across the membrane is $\emptyset_m$, and in general is carried by a mixture of several ionic species. The overall net transmembrane potential is V_m. The flow of the i^{th} ionic species is determined by the conductivity of its channel, g_i, and its equilibrium potential, E_i which is given by the Nernst equilibrium equation:

$$E_i = \frac{RT}{Z_i F} \ln \frac{\eta_i^{extra}}{\eta_i^{intra}} \tag{1.1}$$

where

R = the gas constant, 8.314 joules/mole degree K

T = the absolute temperature, degrees K

F = Faraday's constant, 9.6485×10^4 coul./mole

Z_i = Valence of the i^{th} ion

η_i^{intra} = intracellular concentration of the i^{th} ion, moles$\cdot m^{-3}$

η_i^{extra} = extracellular concentration of the i^{th} ion, moles$\cdot m^{-3}$

At room temperature, Eq. 1.1 becomes approximately

$$V_i = \frac{60}{Z_i} \log \frac{\eta_i^{outside}}{\eta_i^{inside}} (millivolts) \tag{1.2}$$

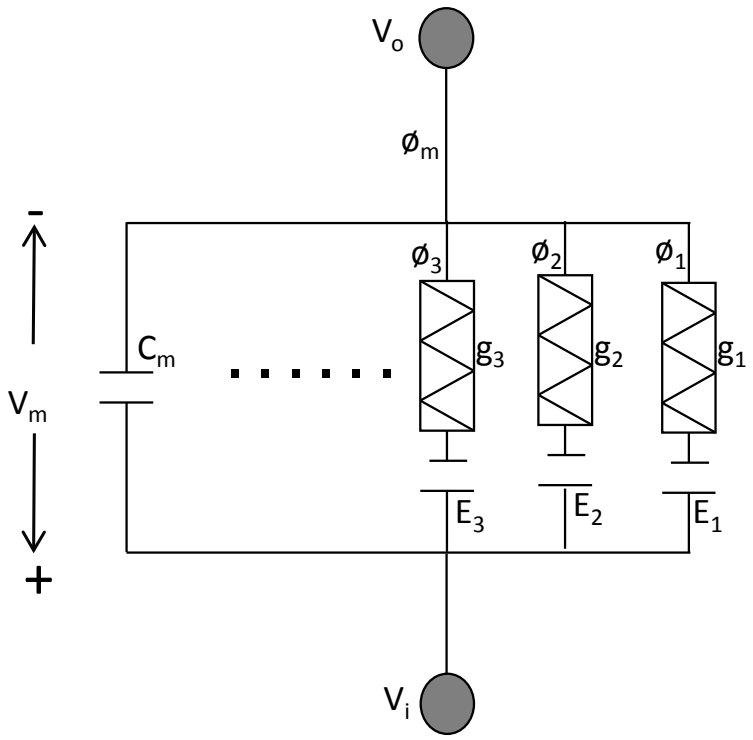

Figure 1.2 : Electrical equivalent circuit model of a cell membrane

Individual ions pass through the cell membrane through discrete ionselective channels. The permeability of the channels may be quite different for different ionic species, and in addition the permeability may change dramatically as a function of the potential difference across the membrane, or as a result of the activation of membrane receptors.

The GoldmanHodgkinKatz flux equation (or GHK flux equation) describes the ionic flux carried by an ionic species across a cell membrane as a function of the transmembrane potential and the concentrations of the ion inside and outside of the

cell. The formulation of the GHK flux equation makes the assumptions: (1) The membrane is a homogeneous substance; (2) The electrical field is constant so that the transmembrane potential varies linearly across the membrane; (3) The ions access the membrane instantaneously from the intra- and extracellular solutions; (4) The permeant ions do not interact; and (5) The movement of ions is affected by both concentration and voltage differences.

The GHK flux equation [4] for an ion species 'i':

$$\phi_i = P_i Z_i^2 \frac{V_m F^2}{RT} \frac{\eta_i^{intra} - \eta_i^{extra} \exp(\frac{-Z_s V_m F}{RT})}{1 - \exp(\frac{-Z_s V_m F}{RT})} \tag{1.3}$$

where

ϕ_i = current density across the membrane carried by ion 'i', A·m^{-2}

P_i = permeability of the membrane to ion 'i', m·s^{-1}

V_m = Transmembrane potential in volts

An implicit definition of the reversal/equilibrium potential is contained in the GHK flux equation [5]. The Nernst equilibrium potential in Eq. 1.1 can be obtained from the GHK formulation in Eq. 1.3 by solving for V_m with $\phi_i = 0$.

1.1.3 Voltage-Clamp Protocol

The voltage clamp is used by electrophysiologists to measure the ion currents across the membrane of excitable cells, such as cardiac myocytes, while holding the membrane voltage at a set level. Cell membranes of excitable cells contain many different kinds of ion channels, some of which are voltage gated. The voltage clamp allows the membrane voltage to be manipulated independently of the ionic currents, allowing the current-voltage relationships of membrane channels to be studied. Advances in

voltage clamp recording techniques and experimental procedures for isolating single cells have fueled the development of many different types of quantitative cell models. Specifically, the development of the patch clamp technique [6] and the enzymatic dispersion technique [7] enabled the recording of reliable voltage clamp data from single cell preparations. The suction-type patch clamp technique fuses a glass pipette with the cell membrane forming a seal with a high resistance on the order of a gigaohm [6]. The enzymatic dispersion technique isolates single cell preparations, eliminating the source of clamp error that previously occurred in multicellular preparations. The improved recording and preparation techniques provide the opportunity to study the gating kinetics of individual ionic membrane currents in single cell preparations, and the accompanying improvement in the quality of measured data has also fostered an improvement in the quality of single cell models developed for the purpose of providing explanations for sub-cellular biophysical phenomena.

1.1.4 Cellular Ca^{2+} Dynamics

As shown in Fig. 1.3, sarcolemmal membrane depolarization triggers Ca^{2+} influx from the extracellular medium by opening dihydropyridine (DHP)-sensitive L-type Ca^{2+} channels (LCCs) predominantly located in sarcolemmal invaginations called transverse tubules. Following diffusion across a small sub-membrane dyadic space, this influx activates ryanodine receptors (RyRs) controlling ryanodine-sensitive Ca^{2+} release channels (RyR) in the junctional portion of the sarcoplasmic reticulum (jSR). Fabiato and Fabiato [8] named the process Ca^{2+}-induced Ca^{2+} release (CICR). Ca^{2+} subsequently diffuses from the dyadic space into the cytoplasm. Contraction of cardiac muscle is triggered by this transient rise in intracellular Ca^{2+} concentration $[Ca^{2+}]_{myo}$. Ultimately, cytosolic Ca^{2+} concentration $[Ca^{2+}]_{myo}$ is returned to rest-

ing levels by combination of: (a) sequestration of Ca^{2+} by sarcoplasmic/endoplasmic reticulum Ca^{2+}-ATPase (SERCA)-type calcium pumps lining the longitudinal portion of the sarcoplasmic reticulum (LSR); (b) Ca^{2+} extrusion from the cytosol by Na^{+}/Ca^{2+} exchangers (NCX) and Ca^{2+}-ATPase pumps on the sarcolemmal membrane (I_{PMCA}); and (c) Ca^{2+} buffering in the dyadic space and cytosol. CICR in cardiac muscle exhibits both graded behavior and a high gain. Graded behavior refers to the observation that SR Ca^{2+} release is proportional to the influx of trigger Ca^{2+} [9], whereas high gain indicates that the sarcolemmal trigger current elicits a high SR Ca^{2+} release flux.

This study of a rat ventricular myocyte is limited to Ca^{2+} related channel, exchanger and pumps (LCC/$I_{Ca,L}$, NCX/I_{NaCa}, I_{PMCA} and SERCA pump), while lacking exclusive Na^{+} or K^{+} related channels and transporters. It is aimed at investigating voltage clamp conditions where channels other than Ca^{2+} are blocked. Its focus on the Ca^{2+} dynamics allows one to comprehend more clearly the important role of Ca^{2+} signalling pathways and feedback control systems in maintaining whole cell homeostasis over a prolonged period of time and examine in detail the genesis of cardiac contraction.

1.2 Cardiac Contractile Mechanism

A sarcomere is the basic unit of a cardiac contractile system. Cardiac tissue is composed of tubular muscle cells called myocytes which in turn comprise of tubular myofibrils. These myofibrils are composed of repeating sections of sarcomeres, which appear under the microscope as dark and light bands.

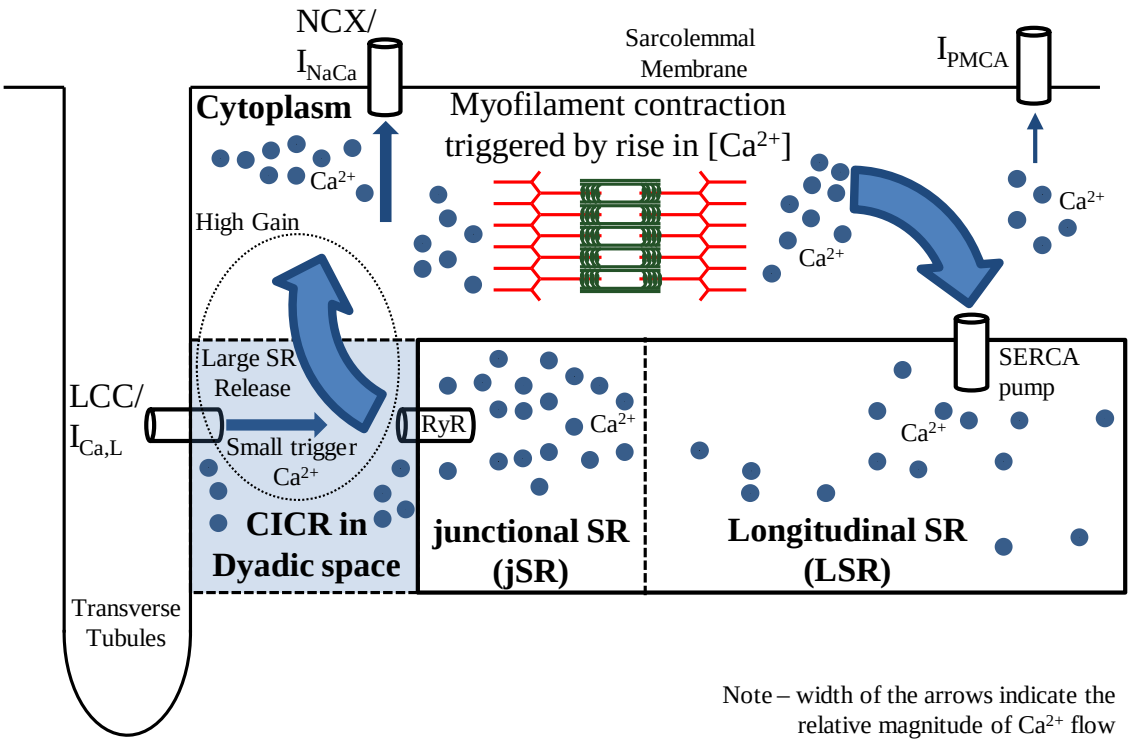

Figure 1.3 : A schematic for intracellular Ca^{2+} flow as a result of Ca^{2+}-induced Ca^{2+} release.

1.2.1 The Sliding Filament Theory

It is well known [10, 11] that one zone of the repeated sarcomere arrangement, the "A band," remains relatively constant in length during contraction (Fig. 1.4). The A band contains thick filaments of myosin, which suggests that the myosin filaments remained central and relatively constant in length while other regions of the sarcomere shortens. The "I band," rich in thinner filaments made of actin, changes its length along with the sarcomere. The sliding filament theory, states that the sliding of the long fibrous proteins actin and myosin past each other generates muscle tension. Because actin is tethered to structures located at the lateral ends of each sarcomere called z discs, any shortening of the actin filament length would result in a shortening

of the sarcomere and thus the muscle. Myosin has a long, fibrous tail and a globular head, which binds to actin when the binding sites on actin are exposed by Ca^{2+} ions.

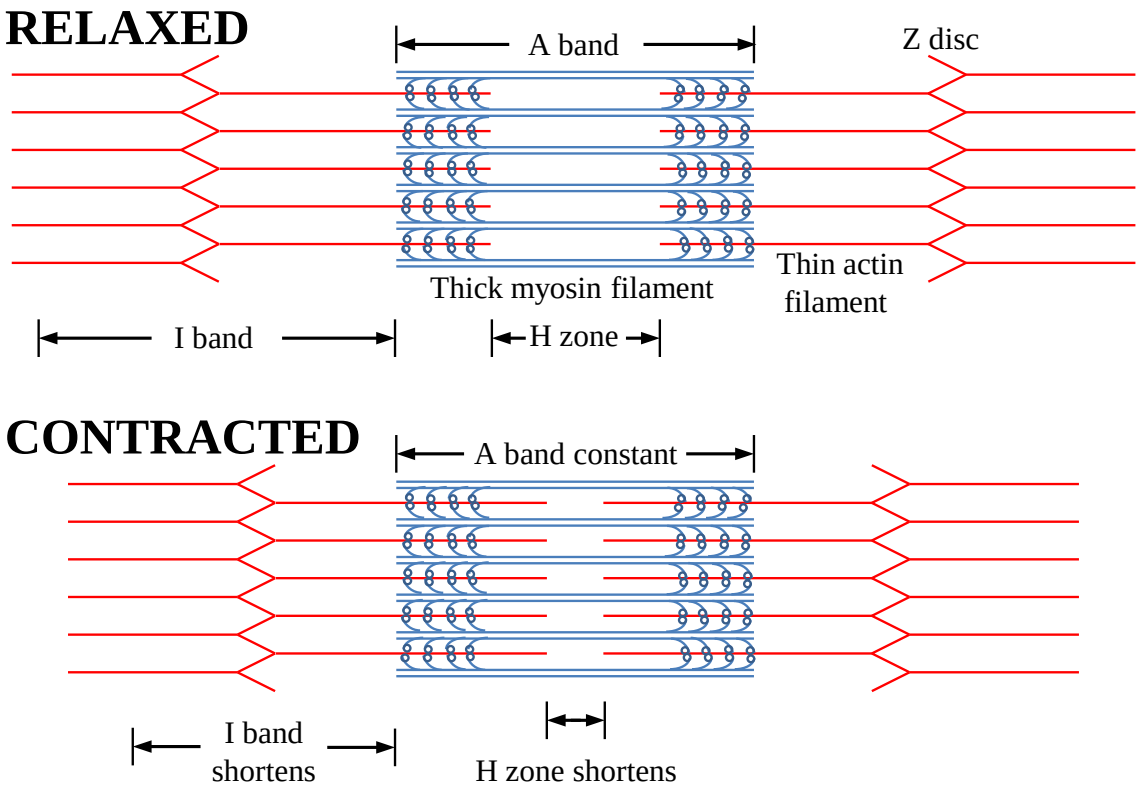

Figure 1.4 : The basic organization of a sarcomere subregion, showing the centralized location of myosin (A band). Actin and the z discs are shown in red.

Calcium and ATP are cofactors (nonprotein components of enzymes) required for the contraction of muscle cells. While ATP supplies the energy, Ca^{2+} is required by two proteins, troponin and tropomyosin, that regulate muscle contraction by blocking the binding of myosin to filamentous actin (Fig. 1.5). In a resting sarcomere, tropomyosin blocks the binding of myosin to actin. For myosin to bind actin, tropomyosin must rotate around the actin filaments to expose the myosin-binding sites. In 1994, William Lehman and his colleagues demonstrated how tropomyosin rotates by studying the shape of actin and myosin in either Ca^{2+}-rich solutions or solu-

tions containing low Ca^{2+} [12]. By comparing the action of troponin and tropomyosin under these two conditions, the authors found that the presence of Ca^{2+} is essential for the contraction mechanism. Specifically, when Ca^{2+} binds to troponin C (TnC; subunit of troponin), it produces a conformational change in troponin I (TnI; subunit of troponin that binds to actin holding the troponin-tropomyosin complex in place) which subsequently detaches from actin allowing a shift in the position of tropomyosin. As the tropomyosin moves away from the myosin-binding sites on actin, it effectively unblocks these binding sites. Once the myosin-binding sites are exposed, and if sufficient ATP is present, myosin binds to actin to begin crossbridge cycling, a process that facilitates the sliding motion of actin and myosin past each other. Then the sarcomere shortens and the muscle contracts. In the absence of Ca^{2+}, this binding does not occur, so the presence of free Ca^{2+} is an important regulator of myofilament contraction.

As stated above, crossbridge cycling forms the basis for movement and force production in muscle cells. Each cycle of myosin binding to actin and the subsequent movement of the thin filament involves the hydrolysis of one ATP molecule. Figure 1.6 outlines the different stages involved in crossbridge cycling. The illustration starts the cycle with a myosin crossbridge attached to actin. This is followed by the binding of ATP which causes the dissociation of myosin from actin. In the absence of ATP, myosin cannot dissociate from actin which causes the muscle to become stiff (rigor mortis). The state where the low-energy myosin head is bound to actin is known as the rigor configuration. ATP hydrolysis causes a change in shape allowing the myosin head to be cocked while the products of ATP hydrolysis (ADP and inorganic phosphate) remain bound to the myosin head. Cocking of the myosin head aligns it with a new binding site on the actin filament. Myosin binds to actin and the power

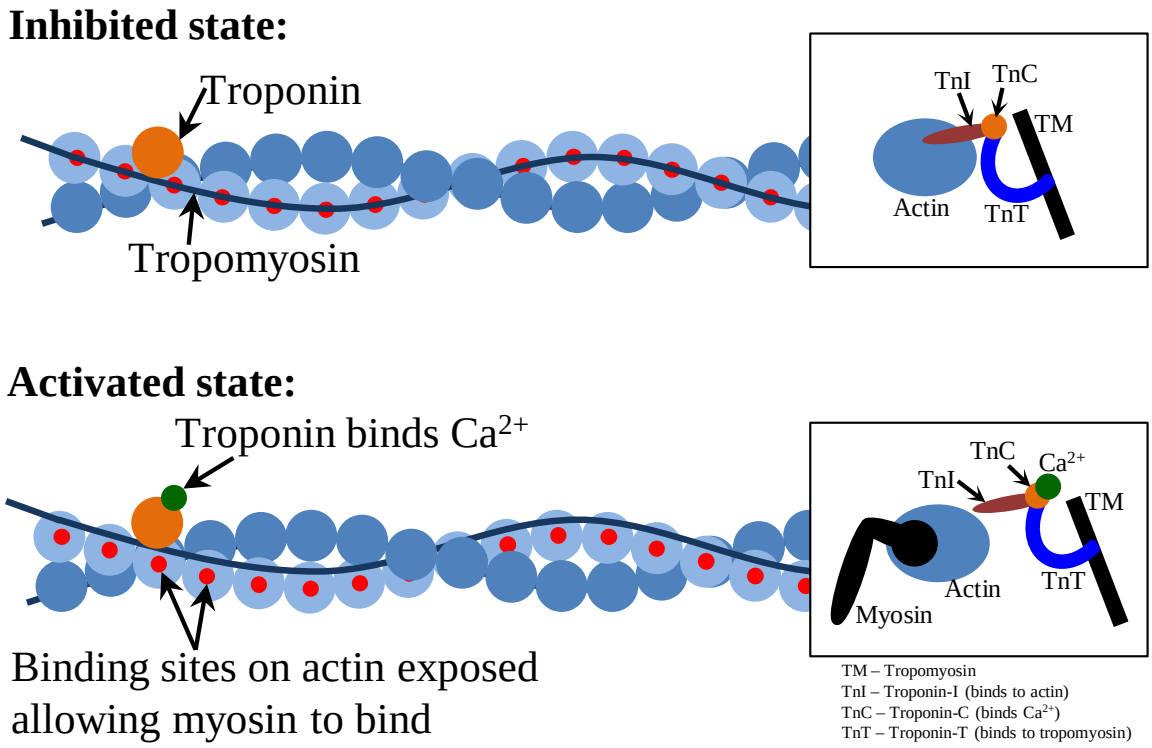

Figure 1.5 : Simplified schematic of actin backbones, shown as blue chains of actin molecules (balls), covered with smooth tropomyosin filaments. Troponin is shown in orange (subunits not distinguished). Upon binding calcium, troponin moves tropomyosin away from the myosin-binding sites on actin (bottom), effectively unblocking it. Troponin C (TnC) binds Ca^{2+}, which stabilizes the activated state, where troponin I (TnI) is no longer bound to actin. Troponin T (TnT) anchors the complex on tropomyosin.

stroke follows. Initial weak binding releases inorganic phosphate and the subsequent stronger binding triggers the power stroke and the release of ADP. The power stroke not only results in the return of the myosin head to its low-energy conformation, it generates force, pulling the thin filament toward the center of the sarcomere. This is followed by binding of another ATP molecule causing dissociation of myosin from actin and a repeat of the cycle. The crossbridges cycle independently from one another and as a result of the large number of independent instantaneous crossbridges

formed, muscle contraction is smooth and not ratchet-like.

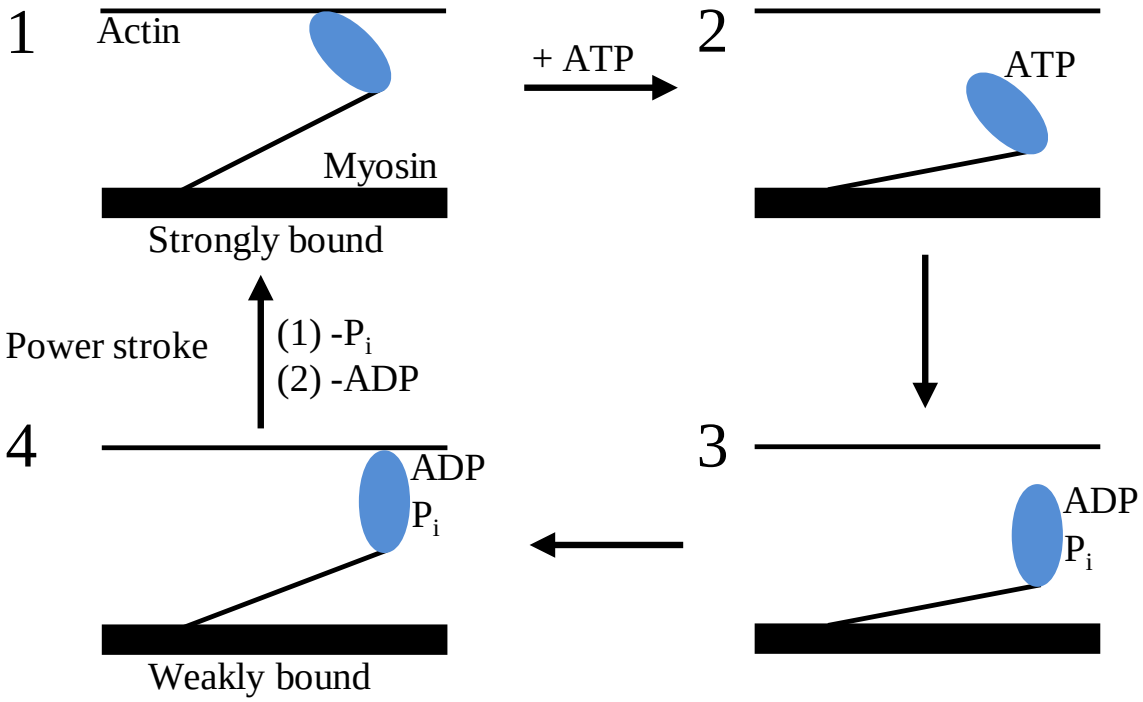

Figure 1.6 : Illustration of the different stages involved in a crossbridge cycle.

1.2.2 Excitation-Contraction Coupling

Excitation-contraction coupling (ECC) is the process whereby a cellular membrane depolarization triggers a myocyte to contract. When a myocyte is depolarized, Ca^{2+} ions enter the cell through LCCs ($I_{Ca,L}$) located on the sarcolemma (Fig. 2.3). This Ca^{2+} triggers a subsequent release of Ca^{2+} that is stored in the sarcoplasmic reticulum (SR) through Ca^{2+}-release channels called ryanodine receptors (RyR in Fig. 2.3). Calcium released by the SR increases the intracellular Ca^{2+} concentration from about 0.1 to 1.0 μM. The free Ca^{2+} binds to troponin C (TnC) which is part of the regulatory complex attached to the thin filaments. When Ca^{2+} binds to TnC, this induces a

conformational change in the regulatory complex such that troponin I (TnI) exposes a site on the actin molecule that is able to bind to the myosin ATPase located on the myosin head. This binding results in ATP hydrolysis that supplies energy for a conformational change to occur in the actin-myosin complex. The result of these changes is a movement (ratcheting) between the myosin heads and the actin, such that the actin and myosin filaments slide past each other hence shortening the sarcomere length. Ratcheting cycles occur as long as the cytosolic Ca^{2+} remains elevated. As the Ca^{2+} entry into the cell decreases and Ca^{2+} is resequestered back into the SR by an ATP-dependent Ca^{2+} pump (SERCA, sarcoplasmic reticulum Ca^{2+}-ATPase) as shown in Fig. 2.3, thus lowering the cytosolic Ca^{2+} concentration and removing Ca^{2+} bound to TnC. To a quantitatively smaller extent, cytosolic Ca^{2+} is transported out of the cell by the sodium-Ca^{2+}-exchanger (NCX). The reduced intracellular Ca^{2+} induces a conformational change in the troponin complex leading, once again, to TnI-mediated inhibition of the actin binding site. At the end of the cycle, a new ATP binds to the myosin head, displacing the ADP, and the initial sarcomere length is restored.

Mechanisms that enhance the concentration of cytosolic Ca^{2+} increase the amount of ATP hydrolyzed and the force generated by the actin and myosin interactions, as well as the velocity of shortening. Physiologically, cytosolic Ca^{2+} concentration is influenced primarily by beta-adrenoceptor-coupled mechanisms. Beta-adrenergic stimulation, as occurs when sympathetic nerves are activated, increases cAMP which in turn activates protein kinase-A to increase Ca^{2+} entry into the cell through L-type Ca^{2+} channels. Furthermore, activation of the cAMP-dependent protein kinase phosphorylates a protein (phospholamban (PLB)) on the SR that normally inhibits Ca^{2+} uptake. This decrease in inhibition by phospholamban leads to an increased

rate of Ca^{2+} uptake by the SR. Therefore, beta-adrenergic stimulation increases the force and shortening velocity of contraction (positive inotropy), and increases the rate of relaxation (positive lusitropy).

Another potential regulatory mechanism for ECC involves altering the sensitivity of TnC for Ca^{2+}. There are investigational drugs that enhance TnC Ca^{2+} sensitivity and thereby exert a positive inotropic influence on the heart. One potential downside with these drugs, however, is that enhanced TnC binding to Ca^{2+} can reduce the rate of relaxation, thereby causing diastolic dysfunction.

In systolic heart failure, ECC can be impaired at several different sites. First, there can be decreased influx of Ca^{2+} into the cell through L-type Ca^{2+} channels (resulting from impaired signal transduction), which decreases subsequent Ca^{2+} release by the SR. There can also be a decrease in TnC affinity for Ca^{2+}, so that a given increase in Ca^{2+} in the vicinity of the troponin complex has less of an activating effect on cardiac contraction. In some forms of diastolic heart failure, there is evidence that the function of the SR ATP-dependent Ca^{2+} pump is impaired. This defect would retard the rate of Ca^{2+} uptake by the SR and reduce the rate of relaxation, leading to diastolic dysfunction.

1.3 Modeling Cardiac Myocytes: A Historical Review

1.3.1 Voltage-Gated Ionic Currents

For many years, HodgkinHuxley (HH) models have been the standard for describing voltage-dependent membrane ion current dynamics [13]. These models introduced the concept of activation and inactivation gates, and related the current through an ensemble of channels to the state of these gates. More recent studies of single-

channel dynamics have shown that HH models have significant limitations, often due to the assumption that channel gates behave independently. This assumption has been relaxed in recent models by using continuous time Markov chains [14] to describe channel gating and ionic currents. Markov chain models are comprised of a number of different states, loosely corresponding to different conformations of channel protein(s) as they undergo activation and inactivation, with transition rates between certain states being voltage and Ca^{2+} dependent. Markov models are parameterized by the state transition rates. These rates reflect the free energy profile between two protein conformations [4] and are determined experimentally. This is done through application of various voltage-clamp protocols, recording current responses, and adjusting the transition rates using minimization algorithms to yield a best fit to the data. Markov models of ion currents are now used extensively. Applications have included quantitative modeling of the effects of channel mutation [15], drugchannel interactions [16] and channel phosphorylation [17] on myocyte responses.

1.3.2 Sarcolemmal Membrane Transporters

The first myocyte model to explicitly describe membrane transporter function was the DiFrancesco-Noble model [18]. The various sarcolemmal pumps and exchangers were modeled as algebraic functions of the relevant intracellular and extracellular Na^+, Ca^{2+}, and K^+ concentrations. This was further refined and constrained using experimental data in the work of Luo and Rudy [19]. In 1998, Shannon et al. [20] proposed a new model of the SR Ca^{2+}-ATPase that included forward- and reverse-current components, each with its own Ca-binding constant and peak forward and reverse rates. This model is now used extensively, and has been integrated into the models of Winslow et al.[21], Puglisi and Bers[22], Shannon et al. [23], and Grandi et

al. [24]. Recently, rigorously constrained elaborate Markovian models of the Na^+K^+ pump [25], the SR Ca-ATPase [26], and Na^+Ca^{2+} exchanger [27] have been published but have not yet been incorporated in whole cell models.

1.3.3 Ca^{2+}-Induced Ca^{2+} Release

Graded Ca^{2+}-induced Ca^{2+} release with high gain is somewhat paradoxical according to Stern [28], in that the positive feedback inherent in such high-gain systems tend to produce regenerative, nearly all-or-none release rather than graded release. Several deterministic models have been developed to explain excitation-contraction (E-C) coupling [29, 30], but none of them can explain the mechanism of graded release at high gain over a wide range of values for sarcolemmal Ca^{2+} current. Stern [28] proposed that such a gradation paradox might be explained if the stimulus for Ca^{2+} release by RyRs were actually the local nanodomains of $[Ca^{2+}]$ generated by nearby L-type channels, rather than the global cytosolic $[Ca^{2+}]_{myo}$. According to this hypothesis, graded control of macroscopic SR Ca^{2+} release can be achieved by graded statistical recruitment of individual, autonomous, all-or-none stochastic release events [31]. In these studies, a distributed differential model of high order that included dynamic interactions between large numbers of individual channels was used to demonstrate this concept. However, rather large amounts of computation time are required with distributed stochastic models of this type. Additional models have sought to characterize the Ca^{2+} release complex, including several [32, 33, 34] based on the stochastic release process adopted by Stern et al. These statistical models have solved the graded release problem, however, they too suffer with extensive computational burden. Other models based on the simplified local control model of CICR developed by Hinch et al. [35] sought to adopt a lower order description of the E-C

coupling process [36, 37] by making an approximation of rapid equilibrium in the dyadic space. However, it is known that the latency from onset of Ca^{2+} entry via the $I_{Ca,L}$ channel to triggered SR Ca^{2+} release is known to increase with decrease in the magnitude of $I_{Ca,L,TT}$ [38], the modeling of which is made possible by considering Ca^{2+} diffusion in the dyadic medium. These models [36, 37] also approximate the SR as a single volume compartment with no distinction between junctional versus the longitudinal (network) SR compartments. However, recent work [39] points towards the important role of the Ca^{2+} refilling rate from the network to junctional SR in controlling RyR release termination via the luminal sensor. Shiferaw et al.[40] developed a computationally tractable model of Ca^{2+} cycling to represent the release of calcium from the SR as a sum of spatially localized events that correspond to Ca^{2+} sparks, assuming the recruitment rate of Ca^{2+} sparks is directly proportional to the whole-cell $I_{Ca,L}$ current. While this approach allows robust release termination, this assumption overlooks the complex calmodulin mediated interaction of the $I_{Ca,L}$ channel with calcium in its vicinity. Although a recent study [41] showed that the protein-protein interactions within the luminal sensor plays a vital role in modulating sarcoplasmic reticulum calcium-release in cardiac myocytes, facilitating robust SR release termination, it is yet to be widely adopted in models of CICR.

1.3.4 Regulation via Cell Signalling

Cardiac ion channels as well as proteins involved in CICR and EC coupling are primary targets for regulation via cell signaling pathways. The most widely studied pathway is that of the β-adrenergic signaling cascade. Early attempts to model the effects of PKA-mediated phosphorylation of these targets on the properties of CICR and the AP involved modeling the stimulated cell by altering the function of the

target proteins based on the measured effects of phosphorylation. Greenstein et al. [42] developed a model of the canine ventricular myocyte in the presence of 1 μM isoproterenol (a β-adrenergic agonist). However, this model did not describe the dynamics of the β-adrenergic signaling pathway. Saucerman et al. [43] developed a differential-algebraic model of the dynamics of the β-adrenergic signaling pathway, and incorporated it into the rabbit myocyte model of Puglisi and Bers [22]. Recently, the model of Saucerman et al. [43] was incorporated into the guinea pig ventricular model of Faber and Rudy [44] in a study of the role of β-adrenergic agonists and antagonists in long-QT syndrome [45].

An important Ca^{2+} cycling regulatory mechanism of recent interest is the signaling pathway involving Ca^{2+}/calmodulin-dependent kinase II (CaMKII), whose target proteins include LCCs, RyRs, PLB, and the SR Ca-ATPase, as well as N^{+} and K^{+} channels [46]. The first model of the cardiac myocyte to integrate the role of CaMKII was presented by Hund and Rudy [47]. Grandi et al. [17] developed a model of CaMKII overexpression in the rabbit ventricular myocyte. Saucerman and Bers [48] incorporated models of CaM, CaMKII, and calcineurin (CaN) into the Shannon et al. [23] model in order to better understand the functional consequences of the different affinities of CaM for CaMKII and CaN. Recently, Hashambhoy et al. [49] described dynamic CaMKII phosphorylation of LCCs in the context of the stochastic, local control canine ventricular myocyte model of Greenstein and Winslow [33].

1.3.5 Coupled Electromechanics

Cardiac cell is a coupled electromechanical system in which membrane depolarization triggers an increase in intracellular Ca^{2+} and contraction of the myofilaments that allows the heart to pump. The affinity of Ca^{2+}-binding regulatory sites on troponin

which is the largest buffer of Ca^{2+} in the cell is thought to be a function of force generated by the myofilaments. The Ca^{2+} transient is known to be altered by force generation [1]. Therefore, including myofilament binding of Ca^{2+} is not only crucial for modeling force generation by the myocyte, but is also important for realistic modeling of cytosolic Ca^{2+} transients and Ca^{2+} cycling. Myofilament dynamics have been captured by various representations ranging from the highly simplified models to complex empirical [50, 51] and biophysical models [1]. While simplified models tend to use an explicit parabolic tension profile [52], the empirical models use predefined expressions to specify the average force developed by the cross bridges, based on experimental observations of isolated muscle contraction under different loading conditions. On the contrary, biophysical models of cardiac myofilament dynamics include descriptions of crossbridge cycling and their elastic properties. Here, we provide an overview of a subset of force generation models that describe both the electrochemical as well as the electromechanical aspect of cardiac cells in order to illustrate the progression of the field. An extensive review of various myofilament models in the literature may be found elsewhere [53, 54, 55].

The HilgemannNoble (HN) model [29] of rabbit atrium incorporated one ordinary differential equation to represent Ca-based activation, and a second to represent crossbridge binding. This formulation was presented as an abstract description of force generation. This basic formulation was carried on to models later developed by Noble and coworkers [56], including model extensions for describing sarcomere length (SL) sensitivity [57]. The HunterMcCullochter Keurs (HMT) [50] model couples a mechanistic myofilament activation model to a fading memory crossbridge model that uses a convolution integral approach. The model includes active force with SL dependence and passive tissue properties. Simulated responses have been compared with a wide

range of experimental measures. The HMT model has been refined [58] and extended [59] recently by incorporation within a model of the rat myocyte AP formulated by Pandit et al. [60]. The Rice-Jafri-Winslow (RJW) model integrated the myofilament model of Rice et al. [61] into the model of the guinea pig action potential formulated by Jafri et al. [62]. The model included a phenomenological representation of cooperative interactions between neighboring troponin/tropomyosin units, including effects of SL. The RJW model has been refined and expanded to reproduce a wider variety of experimental protocols in the Rice et al. model [1]. Importantly, active contraction and re-lengthening can be simulated, and passive muscle properties are included to simulate muscle strips and isolated myocytes, two common experimental preparations. The model has been extended recently by Campbell et al. [63] to replicate canine epicardial, endocardial, and mid-myocardial myofilament responses. Recently, Tran et al. [64] have modified the Rice et al. model to include binding and release of metabolites.

1.4 Mathematical Modeling and Computational Aspects

In comparison to animal or human experiments, reproducing an experiment in-silico has several advantages: (1) repeatability of the experiments and results; (2) complete access to data unlike in-vitro or in-vivo experiments which give insight into only a small set of observed parameters; (3) allows studying different sub-cellular phenomena in isolation. (4) complete control over all the parameters affecting the modeled biophysical phenomena. Hence, computational modeling helps gain mechanistic insight into sub-cellular processes. However, there are various challenges associated with developing numerical models of ventricular myocytes: (1) many sub-cellular biophysical processes including the structure and function of ion channels (proteins),

their mutations and genetic regulation are still only partially understood. Their characteristics are often unknown, or only estimated based on theoretical considerations. Direct observation of sub-cellular events is non-trivial; (2) The mechanisms involved pose a vastly multiscale problem, spanning several orders of magnitude in spatial and temporal scales; (3) Modeling time-evolving, spatially-distributed complex non-linear phenomena is computationally intensive. Despite these challenges, current models of cardiac myocytes have been able to reproduce a large variety of experimental data. Here, we construct a multiphysics model of a rat ventricular myocyte under voltage-clamp conditions describing both its electrochemical as well as electromechanical behavior.

All simulations and analysis were performed on a 2.8GHz Intel® Core™2 Duo CPU-based computer using Microsoft Windows XP operating system. The sarcolemmal membrane charge balance equations, the Ca^{2+} material balance equations in the myoplasm and SR, and the force balance equations describing the model for myofilament contraction constitute a set of 93 ordinary differential equations (ODEs). A fixed-step Merson-modified Runge-Kutta 4th-order numerical integration scheme [65] was used to solve this set of 1st-order differential equations (ODE) describing the dynamic model. The free Ca^{2+} concentration in the dyad is governed by the time courses of the Ca^{2+} fluxes through Ca^{2+} transport systems, as well as by the time course of Ca^{2+} binding to Ca^{2+} buffers present in the junction [66]. Description of the spatio-temporal dynamics of calcium transients in the dyad triggered by Ca^{2+} stimulus (basis of CICR) requires calculation of the partial differential equations (PDE) of the whole reaction-diffusion system. Formation and dissipation of Ca^{2+} gradients around an open channel (DHP-sensitive and Ry-sensitive channels in the dyad) is assumed instantaneous as was validated for microsecond timescale and nanoscopic

space by Naraghi and Neher [67]. Local Ca^{2+} concentration in the vicinity of open channels (located on opposing boundaries of the dyadic space) was calculated as the steady state gradient around a point source [68]. The Ca^{2+} concentration increments from individual channels at each point in space were assumed to be additive [69, 67]. The software kernel follows the changes in the state of trigger and release channels together with variables like membrane voltage and spatial Ca^{2+} concentration to calculate the instantaneous rate constants and estimate the duration of transient events. Crank [70] discusses diffusion problems in a two-phase heterogeneous medium and shows that diffusion through a system of barriers (RyR feet structures in the dyadic cleft space) can be approximated by diffusion in the same region without barriers but with a reduced effective diffusion coefficient. We hence take this approach in modeling the Ca^{2+} diffusion by solving the 2-D Laplacian equation (Appendix C.3, Eq. C.150) in the DCU without explicitly accounting for local potential fields. More specifically, an explicit finite difference scheme was used to solve these Laplacian equations describing Ca^{2+}-diffusion in the dyadic space analogous to the method detailed in Smith et al.[71]. Specifically, a radial symmetry is employed in solving the PDE in the dyadic volume allowing the solution to be computed in a rectangular cross-section discretized into a 20 by 20 cartesian grid. The spatial step size used in the r and z-direction was 10 nm and 0.76 nm respectively (Table B.4). We use the method of lines (discretization in space) to solve the PDE. The full set of ODEs and finite difference equations are solved simultaneously to obtain the complete solution. To construct the voltage-dependent rate functions involved in the 6 state Markovian model for $I_{Ca,L}$, parameter estimation was performed using a non-linear least-squares method [72] to obtain the solution of the system of non-linear ordinary differential equations. Specifically, we have employed an algorithm given by Lau [73]. Execution

of a single cycle which translates to 200 ms at 5 Hz took 21 seconds with a time step of 1μs. Results were visualized using Matlab (Mathworks, Natick, MA) and Origin (OriginLab Corp., Northampton, MA).

1.5 Specific Contributions and Thesis Overview

In this thesis, we use a multiphysics model of a rat ventricular myocyte to examine its electrochemical and electromechanical behavior. At first (Chapter 2), we discusses the construction of the comprehensive mechanistic model of CICR under voltage clamp conditions in the rat ventricular myocyte, which includes electrical equivalent circuit models for both the free sarcolemma and the portion involving junctional transmission, as well as, fluid compartment models for several fluid media within the cell (dyadic cleft space, longitudinal sarcoplasmic reticulum (LSR or Ca^{2+} uptake compartment), junctional sarcoplasmic reticulum (jSR or release compartment), and the cytosolic fluid compartment). An external bathing medium completes our fluid compartment description of the cell (Fig. 2.3). The multiple component model is referred to as the "whole-cell model" (Figures 2.3 and 2.4). We discuss the development of the voltage-gated ion channel $I_{Ca,L}$, sarcolemmal membrane transporters (Na^+/Ca^{2+} exchanger I_{NaCa}, sacrolemmal Ca^{2+}-ATPase pump I_{PMCA} and the Na^+/Cs^+ pump I_{NaCs}), the SR Ca^{2+}-ATPase pump and the RyR release channel. We develop a novel model of a luminal sensor which mediates robust SR release termination allowing long-term Ca^{2+} stability, a feature lacking in recent models describing CICR. We describe the modifications and enhancements made to the approximate model of cooperative activation and crossbridge cycling (Fig. 2.9) reported by Rice et al. [1], which we adopt here to develop a composite model to examine excitation-contraction coupling. This work has been published in Krishna et al. [66].

The composite model developed is used to perform an extensive study (Chapter 3) of cellular Ca^{2+} dynamics. The L-type DHP-sensitive Ca^{2+} channel has a key role in initiating CICR. Though the activation of the $I_{Ca,L}$ channel is solely voltage dependent once activated, the inactivation of the channel is influenced not only by the trans-membrane voltage but also the Ca^{2+} concentration in the vicinity of the channel [74]. We perform a thorough analysis of its activation and inactivation mechanisms by selectively blocking each pathway in the model to gain insight into their relative contribution. Using our deterministic model, we not only establish a graded Ca^{2+}-induced Ca^{2+} release but also demonstrate an extremely valuable characteristic of the CICR process, the high gain associated with it. A small amount of Ca^{2+} entering the DCU via the $I_{Ca,L,TT}$ channel causes a large release of Ca^{2+} from the sarcoplasmic stores via the Ry-sensitive Ca^{2+} release channel on the jSR lumen. The high gain associated with CICR is essential in producing physiological cytosolic Ca^{2+} transients. The strong dependence of RyR release on the jSR Ca^{2+} content is examined and the role of the luminal sensor in modulating CICR is investigated. We hypothesize that the luminal sensor, is a key element responsible for robust post-release RyR inactivation and refractoriness of the Ry-sensitive Ca^{2+} release channel, and is critical in providing realistic fits to cytosolic Ca^{2+} transients and an adequate refilling time for the SR Ca^{2+} stores. We test this hypothesis by simulating an impaired luminal sensor to understand its effect on CICR. The role of Ca^{2+} regulating mechanisms in handling induced Ca^{2+}-perturbations is studied. In particular, several VC protocols including lowering of extracellular calcium to affect Ca^{2+} loading of the sarcoplasmic reticulum (SR), and administration of blockers caffeine and thapsigargin have been utilized to probe the phenomena surrounding SR Ca^{2+} release. Finally, using a rigorous cellular Ca^{2+} balance, we analyze long-term Ca^{2+} stability under conditions

of repetitive stimulation. This work has been published in Krishna et al. [66].

We present a coupled electromechanical study (Chapter 4) to investigate the role of various factors influencing cellular contractile response. In particular, direct factors such as the amount of activator Ca^{2+} available to trigger contraction and the type of mechanical load applied (resulting in isosarcometric, isometric or unloaded contraction) are investigated. We also study the strong impact of temperature (22 to 38°C) on myofilament contractile response. The critical role of myofilament Ca^{2+} sensitivity in modulating developed force is likewise studied. In particular, we model the effect of isoproterenol, a β-adrenergic agonist, which is known to cause a decline in myofilament Ca^{2+} sensitivity as a result of protein kinase A (PKA) mediated phosphorylation of troponin I [55, 75]. We also examine the indirect coupling of intracellular contractile mechanism with the plasma membrane via the Na^{+}/Ca^{2+} exchanger (NCX). Finally, we demonstrate a key linear relationship between the rate of contraction and relaxation, which is shown here to be intrinsically coupled over the full range of physiological perturbations. This work has recently been accepted for publication.

The rate-dependent effects on the Ca^{2+} sub-system in a rat ventricular myocyte are investigated (Chapter 5). We employ our deterministic mathematical model describing various Ca^{2+} signalling pathways under voltage clamp (VC) conditions, to better understand the important role of calmodulin (CaM) in modulating the key control variables Ca^{2+}/calmodulin-dependent protein kinase-II (CaMKII), calcineurin (CaN), and cyclic adenosine monophosphate (cAMP) as they affect various intracellular targets. We study the frequency dependence of the peak force generated by the myofilaments, the force-frequency response (FFR) and demonstrate that our model reproduces positive peak FFR observed in rat ventricular myocytes both in

the presence/absence of cAMP mediated β-adrenergic stimulation. The frequency-dependence of the trigger current ($I_{Ca,L}$) and RyR-release are investigated to provide a quantitative insight into rate-dependence of Ca^{2+}-induced Ca^{2+}-release (CICR). We examine the rate-dependence of the relative role of the sodium-calcium exchanger (NCX) and the SERCA pump and the ensuing frequency-dependence of sarcoplasmic reticulum (SR) Ca^{2+} content. We demonstrate that although rat ventricular myocytes exhibit a positive peak FFR in the presence/absence of beta-adrenergic stimulation, they show a characteristic increase in the positive slope in FFR due to the presence of Norepinephrine or Isoproterenol. We identify cAMP-mediated stimulation, and rate-dependent CaMKII-mediated up-regulation of $I_{Ca,L}$ as the key mechanisms underlying the aforementioned positive FFR.

Integrative modeling provides a quantitative understanding of the relationships between molecular function and the integrated behavior of the cardiac myocyte in health and disease. It allows for studying cellular subsystems in isolation and hence helps in developing an understanding of the cellular genesis for various forms of systolic heart failure and diastolic dysfunction. A thorough understanding of the various Ca^{2+} regulatory mechanisms and signalling pathways in the cell, aids in identifying novel therapeutic targets for drug design.

Chapter 2

Model Development

Our objective was to develop an integrated multiphysics model of the rat ventricular cell under voltage clamp conditions, which includes the description of various Ca^{2+} signalling pathways in the dyadic space, the myoplasmic medium and the sarcoplasmic reticulum (Fig. 2.3) as well as a comprehensive coupled mechanical system describing the contractile machinery responsible for force generation. We use our model to explain Ca^{2+} signaling at the nanoscale level of the dyad and integrate the contributions of many dyads to produce a Ca^{2+} transient and continuous Ca^{2+} balance at the whole-cell level.

Calmodulin mediates the regulation of a variety of Ca^{2+}-dependent signalling pathways in the heart involving CaMKII and CaN [76, 48]. These protein-mediated interactions form the basis for a robust mechanism that enables a cell's response to increased heart rate. CaMKII is reported to be responsive when targeted to Ca^{2+} release sites such as the dyadic cleft, and CaN is responsive to gradual changes in the lower-amplitude myoplasmic Ca^{2+} signals [48]. This heterogenous response is a result of the different affinities of CaMKII and CaN for CaM [76] and the non-uniform distribution of these proteins in the cell. Recent study [77] also attributes a key role in frequency-dependent acceleration of relaxation to activated-CaMKII in the cytosol. The model of the CaM-dependent Ca^{2+} signalling process (Fig. 2.1), which includes a reaction map for cooperative binding of Ca^{2+} to CaM, the scheme for CaM buffering, probabilistic model of CaMKII subunit switching and the reaction map for reversible

binding of CaM, Ca_2CaM and Ca_4CaM to CaN, is adopted from Saucerman et al [48]. However, to reproduce relative local CaMKII and CaN activity, modifications were made to the rate constants for CaM buffering in the dyad (Appendix B, Table B.8).

We incorporate the effects of β-adrenergic stimulation via cAMP-dependent modulation based on a model (Fig. 2.2) derived from Demir et al [78]. Stimulation of β-adrenoceptors by Isoproterenol (Iso) results in the activation of a G protein (g_s) that stimulates Adenylate cyclase (ADC) and enhances the production of cAMP. Subsequently, cAMP may directly or indirectly activate various intracellular targets including ion channels and exchangers. The indirect modulation involves activation of cAMP-dependent Protein kinase A (PKA) before modulation of the channel protein. The reaction kinetics for the cGMP-mediated pathway (Fig. 2.2) involving acetylcholine (ACh), nitric oxide (NO) and soluble guanylate cyclase (sGC) are adopted from Yang et al [79]. Although it is well known that cGMP modulates its targets via protein kinase G (PKG) or phosphodiesterase (PDE), we have refrained from modeling these protein interactions. Given that NO synthase inhibition and/or NO donor had little or only marginal effects on the FFR in rat ventricular myocardium [80], the cGMP level is kept constant in this study.

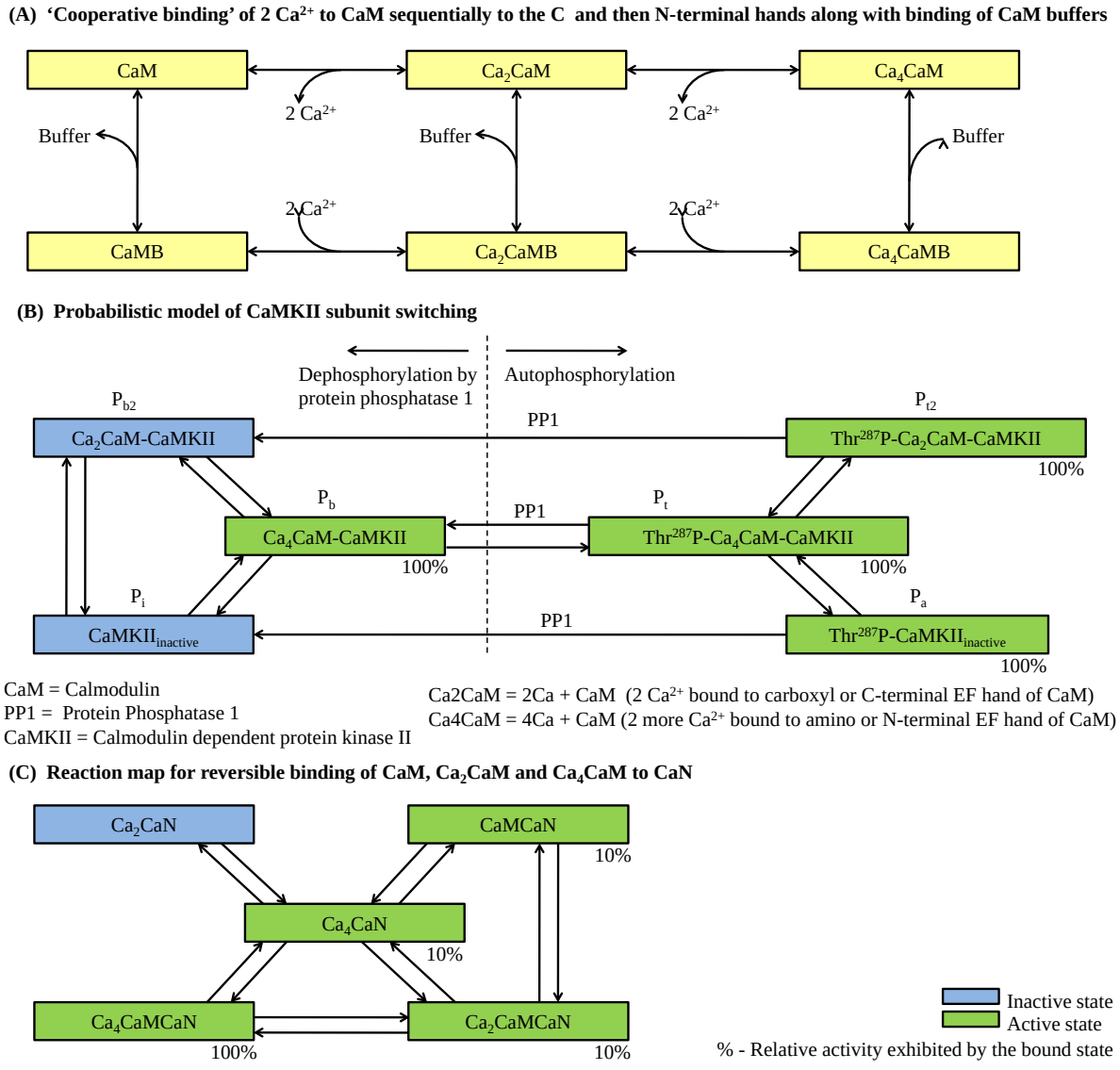

Figure 2.1 : Reaction Maps. (A) Cooperative binding of 2 Ca^{2+} to CaM sequentially to the C and then N-terminal hands along with binding of CaM buffers; (B) Probabilistic model of CaMKII subunit switching; (C) Reaction map for reversible binding of CaM, Ca_2CaM and Ca_4CaM to CaN.

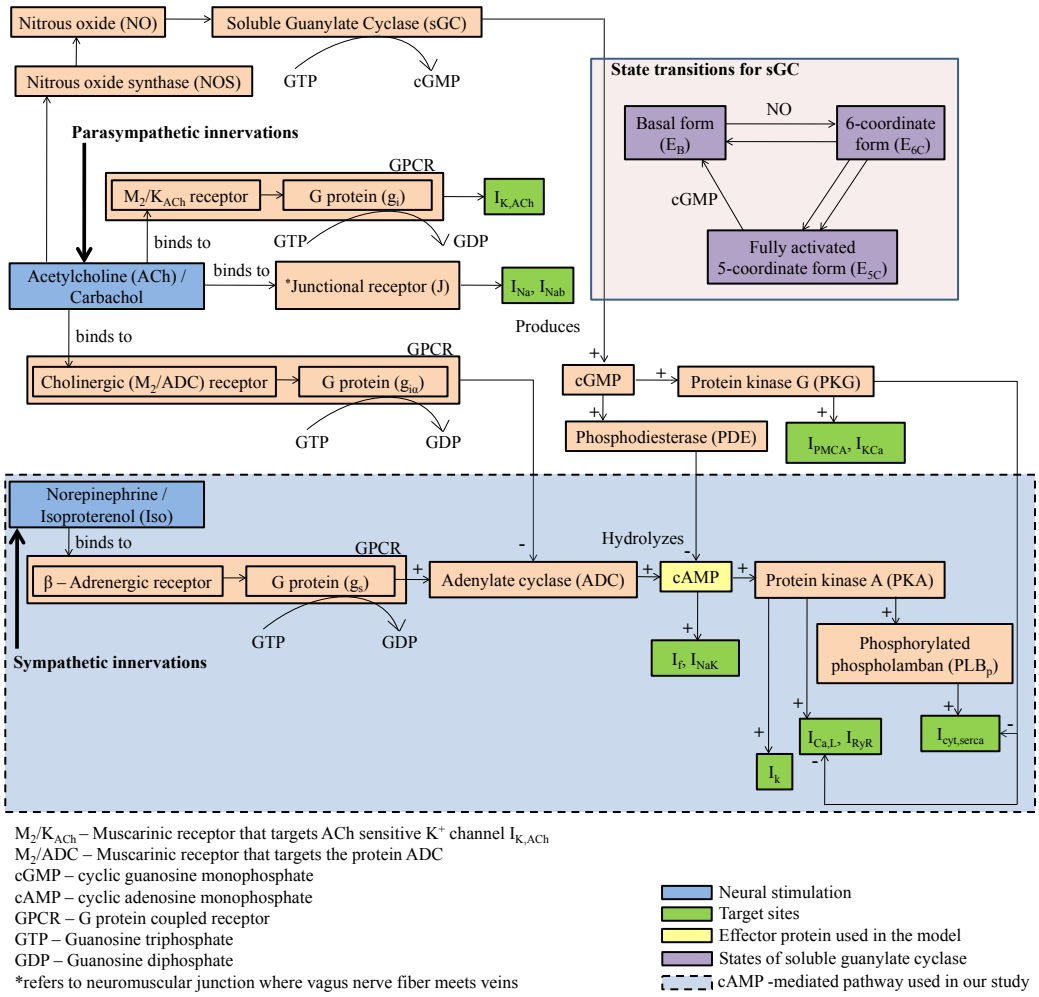

Figure 2.2 : Reaction pathways triggered by sympathetic and parasympathetic neural stimuli invoking cAMP [78] and cGMP-mediated [79] modulation of various subcellular targets respectively. ACh-mediated effects of junctional receptor on Na^+ current and background Na^+ current and extrajunctional muscarinic M_2/K_{ACh} receptor on $I_{K,ACh}$ (direct muscarinic pathway) and cAMP-mediated effects of β-adrenoreceptor (adrenergic pathway) and cholinergic M_2/ADC receptor (indirect muscarinic pathway) on L-type Ca^{2+} ($I_{Ca,L}$), K^+ (I_K), hyperpolarization-activated (I_f), and Na^+/K^+ (I_{NaK})currents are shown†. Although cAMP-dependent modulation of $I_{Ca,L}$ and I_{up} are known to be PKA-mediated, we make use of a lumped cAMP term to model this influence. A similar lumped cAMP term is employed to modulate phosphorylation of PLB which in turn affects the SERCA pump. ACh triggered NO-mediated synthesis of cGMP by sGC is modeled employing a 3-state model for sGC transition based on Yang et al [79]. cGMP is involved in suppressing cAMP activity via PDE. cGMP also enhances I_{PMCA}, Ca^{2+} activated K^+ channel (I_{KCa}) and suppresses $I_{Ca,L}$, $I_{cyt,serca}$ via PKG (not explicitly modeled, but lumped into a cGMP term). †The rat ventricular cell model used in this study is however limited to Ca^{2+} related channel, exchanger and pumps ($I_{Ca,L}$, I_{NaCa}, I_{PMCA} and $I_{cyt,serca}$), while lacking exclusive Na^+ or K^+ related channels and transporters (as shown in Fig. 2, Krishna et al [66]). The part of the model describing cAMP-mediated pathway used in our study is highlighted (blue).

2.1 Electrochemical Description of Ca^{2+} Sub-System

Our model for the electrochemical description of the cell consists of an electrical-equivalent model for the cell membrane and a fluid-compartment model describing the flux of ionic species between the extracellular and several intracellular compartments (cell cytosol, SR and the dyadic coupling unit (DCU), in which resides the mechanistic basis of CICR). The DCU is described as a controller-actuator mechanism, internally stabilized by negative feedback control of the unit's two diametrically-opposed Ca^{2+} channels (trigger-channel and release-channel). It releases Ca^{2+} flux into the cytoplasm and is in turn enclosed within a negative feedback loop involving the SERCA pump, regulating $[Ca^{2+}]_{myo}$. we start with a broad discussion of the elements of the DCU and its Ca^{2+} supply (the jSR), and continue with a progressively more detailed description of the whole cell model. It is important to note that all Ca^{2+} concentrations discussed in the model pertain to unbound Ca^{2+} unless specified.

2.1.1 Membrane Classification

We assume that a continuous membrane barrier exists between the cytoplasm and the external bathing medium (Fig. 2.3A; Fig. 2.4), which consists of two components: a surface sarcolemma (M_{FreeSL} in Fig. 2.5) free of any sub-membrane contact with the junctional sarcoplasmic reticulum (jSR) and the remnant membrane ($M_{JunctionalSL}$ in Fig. 2.5) that does make contact with the jSR via a dyadic space (nanodomain) (Fig. 2.3A). These membrane components have the same basic plasma membrane, but differ in content with regard to total membrane surface area, type and distribution of transmembrane ion channels, ATPase pumps and exchangers, as well as their functional coupling with a dyadic space.

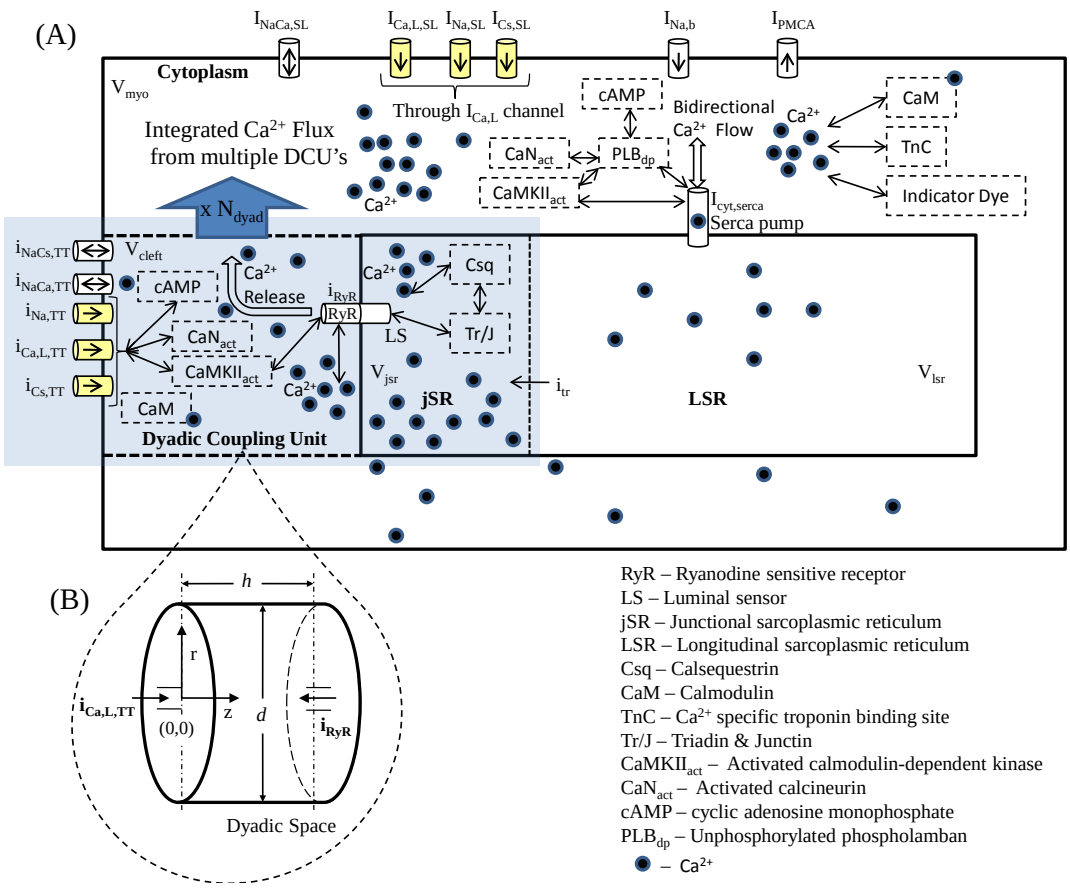

Figure 2.3 : Cellular fluid compartments. (a) Model configuration showing dyadic space, jSR, LSR, cytoplasm and sarcolemma; (b) Inset provides a more detailed description of the dyadic space showing the coupling of the two types of Ca^{2+} channels (trigger and Ca^{2+} release channels) via the dyadic fluid medium. Only one representative dyadic coupling unit is shown, however the whole model contains such 10,000 identical units lumped together.

Ultrastructural information from several cardiac preparations including the rat ventricular cell has been compiled by Bers [55], which can be used to estimate the percentage of the cell membrane in contact with a dyadic space, for either the free surface plasmalemma or for the transverse tubule (TT) which brings the extracellular medium to the plasma membrane of the dyadic coupling unit. Thus, the bounding membrane is divided into two lumped parts (free and coupled) based on the existence

of sub-membrane coupling to a dyadic space (Table B.1). A portion of membrane could be part of a transverse tubular membrane, but if there is no dyadic coupling involved, that membrane would be classified as belonging to the free surface plasmalemma. Another portion of membrane might be part of the bounding outer surface of the cylindrical cell and yet have submembrane coupling to a dyadic space. In this case, it would be classified as belonging to the coupled category. Table B.4 gives values for volumes of the fluid compartments (shown in Fig. 2.5) assumed for the rat ventricular cell, which are largely based on measured data from rat ventricular myocytes [55].

2.1.2 Channel and Exchanger Distribution

Recent research has also shown that besides L-type Ca^{2+} channels, Na^{+}/Ca^{+} exchanger activity is also found predominantly in the T-tubules of rat ventricular myocytes [81]. Our model configuration reflects this finding in that the tubular fraction of $I_{Ca,L}$,I_{NaCa} and I_{NaCs} channels facing a unitary dyadic space are denoted as $i_{Ca,L,TT}$ (source of trigger Ca^{+} into a unitary dyad), $i_{NaCa,TT}$ and $i_{NaCs,TT}$ respectively (Fig.2.4). The free sarcolemmal component of these same channels are denoted as $I_{Ca,L,SL}$, $I_{NaCa,SL}$ and $I_{NaCs,SL}$ respectively. $I_{Ca,L,TT}$ is the total current entering through L-type Ca^{2+} channels via all the dyadic units (N_{dyad}). We define the total L-type current $I_{Ca,L}$ as the combination of $I_{Ca,L,TT}$ and $I_{Ca,L,SL}$ (i.e., $I_{Ca,L} = I_{Ca,L,TT} + I_{Ca,L,SL}$). $I_{Ca,L}$ in our model is mostly (90%) from the L-type Ca^{2+} current in the T-tubules, since Kawai et al.[82], found L-type current to be highly concentrated (9-fold) in the T-tubules ($I_{Ca,L,TT}$) vs. the cell surface sarcolemma ($I_{Ca,L,SL}$) of rat ventricular myocytes. We described the $I_{Ca,L}$ channel using a 6-state Markovian model as shown in Fig. 2.6A. The distribution of I_{NaCa} and I_{NaCs} correspond to that

of $I_{Ca,L}$ channel in order to ensure Ca^{2+} and Na^{+} ion balance.

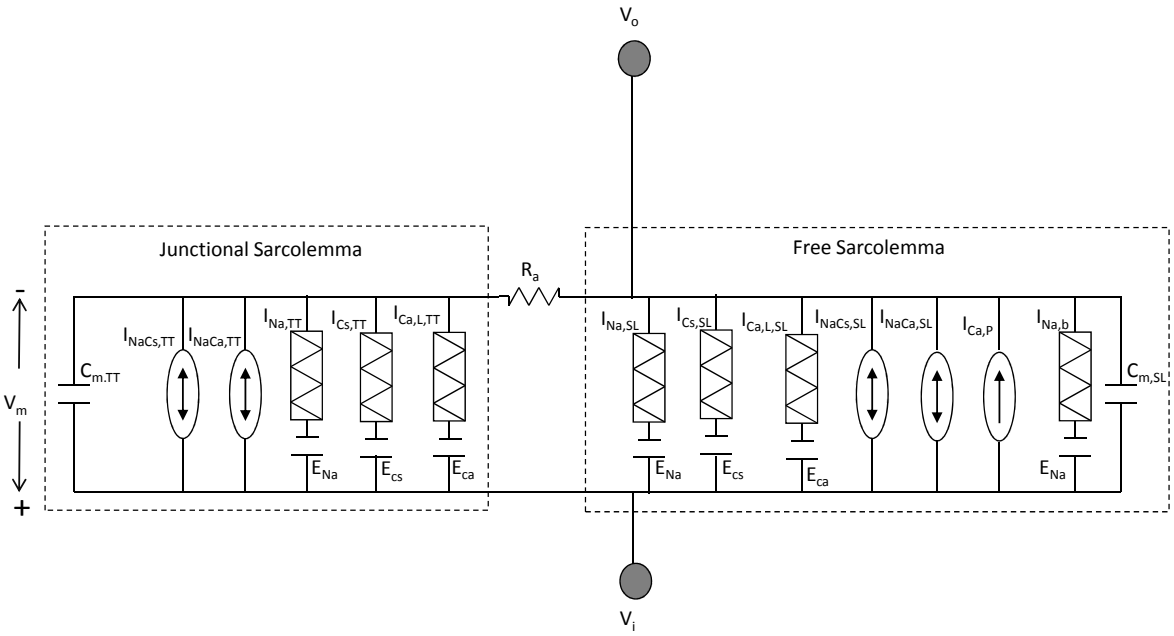

Figure 2.4 : $C_{m,TT}$: membrane capacitance of the junctional sarcolemmal membrane coupled with the dyadic space; $C_{m,SL}$: membrane capacitance of the uncoupled free sarcolemmal membrane; ; Currents through the uncoupled free sarcolemmal membrane are (a) $I_{Ca,L,SL}$: L-type calcium current, (b) $I_{Na,SL}$: sodium current through the DHPR channel, (c) $I_{Cs,SL}$: cesium current through the DHPR channel, (d) $I_{NaCa,SL}$: sodium-calcium exchanger current, (e) $I_{NaCs,SL}$: sodium-cesium exchanger current, (f) I_{PMCA}: calcium pump current, (g) $I_{Na,b}$: background sodium current; Currents through the junctional sarcolemmal membrane coupled with a dyadic space are (h) $I_{Ca,L,TT}$: L-type calcium current; (i) $I_{Na,TT}$: sodium current through the DHPR channel, (j) $I_{Cs,TT}$: cesium current through the DHPR channel, (k) $I_{NaCa,TT}$: sodium-calcium exchanger current, (l) $I_{NaCs,TT}$: sodium-cesium exchanger current; V_o: potential in external medium; V_i: intracellular potential; The coupling resistance between the surface sarcolemma and the transverse tubules being very small is neglected in our model hence V_m: common transmembrane potential across both uncoupled and coupled membranes.

Since our study is focused on voltage clamp testing of Ca^{2+} transients in rat ventricular cells, we assume that the majority of Na^{+} and K^{+} channels are blocked by either the holding potential used (-40 mV) or appropriate blocking agents. Thus,

these channels are not modeled, and we assume that only the dihydropyridine (DHP) - sensitive Ca^{2+} channels, the electrogenic pumps, Na^{+}/Ca^{+} exchangers and Na^{+}/Cs^{+} pumps expressed in the free and/or coupled sarcolemmal membranes contribute to the voltage clamp response.

2.1.3 The SR Fluid Compartment

The SR is an intracellular organelle that consists of two lumped fluid compartments (the jSR and LSR) that communicate (Fig. 2.3A; Fig. 2.5). Like the sarcolemma, the bounding membranes of the jSR and LSR are differentiated regarding their ionic current content and degree of coupling with the sarcolemma. With regard to ionic currents, the LSR membrane has a thapsigargin-sensitive SERCA pump for pumping Ca^{2+} into the LSR lumen against a concentration gradient. In contrast, the jSR membrane contains an outwardly directed ryanodine (Ry)-sensitive channel for Ca^{2+} release from the jSR to the dyadic space. The jSR fluid compartment contains the Ca^{2+} binding protein calsequestin as well as the proteins triadin and junctin, which interact with the ryanodine receptor (RyR) and calsequestrin. This co-located configuration of the RyR receptor, along with the proteins calsequestrin, triadin and junctin which exist on the luminal side of the jSR membrane, constitutes a jSR Ca^{2+} release regulating mechanism called the luminal sensor (Fig. 2.6B; Fig. 2.8). The protein-protein interaction between them plays an important role in regulating the open-state of the RyR Ca^{2+} release channel [41]. A six-state Markovian scheme (Appendix C.1, Eqs. C.90-C.95) is used to describe the dynamics of this interaction and it is called the SR luminal Ca^{2+} sensor. Fig. 2.6B shows a functional diagram of the luminal sensor and its output state is shown connected to the four-state RyR model. Specifically, the sensor adjusts Ca^{2+} dependent rate functions within the ryanodine

receptor model, which affects the open probability P_o of the SR Ca^{2+} release channel.

With regard to coupling, the DHP and Ry-sensitive Ca^{2+} channels are assumed to be located on opposite sides of the small dyadic fluid space (nanodomain) as shown in Fig. 2.7, and coupled functionally by a CICR mechanism. The dyadic space is assumed to be in fluid communication with the cell cytoplasm via a restricted diffusion region. In contrast, the LSR is not functionally coupled to the sarcolemma, but rather is in contact with the cytoplasm via the SERCA pump (as shown in Fig. 2.5).

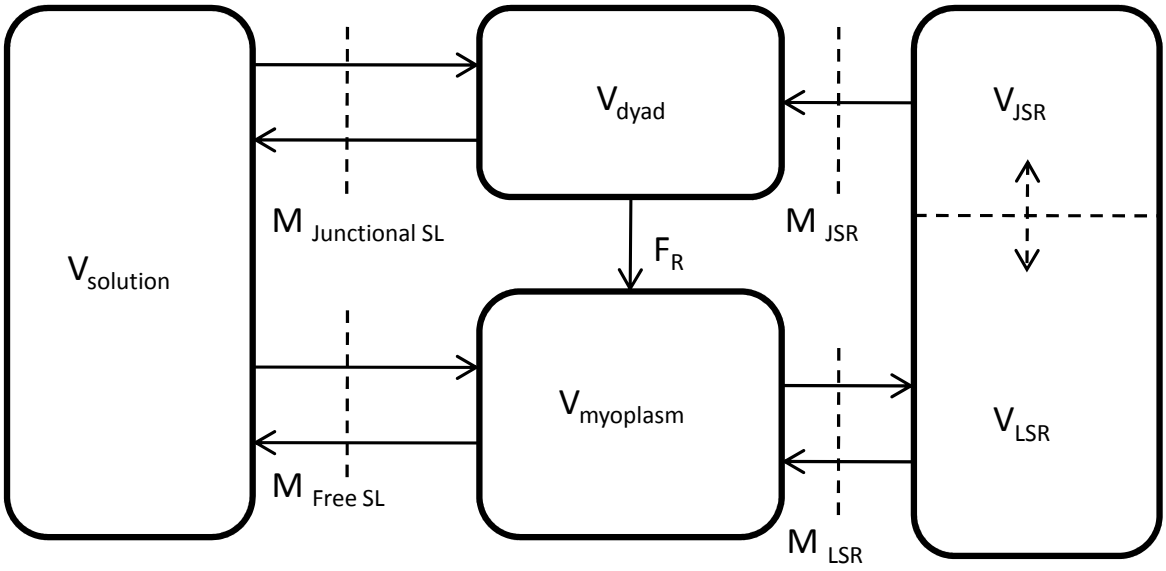

Figure 2.5 : Representative fluid compartment model, showing membrane surface area separating different compartments. M_{FreeSL}: free sarcolemmal membrane; $M_{JunctionalSL}$: junctional sarcolemmal membrane; M_{jSR}: junctional SR membrane; M_{LSR}: Longitudinal SR membrane.

2.1.4 The Dyadic Coupling Unit (DCU)

In describing this functional unit it is necessary to provide progressively more detailed descriptions of the component elements of the individual dyad, particularly the geometrically opposed DHP and Ry-sensitive Ca^{2+} channels, as well as the geometry and

buffering properties of the small dyadic space. As will be shown, we have described the dynamics of both types of Ca^{2+} channels using Markovian state models (Fig. 2.6) which include features such as Ca^{2+} mediated channel inactivation, a graded CICR process with a "calcium gain" of approximately 6-7, and two-dimensional Ca^{2+} diffusion within the dyadic space. Crank [70] discusses diffusion problems in a two-phase heterogeneous medium and shows that diffusion through a system of barriers (RyR feet structures in the dyadic cleft space) can be approximated by diffusion in the same region without barriers but with a reduced effective diffusion coefficient. We hence take this approach in modeling the Ca^{2+} diffusion by solving the 2-D Laplacian equation (Appendix C.3, Eqs. C.150-C.153) in the DCU without explicitly accounting for local potential fields. The DHP-sensitive $i_{Ca,L,TT}$ channel brings in trigger Ca^{2+} (0.1 pA which is of the same order as measured by Wang et. al. [38]) causing a sparklet (a local increase in Ca^{2+} concentration at the mouth of the channel). This trigger Ca^{2+} causes a release from a cluster of opposing RyR channels, causing a spark. This combined release from a cluster of RyR channels causing a spark is represented as the release from a unitary RyR channel (i_{RyR}) in our model (shown in Fig.2.7).The characteristics of elemental Ca^{2+} release from a unitary RyR channel in our model agrees with data in terms of amplitude which is of the order of 2 pA (reported by Cheng et al. [83] and Blatter et al. [84]) and duration (full duration at half maximum (FDHM)) which is of the order of 50 ms (reported by Zima et al. [39]).

The single DCU in our model represents the lumped activity of a large number of individual dyads (e.g. 10,000), and it is charged with the task of forming the cytosolic Ca^{2+} transient (hence mechanical contraction) each beat of the cardiac muscle cell. In response to tonic application of voltage clamp pulses, the DCU strongly depends on an adequate supply of Ca^{2+} from the SR. The measurements of Diaz et al. [85]

show that, although trigger current may be supplied regularly by tonic voltage clamp pulses, there is an inherent steady-state dependence of the magnitude of Ca^{2+} release on the particular value of SR Ca^{2+} content (i.e., there is a relationship between SR Ca^{2+} content and peak $[Ca^{2+}]_{myo}$; Fig.4 Diaz et al.[85]). This plot gives us a glimpse of the input-output relationship of the dyadic coupling unit and indicates that SR Ca^{2+} content is an important controlling variable for the CICR process implemented by the DCU model.

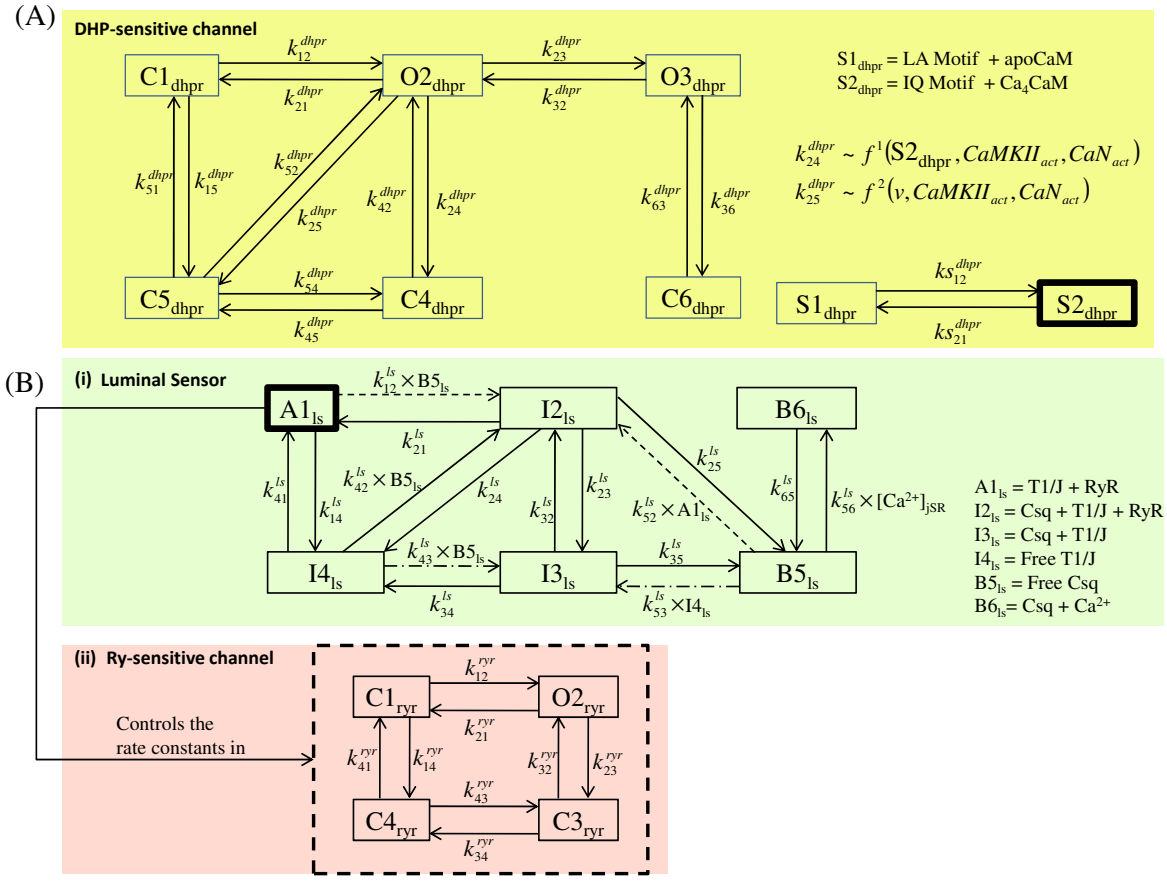

Figure 2.6 : Calcium channel dynamics. Calcium channel dynamics. (a) Markovian model describing the DHP-sensitive Ca^{2+} channel, and (b) Markovian model of the Ry-sensitive Ca^{2+} channel and the luminal SR Ca^{2+} sensor. Input from the luminal SR Ca^{2+} sensor modulates the rate constants in the model of Ry-sensitive channel exercising the indirect bias of luminal $[Ca^{2+}]_{jSR}$ on the RyR receptor.

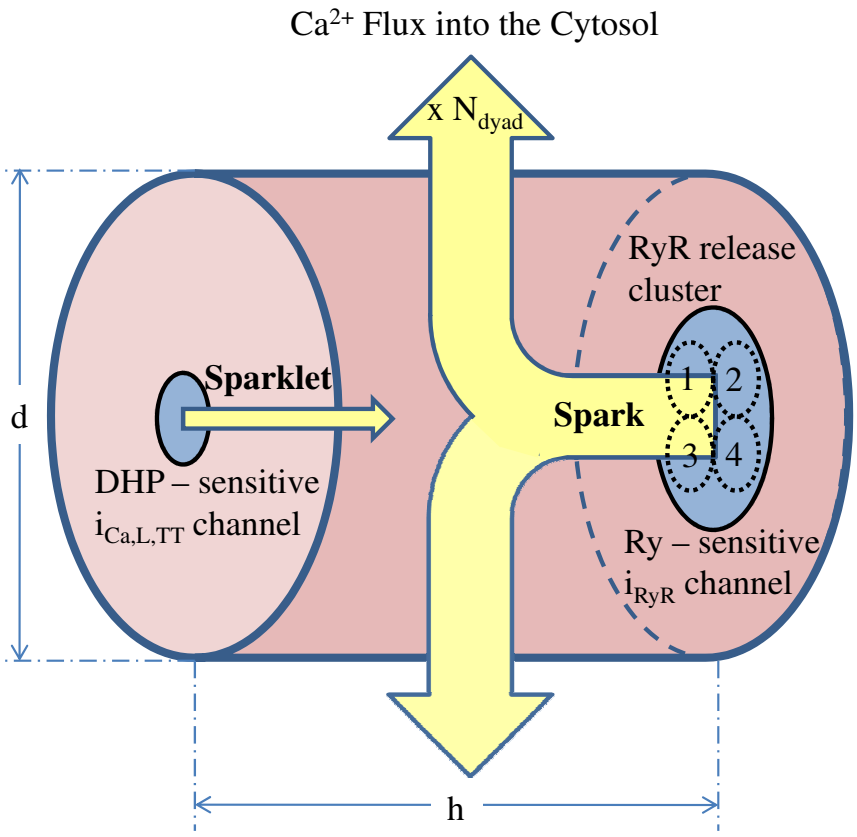

Figure 2.7 : Schematic of the LCC-RyR coupling. The dyadic cleft allows Ca^{2+} signaling between a DHP-sensitive Ca^{2+} channel opposing a cluster of Ry-sensitive Ca^{2+} channels (represented as the release channel i_{RyR} in our model). The trigger sparklet due to Ca^{2+} entering via DHP-sensitive $i_{Ca,L,TT}$ channel causes a spark as a result of release from a cluster of opposing RyR channels. The large amount of Ca^{2+} released subsequently diffuses into the cytosol.

2.1.5 L-Type Ca^{2+} Current

A multiple state characterization of $I_{Ca,L}$ in rat ventricular myocytes has been reported previously by our group [86]. The gating scheme used in this $I_{Ca,L}$ model has an additional high voltage state $C6_{dhpr}$ as shown in Fig. 2.6A which is introduced to reproduce $I_{Ca,L}$ tail currents. Upon voltage-dependent activation, the channel achieves the primary open state $O2_{dhpr}$. The degree of opening is enhanced in the

presence of activated calmodulin-dependent kinase ($CaMKII_{act}$) [87, 49, 88] which is known as Ca^{2+}-dependent facilitation (CDF). CaMKII has been shown to tether to the $I_{Ca,L}$ channel [89] functioning as a Ca^{2+} signalling sensor for facilitation. The open probability of the $I_{Ca,L}$ channel is also increased in the presence of activated calcineurin (CaN_{act}) [90] facilitating Ca^{2+} entry [91]. Our model incorporates CDF by allowing the rate constants in the 6-state Markovian model of the $I_{Ca,L}$ channel (k_{24}^{dhpr}, k_{25}^{dhpr} and k_{12}^{dhpr} in Fig. 2.6A) to be a function of the available active CaMKII and CaN. CDF is implicated in causing a gradual increase in amplitude and an accompanying decrease in inactivation over consecutive pulses after a resting interval [92]. Enhancement of $I_{Ca,L}$ caused by activated-CaMKII and CaN plays a key role in negating the effects of incomplete $I_{Ca,L}$ channel recovery at faster heart rates, thus helping to improve cardiac performance during exercise. The gating scheme features two different pathways for inactivation of the open state. The pathway $O2_{dhpr} \leftrightarrow C5_{dhpr}$ accounts for voltage-dependent inactivation, whereas the pathway $O2_{dhpr} \leftrightarrow C4_{dhpr} \leftrightarrow C5_{dhpr}$ with Ca^{2+}-calmodulin (Ca_4CaM) dependent rate constant k_{24}^{dhpr} accounts for the fast and slow phases of Ca^{2+}-dependent inactivation (CDI) [93]. In CDI, Ca^{2+} that enters the dyad either via the $I_{Ca,L}$ channel or through RyR release from the jSR binds to the protein Calmodulin (CaM) which is tethered to the C-terminus of the $I_{Ca,L}$ channel [94], modulating the interaction of CaM with the Ca^{2+} channel. Leucine-Alanine (LA) and Isoleucine-Glutamine (IQ) are 2 adjacent motifs in the Ca^{2+} sensing domain of the C-terminus of the $I_{Ca,L}$ channel. A Ca^{2+}-dependent switch of CaM from LA to IQ motif removes CaM from the inner mouth of the channel pore, thus causing an enhancement in inactivation by facilitating the constriction of the pore [95, 96]. CDI is a critical negative feedback mechanism which causes decreased Ca^{2+} entry via $I_{Ca,L}$ when the SR load is high with an accompanying large myoplasmic Ca^{2+} transient,

and it results in increased Ca^{2+} entry via $I_{Ca,L}$ when $[Ca^{2+}]_{myo}$ is small due to a low SR load. A 2-state Markovian model allows Ca^{2+} mediated interaction between calmodulin and the $I_{Ca,L}$ channel. As shown in Fig. 2.6A, state $S2_{dhpr}$, which denotes Ca_4CaM bound to the IQ-motif of the $I_{Ca,L}$ channel, modulates calmodulin dependent Ca^{2+}-induced inactivation. This is in agreement with the findings of Nikolai M. Soldatov [97]. Our approach to modeling the effects of the proteins CaM, $CaMKII$, and CaN on the $I_{Ca,L}$ channel was based on the premise that they are co-localized with the channel itself [90]. Most of the beat-to-beat modulation is produced by CaM and $CaMKII$, whereas CaN is constitutively active in the dyad [48]. Although CDF and CDI of $I_{Ca,L}$ coexist, CDI responds much faster (within the same beat) than CDF (over several beats).

Our previous study [86] was focused on the characterization of the $I_{Ca,L}$ channel under conditions of low $[Ca^{2+}]$ in the dyadic space and myoplasm. In fact, Ca^{2+}-release from the jSR was blocked by administering a relatively high dose of ryanodine (20 μM) in all experiments. Therefore, to study the additional influence of SR Ca^{2+} release on $I_{Ca,L}$, we modified the original $I_{Ca,L}$ model to better characterize the process of Ca^{2+}-dependent inactivation. In the modified $I_{Ca,L}$ model, majority of the structure for the 6-state dynamic scheme remains the same, however changes have been made to the voltage-dependent inactivation rate function (k_{25}^{dhpr}), and the Ca_4CaM dependent inactivation rate function (k_{24}^{dhpr}). The specific formulas for the Markovian state equations and the modified k_{25}^{dhpr} and k_{24}^{dhpr} functions used in this study are given in Appendix C.1 (Eqs. C.5-C.52). Our adjustments consist of reducing the contribution from voltage-dependent inactivation process and strengthening the Ca_4CaM-dependent inactivation process. The rate constants k_{36}^{dhpr} and k_{63}^{dhpr} are constructed in order to provide a re-excitation window during the return of the clamp

voltage to the resting potential. With these adjustments, the Markovian state description for $I_{Ca,L}$ can provide good fits to measured $I_{Ca,L}$ data under both test conditions (presence and absence of ryanodine -sensitive Ca^{2+} release) as well as produce tail currents during repolarization from large clamp voltages ($\geq$ 40 mv).

Rate-dependent increases in $I_{Ca,L}$ can also be caused by frequency-dependent increase in β-adrenergic stimulation increasing the level of available cAMP (Table B.12), which in turn causes an enhancement in $I_{Ca,L}$ channel current via protein kinase-A (PKA). Although PKA is involved in the indirect regulation of the $I_{Ca,L}$ channel, its effect is considered lumped into the conductance term in the ionic current description (Appendix C.1, Eqs. C.1-C.2). The effect of β-adrenergic stimulation via cAMP, particularly its dose-dependent influence on L-Type Ca^{2+} channels both in terms of modifying the single channel behavior such as Ca^{2+} ion permeability as well as overall channel recruitment characteristics, is not clearly understood. While cAMP has been shown to increase channel open probability [98, 99], increased levels of cAMP also result in increased phosphorylation of L-type Ca^{2+} channels, causing an increased permeability to Ca^{2+} ions [100, 101, 99].

2.1.6 Calcium Buffering in the Dyadic Space

Previous modeling work by Post et al.[102], and Post and Langer [103] considered the effect of Ca^{2+} binding sites on the inner sarcolemmal leaflet. Following these authors, we included low-affinity ($k_d = 1.1$ mM) and high-affinity ($k_d = 1.3$ μM) Ca^{2+} binding sites on sarcolemmal wall boundary of cylindrical dyadic space. The presence of these membrane bound sarcolemmal Ca^{2+} binding sites in our model has significant physiological implications, in that it prevents local dyadic Ca^{2+} concentration near the "mouth" of DHP-sensitive $I_{Ca,L}$ channel from becoming excessively high. Allowing

such a condition to occur can cause a reversal of the $I_{Ca,L}$ current, which does not occur physically during normal jSR release. Addition of these sarcolemmal Ca^{2+} binding sites does not significantly slow the build-up of Ca^{2+} within the dyadic space, nor is the Ca^{2+}-induced Ca^{2+} release mechanism affected[104].

2.1.7 Ca^{2+} Release Channel

The gating characteristics of the Ry-sensitive release channel are not only modulated by the dyadic Ca^{2+} concentration at its mouth but also the jSR Ca^{2+} concentration via the luminal sensor. Several RyR gating schemes have been deduced from isolated RyR currents measured in lipid bilayers, including: (1) the 4-state scheme developed by Keizer and Levine [105] with 4 Ca^{2+} binding for activation and 3 Ca^{2+} binding for inactivation to explain the "adaptation" of the RyR observed by Gyorke and Fill [106]; (2) the 6-state scheme suggested by Zahradnikova and Zahradnik [107], which allowed opening the RyR channel upon binding of a single calcium ion; and (3) the Markov model proposed by Keizer and Smith [108], which can be dynamically switched among the six, five and four-state representations during the simulation as Ca^{2+} levels vary. Stern et al.[31] demonstrated that none of these schemes yielded stable local control of SR release, even with extensive adjustment of parameters. Stern et al. [31] further reported that all schemes resulted in models that manifested local instability, as indicated by failure of release to terminate after activation, or global instability caused by spontaneous activation by resting $[Ca^{2+}]_{myo}$. Since many of the kinetic gating schemes derived from lipid bi-layer data fail to support stable E-C coupling in simulations, he concluded that the RyR gating process in situ may differ considerably from that in bi-layers.

Our gating scheme is patterned after the release channel used in the model of

Stern, Pizarro and Rios [109] (Fig. 2.6B), where the channel is assumed to have four states: rest (closed), activated (open), inactivated (closed) and refractory (closed). The activation gate is opened by the simultaneous, cooperative binding of two Ca^{2+} ions, whereas inactivation depends on the binding of a single Ca^{2+} ion. Four additional features have been built into our model: (a) the crucial role of the luminal SR Ca^{2+} sensor (Fig. 2.8) in assisting the inactivation of the RyR channel is modeled via the dependence of all the rate constants in the 4-state RyR model, on the degree of interaction between the RyR and the proteins triadin and junctin (Fig. 2.6B); (b) $CaMKII_{act}$ dependent enhancement in RyR release [110, 111, 112, 113] is modeled via the rate functions k_{12}^{ryr}, k_{41}^{ryr}, k_{43}^{ryr} and k_{32}^{ryr}; (c) a stronger Ca^{2+} dependent inactivation of the RyR channel (at a fixed depolarization level), is adopted to reflect recent observations that the inactivation of the RyR depends on the high local Ca^{2+} concentration consequential to their own Ca^{2+} release [114]; and (d) inactivation of the RyR at different depolarization levels is made dependent on local Ca^{2+} concentration (i.e., $[Ca^{2+}]_{ryr}$ at the "mouth" of the RyR channel on the dyadic side) as per Wier et al. [115] and Zucchi et al. [116]. Our initial studies indicated that the repriming rate (k_{32}^{ryr}) in the RyR gating scheme of Stern et al. [109] was quite large, which can lead to a saturated open probability of the Ca^{2+} release channel. This occurs during the later phase of channel inactivation, where the large value of k_{32}^{ryr} tends to reactivate the channel, resulting in saturated Ca^{2+} release. Therefore, we utilized a value of k_{32}^{ryr} that is 10% of that used by Stern et al. [109], and further assumed that the unitary permeation flux of the jSR release channel is proportional to jSR luminal Ca^{2+} concentration ($[Ca^{2+}]_{jSR}$). The specific equations for the Ca^{2+} release model are given in Appendix C.1 (Equations C.76-C.95).

CaM that is tethered to the Ry-sensitive Ca^{2+} channel [117] facilitates frequency-

dependent CaMKII and CaN-assisted modulation of that channel. Although CaMKII is known to bind to the RyR [118, 119, 120], the effect of this association has not yet been resolved. In lipid bilayer studies, CaMKII has been shown to increase [118, 121, 119] or decrease [122] RyR open probability. In studies on rat ventricular myocytes, it has been shown that endogenous CaMKII has an activating effect on the RyR Ca^{2+} release channel [110, 111, 112, 113]. However, a contrasting study shows that constitutively active CaMKII depresses RyR release [123]. Thus, the functional consequence of phosphorylation of RyR by CaMKII remains controversial. Since the bulk of the published literature on this topic points toward an activating effect of CaMKII on RyR, this concept is adopted in our model. Although CaN is reported to regulate ryanodine receptor Ca^{2+} release channels in rat heart [124], we have refrained from modeling its influence on the RyR channel because CaN is known to be constitutively active in the dyad [48] exhibiting only minor frequency-dependent modulation in its level, hence making its rate-dependent regulatory role insignificant.

2.1.8 Luminal RyR sensor

The RyR Ca^{2+} release is modulated by a multi-molecular Ca^{2+} signalling complex which is localized to the junctional SR [125, 126, 127]. This complex consists of the ryanodine receptor (RyR) which functions as a Ca^{2+} conducting pore [128, 129], calsequestrin (CS) which acts as the Ca^{2+} binding protein [130, 131], and the junctional SR transmembrane proteins triadin [132] and junctin [133]. It was known previously that the proteins triadin and junctin anchor calsequestrin to the ryanodine sensitive receptor [132]. More recently, it has been observed that the protein-protein interactions between triadin, calsequestrin and RyR modulate sarcoplasmic reticulum calcium-release in cardiac myocytes [41]. Triadin and junctin are structurally

homologous proteins [134], but the functional differences in their roles are unclear at present. Therefore we have refrained from modeling these proteins separately with unique roles, and will hereafter only mention triadin. The RyR model proposed by Shannon et al. [23] takes a heuristic approach towards free SR Ca^{2+} concentration dependent luminal control of the RyR channel. Our detailed biophysical model of the luminal sensor is strongly based on the recent findings of Terentyev et al. [41] which uncovers complex $[Ca^{2+}]_{jSR}$ dependent, CS mediated mechanistic interaction of the protein triadin with the RyR channel.

The triadin protein facilitates SR Ca^{2+} release by sensitizing the RyR to activation by the trigger current $I_{Ca,L,TT}$. This is incorporated in our model by allowing the rate constants in the 4-state Markovian model for the RyR (Fig. 2.6B-ii) channel to be functions of the activated state $A1_{ls}$, which represents the degree of binding between triadin and RyR, in the 6-state model for the luminal sensor (Fig. 2.6B-i).The degree of triadin assisted anchoring of CS to the RyR channel [132, 133] is denoted by the state $I2_{ls}$. Triadin is also known to exist in a form bound to CS alone [41] denoted by the state $I3_{ls}$ and in its free unbound form represented as $I4_{ls}$ in the model. CS which is known to exist in a Ca^{2+} bound form modeled by $B6_{ls}$ also modulates SR Ca^{2+} release by influencing the open probability of the RyR channel [135, 136, 137], via interactions with Triadin [125, 136, 41]. The degree of unbound CS is denoted by $B5_{ls}$ in the model.

During the diastolic period the relatively large concentration of available free Ca^{2+} in the SR results in most of the CS being bound to Ca^{2+}, decreasing the degree of interaction between CS and triadin. This enables a strong interaction between the available unbound triadin and the RyR channel increasing its propensity for trigger Ca^{2+} induced SR release. Our model incorporates this property by facilitating move-

ment of states towards $A1_{ls}$ and $B6_{ls}$ in the presence of large SR Ca^{2+} concentration. Following SR Ca^{2+} release, a reduced luminal Ca^{2+} concentration in the jSR causes an increase in the amount of free calsequestrin ($B5_{ls}$ in the model) available to bind with triadin. This results in a decrease in the extent of interaction between triadin and RyR ($A1_{ls}$ in the model), thus inhibiting the RyR channel and leading to robust termination of SR Ca^{2+} release in cardiac myocytes [136]. This release termination mechanism is incorporated in our combined RyR-Luminal sensor model (Fig. 2.6B and Appendix C.1, Equations C.76-C.95).

Due to the lack of in-vivo measurements on individual state transitions, the rate constants in our novel luminal sensor model are chosen such that (i) the triadin mediated sensitization of the RyR channel (via $A1_{ls}$) provides adequate peak RyR release which translates into the upstroke velocity of the cytosolic Ca^{2+} transient; (ii) the luminal sensor mediated RyR channel inactivation (via $A1_{ls}$) causes timely release termination resulting in a cytosolic Ca^{2+} transient duration, physiological for a rat ventricular myocyte; (iii) the rate of post-release RyR recovery results in appropriate channel refractory characteristics. In the case of channels where there is an interaction between ion flow (which is not at equilibrium) and its gating mechanism the microscopic reversibility criteria does not hold true [138, 139]. The RyR channel which is solely modulated by $[Ca^{2+}]$ (both on the dyadic side ($[Ca^{2+}]_{ryr}$) as well as the luminal side ($[Ca^{2+}]_{jSR}$)) experiences a strong interaction of Ca^{2+} flow through itself and its gating mechanism described as $[Ca^{2+}]_{ryr}$ induced self-inhibition and the luminal sensor induced inactivation. Hence, the rate constants of the luminal sensor model (Fig. 2.6B-i) are not constrained by microscopic reversibility criteria. However, a stability constraint in the form of, the sum of probabilities of all possible states corresponding to triadin ($A1_{ls}$, $I2_{ls}$, $I3_{ls}$, $I4_{ls}$) and CS ($I2_{ls}$, $I3_{ls}$, $B5_{ls}$, $B6_{ls}$)

being equal to one is explicitly imposed (Appendix C.1, Equations C.90-C.91) on the model of the luminal sensor in order to avoid run-off.

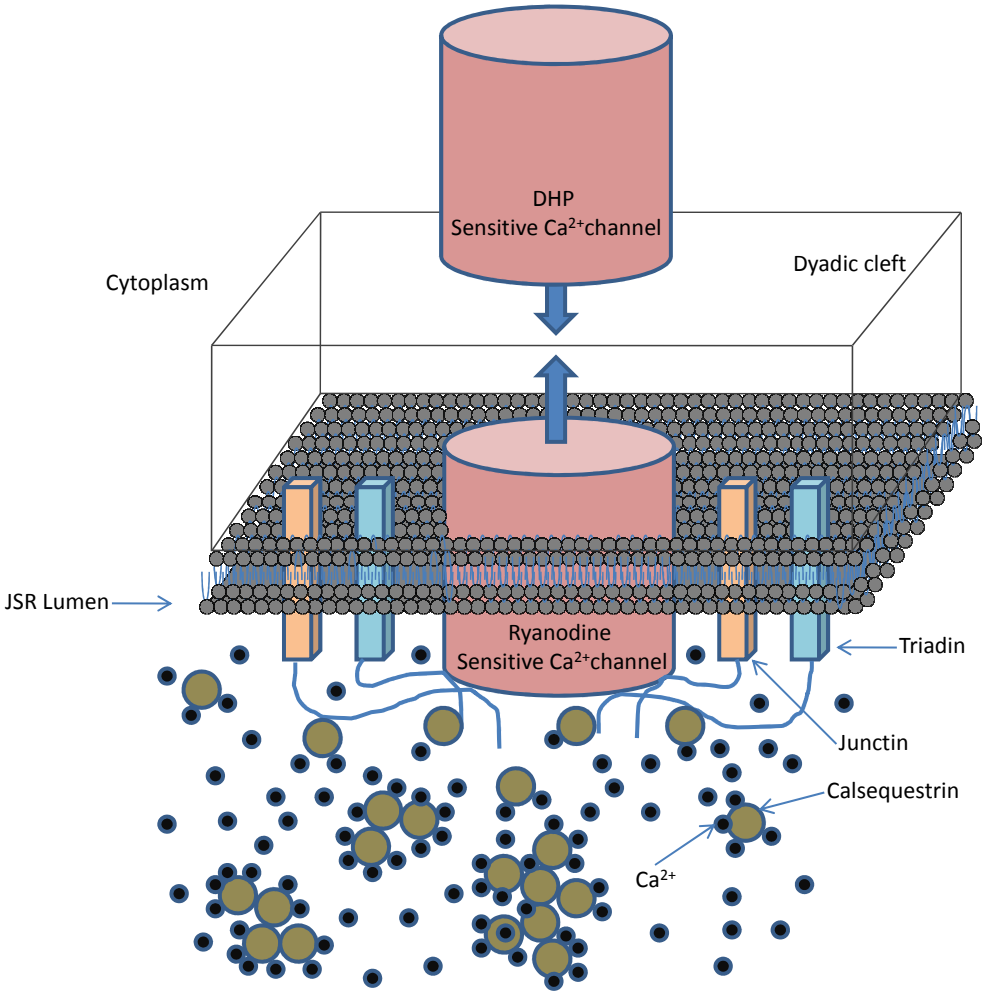

Figure 2.8 : Schematic of the CICR subsystem. The dyadic coupling unit comprises of a DHP-sensitive Ca^{2+} channel opposing a Ry-sensitive Ca^{2+} channel. The transmembrane proteins triadin and junction along with calsequestrin mediate the interaction between the luminal Ca^{2+} and the RyR thus regulating the release of Ca^{2+} flux from the jSR into the dyadic space.

2.1.9 Ca^{2+} Buffering in Myoplasm and SR

Ca^{2+} buffers play an important role in sequestering a fraction of the total Ca^{2+} released during E-C coupling and contraction. These buffers include: (a) calmodulin (CaM), which is assumed to be uniformly distributed in the myoplasm and dyadic space; (b) troponin in the bulk myoplasm; and (c) calsequestrin (CS) in the jSR. The dyadic space has been shown to be accessible to calmodulin (CaM), but mostly inaccessible to fluorescent dyes [140, 141]. Therefore, we consider the dyadic space filled with calmodulin, but not fluo-3. This provides a more direct calcium communication pathway between the DHP and Ry receptors. The rate constants for Ca^{2+} binding to calmodulin were based on a model from [71], whereas those for Ca^{2+} binding to troponin were taken from Potter and Zott [142]. Rate constants used to describe Ca^{2+} binding to calsequestrin were based on the study of Cannell and Allen [143], whereas those for Ca^{2+} binding to troponin-Mg complex were adopted from Lindblad et al.[144].

It is well recognized that fluorescent indicator dyes introduced into the cytosol also act as Ca^{2+} buffers [71], even at submillimolar concentrations [114]. In our simulations, we have used 100μM fluo-3. We assume that the quantity observed experimentally as a "calcium concentration" signal is actually the calcium complexed with fluo-3, or [CaF3]. The differential equation describing the change in [CaF3] with time is given in Appendix C.2 (Eq. C.141) which follows from Shannon et al.[145].

2.1.10 Ca^{2+}-Uptake

Cytosolic Ca^{2+} is pumped into the LSR (Fig. 2.3A) by a Ca^{2+}-ATPase, which lowers $[Ca^{2+}]_{myo}$ and helps to induce relaxation in cardiac muscle. The transport reaction involves two Ca^{2+} ions and one ATP molecule [146], and it is represented by the

description given for $I_{cyt,serca}$ and $I_{serca,sr}$ in Appendix C.1 (Eqs. C.53-C.66). The model used for the uptake pump is adopted from Koivumaki et al. [147] and takes into account both the forward flux of Ca^{2+} from the cytosol to the LSR lumen and the backward flux from the LSR to the cytosol along with the Ca^{2+} buffering action of the SERCA protein. The phospholamban (PLB) to SERCA ratio has been fixed to 1.0, assuming almost equal availability of both the proteins. Frequency-dependent CaMKII activity is known to cause an acceleration of relaxation [148, 77]. $CaMKII_{act}$ affects the SERCA pump via direct phosphorylation assisting in enhancement of SR Ca^{2+} transport by increasing the pumping rate [149] and indirectly via phosphorylation of PLB [148] relieving the inhibition caused by PLB on the SERCA pump in turn increasing the sensitivity of the pump for Ca^{2+} uptake. These two effects are modeled by allowing the rate constants for Ca^{2+}+ binding to/release from the SERCA pump as well as the rate constant for phosphorylation of PLB to be a function of $CaMKII_{act}$ in the cytosol. These two effects cause enhancement in SR Ca^{2+} uptake in an activity-dependent fashion. In CaN knock-out mice, decreasing phosphorylation of PLB allowed an increased level of inhibition of the SERCA pump, which resulted in poor muscle contraction and relaxation [150, 151, 152]. However, it is unclear if this behavior is a result of other compensatory mechanisms such as decreased CaMKII expression or enhanced PLB to SERCA ratio. On the contrary, CaN has been reported to inhibit SERCA activity in isolated non-failing human myocardium [153] in-vitro. Hence, we model the role of CaN in rate-dependent inhibition of the SERCA pump via PLB dephosphorylation by allowing the rate constant for phosphorylation of PLB to be dependent on available active CaN in the myoplasm. With increasing heart rates, β-adrenergic stimulation results in increasing levels of cAMP in vivo (Table B.12 shows values for maximal β-adrenergic stimulation), which

in turn phosphorylates PLB via PKA, causing enhanced uptake by the SERCA pump (Appendix C.1, Eqs. C.62-C.66). Together, activity-dependent recruitment of these CaMKII and cAMP-mediated effects at high frequencies counter the effect of CaN as well as decreasing cardiac cycle duration on SR refilling. The current $I_{cyt,serca}$ dictates the transport of Ca^{2+} between the cytosol and the SERCA protein. Similarly, the current $I_{serca,sr}$ dictates the transport of Ca^{2+} between the SERCA protein and the LSR. The difference in these Ca^{2+} currents accounts for the Ca^{2+} buffered by the SERCA protein. The jSR is subsequently refilled by Ca^{2+} diffusion from the LSR. The differential equations describing the Ca^{2+} balance and particularly the transfer between two separate SR compartments (jSR and LSR) are provided in Appendix C.1 (Eq. C.75).

2.1.11 Ca^{2+}-Extrusion via Sarcolemmal Ca^{2+} Pump

Although the sarcolemmal Ca^{2+}-pump has a high affinity for $[Ca^{2+}]_{myo}$, its transport rate is far too slow for it to be an important factor in Ca^{2+} fluxes during the cardiac cycle. It might, however be more important in long-term extrusion of Ca^{2+} by the cell. Our model of the plasma membrane Ca^{2+} ATPase pump current is adopted from Sun et al. [86]. We have used a constant value of half activation constant kmpca = 0.5μM in our model on the basis of measurements by Caroni et al [154].

2.1.12 Ca^{2+}-Extrusion via Na^{+}/Ca^{2+} Exchanger

In mammalian cardiac cells, it is generally accepted that the Na^{+}/Ca^{2+} exchanger has a stoichiometry of $3Na^{+}$:$1Ca^{2+}$ [155]. I_{NaCa} (again, the combination of $I_{NaCa,TT}$ and $I_{NaCa,SL}$) is important in removing Ca^{2+} during twitch relaxation, in competition with I_{up}. A simple thermodynamic Na^{+}/Ca^{2+} exchanger current model [19] may be

sufficient to predict the direction of Ca^{2+} transport by Na^{+}/Ca^{2+} exchange and the driving force, however the amplitude is subject to kinetic limitations (depending on substrate concentrations). A more comprehensive Na^{+}/Ca^{2+} exchanger current equation [156] is adopted in our model, which includes factors for allosteric Ca^{2+} activation and the transport for Na^{+} and Ca^{2+} inside and out. The maximal flux through the exchanger V_{max} is estimated to ensure that the Ca^{2+} ion transport (which is voltage dependent) via the Na^{+}/Ca^{2+} exchanger matches the influx of Ca^{2+} via the $I_{Ca,L}$ channel [157, 158], maintaining whole cell Ca^{2+} homeostasis.

2.1.13 Na^{+}/Cs^{+} Pump

The Na^{+}/K^{+} pump, helps in maintaining homeostasis of the intracellular Na^{+} ion concentration. ATPase activity powers the pump, as it generates an outward Na^{+} flux and an inward K^{+} flux with a Na^{+} to K^{+} stoichiometry of 3 to 2 [159]. However, in our experimental protocol, external solution in the bath was normal Tyrode (1 mM Ca^{2+}) with Cs^{+} substituted for K^{+} in order to block the inward rectifier K^{+} current. The internal solution in the pipette contained Cesium aspartate supplemented with 20 mM $CsCl$, 3 mM Na_2ATP, 3.5 mM $MgCl_2$ and 5 mM HEPES.

Activation of the electrogenic sodium pump in mammalian non-myelinated nerve fibres [160], skeletal muscle [161] and rat brain cells [162] by Cs^{+} is reported in the literature. It is observed that the late effects of reducing extracellular K^{+} concentration ($[K^{+}]_o$) to 0 mM in mammalian cardiac muscle can be prevented by including appropriate concentrations of other activator cations of the Na^{+}/K^{+} pump such as Cs^{+} in the 0 mM $[K^{+}]_o$ bathing solution [163]. Monovalent cations (including Cs^{+}) were also added to K^{+} free bathing solution to reactivate the sodium pump in guinea-pig ventricular myocytes [164]. The effectiveness of Cs^{+} as an external cation in activating

the electrogenic sodium pump is known to be lesser than potassium [163].

We have represented I_{NaCs} in our model by the expression for Na^+/K^+ pump formulated by Linblad et al. [144] replacing K^+ ion concentrations with the Cs^+ ion concentration. While ensuring whole cell Na^+ ion balance, the peak Na^+/Cs^+ pump current is modified to be one-sixth to account for the decreased potency of the cation Cs^+ in activating the pump. The voltage-dependence of I_{NaCs} is adopted from the data on Na^+/K^+ pump from Hansen et al.[165].

2.2 Mechanical Description of Myofilament Contractile System

Our model for cardiac contractile mechanics (Fig. 2.9) is based on the approximate model of cooperative activation and crossbridge cycling reported by Rice et al. [1] with the following modifications: (a) the first-order rate constants for the transformation of the troponin/tropomyosin regulatory complex (outside the single overlap region between the thick and thin filaments) from a crossbridge non-permitting state to a crossbridge permitting state and vice-versa are chosen as 500 s-1 and 50 s-1 respectively in order to reproduce results reported by Rice et al. [1]; (b) the β-adrenergic agonist isoproterenol (ISO) is known to cause a decrease in myofilament Ca^{2+} sensitivity via an increase in [cAMP] which causes a protein kinase A (PKA) mediated phosphorylation of troponin I [55, 75] at Ser23/Ser24. Specifically, a two-state Markovian model is added to allow cAMP-dependent PKA-mediated interaction between troponin I (TnI) and the Ca^{2+}-binding regulatory site on troponin. As shown in Fig. 2.9, state TnI_u, which denotes the unphosphorylated form of TnI, modulates the Ca^{2+} affinity of the regulatory site on troponin. This is in agreement with the findings of

Messer et al. [166]. We model the effects of [cAMP] by allowing the cumulative activation rate constant for Ca^{2+}-binding to the troponin regulatory site to be a function of unphosphorylated TnI (TnI_u), the availability of which is in turn dependent on the amount of [cAMP] present (Appendix C.4, Eqs. C.158,C.162); (c) the large Q_{10} values used by Rice et al. (Qf_{app}, Qh_f, Qh_b and Qg_{xb}, Table 1, [1]) are decreased from 6.25 to 2.25 in order to reproduce temperature dependence of peak force developed in intact thin rat ventricular trabeculae [167]. Although a calmodulin (CaM) mediated pathway has been reported [168] to be responsible for modulation of myofibrillar Ca^{2+}-sensitivity (implying a possible CaM mediated role for Ca-dependent kinases or phosphatases in regulating myofilament contractility, particularly in frequency dependent acceleration of relaxation), we refrain from modeling this effect as the molecular mechanisms involved remain unresolved.

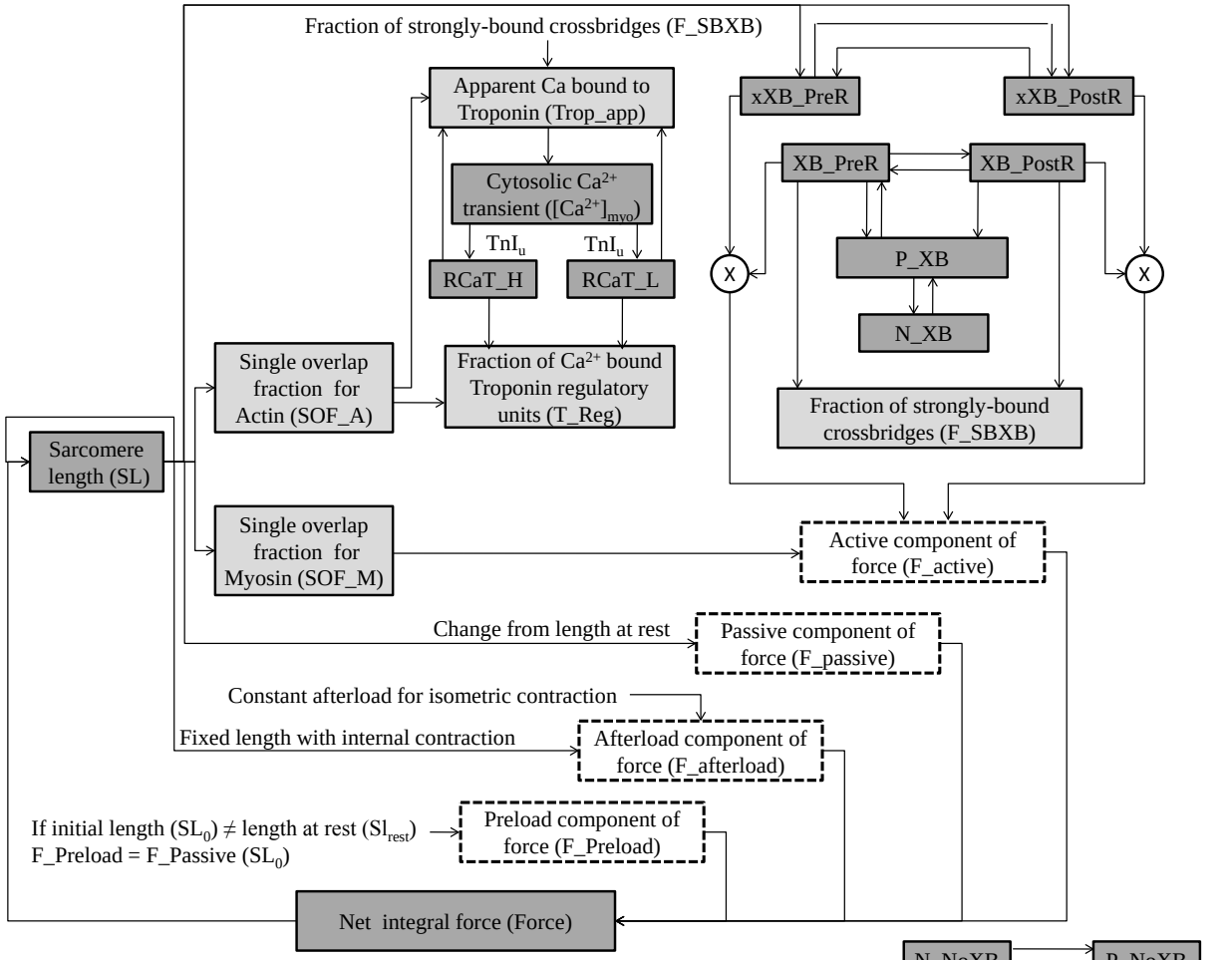

RCaT_H - Fractional population of Ca^{2+} bound high affinity regulatory site on Troponin
RCaT_L - Fractional population of Ca^{2+} bound low affinity regulatory site on Troponin
N_NoXB - Non-permissive confirmation of the regulatory protein with no nearby crossbridges
P_NoXB - Permissive confirmation of the regulatory protein with no nearby crossbridges
N_XB - Non-permissive confirmation of the regulatory protein
P_XB - Permissive confirmation of the regulatory protein
XB_PreR - Fractional occupancy of the strongly bound pre-rotated state (before isomerization)
XB_PostR - Fractional occupancy of the strongly bound post-rotated state (after isomerization)
xXB_PreR - Mean distortion corresponding to state XB_PreR
xXB_PostR - Mean distortion corresponding to state XB_PostR
TnI_u – Unphosphorylated troponin I
TnI_p – Phosphorylated troponin I

Figure 2.9 : Cooperative activation and crossbridge cycling. (Cont.)

Figure 2.9 : Model for cardiac electro-mechanics and force generation based on Rice et al. [1] shows states in non-permissive and permissive confirmations of the regulatory proteins. The permissive state transitions into a pre-rotated (XB_PreR) state having a strongly bound crossbridge with the head extended. The transition to the post-rotated (XB_PostR) force-generating state represents the isomerization to induce strain in the extensible neck region. Activation is triggered by the fraction of Ca^{2+} bound troponin regulatory units (T_Reg) which sets the rate constant for transition between the non-permissive (N_XB) to permissive (P_XB) confirmation of the regulatory protein using a strong nonlinearity function to indicate cooperativity. The model assumes that troponin for regulation has affinity set by the thin filament overlap. The affinity for apparent Ca^{2+} binding (used to perturb $[Ca^{2+}]_{myo}$), not only depends on thin filament overlap but also increases as crossbridges strongly bind to populate the pre-rotated and post-rotated states. The regulatory and apparent Ca^{2+} binding terms are calculated separately to avoid a global feedback from strongly-bound crossbridges to Ca^{2+} binding causing nonphysiological Ca^{2+} sensitivity [1].

Chapter 3

Cellular Ca^{2+} Dynamics

3.1 Background

Contraction of cardiac muscle is triggered by a transient rise in intracellular Ca^{2+} concentration $[Ca^{2+}]_{myo}$. Sarcolemmal membrane depolarization triggers Ca^{2+} influx from the extracellular medium by opening dihydropyridine (DHP)-sensitive L-type Ca^{2+} channels. Following diffusion across a small sub-membrane dyadic space, this influx activates ryanodine receptors (RyRs) controlling ryanodine-sensitive Ca^{2+} release channels in the junctional portion of the sarcoplasmic reticulum (jSR). Fabiato and Fabiato [8] named the process calcium-induced calcium release (CICR). Ca^{2+} subsequently diffuses from the dyadic space into the cytosol. Ultimately, intracellular Ca^{2+} concentration $[Ca^{2+}]_{myo}$ is returned to resting levels by combination of: (a) Ca^{2+} buffering in the dyadic space and cytosol; (b) sequestration of Ca^{2+} by sarcoplasmic/endoplasmic reticulum Ca^{2+}-ATPase (SERCA)-type calcium pumps lining the longitudinal portion of the sarcoplasmic reticulum (LSR); and (c) Ca^{2+} extrusion from the cytosol by Na^{+}/Ca^{2+} exchangers and Ca^{2+}-ATPase pumps on the sarcolemmal membrane.

CICR in cardiac muscle exhibits both graded behavior and a high gain. Graded behavior refers to the observation that SR Ca^{2+} release is proportional to the influx of trigger Ca^{2+} [9], whereas high gain indicates that the sarcolemmal trigger current elicits a high SR Ca^{2+} release flux. Graded Ca^{2+} release with high gain is

somewhat paradoxical according to Stern [28], in that the positive feedback inherent in such high-gain systems tend to produce regenerative, nearly all-or-none release rather than graded release. Several deterministic models have been developed to explain excitation-contraction (E-C) coupling [29, 30], but none of them can explain the mechanism of graded release at high gain over a wide range of values for sarcolemmal Ca^{2+} current.

Stern [28] proposed that such a gradation paradox might be explained if the stimulus for Ca^{2+} release by RyRs were actually the local nanodomains of $[Ca^{2+}]$ generated by nearby L-type channels, rather than the global cytosolic $[Ca^{2+}]_{myo}$. According to this hypothesis, graded control of macroscopic SR Ca^{2+} release can be achieved by graded statistical recruitment of individual, autonomous, all-or-none stochastic release events [31]. In these studies, a distributed differential model of high order that included dynamic interactions between large numbers of individual channels was used to demonstrate this concept. However, rather large amounts of computation time are required with distributed stochastic models of this type. Additional models have sought to characterize the Ca^{2+} release complex, including several [32, 33, 34] based on the stochastic release process adopted by Stern et al. These statistical models have solved the graded release problem, however, they too are complicated and computationally very expensive. Other models based on the simplified local control model of CICR developed by Hinch et al. [35] sought to adopt a lower order description of the E-C coupling process [36, 37] by making an approximation of rapid equilibrium in the dyadic space. The latency from onset of Ca^{2+} entry via the $I_{Ca,L}$ channel to triggered SR Ca^{2+} release is known to increase with decrease in the magnitude of $I_{Ca,L,TT}$ [38], the modeling of which is made possible by considering Ca^{2+} diffusion in the dyadic medium. These models [36, 37] also approximate the SR as a single

volume compartment with no distinction between junctional versus the longitudinal (network) SR compartments. However, recent work [39] points towards the important role of the Ca^{2+} refilling rate from the network to junctional SR in controlling RyR release termination via the luminal sensor. Shiferaw et al.[40] developed a computationally tractable model of Ca^{2+} cycling to represent the release of calcium from the SR as a sum of spatially localized events that correspond to Ca^{2+} sparks, assuming the recruitment rate of Ca^{2+} sparks is directly proportional to the whole-cell $I_{Ca,L}$ current. This assumption overlooks the complex calmodulin mediated interaction (calcium dependent facilitation (CDF) and calcium dependent inactivation (CDI)) of the $I_{Ca,L}$ channel with calcium in its vicinity. It also demands a large amount of computation.

Numerically, distributed as well as statistical models tend to be computationally expensive due to the inherent repetition involved in the computation. In a spatially distributed model, simultaneous solution for dynamics in identical compartments distributed in space would amount to a large computational cost. In statistical models inference is drawn based on multiple runs of identical events which translate into a prolonged simulation time. Hence, these models are cumbersome to implement, particularly in larger multiple-cell simulations. Consequently, we consider a deterministic approach to the characterization of CICR. Specifically, we develop a lumped model of the Ca^{2+} release complex that includes: (a) a sub-sarcolemmal dyadic cleft space separating the sarcolemmal and jSR membranes; (b) a single DHP-sensitive Ca^{2+} channel on the sarcolemmal membrane; and (c) a single equivalent Ry-sensitive channel arranged symmetrically on the opposing jSR membrane that represents the output of a local cluster of Ry-sensitive channels facing the DHP-sensitive channel. Based on morphological data compiled by Bers [55], we further assume that each ventricular

cell contains 10,000 of these dyadic Ca^{2+} release units, and that they are associated with the fraction of the sarcolemmal membrane that is coupled with the jSR. That is, we partition the sarcolemma into free and dyadically coupled sarcolemmal membrane, and associate each with a different fluid compartment: the cell cytosolic medium in the case of the free sarcolemmal membrane, and the dyadic cleft space medium in the case of the dyadic-coupled fraction. In a sense, we build on Stern's [28] local domain concept by considering the aforementioned local nanodomains identical, but focusing on the nonlinear dynamics of the two different types of Ca^{2+} channel in the dyadic coupling unit. Our deterministic model although is very descriptive, is computationally tractable and has a run time of 21 sec (including recording of 73 variables of type double on a data file) for 1 cycle of 4Hz voltage clamp stimulation.

3.2 Experimental Methods

Rat ventricular myocytes were prepared from 200-300 g male Sprague Dawley rats by dissociation with collagenase, as previously described [169]. All experiments were performed under conventional whole cell recording conditions with a List EPC-7 patch clamp, recording fluorescence from nearly the entire cell, as described by Fan and Palade [169]. Recordings from an individual cell were rarely extended beyond 10 min in order to reduce as much as possible both escape of dye from the cell and Ca^{2+} current rundown. External solution in the bath was normal Tyrode (1 mM Ca^{2+}) with Cs^{+} substituted for K^{+} for purposes of blocking inward rectifier K^{+} currents. The internal solution in the pipette contained Cs aspartate supplemented with 20 mM $CsCl$, 3 mM Na_2ATP, 3.5 mM $MgCl_2$ and 5 mM HEPES. Holding potential was -40 mV.

3.3 Results

The DCU is a fundamental element in the mechanism of CICR. The sequence of events resulting in CICR is triggered by the Ca^{2+} entering through the $I_{Ca,L}$ channel. The characteristics of this channel are hence examined in detail to understand its voltage and Ca^{2+} dependent behavior. The ability of the $I_{Ca,L}$ channel to facilitate graded RyR release is noted. The high gain associated with RyR release is quantified. This is followed by a study of the properties of the RyR channel with a particular emphasis on its inactivation mechanism. The Ca^{2+} mediated interaction between these channels is investigated in detail. This is followed by an effort to understand the role of $[Ca^{2+}]_{jSR}$ in CICR. In particular, the relationship of the peak cytosolic calcium transient and the SR Ca^{2+} content is examined. The effect of modulatory agents like caffeine and thapsigargin on SR release/uptake is studied to understand the significance of these mechanisms in facilitating a normal CICR.

3.3.1 L-type Ca^{2+} Current ($I_{Ca,L}$)

The L-type DHP-sensitive Ca^{2+} channel has a key role in initiating CICR. Hence a thorough analysis of its activation and inactivation mechanisms is considered here. Though the activation of the $I_{Ca,L}$ channel is solely voltage dependent once activated, the inactivation of the channel is influenced not only by the trans-membrane voltage but also the Ca^{2+} concentration in the vicinity of the channel [74]. The relative contribution of the voltage-dependent and Ca^{2+}-dependent inactivation pathways in the $I_{Ca,L}$ channel model can be studied by selectively blocking each pathway in the model. Figure 3.1 shows the model-generated waveform for $I_{Ca,L}$ under three conditions; (i) control case with both voltage and calcium dependent inactivation pathways intact; (ii) ryanodine applied to allow only the voltage-dependent inactivation and

the Ca^{2+}-dependent inactivation via $I_{Ca,L}$ self-inhibition in the absence of RyR release; and (iii) Ca^{2+} substituted with Ba^{2+} to facilitate only the voltage-dependent inactivation pathway and block all Ca^{2+} dependent inactivation pathways ($k24_{dhpr}$ set to zero). The protocol used in case (i) was a 50ms pulse with clamp voltages ranging from 10mv to 40mv in steps of 10mv from a holding potential of -40 mV. In case (ii) and (iii) the pulse duration was increased to 200ms to replicate the data.

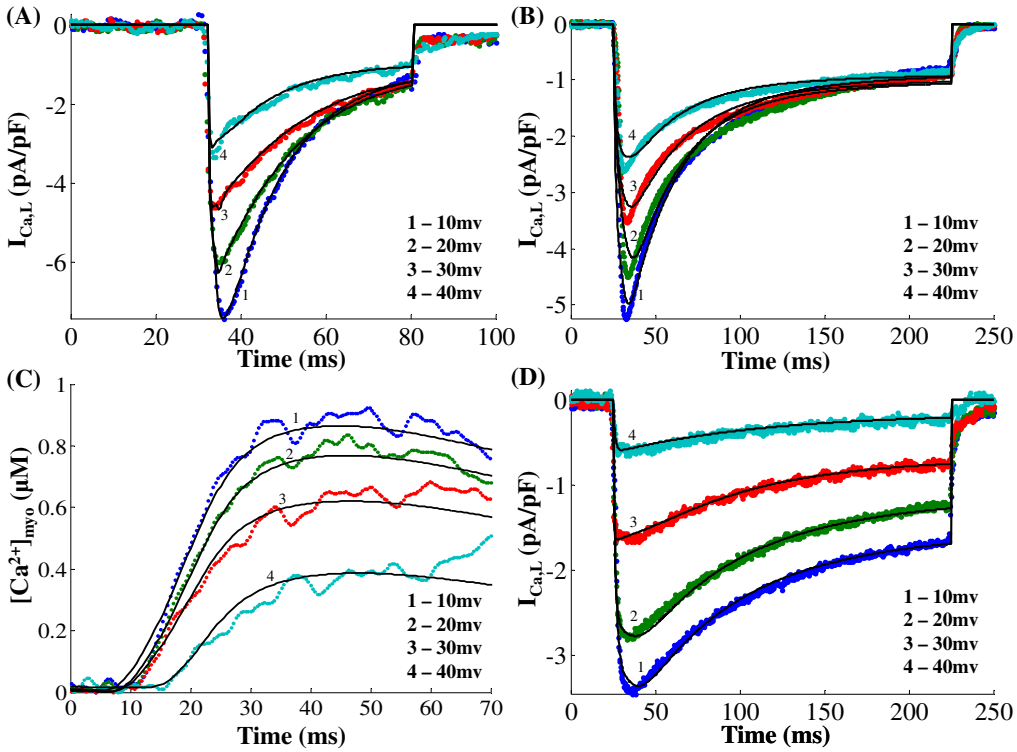

Figure 3.1 : Model generated and experimentally obtained data from a rat ventricular myocyte clamped to voltages between 10 and 40 mv in steps of 10 mv. The holding potential used is -40 mv. Data is obtained from Dr. Philip. T. Palade's lab. (A) $I_{Ca,L}$ in the presence of Ca^{2+} release from the Ry-sensitive channel. The pulse duration used is 50 ms. (B) $I_{Ca,L}$ with Ryanodine administered to block RyR release. The pulse duration used is 200 ms. (C) Global cytosolic calcium transients $[Ca^{2+}]_{myo}$ in the presence of RyR release. The pulse duration used is 50ms (D) $I_{Ca,L}$ using Barium as the charge carrier in the absence of RyR. The pulse duration used is 200 ms. Solid traces are the model-generated results and dotted lines represent the data.

Measured data obtained using the same voltage clamp pulse under all three conditions (Control, Ryanodine application and Barium substitution) is shown for comparison (data obtained from Dr. Palade's lab was pre-processed to eliminate transients produced by changing clamp voltage in order to obtain model fits using a non-linear least-squares method [72]). The degree of $I_{Ca,L}$ channel opening is known to be enhanced in the presence of $CaMKII_{act}$ [88] which is known as Ca^{2+}-dependent facilitation (CDF). According to Bers et al. [88] the positive regulation of the channel by $CaMKII_{act}$ requires Ca^{2+} influx (it is not seen when Ba^{2+} is the charge carrier as in Fig. 3.1D and is more strongly apparent when local Ca^{2+} influx is amplified by SR Ca^{2+} release as in Fig. 3.1A). Increase in $CaMKII_{act}$ seems to play an important function in enhancing $I_{Ca,L}$ peak amplitude [170], suggesting a critical role for Ca^{2+}-dependent facilitation. Our model generated results also indicate that a stronger CDF (in Fig. 3.1A) in the presence of RyR Ca^{2+} release causes an enhancement in $I_{Ca,L}$ peak amplitude (compare the model fits to data in Fig. 3.1A (presence of RyR release) with Fig. 3.1B (no RyR release) and Fig. 3.1C (Ca^{2+} substituted by Ba^{2+})). It is important to note that the peak of the $I_{Ca,L}$ current is reached after the RyR open probability reaches its maximum value owing to the faster dynamics of the RyR channel. Our simulations indicate that following the inward current peak, Ca^{2+}-dependent inactivation (CDI) is much faster and dominates the response for the duration of voltage clamp (30 ms <t <80 ms). In addition, a comparison of Figs. 3.1A and 3.1B shows that, Ca^{2+}-dependent inactivation (CDI) caused by Ca^{2+} release from Ry-sensitive channels is much more significant than the self-inhibition produced by Ca^{2+} influx via $I_{Ca,L}$ itself. The graded behavior of the cytosolic Ca^{2+} transient is shown in Fig. 3.1C. Voltage dependent inactivation (VDI) is relatively slow compared with CDI and is best seen in Fig. 3.1D where all Ca^{2+} inactivation

effects have been blocked by Ba^{2+} substitution for Ca^{2+}. Under RyR blockade (Fig. 3.1B), the relatively slow VDI has its major effect during the late phase of the long voltage clamp pulse (e.g., beyond 100 ms) and in a time range where CDI is relatively constant. Quantitative analysis of movement of states (during the depolarizing pulse duration of 50ms) via different pathways in the six state Markovian model shows that 68.24% of the total inactivation of $I_{Ca,L,TT}$ is via the calcium dependent $O2_{dhpr}$-$C4_{dhpr}$ pathway, owing to the large Ca^{2+} concentration which the channel is exposed to in the dyad. In contrast, only 19.21% of the total inactivation of $I_{Ca,L,SL}$ is via the calcium dependent $O2_{dhpr}$-$C4_{dhpr}$ pathway, because of the low cytoplasmic Ca^{2+} concentration in the vicinity of the channel. Considering the total $I_{Ca,L}$ current ($I_{Ca,L,TT} + I_{Ca,L,SL}$), around 63.34% of the $I_{Ca,L}$ channel inactivation is via the Ca^{2+} dependent pathway.

Figure 3.2A shows a comparison of model generated and experimentally obtained $I_{Ca,L}$ data (obtained from Dr. Palade's lab and pre-processed to eliminate transients produced by changing clamp voltage in order to obtain model fits using a non-linear least-squares method [72]) from a rat ventricular myocyte (different from the cell used to obtain data in Fig. 3.1) at negative (-30 mv $\leq$ v $\leq$ 0 mv) clamp voltages. The corresponding graded behavior of the cytosolic Ca^{2+} transient is shown in Fig. 3.2C. Figure 3.2B shows the well known [115] bell-shaped dependence of the peak $[Ca^{2+}]_{myo}$ on the clamp voltage.

Figure 3.3 shows model generated normalized $I_{Ca,L}$ obtained by a voltage clamp to 10mv from a holding potential of -40mv using the following protocols. Case 1: Normal release is allowed where, following CICR, a strong Ca^{2+} dependent inactivation inhibits the $I_{Ca,L}$ current as seen in the plot numbered 1 (data obtained from Dr. Palade's lab). Case 2: Ryanodine applied to block RyR release; Ca^{2+} entering

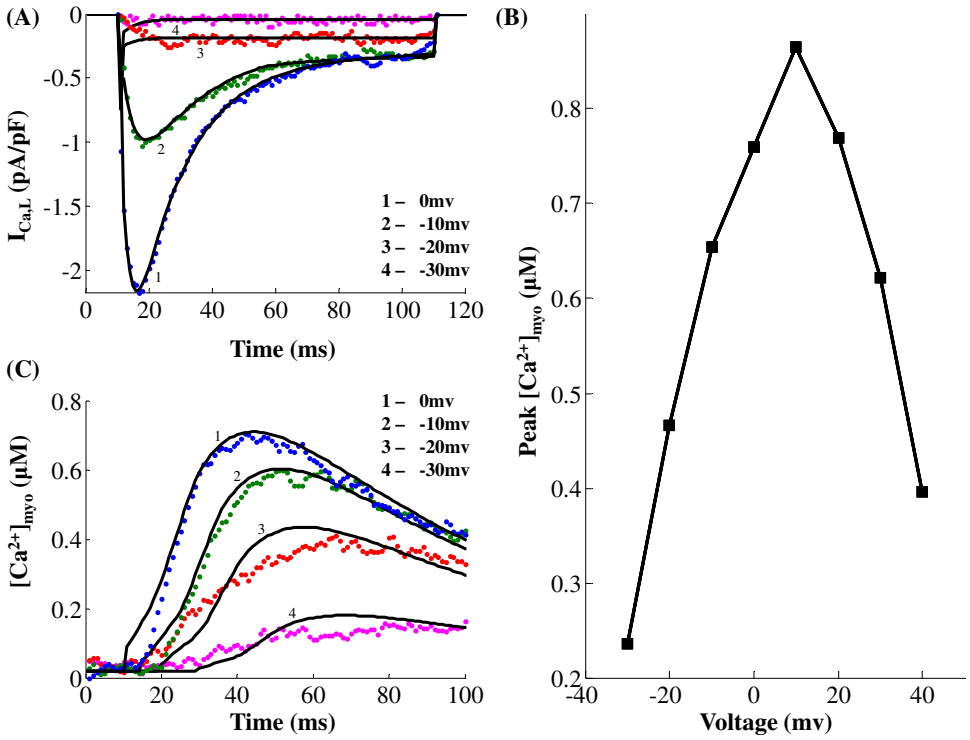

Figure 3.2 : Model generated and experimentally obtained data from a rat ventricular myocyte clamped to voltages between -30 and 0 mv in steps of 10 mv. The holding potential used is -40 mv. Data is obtained from Dr. Philip. T. Palade's lab. (A) $I_{Ca,L}$ invoked by negative clamp voltages in the range of -30 mv to 0 mv in steps of 10 mv. The pulse duration used is 100 ms. (B) Peak $I_{Ca,L}$ dependance on clamp voltage. (C) Global cytosolic calcium transients $[Ca^{2+}]_{myo}$ at negative (-30 mv $\leq$ v $\leq$ 0 mv) clamp voltages. The pulse duration used is 100ms (D) Peak cytosolic calcium transients ($[Ca^{2+}]_{myo}$) dependence on clamp voltages. Solid traces are the model-generated results and dotted lines represent the data.

via the $I_{Ca,L}$ channel causes Ca^{2+} induced inactivation, although the magnitude of inhibition is far less than in the control case. Case 3: Ba^{2+} substitution for Ca^{2+} to completely suppress the Ca^{2+} inactivation mechanism; the only inactivation pathway present is the slow voltage dependent pathway [171], which causes substantially reduced recovery compared to cases 1 and 2. Besides the inactivation, it can be seen from Fig. 3.3 that the rate of channel activation, which is evident in the slope of the

individual plots during the initial activation phase, is faster in the presence of RyR Ca^{2+} release (a result of enhanced CDF in the presence of elevated Ca^{2+} levels). This highlights the important role of Ca^{2+} in regulating $I_{Ca,L}$ channel opening and thus controlling the amount of extracellular Ca^{2+} entering the cell.

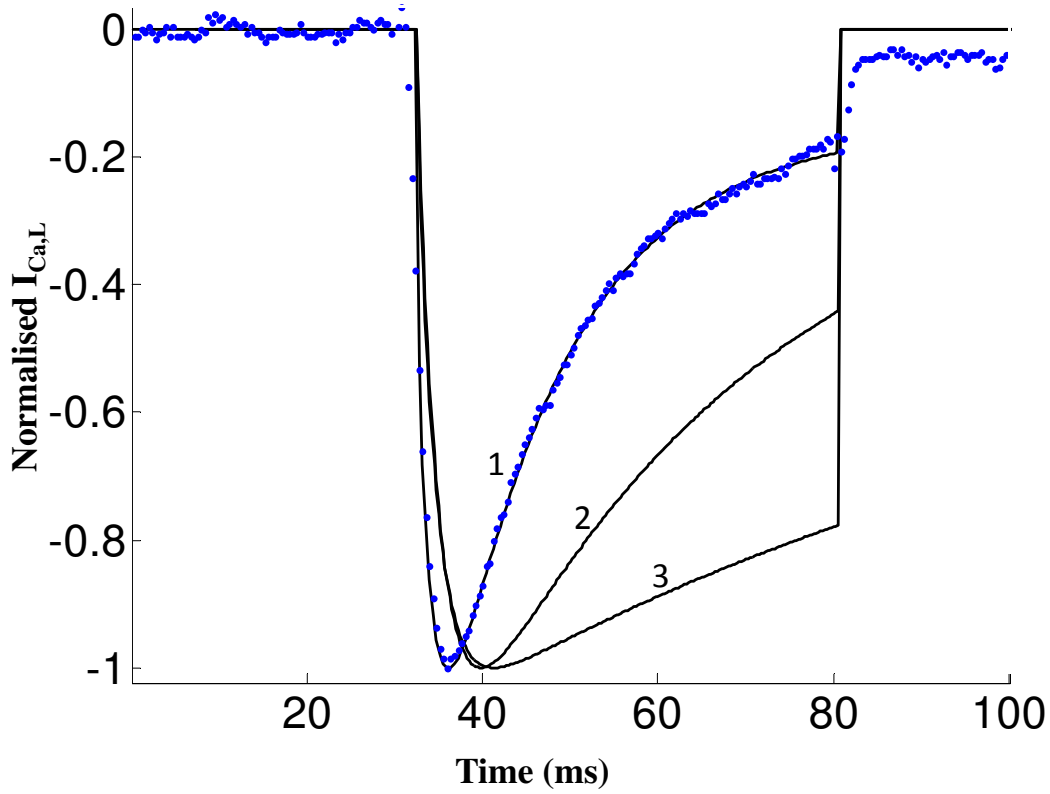

Figure 3.3 : $I_{Ca,L}$ inactivation pathways. Voltage clamp protocol used is a 50 ms step pulse to 10 mv from a holding potential of -40 mv. Both model generated results and the data are normalized for easy comparison (1) Control case where both voltage and calcium dependent inactivation pathways are intact. Solid trace is the model-generated result and the dotted line represents the data obtained from Dr. Philip. T. Palade's lab; (2) voltage-dependent inactivation exists however Ca^{2+}-dependent inactivation is only via $I_{Ca,L}$ self-inhibition without RyR release; (3) Only voltage-dependent inactivation pathway preserved by blocking all Ca^{2+} dependent pathways.

3.3.2 $\mathbf{I_{Ca,L,TT}}$ - Dependent Graded SR-Release

One of the most important characteristics of the CICR mechanism is the modulation of the RyR Ca^{2+} release based on the amount of trigger calcium delivered via the DHPR channel. The voltage-controlled $I_{Ca,L}$ channel is the link between the extracellular excitation and the intracellular Ca^{2+} release. As shown in Fig. 3.4A, our model reproduces graded release. It is important to note that the onset of the Ca^{2+} transient is also modulated based on the magnitude of the trigger calcium available to initiate release, as shown in Fig. 3.4A-iii. This is due to the fact that the rate of increase in the open probability of the Ry-sensitive Ca^{2+} release channel is controlled by the amount of trigger Ca^{2+} present at the 'mouth' of this channel, which in-turn is graded by the amount of trigger Ca^{2+} entering the DCU by means of the DHP-sensitive $I_{Ca,L,TT}$ channel. This mechanism is incorporated in our model by allowing the rate constants in the 4-state Markovian model of the Ry-sensitive Ca^{2+} release channel (Fig. 2.6) to be $[Ca^{2+}]_{ryr}$ dependent. Small changes in $i_{Ca,L,TT}$ cause modulation of pre-release $[Ca^{2+}]_{ryr}$, which dictates the propensity of the RyR channel for a Ca^{2+} release. The pre-release values of the rate constants in the 4-state Markovian model of the RyR channel (nonlinear dependence on $[Ca^{2+}]_{ryr}$ as shown in Appendix C.1, Eqs. C.82-C.87) along with the diastolic $[Ca^{2+}]_{jSR}$ (which is kept constant in Fig. 3.4) set the peak RyR open probability achieved by the RyR channel as well as the peak $[Ca^{2+}]_{myo}$. The use-dependent adaptation of the RyR channel [38] is reflected in its non-linear response to trigger Ca^{2+}. As shown in Figures 3.4B-iii, iv, the delay in the onset of cytosolic Ca^{2+} transient closely follows the modulation of the onset of RyR release. Though occurring in separate compartments, the peak of cytosolic Ca^{2+} transient also tracks the maximum value attained by the open probability of the Ry-sensitive Ca^{2+} release channel. Here, the clamp voltage was held

constant at 10 mv to avoid the interference of voltage dependent Ca^{2+} transport via the Na^{+}/Ca^{2+} exchanger which is co-located [172] with the $I_{Ca,L}$ channel in the dyad and the scaling down of $I_{Ca,L,TT}$ corresponds to a fast flicker block of the channels by dihydropyridine.

The slow rising foot that precedes the rapid upstroke (trace at position 0 in Fig. 3.4B-i and B-ii) is the contribution from a single sparklet (Fig. 2.7), which is the result of Ca^{2+} release from a single $i_{Ca,L,TT}$ channel in our model (0.1 pA), which is of the same order as reported by Wang et. al. [38] bringing trigger Ca^{2+} into a unitary dyad. This L-type Ca^{2+} channel (LCC) triggers release from a cluster of RyR channels causing a Ca^{2+} spark (Fig. 2.7), which results in the rapid increase in $[Ca^{2+}]_{dyad}$ that follows the foot (shown in Fig. 3.4B-i and B-ii). As shown in Fig. 3.4B, the latency from the onset of the sparklet foot to the triggered Ca^{2+} spark increases with decrease in the magnitude of $i_{Ca,L,TT}$ [38]. The SR Ca^{2+} release flux underlying a typical Ca^{2+} spark corresponds to approximately 2 pA [83, 84, 38]. From RyR single channel conductance measurements in lipid bilayer studies [173], a Ca^{2+} spark translates into a release from around 4 RyR channels (also reported by Blatter et. al. [84]). This single Ca^{2+} spark corresponds to a unitary RyR release (2 pA) in our model. Our model does not attempt to reproduce the stochastic kinetics of the single channel LCC-RyR coupling; however it mimics accurately the average behavior of this stochastic process which is the net Ca^{2+} release flux into the cytosol causing the Ca^{2+} transient. This on/off stochastic nature of the coupling was used earlier to explain the release termination via stochastic attrition. However, it is now known [41] that the luminal sensor plays a fundamental role in an active extinguishing mechanism [114] that effects a robust $[Ca^{2+}]_{jSR}$ - dependent closure of the RyR channel. This mechanism for inactivation of the Ry-sensitive Ca^{2+} release channel is accounted for

in our model.

Cytosolic Ca^{2+} transient is also graded by the duration of the $I_{Ca,L,TT}$ trigger current controlled by the voltage clamp pulse duration. Our model also shows that triggered release can be prematurely stopped by rapid repolarization [174, 175, 176]. The effect of depolarization duration on the time course of the cytosolic Ca^{2+} transient is indicated in Fig. 3.5 where the duration of the voltage clamp pulse is decreased from 80 ms to 5 ms (while keeping the clamp voltage constant at 10 mv) resulting in premature stoppage of release and thus a decrease in peak cytosolic Ca^{2+} transient. This effect is a combined result of (i) the modulation of release due to pulse duration dependent change in the amount of trigger Ca^{2+} entering the dyadic coupling unit (DCU) and (ii) the pulse duration dependent change in the relative role of the Na^{+}/Ca^{2+} exchanger co-located in the DCU.

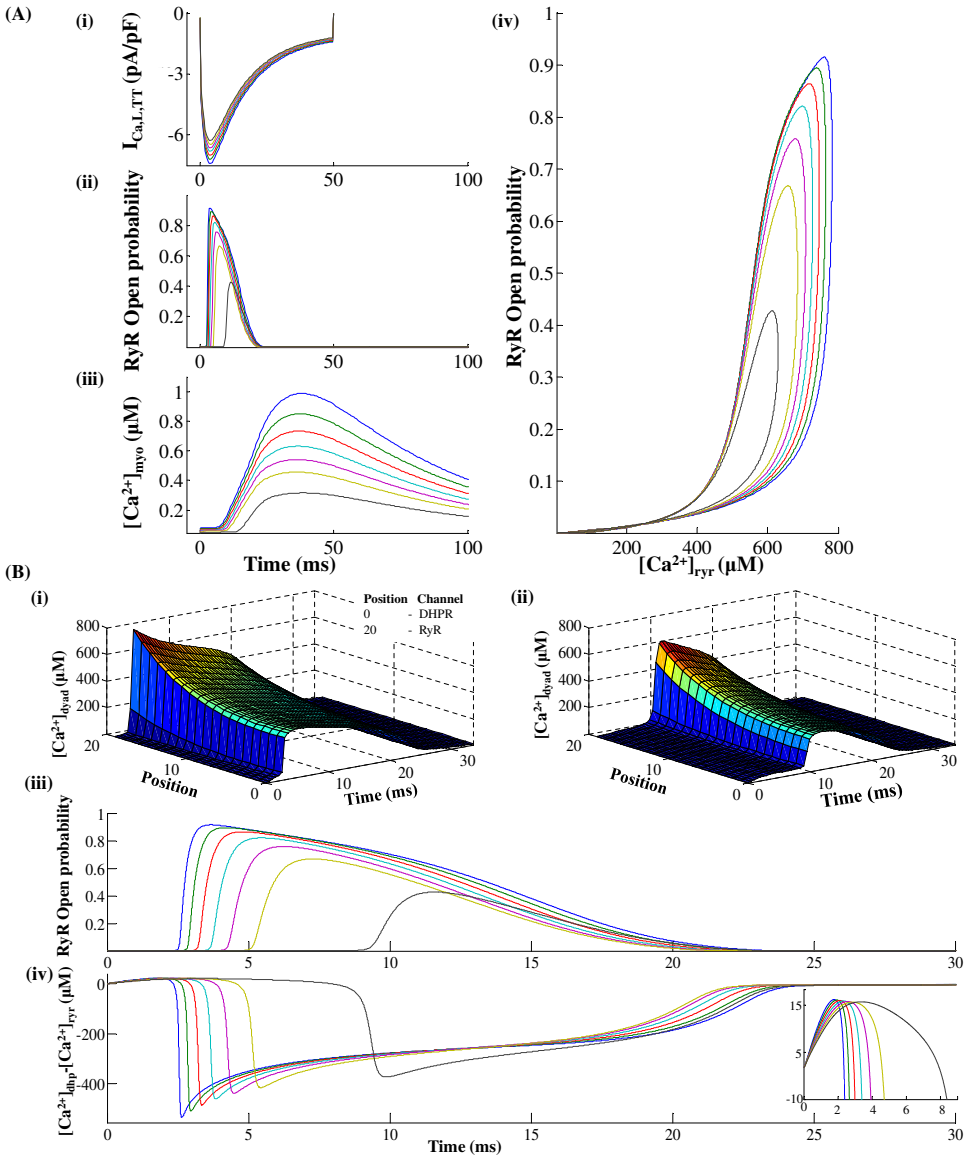

Figure 3.4 : SR calcium release graded by the trigger current $I_{Ca,L,TT}$. (A) - (i) Decreasing trigger current $I_{Ca,L,TT}$ (ii) With decreasing trigger current, RyR open probability shows a graded decrease in its peak as well as an increasing delay in its onset (iii) Cytosolic calcium transient follows the trend shown by the RyR release channel (a graded decrease in peak and increasing delay in onset) (iv) RyR open probability vs $[Ca^{2+}]_{ryr}$ for increasing trigger current $I_{Ca,L,TT}$. (B)- (i)Concentration profile in the dyad as a result of RyR release caused by a largest trigger current (see part A(i)) (ii)Concentration profile in the dyad as a result of RyR release caused by a smallest trigger current (see part A(i)) (iii) With decreasing trigger current, RyR open probability shows a graded decrease in its peak as well as an increasing delay in its onset (shown on an expanded time scale) (iv)Difference in concentration between the mouth of the DHP and Ry-sensitive Ca^{2+} channels. (Inset shows the cross-over when this difference becomes negative indicating trigger current dependent latency involved in release).

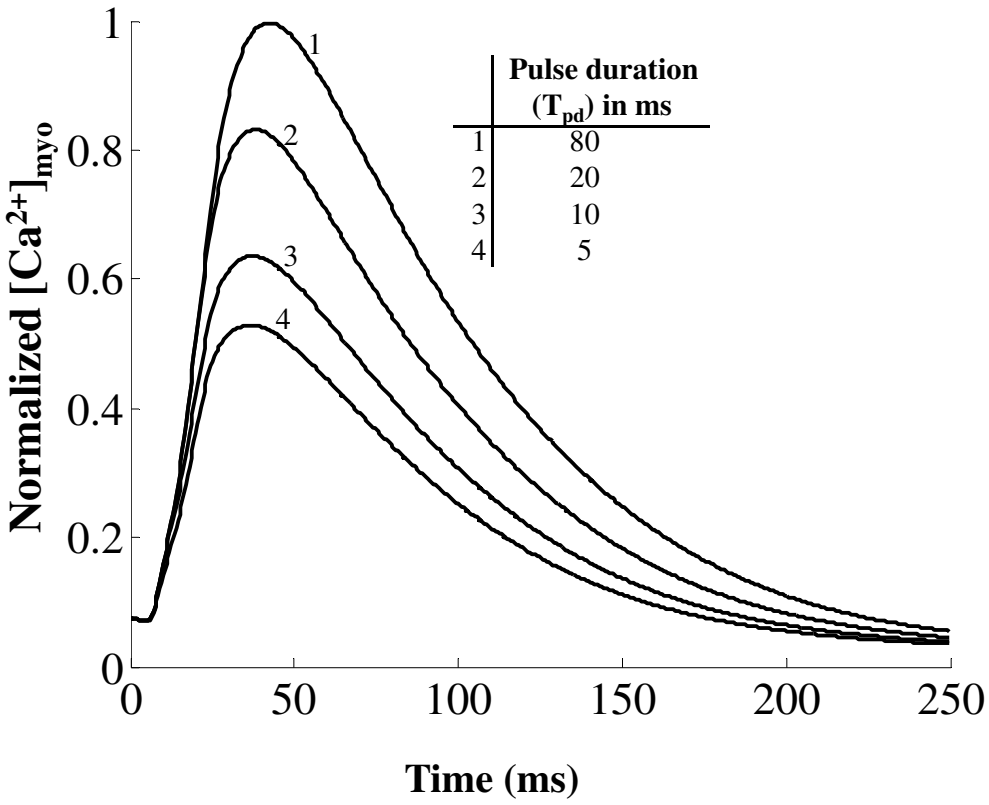

Figure 3.5 : The effect of changing the duration of depolarizing pulses T_{pd} on the time course of the $[Ca^{2+}]_{myo}$ transient. Voltage clamp protocol used is a step pulse to 10mv from a holding potential of -40 mv. Normalized $[Ca^{2+}]_{myo}$ transient corresponding to depolarizing pulses of 5, 10, 20, and 80 ms duration. This model-generated result shows similarity to data in Fig. 2, Cannell et al. [174] showing pulse-duration dependent changes in cytosolic Ca^{2+} concentration.

3.3.3 High Gain of Ca^{2+} Release

Besides the graded release, an extremely valuable characteristic of the CICR process is the high gain associated with it. A small amount of Ca^{2+} entering the DCU via the $I_{Ca,L,TT}$ channel causes a large release of Ca^{2+} from the sarcoplasmic stores via the Ry-sensitive Ca^{2+} release channel on the jSR lumen that interacts with the DCU. This high gain is essential in producing physiological cytosolic Ca^{2+} transients

when 10000 of these DCU's operate in tandem. Two different definitions of the gain or amplification factor due to CICR have been adopted in our model simulations, namely the ratio of:

1. average integrated RyR flux to average integrated DHPR flux [32]; and
2. the peak Ca^{2+} transient in the presence of CICR to the peak calcium transient in its absence, contributed by the trigger calcium alone [28].

Thus, criterion (1) measures calcium gain observed in the dyadic space, whereas criterion (2) measures gain observed in the cytosolic space.

With regard to the dyadic space, Fig. 3.6A shows the Ca^{2+} flux through DHPR and RyRs, respectively. Figure 3.6B shows cytosolic calcium transients under conditions of ryanodine blockade and with RyR Ca^{2+} release. Based on our measurements, there is approximately a 2 ms delay from the onset of the DHPR influx to the initiation of the RyR release flux.

At a clamp voltage of 10 mv, criterion (1) applied to our simulation yields an integrated flux ratio of 6.39, whereas a gain of 5.75 is calculated using criterion (2). By either method, a CICR amplification factor of approximately 6 is calculated, which is similar to that reported by Stern [28]. This result is also consistent with gain calculations from the measured data of Fan and Palade [169] on rat ventricular cells. They estimated a gain of approximately 7 using comparisons of the rates of rise of Ca^{2+} transients in the presence and absence of ryanodine. The model generated results are obtained by using a voltage clamp protocol of a 50ms step pulse to 10mv from a holding potential of -40mv.

The inset in Fig. 3.6A shows the voltage dependence of CICR gain formulated using criterion (1). Our model shows a decline in gain as the clamp voltage is increased

from -30 mv to 20 mv [115, 177]. However, any further increase in clamp voltage results in a small increase in gain (Fig. 1C, Altamirano et al. [178]). It is important to note that, with increasing clamp voltage, the decreased ability of the Na^{+}/Ca^{2+} exchanger (which is co-located [172] in the dyad) to extrude Ca^{2+} partially compensates for the declining trigger current, in facilitating SR release and hence assists in increasing CICR gain.

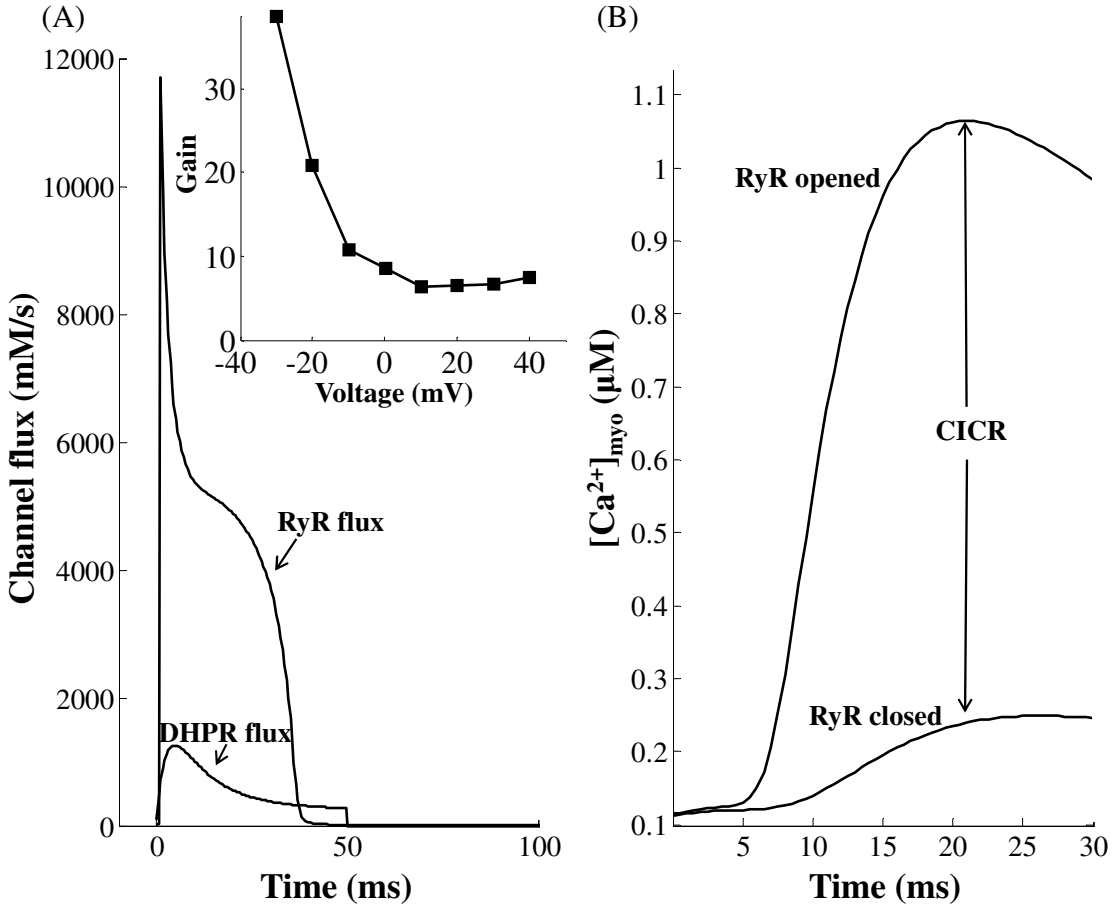

Figure 3.6 : High gain associated with CICR. Voltage clamp protocol used is a 50ms step pulse to 10mv from a holding potential of -40 mv. (A) Gain formulation by comparison of Ca^{2+} flux through the DHP sensitive and RyR sensitive Ca^{2+} channels. The voltage dependence of gain measured using this method is shown in the inset. (B) Gain formulation by comparison of cytosolic calcium transient formed in the presence and absence of RyR Ca^{2+} release.

3.3.4 RyR Refractory Characteristics

Given the fact that the CICR mechanism has a high gain associated with it, it could be prone to unstable behavior if not for the refractory characteristics of the Ry-sensitive release channel [179]. It is now known [41] that the luminal sensor plays a fundamental role in an active extinguishing mechanism [114] effecting a $[Ca^{2+}]_{jSR}$ dependent robust closure of the RyR channel which is accounted for in our model. The RyR release fails to become regenerative due to the role of the luminal sensor which after a release occurs, forces the RyR channel into an absolute refractory state followed by a relative refractory state as shown in Fig. 3.7C. When the RyR channel is in the absolute refractory period, $[Ca^{2+}]_{ryr}$ drops to a level much below what is caused by a sparklet (trigger Ca^{2+}) hence it robustly avoids re-excitation. This extremely critical refractory feature of the channel enabled by the RyR luminal sensor acts as a protective mechanism against premature Ca^{2+} release in the wake of a secondary excitation that occurs before jSR can be filled back to the control level. The refractory nature of the channel is caused by the $[Ca^{2+}]_{jSR}$ dependent inhibition induced by the protein triadin from the luminal side of the RyR channel. This restraining lock on the RyR channel assists in reloading the jSR.

A dual stimulus protocol (S1-S2) was employed to study RyR refractoriness. The RyR channel was stimulated initially by stimulus trigger current S1, followed after an interval (T_2 in Fig. 3.7A) by an identical stimulus current S2. Each of the two stimuli directed into the dyadic coupling unit is the dyadic component ($I_{Ca,L,TT}$) of trace 1 ($I_{Ca,L}$ evoked by a 10 mv clamp pulse) in Fig. 3.1A with a peak amplitude of 6.657 pA/pF and a duration (T_1 in Fig. 3.7A) of 50 ms. The stimuli S1 & S2 were kept identical to delineate the effects of RyR refractoriness on CICR. The time interval between the two stimuli (T_2) was gradually reduced from 250 ms to 50 ms in

steps of 25 ms to observe the effects of partial recovery of the RyR channel.

As seen in Fig. 3.7, the decrease in interval between stimuli causes partial recovery of $[Ca^{2+}]$ level in the jSR which manifests in increasing levels of unbound version of the protein calsequestrin, which tends to bind with triadin. As more triadin binds to calsequestrin, there is less left to bind to the luminal side of RyR to activate the channel for CICR. This signaling sequence mediated by the luminal sensor via the interaction of proteins calsequestrin and triadin, allows only a partial SR Ca^{2+} release based on the degree of SR Ca^{2+} content recovery. This is an important feature that helps restore the jSR Ca^{2+} content at the end of every cycle. The RyR channel in our model has an absolute refractory period of 75 ms and a relative refractory period of 250 ms (Fig. 3.7C). These results are consistent with the refractory period measurements by Sobie et al [180] on rat ventricular myocytes. When the RyR channel is in the absolute refractory period, $[Ca^{2+}]_{RyR}$ drops to a level much below what is caused by a sparklet (trigger Ca^{2+}) and hence robustly avoids re-excitation. However, when the RyR channel is in the relative refractory period, a partial release (Fig. 3.7C) is possible, despite the RyR receptors affinity for release being low.

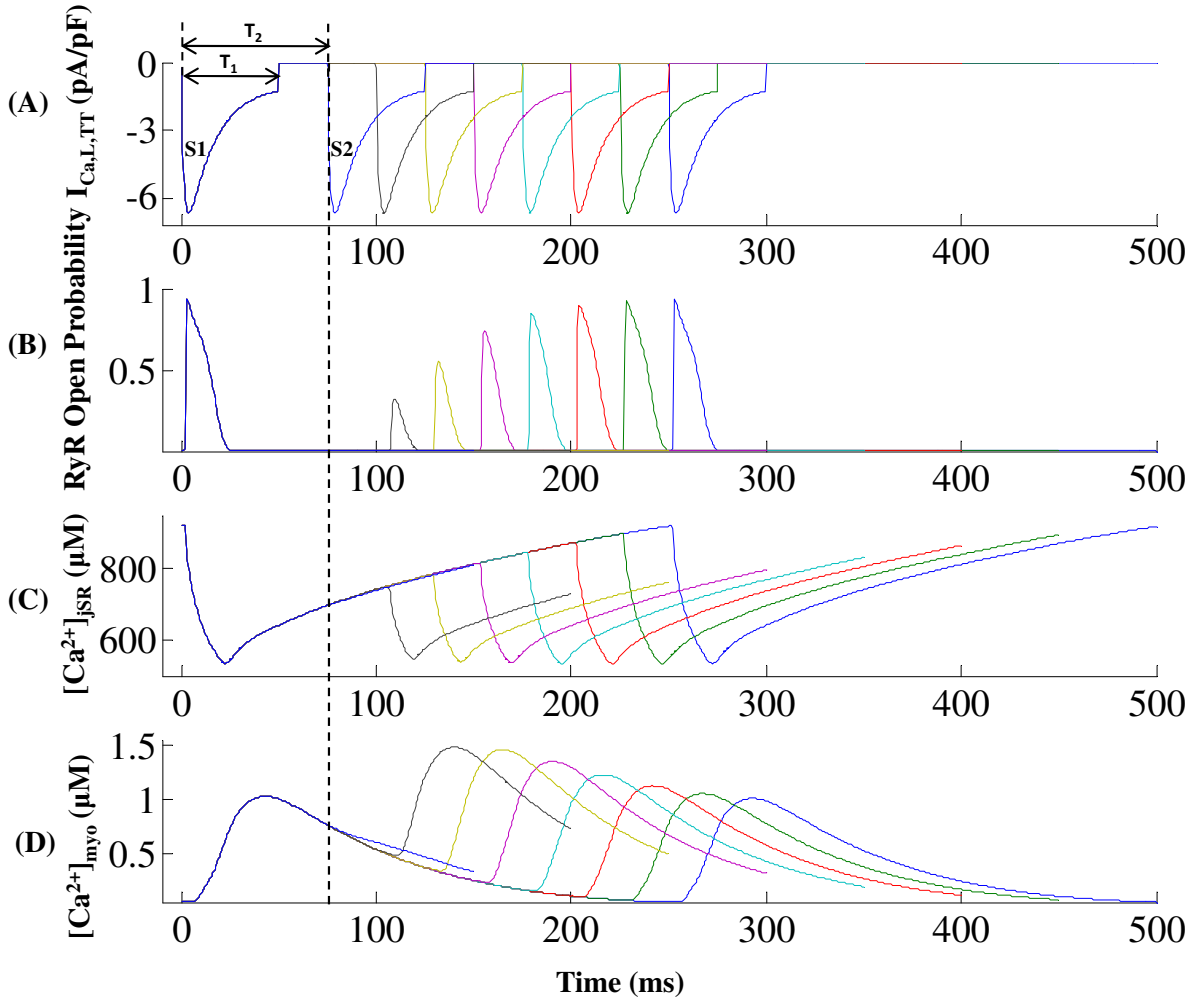

Figure 3.7 : RyR refractory characteristics. (A) The stimulation protocol comprises of two consecutive stimuli S1 & S2, both of which are identical to the dyadic component ($I_{Ca,L,TT}$) of trace 1 ($I_{Ca,L}$ evoked by a 10 mv clamp pulse) in Fig. 3.1A with a peak amplitude of 6.657 pA/pF and a duration (T_1) of 50 ms. These are applied with their separation in time (T_2) increasing from 50ms to 250 ms in steps of 25 ms. (B) The RyR sensitive Ca^{2+} release channel shows refractory characteristics with an absolute refractory period of 50 ms and a relative refractory period of 250 ms. (C) The corresponding $[Ca^{2+}]_{jSR}$ traces reflect partial RyR recovery. (D) Cytosolic calcium transient recovers completely after 250 ms. The dotted line indicates lack of RyR release when $T_2 = 75$ ms due to insufficient RyR recovery.

Figures 3.8A and B show the steady state $[Ca^{2+}]_{myo}$ and $[Ca^{2+}]_{jSR}$ predicted by the model, with and without a functioning luminal sensor, respectively. The

stimulation protocol used is a pulse train of amplitude (-40 mv to 10 mv), duration (50 ms) and frequency of 4.0 Hz which is applied for a period of 2.5 sec. The value of the luminal control of the RyR channel in allowing adequate SR filling can be seen in Fig. 3.8 where, in the presence of the luminal sensor the cell maintains a normal cytosolic Ca^{2+} transient (Fig. 3.8A-i). This is made possible due to sufficient SR filling (Fig. 3.8A-ii) as a result of RyR refractoriness. However, inactivation of the RyR channel is also known to depend on the high local Ca^{2+} concentration consequential to its own Ca^{2+} release [114]. The lack of a luminal sensor forces the RyR channel to solely rely on Ca^{2+} dependent inactivation mechanism. The resulting inadequate RyR inactivation depletes diastolic $[Ca^{2+}]_{jSR}$ level (Fig. 3.8B-ii) causing the cytosolic Ca^{2+} transient to diminish to new lowered steady state values (shown in Fig. 3.8B-i). The absence of the luminal sensor is modeled by setting the value of the luminal sensing variable ('var' in the model) to a level consistent with it's normal value under 4Hz, voltage clamp stimulation. This mimics the case where the luminal sensor is insensitive to changes in $[Ca^{2+}]_{jSR}$ and hence non-functional. It is important to note that the decrease (37.07%) in diastolic SR level (as indicated in Fig. 3.8B-ii) is due to the lack of a luminal control on the RyR channel resulting in a reduced rate of RyR recovery which in turn reflects in a compromised SR filling rate. Hence, the presence of a luminal sensor which monitors the SR Ca^{2+} content, is key to long term Ca^{2+} stability in the cell.

3.3.5 CICR Modulation by the jSR Ca^{2+} Content

From the refractory characteristics of the RyR channel, it is evident that the RyR release is strongly dependent on the jSR Ca^{2+} content. In fact, the SR Ca^{2+} release through the RyR channel depends on: (a) the amount of trigger Ca^{2+} entering by

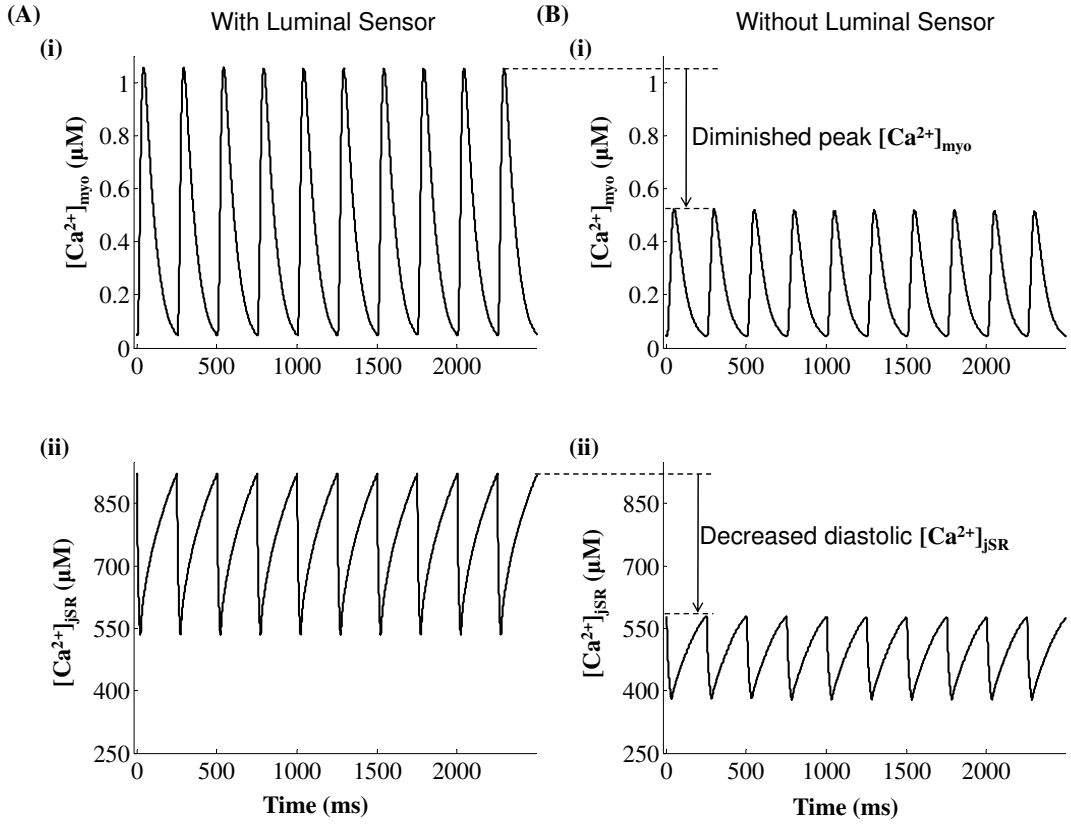

Figure 3.8 : Application of a train of voltage clamp pulses (amplitude -40 to 10 mV; duration 50 ms) for a period of 2.5 sec. Pulse repetition rate is 4.0 Hz. Luminal sensor is intact in A and removed in B. Both A and B are steady state responses to voltage clamp stimulation. A-(i) $[Ca^{2+}]_{myo}$ transients with normal amplitude. A-(ii) Sustained SR filling due to robust RyR inactivation. B-(i) Diminishing $[Ca^{2+}]_{myo}$ transients indicate poor SR filling. B-(ii) Lowered $[Ca^{2+}]_{jSR}$ levels indicating inadequate refilling of SR stores due to lack of RyR refractoriness.

means of the $I_{Ca,L,TT}$ channel (b) the concentration gradient of Ca^{2+} between the jSR and the mouth of the RyR channel in the dyadic space and (c) the open probability of the RyR channel modulated by the interaction between the luminal sensor and the RyR protein. The SR Ca^{2+} released also inactivates the trigger current $I_{Ca,L,TT}$ (as shown in Fig. 3.1), hence causing an indirect self-inhibition of RyR release.

Figure 3.9 shows a phase plot of RyR open probability ($O2_{ryr}$) versus the Ca^{2+}

concentration at the mouth of the RyR channel in the dyadic space $[Ca^{2+}]_{ryr}$ constructed from model-generated data for a pulse of amplitude -40 mv to 10 mv and a duration of 50 ms. The pre-release diastolic $[Ca^{2+}]_{jSR}$ is 918 μM. Following excitation by the trigger current during phase A, the RyR channel begins to open, allowing Ca^{2+} flux into the dyad and elevating $[Ca^{2+}]_{ryr}$ at the mouth of the RyR channel. The rate of opening of the channel is Ca^{2+} dependent; hence as $[Ca^{2+}]_{ryr}$ increases, RyR open probability increases first slowly and then ever more rapidly. With this onrush of Ca^{2+}, $[Ca^{2+}]_{ryr}$ rapidly equilibrates with the $[Ca^{2+}]_{jSR}$, reducing and eventually abolishing the concentration gradient across the channel. $[Ca^{2+}]_{ryr}$ soon reaches its maximum value (T1 in Fig. 3.9) and begins to track the decrease in $[Ca^{2+}]_{jSR}$, there being no further significant concentration gradient existing between $[Ca^{2+}]_{jSR}$ and $[Ca^{2+}]_{ryr}$ at the mouth of the RyR channel. During phase B, the rate of rise in RyR open probability decreases due to decreasing $[Ca^{2+}]_{ryr}$ and the onset of self-inhibition due to the large values of Ca^{2+} concentration at the mouth forcing the RyR open probability to attain its maximum value (T2 in Fig. 3.9). This is followed by phase C, where the RyR open probability begins to decrease slowly, initiating channel recovery due to decreasing overall $[Ca^{2+}]_{dyad}$ levels as a result of (a) Ca^{2+} fluxing out of the dyad into the cytosol, (b) lack of a drive from SR release due to drastically diminished Ca^{2+} gradient at the mouth of the RyR channel and (c) continued Ca^{2+} induced self-inhibition. Decreasing levels of free Ca^{2+} in the jSR force a strong RyR inactivation via the luminal sensor (beginning at T4 and continuing throughout phase D; Fig. 3.9), which in turn causes a sharp decline in RyR open probability. The minimum value of $[Ca^{2+}]_{jSR}$ occurs at T5, and the channel is ultimately closed at T6 (Fig. 3.9). The luminal sensor mediated inactivation assists in robust $[Ca^{2+}]_{jSR}$ recovery.

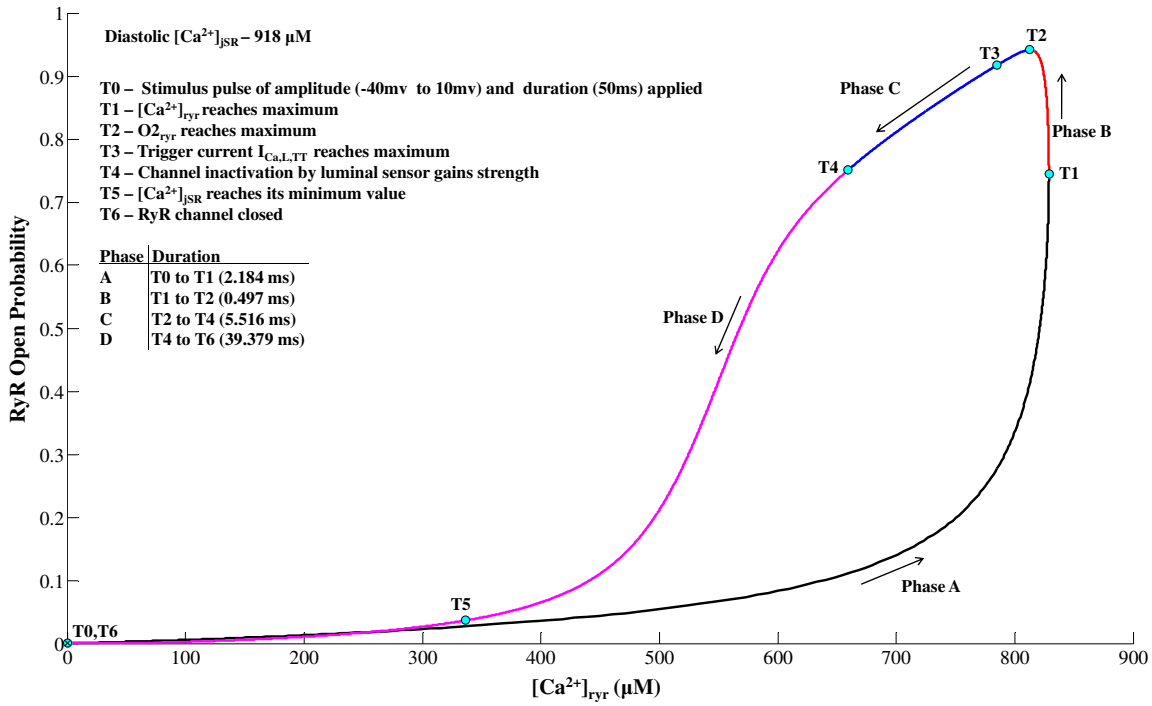

Figure 3.9 : RyR open probability modulation by concentration at the mouth. The pre-release diastolic $[Ca^{2+}]_{jSR}$ is 918 μM. The stimulation protocol used is a pulse of amplitude (-40 mv to 10 mv) and duration (50 ms). Phase A - As a result of excitation by the trigger current, $[Ca^{2+}]_{ryr}$ initially increases rapidly with a small accompanying rise in RyR open probability followed by steeper increase to peak $[Ca^{2+}]_{ryr}$ with a large increase in RyR open probability.; Phase B - RyR open probability increases to its maximum value at a declining rate reflecting a falling $[Ca^{2+}]_{ryr}$ level and onset of Ca^{2+} induced self-inhibition; Phase C - Decreasing $Ca^{2+}{}_{dyad}$ and continued Ca^{2+} induced self-inhibition, begins the channel recovery process; Phase D - Decreasing $[Ca^{2+}]_{jSR}$ forces a strong RyR inactivation via the luminal sensor hence robustly closing the channel.

3.3.6 Cytosolic Peak [Ca^{2+}] Dependence on SR Ca^{2+} Content

Fig. 3.10A shows three characteristic regions in the plot of the peak $[Ca^{2+}]_{myo}$ vs $[Ca^{2+}]_{jSR}$. In Region I, where the jSR load is small, two things occur: (a) RyR release is reduced, as is the basal intracellular Ca^{2+} concentration, and (b) Ca^{2+} dependent inactivation of the $I_{Ca,L,TT}$ channel is reduced due to the lowered dyadic

Ca^{2+} concentration, which allows for greater Ca^{2+} entry into the dyadic space via the $I_{Ca,L}$ channel. This increase in trigger current results only in a very small increase in Ca^{2+} release, because of the inhibition of the Ry-sensitive channel caused by the luminal sensor in response to low SR Ca^{2+} content. Thus, these factors cumulatively result in only a small linear increase in the peak $[Ca^{2+}]_{myo}$ with increasing SR Ca^{2+} content in Region I. The behavior in Region I corresponds to traces 7-1 in Fig. 3.10B (shows phase plots of $O2_{ryr}$ vs $[Ca^{2+}]_{ryr}$ for different steady state $[Ca^{2+}]_{jSR}$ concentrations), where the peak RyR open probability shows very small gradual increase with increasing levels of diastolic pre-release $[Ca^{2+}]_{jSR}$ for a constant trigger Ca^{2+} input via $I_{Ca,L}$. The steady state diastolic $[Ca^{2+}]_{jSR}$ levels being low, the maximum RyR open probability values attained are low. Although the peak $[Ca^{2+}]_{ryr}$ does not increase substantially as the diastolic $[Ca^{2+}]_{jSR}$ levels increase from 317μM to 673μM, the area enclosed by the $[Ca^{2+}]_{ryr}$ - $O2_{ryr}$ loop (which indicates the amount of SR Ca^{2+} released into the dyad) increases exponentially due to increasing peak RyR open probability combined with the increasing difference between rate of activation and inactivation with rate of activation increasing faster than the rate of channel inactivation. In Region II of Fig. 3.10A, increasing SR Ca^{2+} content begins to translate into a substantial increase in peak $[Ca^{2+}]_{myo}$. This is because increasing diastolic $[Ca^{2+}]_{jSR}$ causes a significant increase in the peak RyR open probability, as shown in Fig. 3.10C, which translates into a commensurate increase in the peak of the cytosolic Ca^{2+} transient. The inhibiting role of the luminal sensor is relieved with building $[Ca^{2+}]_{jSR}$ levels. The nonlinearity observed between the diastolic $[Ca^{2+}]_{jSR}$ levels 673μM (Fig. 3.10B) and 734μM (Fig. 3.10C) at the transition between Regions I and II corresponds to the existence of a threshold characteristic for RyR release [181, 182]. As the diastolic $[Ca^{2+}]_{jSR}$ levels increase beyond 734μM, the area enclosed

by the $[Ca^{2+}]_{ryr}$ - $O2_{ryr}$ loop increases substantially reaching a maximum value at $[Ca^{2+}]_{jSR}$ level of 948μM not only due to a significant increase in both peak $[Ca^{2+}]_{ryr}$ and peak $O2_{ryr}$ but also due to a rapid increase in rate of RyR activation resulting in a much larger difference in rate of activation and inactivation. Region III exhibits a large rapid increase in peak $[Ca^{2+}]_{myo}$ due to the large RyR Ca^{2+} release associated with the high SR Ca^{2+} content. However, it is important to note that this is not a result of increasing peak RyR open probability, which begins to plateau for steady state $[Ca^{2+}]_{jSR}$ values larger than 850μM (traces 6-1 in Fig. 3.10C). The continuing rapid increase in peak cytosolic Ca^{2+} concentration in region III is a combined result of: (a) increased release owing to large SR Ca^{2+} content; (b) large values for saturated RyR open probability supported by an increase in the area contained by each loop as seen in traces 6-1 of Fig. 3.10C; and (c) saturated operation of the SERCA pump which acts as a predominant buffer in restoring the Ca^{2+} concentration levels in the cytosol after RyR release [147]. As the diastolic $[Ca^{2+}]_{jSR}$ levels increase beyond 948μM, the area enclosed by the $[Ca^{2+}]_{ryr}$ - $O2_{ryr}$ loop begins to decrease despite increasing peak $[Ca^{2+}]_{ryr}$ due to saturation of the peak RyR open probability and increasing rate of RyR channel inactivation due to large values of local Ca^{2+} concentration ($[Ca^{2+}]_{ryr}$) assisting in faster recovery [114]. This model generated relationship between the peak $[Ca^{2+}]_{myo}$ and the pre-release $[Ca^{2+}]_{jSR}$ agrees with Fig. 4 in Diaz et. al. [85].

As seen in traces 1-10 of Fig. 3.10C, during the initial activation of a RyR channel (linear region of phase A in Fig. 3.9), at any specific $[Ca^{2+}]_{ryr}$ the RyR open probability takes a lower value despite a higher steady state diastolic $[Ca^{2+}]_{jSR}$ level. This decreasing slope with increasing diastolic, pre-release $[Ca^{2+}]_{jSR}$ reflects a faster rate of rise in $[Ca^{2+}]_{ryr}$ for a larger pre-release SR content with a very small accompanying increase in the RyR open probability.

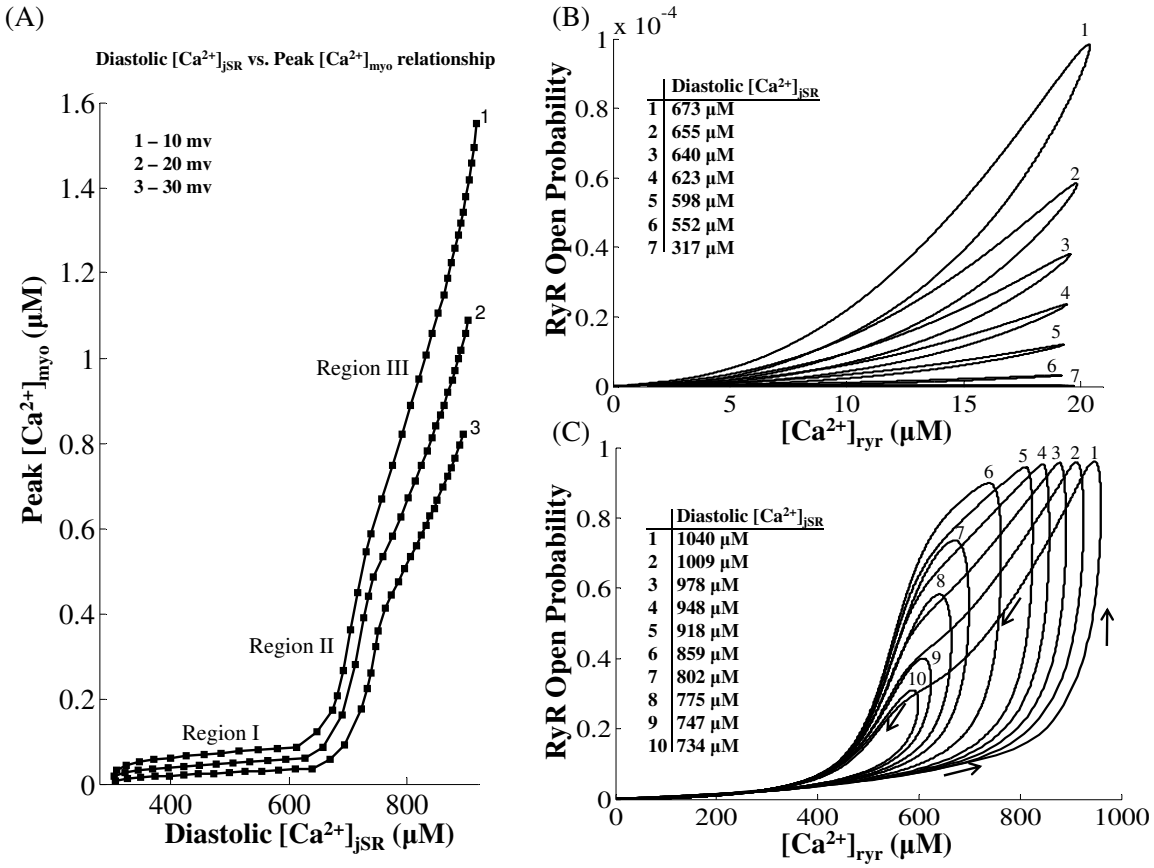

Figure 3.10 : (A) Relation between the peak of the cytosolic Ca^{2+} transient and the diastolic $[Ca^{2+}]_{jSR}$. Region I: The peak RyR open probability is very small owing to the low SR Ca^{2+} content. This causes the peak Ca^{2+} transient to be very small. Region II: Increasing SR Ca^{2+} content causes an increase in the peak RyR open probability and hence in the peak of the cytosolic Ca^{2+} transient. Region III: A large rapid increase in the peak ${Ca^{2+}}_{myo}$ is observed due to the large RyR Ca^{2+} release associated with the high SR Ca^{2+} content and saturation of RyR open probability. This model-generated result shows similarity to data in Fig.4, Diaz et al. [85].(B) Dependence of RyR open probability ($O2_{RyR}$) on diastolic ${Ca^{2+}}_{jSR}$. Increasing pre-release diastolic ${Ca^{2+}}_{jSR}$ results in increasing peak $O2_{RyR}$. However, owing to the low SR Ca^{2+} levels the peak open probability is very small. The stimulation protocol used is a pulse of amplitude -40 mv to 10 mv with a duration of 50 ms. (C) Dependence of RyR open probability ($O2_{RyR}$) on diastolic ${Ca^{2+}}_{jSR}$. Increasing diastolic ${Ca^{2+}}_{jSR}$ results in a linearly increasing peak $O2_{RyR}$. In the open probability saturation region the increase in peak cytosolic Ca^{2+} transient is sustained by increasing the area contained by each loop as seen in traces numbered 5 to 1. The progress in time occurs along the arrow indicated on trace 1. The stimulation protocol used is a pulse of amplitude -40 mv to 10 mv with a duration of 50 ms.

3.3.7 Ca^{2+} Release and its Effect on $I_{Ca,L}$

3.3.8 Caffeine

Adachi-Akahane et al. [141] investigated $I_{Ca,L}$-induced Ca^{2+} release in rat ventricular myocytes in the presence and absence of caffeine, which altered $[Ca^{2+}]_{myo}$. Using their protocols and data as a guide, we modeled the effect of caffeine on jSR Ca^{2+} release and its subsequent effect on $I_{Ca,L}$. Specifically, a Boltzman relationship was adopted to simulate the binding of caffeine to the ryanodine receptor increasing channel conductance, which in turn enhances jSR Ca^{2+} release. The process is assumed to be dose-dependent, with an open probability of 0.5 at a caffeine concentration of 5 mM (Appendix C.1, Eq. C.89).

Figures 3.11A and 3.11B show model-generated $[Ca^{2+}]_{myo}$ responses in myocytes dialyzed with 2 mM Fura-2, where a simple voltage clamp pulse (-40mV to 0 mV) is applied in the presence and absence of caffeine. $I_{Ca,L}$ waveforms associated with these two protocols are shown in Fig. 3.11C. In protocol A, conducted at normal rest levels of $[Ca^{2+}]_{myo}$ (30 nM), the depolarizing test pulse to 0 mV from the holding potential of -40 mV for 0.1 sec fully activates $I_{Ca,L}$, which in turn triggers a rapid but small amplitude Ca^{2+} transient (a rise from 30 nM to 95 nM as shown in Fig. 3.11A. Protocol B starts with an application of 5 mM caffeine for a period of 1.0 sec (open state probability of RyR channel is 0.5), followed by the same depolarizing test pulse applied at 1.0 sec. The conditioning caffeine pulse induces a $[Ca^{2+}]_{myo}$ transient rising from a resting value of 30 nM to a peak value of 110 nM (Fig. 3.11B, first peak -note the different timescale). The short depolarizing pulse activates $I_{Ca,L}$, which triggers a much smaller $[Ca^{2+}]_{myo}$ transient via CICR (30 nM, Fig. 3.11B, second peak). This $I_{Ca,L}$-evoked Ca^{2+} transient in response to the voltage pulse is smaller in amplitude

than control (Fig. 3.11A), due to: (a) reduction in RyR release due to depletion in $[Ca^{2+}]_{jSR}$ ($[Ca^{2+}]_{jSR}$ drops from 1.25 mM to 0.25 mM with caffeine application).; and (b) the strong competing role of the luminal RyR sensor in inactivating the RyR channel in response to the post-caffeine, low SR content. The $I_{Ca,L}$-inactivation characteristics undergo a change as shown in Fig. 3.11C, where trace B inactivates more slowly compared to the control $I_{Ca,L}$ (trace 1). After exposure to caffeine, the overall amplitude of $[Ca^{2+}]_{dhp}$ during release does not increase as much as in the control case, since jSR Ca^{2+} release is reduced. Consequently, Ca^{2+} dependent inactivation (during release) of $I_{Ca,L}$ after caffeine application is not as strong as that in the control case. However, the baseline level of Ca^{2+} concentration at the mouth of the DHP channel ($[Ca^{2+}]_{dhp}$) is elevated following caffeine application, causing sustained inactivation resulting in the crossover of the current trace in Fig. 3.11C. This is consistent with the observation of Cens et al. [104], that Ca^{2+} induced inactivation is a result of calmodulin mediated sensing of the local Ca^{2+} concentration.

3.3.9 Thapsigargin

Analogous to the experimental protocol of Adachi-Akahane et al. [141] dealing with thapsigargin blockade of the SERCA pump (their Fig. 9), we apply a series of voltage pulses (-40 mV to 0 mV, duration 0.1 sec, frequency 0.05 Hz) to our cell model, modified by blockade of the SERCA pump and addition of 2mM Fura-2. Figure 3.12 shows that when Ca^{2+} uptake is blocked, SR Ca^{2+} content declines, as does the jSR Ca^{2+} release with each voltage pulse (Fig. 3.12A). Considerable time is consumed after thapsigargin application, before SR Ca^{2+} content is finally exhausted (8-10 beats at 0.05 Hz; Fig. 3.12A). As the magnitude of the $[Ca^{2+}]_{myo}$ transient decreases, the $[Ca^{2+}]_{dhp}$ dependent inactivation of $I_{Ca,L}$ slows (Fig. 3.12B), resulting in an enhanced

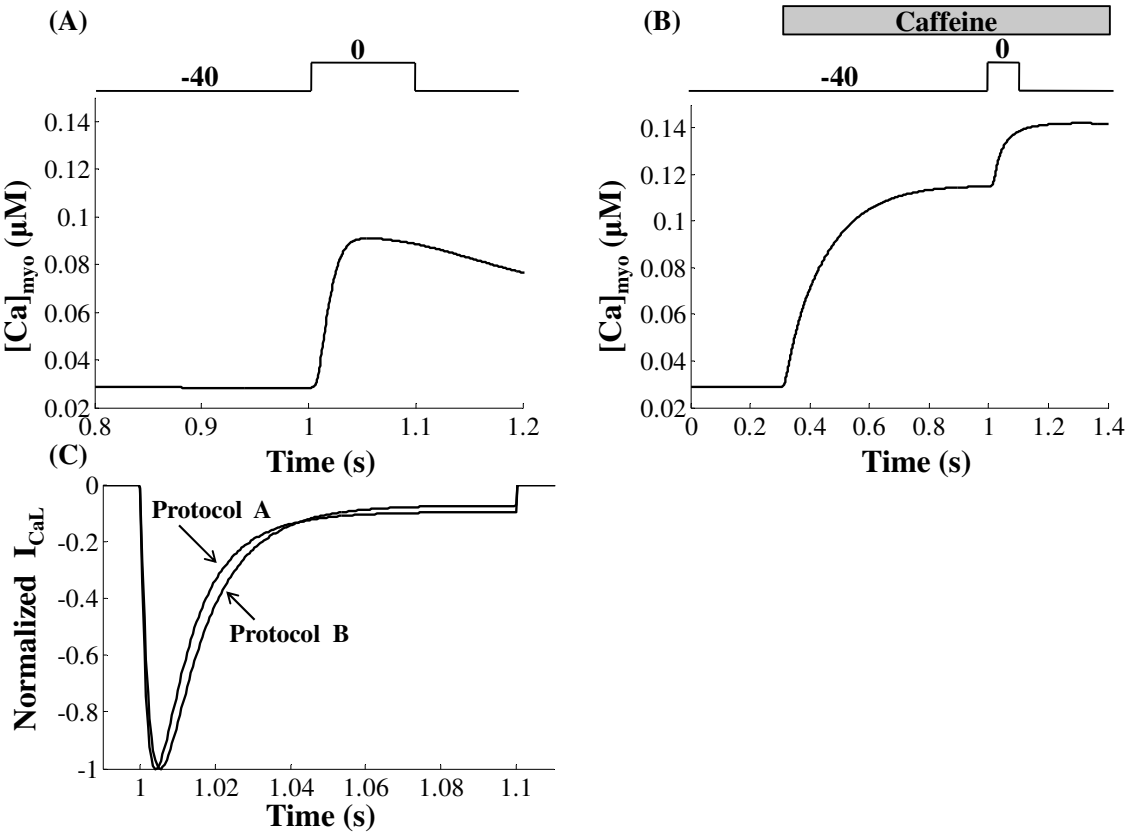

Figure 3.11 : Model-simulated effects of the application of caffeine on $I_{Ca,L,TT}$ and $[Ca^{2+}]_i$ in a cell dialyzed with 2 mM Fura-2. Changes in $[Ca^{2+}]_{myo}$ resulting from: (A) application of a simple depolarizing pulse from -40 mV to 0 mV, and (B) the same depolarizing pulse following pre-exposure to caffeine (5 mM). Panel (C) compares the $I_{Ca,L}$ waveforms associated with these protocols. This model-generated result shows similarity to data in Fig. 3, Adachi-Akahane et al. [141].

peak.

For a given clamp amplitude, a decrease in jSR Ca^{2+} content decreases Ca^{2+} release, producing decreased Ca^{2+} concentration at the dyadic side of the DHP-sensitive channel. Consequently, a smaller amount of calcium-calmodulin complex (Ca_4CaM) is activated, leading to a lower degree of Ca^{2+} dependent inactivation. Thus, $I_{Ca,L}$ peak is enhanced, as shown in Fig. 3.12B, increasing the area under the waveform,

corresponding to an increased amount of Ca^{2+} entering the cell. This inverse relationship between jSR Ca^{2+} content and the amount of trigger Ca^{2+} entering the dyadic space for a given clamp voltage is the essence of the feedback mechanism maintaining the efficacy of CICR. This mechanism is operational even in the presence of high concentrations of cytoplasmic Ca^{2+}-buffers, since the small dimensions of the dyadic space allow jSR released Ca^{2+} to reach its destination (i.e., the DHP receptor) before being captured by the buffers [183].

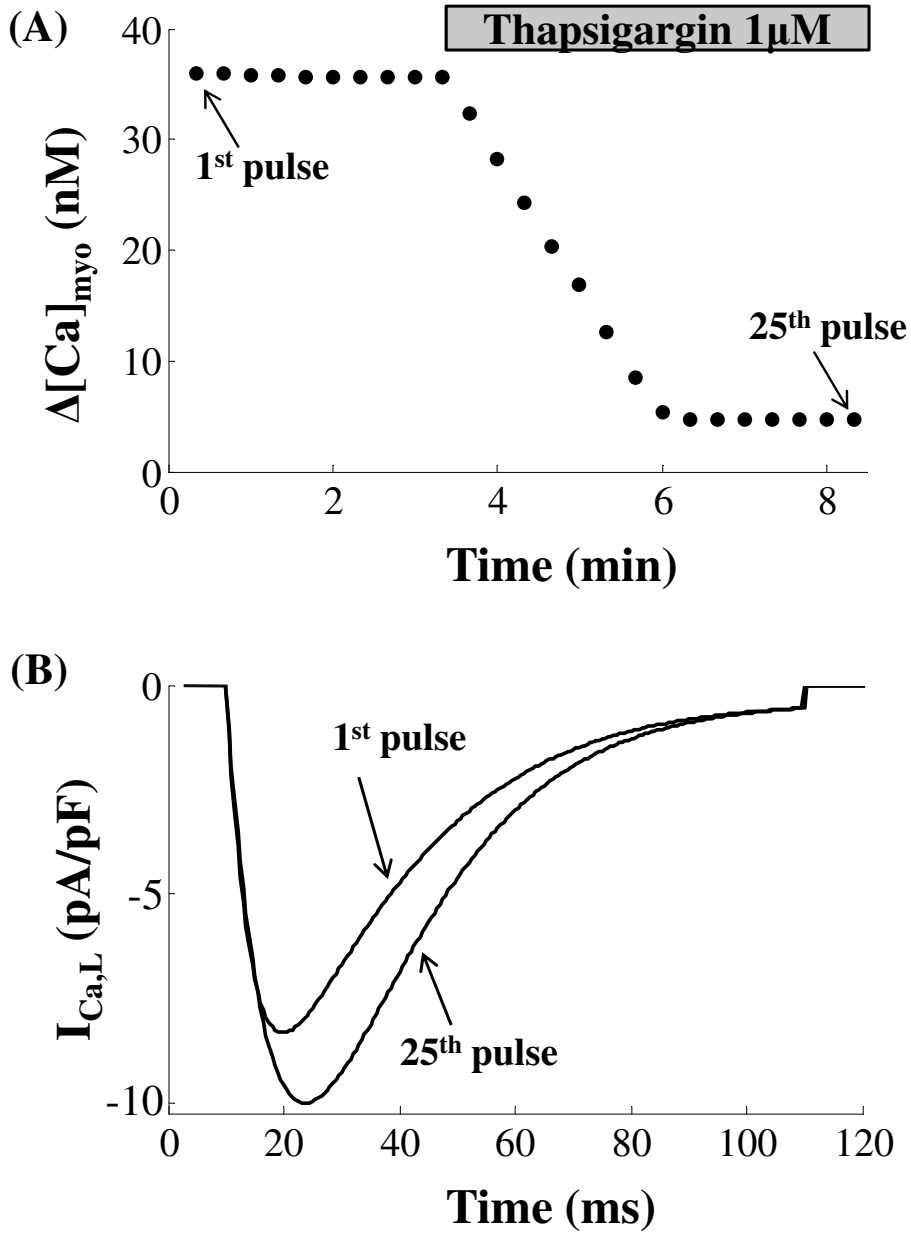

Figure 3.12 : In rat ventricular myocytes dialyzed with 2 mM Fura-2, thapsigargin gradually abolishes $[Ca^{2+}]_{myo}$ transients and decreases the rate of inactivation of $I_{Ca,L}$. This result is generated by the model, in response to a pulse train of amplitude (-40 mV to 0 mV), duration (0.1 sec) and frequency of 0.05 Hz. (A) Time course of the effect of thapsigargin on $\Delta[Ca^{2+}]_i$. (B) L-type Ca^{2+} currents at the times indicated in (A). This model-generated result shows similarity to data in Fig.11, Adachi-Akahane et al. [141].

3.3.10 Effect of Modulation of $[Ca^{2+}]_o$

Increase in $[Ca^{2+}]_o$ causes an increase in entry of extracellular Ca^{2+} into the cell via the $I_{Ca,L}$ channel. This results in an increase in SR Ca^{2+} content, as shown in Fig. 3.13B. Aided by an increase in trigger Ca^{2+} as well as a larger SR Ca^{2+} content, the RyR release is enhanced. This increase in SR release assisted by impaired Na^+/Ca^{2+} exchange due to elevated $[Ca^{2+}]_o$ manifests in an increase in the peak Ca^{2+} concentration levels in the cytosol, as shown in Figure 3.13A. Similarly, a decrease in extracellular Ca^{2+} levels causes a decrease in trigger Ca^{2+} available to cause CICR, which results in a decrease in peak $[Ca^{2+}]$ levels in the cytosol, as shown in Fig.3.13C. Reduced Ca^{2+} entry into the cell via $I_{Ca,L}$, translating into decreased availability of post-release Ca^{2+} in the cytosol, causes reduction in SR filling via the bi-directional SERCA pump. The corresponding drop in the SR Ca^{2+} content is evident in Fig. 3.13D. Although, our model-generated results show similarity to data in Fig. 2, Diaz et al. [184], our result in Fig. 3.13D does not confirm an increase in SR Ca^{2+} content with a decrease in $[Ca^{2+}]_o$ as reported in Fig. 2B, Diaz et al. [184]. On the contrary, they agree with the data in Fig. 5, Diaz et al. 1997 which shows a decrease in free diastolic steady-state SR Ca^{2+} content with decrease in $[Ca^{2+}]_o$ in cells not showing spontaneous release. In this study, we have attempted to isolate the effects of changes in $[Ca^{2+}]_o$ on intracellular Ca^{2+} levels by ensuring that there are no voltage dependent effects on Ca^{2+} transport via the $I_{Ca,L}$ channel, Na^+/Ca^{2+} exchanger or the plasma membrane Ca^{2+} ATPase pump. The simulation protocol used in our study (reproduced from Diaz et al. [184]),is a pulse train of amplitude (-40 mv to 0 mv), duration (100ms) and a frequency of 0.5 Hz. However, it is important to note that, for any constant extracellular Ca^{2+} concentration, in response to a voltage clamp pulse train, increasing clamp potential (>10mv) results in a decrease in steady

state SR Ca^{2+} content as a result of the dominating effect of reduced Ca^{2+} entry via the $I_{Ca,L}$ channel despite a decrease in net Ca^{2+} extrusion via the Na^{+}/Ca^{2+} exchanger per cycle.

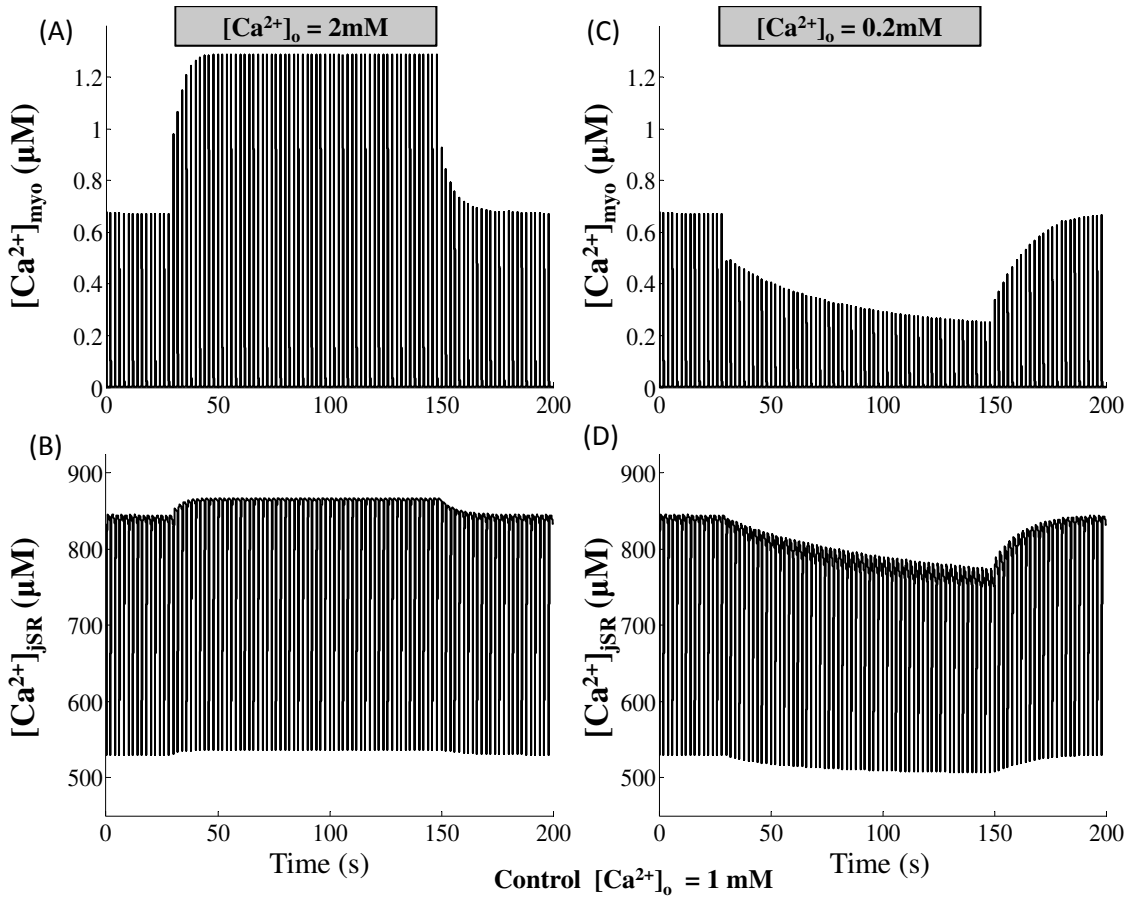

Figure 3.13 : The effects of changing external Ca^{2+} concentration on cytoplasmic Ca^{2+} and SR Ca^{2+} content. The stimulation protocol used is a pulse train of amplitude (-40 mv to 0 mv), duration (100 ms) and frequency of 0.5 Hz. (A) Following sudden rise in $[Ca^{2+}]_o$ the instantaneous increase in $[Ca^{2+}]_{myo}$ occurs due to more Ca entry, followed by a gradual staircase rise due to the the change in SR content; (B) Changes in $[Ca^{2+}]_{myo}$ forced by a sudden decrease in $[Ca^{2+}]_o$; (C) Changes in $[Ca^{2+}]_{jSR}$ due to increased $[Ca^{2+}]_o$; (D) Changes in $[Ca^{2+}]_{jSR}$ due to reduced $[Ca^{2+}]_o$. This model-generated result shows similarity to data in Fig. 2, Diaz et al. [184].

3.3.11 Ca^{2+} Balance Under Conditions of Repetitive Stimulation

Our model exhibits long term Ca^{2+} stability. Analogous to the experimental protocols of Negretti el al. [185], we studied the dynamic aspects of the calcium balance in the cell model by subjecting it to repetitive voltage clamps of different durations. For stable steady-state operation, Ca^{2+} entry into the cytosol via $I_{Ca,L}$ must exactly balance Ca^{2+} efflux. Changing the rate or pattern of stimulation can have significant effects on the cell's cytosolic Ca^{2+} balance and subsequent contractile response [55]. To demonstrate Ca^{2+} balance in our model, long (Fig. 3.14A) or short (Fig. 3.14B,C and D) voltage clamp pulses were applied at a selected repetition frequency, and the resultant changes in $[Ca^{2+}]_{myo}$ were correlated with sarcolemmal and SR Ca^{2+} fluxes. Analogous to the protocol of Negretti et al.[185], pulse trains were applied from a holding potential of -40 mV to +10 mV, with durations of either 800 ms (long-pulse) or 100 ms (short-pulse) at a frequency of 0.33 Hz, for a total test duration of 2 minutes (40 pulses). In analyzing the Ca^{2+} balance, the amount of electric charge Q transferred per pulse was calculated according to the equation: $\int_0^T$ I(t) dt, where I(t) can be $I_{Ca,L}$, I_{NaCa}, I_{PMCA}, I_{ryr}, $I_{cyt,serca}$, and T is 1 cycle duration (3ms for 0.33 Hz stimulation).

Numerical integration was carried out with respect to steady-state levels, hence only activating currents and leakage currents were considered (background Ca^{2+} current is neglected). The results of the Ca^{2+} balance are presented in a manner where relative Ca^{2+} fluxes can be easily compared. We note that in evaluating the integral of the combined exchanger current I_{NaCa}, the integral is multiplied by a factor of 2 to account for the fact that the exchanger stoichiometry is $3Na^+$ per Ca^{2+} (the exchanger transports 1 net charge per Ca^{2+}, whereas all other Ca^{2+} currents transport 2 charges per Ca^{2+}).

3.3.12 Long-Pulse Protocol

During repetitive long-pulse (800 ms) stimulation, transient Ca^{2+} fluxes cross the sarcolemmal and SR membranes in both directions (inward (into the cytoplasm) and outward). However, $[Ca^{2+}]_{myo}$ returns to control levels by the end of the long-pulse stimulation protocol. The long-pulse stimulation protocol thus serves as a means of studying the steady-state balance of Ca^{2+} influx and efflux to and from the cytoplasm, under control conditions. In contrast, this Ca^{2+} balance is not present in the short-pulse protocol, and $[Ca^{2+}]_{myo}$ is elevated at pulse termination. Our long-pulse simulations show that: (1) the magnitude of individual Ca^{2+} transients do not change during the 40 pulse sequence; (2) the peak calcium release current (I_{ryr}) has a constant magnitude; and (3) the occupancy of the calsequestrin Ca^{2+} buffer in the jSR compartment is reduced by 15% as a result of Ca^{2+} release during each cycle. Although Ca^{2+} fluxes cross the sarcolemma and SR membranes in either direction, the integral of each of these currents (indicating charge transfer) over the pulse repetition interval is a constant. Figures 3.14A shows this well, in that, the charge transfer for each model current (large or small) is a constant, indicating no net loss of Ca^{2+} nor consecutive-pulse Ca^{2+} depletion (or augmentation) in the jSR compartment under the long-pulse protocol. In Fig. 3.14, we refer to Ca^{2+} influx and efflux through the bounding cell membrane (sarcolemma and T-tubule) as "external fluxes" (i.e., $I_{Ca,L}$, I_{NaCa}, and I_{PMCA}), whereas SR membrane Ca^{2+} fluxes (I_{ryr}, $I_{cyt,serca}$) are called "internal fluxes." By convention, inward fluxes are negative (e.g. $I_{Ca,L}$) and outward positive (e.g., I_{NaCa} and I_{PMCA}). Figure 3.14A shows that the integrated external fluxes sum to zero. The average Ca^{2+} charge entering the cell via $I_{Ca,L}$ is 603.28 pC (pico-coulomb), and the sum of averaged Ca^{2+} charges extruded from the cell via I_{NaCa} and I_{PMCA} is 603.28 pC (602.2 pC by I_{NaCa} and 1.08 pC by

I_{PMCA}. Figure 3.14A also shows the magnitudes of the integrated internal fluxes, which sum to zero as well. In calculating inward and outward Ca^{2+} fluxes relative to the SR lumen, we consider an inward flux (e.g., $I_{cyt,serca}$) negative and an outward flux positive (e.g., I_{ryr}). The integral of I_{ryr} is 751.8 pC, compared with integral of the $I_{Ca,L}$ trigger current (603.28 pC). The calcium gain of CICR calculated in this way is low owing to the increased entry of Ca^{2+} via the trigger current $I_{Ca,L}$ for a prolonged duration of 800ms compared to 50ms previously. The integral of SR Ca^{2+} uptake is 751.8 pC. These two internal component currents yield flat integral values during long-pulse stimulations and sum to zero.

3.3.13 Short-Pulse Protocol

Decreasing the length of the depolarizing pulse to 100 ms (short pulse) has a pronounced effect on the recovery of contraction (Fig. 3.14B, 3.14C and 3.14D). Compared with the relatively flat amplitude of $[Ca^{2+}]_{myo}$ observed with stimulation by long pulses, short pulse stimulation produces a negative staircase (Fig. 3.14B) in agreement with the data (Negretti et al.[185]), wherein the peak magnitude decays exponentially to a steady state level of 60% of the initial value. Figure 3.14B also shows that the model predicts a similar exponential decay in jSR Ca^{2+} concentration $[Ca^{2+}]_{jSR}$. Both of these indicators show a net loss of Ca^{2+} from the cell. Figure 3.14C and 3.14D show the transient charge movements associated with the external and internal Ca^{2+} currents respectively during application of the short-pulse train, which are indicative of an elevated Ca^{2+} load and resultant Ca^{2+} imbalance when the pulse train is first applied. Balance is achieved, but at new lower values of $[Ca^{2+}]_{myo}$ and $[Ca^{2+}]_{jSR}$. For convenient comparison, all internal fluxes are made positive and all external fluxes negative. Figure 3.14C shows that I_{NaCa} plays a significant role in

forming the transient response seen in the short-pulse protocol in extrusion of excess Ca^{2+} load on the cell. The decreasing amplitude of the Ca^{2+} transient causes a decreased LSR uptake current ($I_{cyt,serca}$), which in turn causes a decrease in $[Ca^{2+}]_{jSR}$ resulting in decreased release (I_{ryr}). With successive pulses, $I_{cyt,serca}$ and I_{ryr} decline further, mirroring the exponential decline in I_{NaCa} toward balance. At steady state, the external and internal fluxes reach the new equilibrium, where the sum of the integrals of external currents and the sum of the integrals of internal currents are zero.

3.3.14 Long-Term Calcium Stability at Higher Pacing Rates

Most VC experiments on cardiac cells are usually conducted at low stimulation rates. Our simulations of typical VC experiments at these low rates all exhibit long term calcium stability (Figures 3.11, 3.12, 3.13 and 3.14). However, our model can also exhibit sustained calcium balance at higher pacing rates. Figure 3.8A shows steady state cytosolic Ca^{2+} transients in response to a repetitive 4 Hz (which is more physiological for a rat ventricular myocyte) voltage clamp stimulation lasting for 2.5 seconds. The sustained peak and basal Ca^{2+} levels of $[Ca^{2+}]_{myo}$ over this prolonged time frame are indicative of long tern Ca^{2+} stability in the model. The corresponding $[Ca^{2+}]_{jSR}$ profile over 2.5 seconds is also shown in Figure 3.8A, which indicates sustained SR filling owing to the luminal sensor mediated control of the RyR channel. The stimulation protocol used is a pulse train of amplitude (-40 mv to 10 mv), duration (50 ms) and frequency of 4.0 Hz.

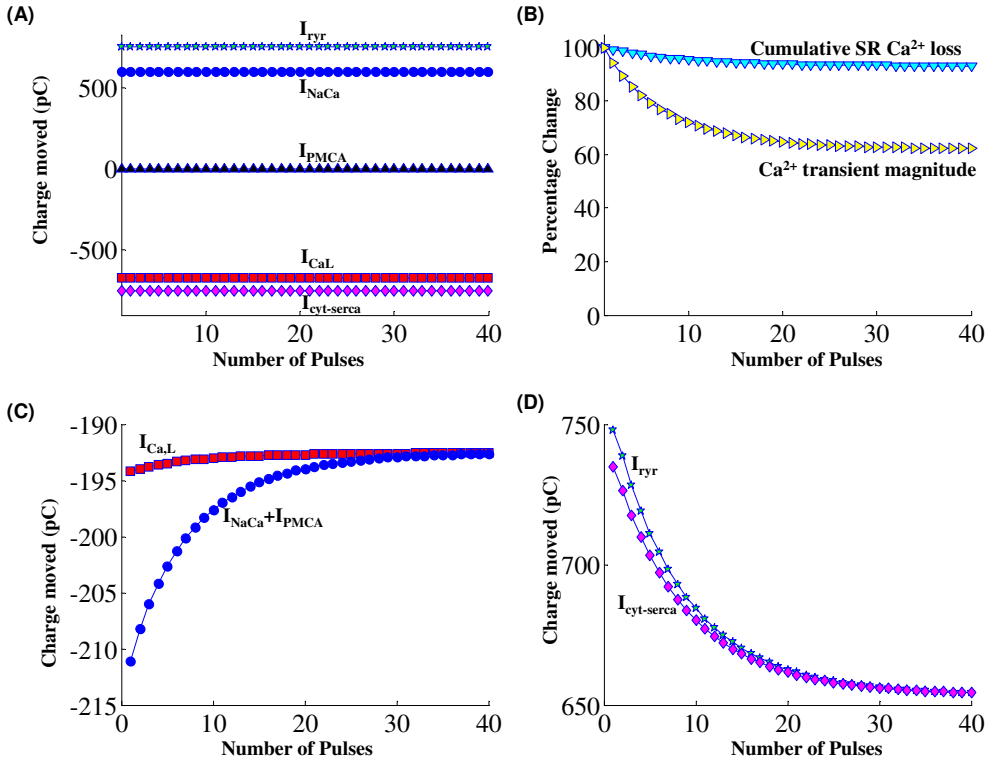

Figure 3.14 : The stimulation protocol used is a pulse train of amplitude (-40 mv to 10 mv) and frequency of 0.33 Hz.(A) Integrals of external and internal Ca^{2+} currents on stimulation with repetitive long pulses (800 ms); (B) Percentage of changes in $[Ca^{2+}]_{myo}$ peak magnitude and cumulative SR Ca^{2+} loss on stimulation with repetitive short pulses (100 ms); (C) Integrals of external Ca^{2+} currents with short-pulse stimulations (100 ms); (D) Integrals of internal Ca^{2+} currents with short-pulse stimulations (100 ms). This model-generated result shows similarity to data in Fig. 3 and Fig. 5, Negretti et al. [185].

3.3.15 Secondary $[Ca^{2+}]_{myo}$ Transients Induced by "Tail Currents"

Our voltage clamp simulations have dealt with clamp voltages in the range -30 mV $\leq$ V $\leq$ 40 mV. Some experimental studies [174, 9, 186] however have employed even larger clamp voltages (40 mV $\leq$ V $\leq$ 60 mV) to explore the high voltage behavior of the DHP-sensitive calcium channel. Such large clamp voltages elicit a brief Ca^{2+} influx called a "tail current," which has been shown to trigger RyR release and hence

cause contraction during repolarization [174, 9]. The secondary Ca^{2+} transient induced by the "tail current" is a critical argument in favor of CICR as these "tail currents" are not observed in skeletal muscle where the membrane potential directly controls SR Ca^{2+} release [186]. Our model reproduces this secondary Ca^{2+} transient observed during the return to resting potential from a large clamp voltage ($\geq$40 mV). Figure 3.15A shows a cartoon depicting the voltage clamp stimulation protocol used in our study where a pulse of amplitude (-40 mV to +50 mV) is employed with the pulse duration (T_p; Fig. 3.15A) increasing from 50 ms (trace 1) to 200 ms (trace 7) in steps of 25 ms. The clamp potential transition time (T_t) is fixed at 1ms. The peak of the "tail current" at the end of the pulse is $\sim$25 times larger than the peak of the $I_{Ca,L}$ current observed at the beginning of the pulse. This is in agreement with model generated VC data reported by Geenstein et al.([8]; Fig. 8). Figure 3.15B shows that, with an increase in clamp pulse duration, there is a corresponding increase in the peak of the tail current (see traces 1-7) until the effect ultimately saturates. Corresponding to this increase in peak $I_{Ca,L}$ tail current, there is an increase in the open probability of the RyR Ca^{2+} channel, with RyR Ca^{2+} release indicated by the corresponding decrease in $[Ca^{2+}]_{jSR}$ (panel C) and increase in $[Ca^{2+}]_{myo}$ (panel D). We note from Fig. 3.15C that for a shorter 50 ms VC pulse, there is no RyR Ca^{2+} release although an $I_{Ca,L}$ tail current is produced. This tail current produced with the 50 ms pulse slightly augments the $[Ca^{2+}]_{myo}$ transient just after its peak (trace 1, panel E), but there is no corresponding decrease in the $[Ca^{2+}]_{jSR}$ transient (trace 1, panel D) indicating no RyR Ca^{2+} release. At the end of this short pulse (50 ms), the RyR channel is in fact in its absolute refractory period. The small secondary increase in $[Ca^{2+}]_{myo}$ transient as seen in data corresponding to trace 4 of Fig. 3.1C is a result of the large Ca^{2+} influx via the $I_{Ca,L}$ "tail current." During this phase,

the Na^+/Ca^{2+} exchanger is biased to extrude Ca^{2+} out of the dyad, and hence cannot be responsible for this secondary rise in the cytosolic Ca^{2+} transient. As pulse duration is increased beyond 100 ms the "tail current" causes a gradual increase in RyR open probability (traces 3-7 in Fig. 3.15) indicating progressive recovery from the refractory period. Minimum value of $[Ca^{2+}]_{jSR}$ in traces 3-7 of Fig. 3.15D show increase in SR Ca^{2+} release with increasing pulse duration as a result of adequate RyR channel recovery and increasing $I_{Ca,L}$ "tail current." Cytosolic Ca^{2+} transients shown in Fig. 3.15E indicate "tail current" induced secondary RyR release for pulse duration $\geq$100 ms. It has also been previously reported [187] that recruitment of an additional population of previously 'silent' Ca^{2+} channels could cause facilitation of tail currents at increasingly large clamp voltages with a time-dependence associated with the recruitment process. Our model not only accounts for the contribution of the already open channels (in states $O2_{dhpr}$ & $O3_{dhpr}$) to the tail current during repolarization but also allows for the voltage- and time-dependent recruitment of 'silent' Ca^{2+} channels modeled using a high voltage state $C6_{dhpr}$. This study proves to be an adjunct to the study presented in Fig. 3.7 in establishing the refractory nature of the RyR channel.

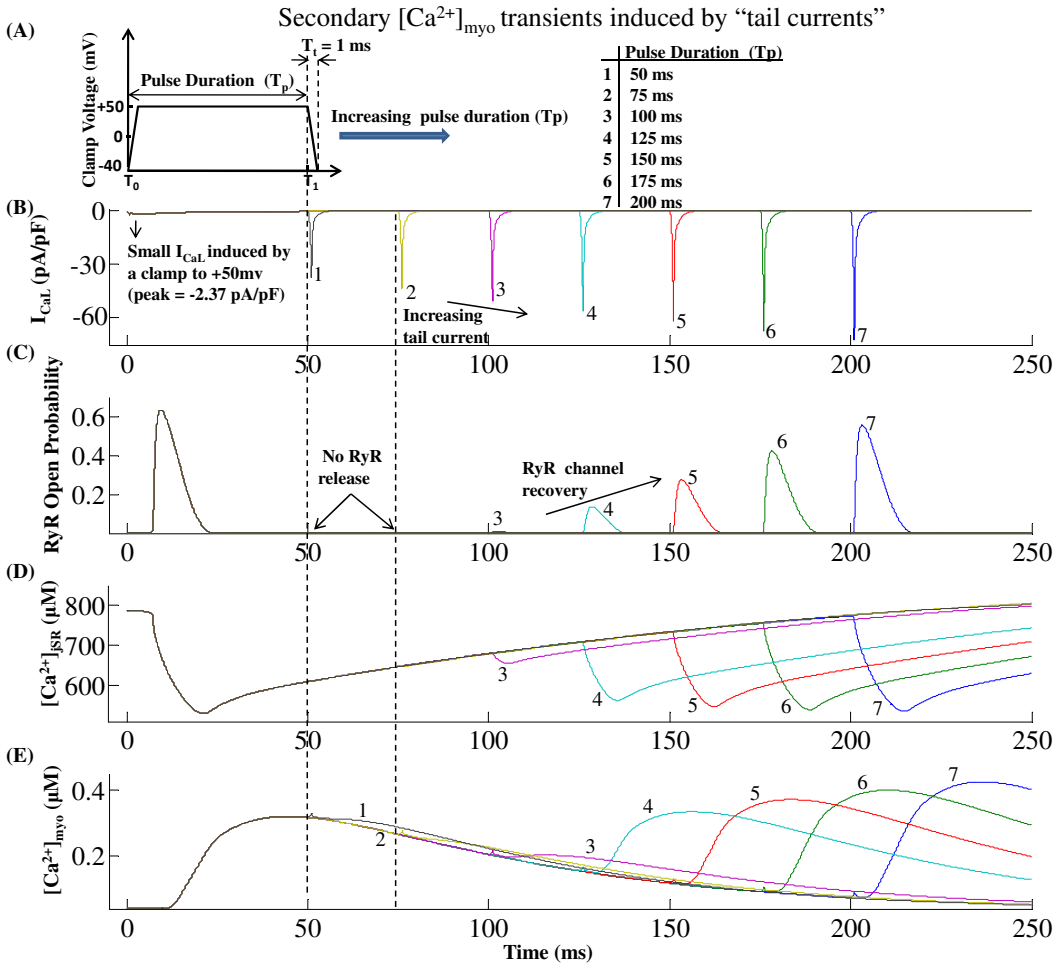

Figure 3.15 : The stimulation protocol used is a pulse of amplitude (-40 mv to +50 mv) with pulse duration T_p increasing from 50 ms (trace 1) to 200 ms (trace 7) in steps of 25 ms. (A) A cartoon depicting the voltage clamp stimulus protocol where, pulse duration (T_p) is varied to obtain traces 1-7 and the clamp potential transition time (T_t) fixed at 1ms. (B) $I_{Ca,L}$ tail currents elicited during repolarization from +50 mv to -40mv. (C) Open probability of the RyR channel indicating gradual recovery from the refractory period (D) $[Ca^{2+}]_{jSR}$ traces show increase in RyR release with increasing pulse duration as a result of adequate RyR channel recovery. (E) Cytosolic calcium transients indicate secondary RyR release caused by tail currents.

3.3.16 Cytosolic Buffering

In our model, cytosolic buffering is attributed to several factors including: (a) calmodulin (CaM); (b) the Ca^{2+}-specific (Tc) troponin binding site; (c) the $Ca^{2+} - Mg^{2+}$

competitive troponin binding site; and (d) the fluorescent indicator dye Fluo3 used to detect changes in $[Ca^{2+}]_{myo}$. The effects of the component buffers in helping to maintain a low $[Ca^{2+}]_{myo}$ are shown in Fig. 3.16 in terms of occupancy functions, such as O_C (fractional occupancy of calmodulin by Ca^{2+}), O_{tc} (fractional occupancy of troponin-Ca sites by Ca^{2+}), O_{tmgc} (fractional ocupancy of troponin-Mg sites by Ca^{2+}), O_{tmgmg} (fractional occupancy of troponin-Mg sites by Mg^{2+}) in the cytosol, and O_{calse} (fractional occupancy of calsequestrin by Ca^{2+}) in the jSR Ca^{2+} release compartment. Figure 3.16 shows that when the Ry-sensitive Ca^{2+} release channel is triggered, the jSR releases Ca^{2+} and the occupancy O_{calse} in the jSR, declines from 68% to 37%. Ca^{2+} release from the jSR induces fast Ca^{2+} binding by calmodulin and troponin in the cytosol, as represented by the increases of O_c (0.29) and O_{tc} (0.16) in Fig. 3.16. Interactions between Ca^{2+} and the troponin-Mg sites result in an increase in occupancy of these sites by Ca^{2+} (O_{tmgc}), and a decrease in occupancy by Mg^{2+} (O_{tmgmg}).

3.4 Discussion

It is well-established that mammalian cardiac excitation-contraction coupling is mediated by calcium-induced calcium release (CICR). We have developed a comprehensive mechanistic model of CICR under voltage clamp conditions in the rat ventricular myocyte, which includes electrical equivalent circuit models for both the free sarcolemma and that portion involving junctional transmission, as well as, fluid compartment models for several fluid media within the cell (dyadic cleft space, longitudinal sarcoplasmic reticulum (LSR or Ca^{2+} uptake compartment), junctional sarcoplasmic reticulum (jSR or release compartment), and the cytosolic fluid compartment). An external bathing medium completes our fluid compartment description of the cell

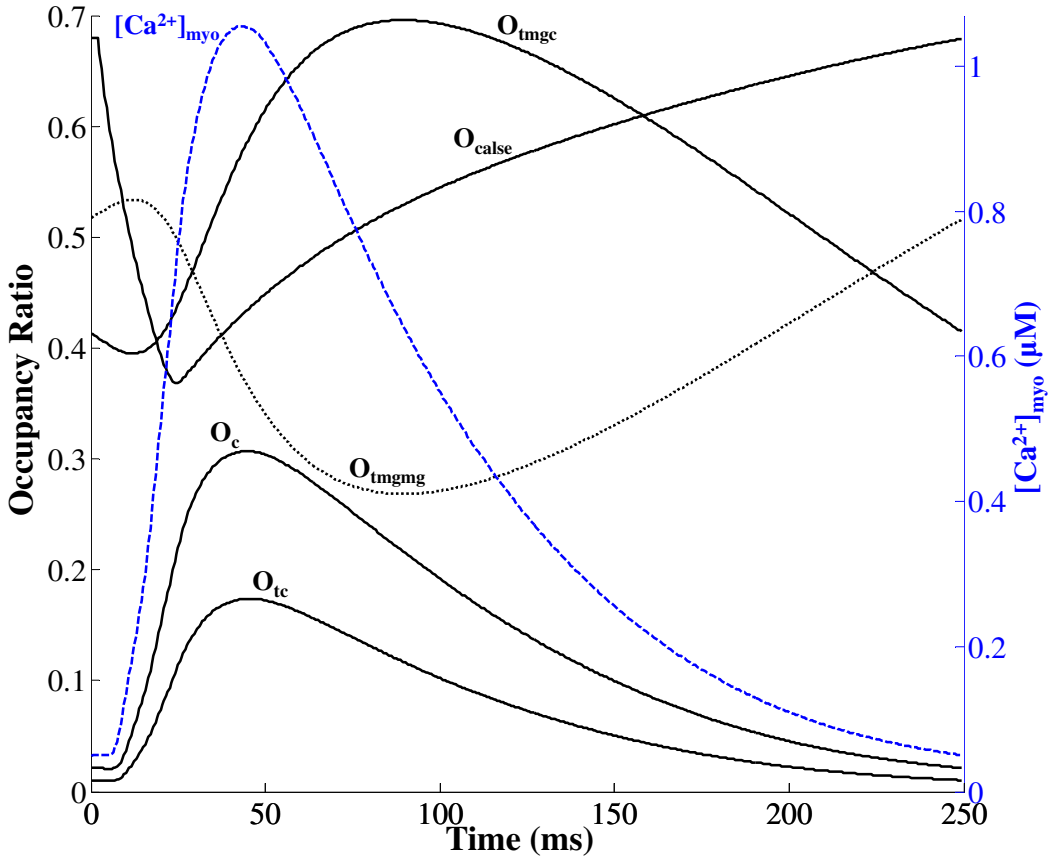

Figure 3.16 : Contributions of fractional occupancy of Ca^{2+} buffers in SR and cytoplasm. Transfer from O_c and O_{tc} to O_{tmgc} occurs as a result of the pulse stimulation. O_{tmgmg} is shown as a dotted line as it does not reflect Ca^{2+} binding. The corresponding $[Ca^{2+}]_{myo}$ is overlayed (note the different axis)

Fig. 2.3. The multiple component model is referred to as the "whole-cell model" (Figures 2.3 and 2.4). We have probed the mechanisms regulating Ca^{2+} in the cell. In particular, we have focused on the dyadic mechanisms effecting CICR.

The dyadic controller is a finely tuned coupling device consisting of two opposed Ca^{2+} channels separated by a small dyadic space (Fig. 2.3B): the sarcolemmal DHP-sensitive "trigger" channel and the Ry-sensitive jSR Ca^{2+} release channel. The trigger channel is voltage-activated and is driven in our simulations by a voltage clamp pulse

which opens the channels, admitting Ca^{2+} influx (trigger current) to the dyadic space. After diffusion within the dyadic space, trigger Ca^{2+} affects the Ca^{2+} dependent open probability of the jSR Ca^{2+} release channel over a small range of Ca^{2+} concentrations. Clamp voltage magnitude strongly affects the $I_{Ca,L}$ current and hence the amount of Ca^{2+} delivered to the dyadic space, but the range over which the Ca^{2+} concentration at the mouth of the Ca^{2+} release channel changes (in the absence of RyR release) is quite small (23.42μM to 8.82μM for a change in VC from 10mv to 40mv). The RyR-mediated Ca^{2+} release is activated by trigger current, but the release itself is affected by the concentration gradient between the jSR and the dyadic space, and the temporal and refractory properties of the ryanodine receptor (Fig. 3.7). The four-state RyR model is informed regarding supply Ca^{2+} content by the jSR luminal sensor, a novel feature in our model which characterizes the important protein-protein interactions between calsequesterin, triadin/junctin and the RyR receptor. Triadin/junctin strongly regulates the sensitivity of RyR to trigger Ca^{2+}. Hence the luminal sensor, which is a key element responsible for robust post-release RyR inactivation and refractoriness of the Ry-sensitive Ca^{2+} release channel, is critical in providing realistic fits to cytosolic Ca^{2+} transients and an adequate refilling time for the SR Ca^{2+} stores. Ca^{2+} release is thus graded with Ca^{2+} concentration at the mouth of Ca^{2+} channel in a very sensitive manner with a gain of approximately 7, as is shown in Fig. 3.6.

The sarcolemmal portion of the dyadic membrane defining the dyadic space contains voltage-sensitive Ca^{2+} channels and deals with changes in the external environment of the ventricular cell (e.g., membrane response to changes in transmembrane potential and chemical signaling agents). It integrates these various stimuli and delivers a trigger current to the small dyadic space. In contrast, the jSR membrane lining the opposite boundary of the dyadic space is concerned with the adequacy of

Ca^{2+} release in CICR. It contains Ry-sensitive Ca^{2+} channels that require a Ca^{2+} concentration gradient directed across the channel and into the dyadic space for their operation. Thus, jSR Ca^{2+} concentration must be maintained within an acceptable range so that calcium is always available for ready release. The relationship between jSR Ca^{2+} content and peak $[Ca^{2+}]_{myo}$ is shown in Fig. 3.10A. The LSR compartment connects the jSR compartment with the cytosolic compartment. It feeds make-up calcium to the jSR, by using a SERCA pump to actively draw in Ca^{2+} from the myoplasm. Pumping rate is controlled by the cytosolic Ca^{2+} concentration $[Ca^{2+}]_{myo}$ as well as the LSR Ca^{2+} concentration $[Ca^{2+}]_{LSR}$ as part of a mechanism for replenishing and maintaining jSR Ca^{2+} stores. Our model also incorporates the Ca^{2+} induced CaM mediated effects of CaMKII and CaN on targets such as the DHP-sensitive $I_{Ca,L}$ channel, Ry-sensitive Ca^{2+} release channel, as well as the SR Ca^{2+} ATPase pump. Provision for the effects of phospholamban on SERCA has also been included.

The voltage-gated and chemically gated channels of the dyad are tightly coupled by feedback mechanisms that involve Ca^{2+} signaling. Although physically separated, the voltage-sensitive Ca^{2+} channel (Figure 3.3) as well as the Ry-sensitive release channel (Phase C in Figure 3.9) are inhibited by increased Ca^{2+} levels in the dyadic space [116]. In earlier models which lacked the luminal sensor, RyR self-inhibition by dyadic Ca^{2+} was the only mechanism besides stochastic attrition (both of which are inadequate in effecting a robust RyR channel closure) that was given the role of initiating RyR recovery. This has been tested in our model by artificially clamping all the variables (including concentration at the mouth of the RyR channel) to the levels reached at T2 in Fig. 3.9 despite which the RyR open probability, begins to decline in phase C of Fig. 3.9 showing the self-inhibitory role of high dyadic Ca^{2+} concentration. Our model predicts (data not shown) that this Ca^{2+} signaling

continues even in the presence of high concentrations of Ca^{2+} buffering agents in the cytosol (in agreement with the data of Adachi-Akahane et al. [141] and Diaz et al. [184]). Tight coupling between the DHP and Ry-sensitive Ca^{2+} channels within the dyadic space thus preserves the mechanism of CICR under these extreme conditions.

Regulation of cytosolic Ca^{2+} concentration $[Ca^{2+}]_{myo}$ is evident at the cellular level. It is affected strongly by the voltage and $[Ca^{2+}]_{myo}$-dependent properties of the sarcolemmal currents I_{NaCa} and $I_{Ca,L}$, as well as the $[Ca^{2+}]_{myo}$-dependent properties of the I_{PMCA} and SERCA pumps. We demonstrate a model-generated whole-cell Ca^{2+} balance, which shows the importance of the Na^{+}/Ca^{+} exchanger in extruding the Ca^{2+} that has entered the cell under normal activity, and also any excess that might occur when cytosolic Ca^{2+} levels rise. The variety of experiments emulated in this study demonstrates quantification of Ca^{2+} balances for all external and internal Ca^{2+} fluxes and shows that the model has long-term stability in regulating cytosolic Ca^{2+}, as shown in the 120-sec duration experiments of Negretti et al. (Fig. 3.14) at a pulse repetition rate of 0.33 Hz., and the faster paced stimulation at 4Hz shown in Fig. 3.8A.

We have examined the dyadic component of the $I_{Ca,L}$ with regard to its Ca^{2+} -dependent inactivation as a function of jSR Ca^{2+} content (Fig. 3.11C). Trigger current is voltage-dependent and therefore parameterized by clamp pulse amplitude (Fig. 3.1A). In addition, its inactivation is Ca^{2+} dependent, especially during Ca^{2+} release. At a constant depolarizing voltage pulse, the pre-release jSR Ca^{2+} content dictates the peak of the cytosolic Ca^{2+} transient (Fig. 3.10A), by controlling peak Ca^{2+} concentration in individual dyads. As jSR Ca^{2+} content increases, so does the peak dyadic Ca^{2+} concentration, and the amount of sarcolemmal Ca^{2+} influx declines due to greater Ca^{2+} dependent inactivation. This autoregulatory feedback

mechanism helps to establish a stable operating point for jSR Ca^{2+} content. Transient ***increases*** in jSR Ca^{2+} content bring about increases in Ca^{2+} release, but reflexly, decrease sarcolemmal Ca^{2+} influx via $I_{Ca,L}$. Coupled with other dyadic and extra-dyadic mechanisms (I_{NaCa}) that decrease $[Ca^{2+}]_{myo}$ and hence Ca^{2+}-uptake via the SERCA pump, jSR Ca^{2+} content decreases. For ***decreases*** in jSR Ca^{2+} content, the opposite occurs, so that regardless of the sign of the perturbation in jSR Ca^{2+} content, it tends to stay constant in the steady-state. This is an important feature of the dyadic mechanism that preserves the integrity of CICR. The gain of this feedback system about the operating point is visualized as the slope of the peak Ca^{2+} transient vs SR Ca^{2+} content characteristic (Fig. 3.10A) for a given voltage pulse level. Observing this figure, we note that there is a linear operating range beyond which the system gain increases dramatically. Our model results also show that a decrease of jSR Ca^{2+} content (simulated either by a decrease of Ca^{2+} uptake into the LSR by thapsigargin or an increase of Ca^{2+} leak out of the jSR by caffeine) decreases systolic $[Ca^{2+}]_{myo}$, and hence the model might serve as a useful adjunct in a study of heart failure, where decreased contractility as a result of diminished Ca^{2+} transients are commonly observed [188].

3.4.1 Model Limitations

(a) This model of a rat ventricular myocyte is limited to Ca^{2+} related channel, exchanger and pumps ($I_{Ca,L}$, I_{NaCa}, I_{PMCA} and SERCA pump), while lacking exclusive Na^{+} or K^{+} related channels and transporters and is based on data at positive potentials in the range 10 mV $\leq$ V $\leq$ 40 mV. It is aimed at mimicking voltage clamp conditions where channels other than calcium are blocked, and it cannot be used to study experiments involving the generation of action potentials.

However, its focus on the Ca^{2+} dynamics allows one to comprehend more clearly the important role of Ca^{2+} signalling pathways and feedback control systems in maintaining whole cell homeostasis over a prolonged period of time.

(b) A single dyadic space in our model has one representative, lumped DHP-sensitive and Ry-sensitive Ca^{2+} channel, on opposing sarcolemmal and SR surfaces respectively. This simplified configuration does not conform to detailed structural information regarding the geometrical relationships between DHP and RyR-sensitive Ca^{2+} channels [189, 126, 190] and thus cannot be used to draw conclusions about this part of the EC coupling process. However, our lumped abstraction forms a functional model of the dyadic coupling unit that can produce accurate predictions of cytosolic Ca^{2+} transients. The effectiveness of this model is further demonstrated by its ability to accurately characterize the interaction between the DHP and Ry-sensitive Ca^{2+} channels, including pulse duration dependent termination of release (Fig. 3.5), Ca^{2+} dependent inactivation of $I_{Ca,L}$ (Figures 3.1, 3.3), as well as the wide variety of whole-cell voltage clamp protocols (Figures 3.11, 3.12, 3.13 and 3.14).

(c) Although our model provides secondary Ca^{2+} tail transients elicited by $I_{Ca,L}$ "tail currents" (Fig. 3.15), this aspect of the model has not been verified extensively due to paucity of measured VC data showing tail transients over the high voltage range ($40 \leq V \leq 60$) in rat ventricular myocytes. Our $I_{Ca,L}$ tail currents are in general agreement with model generated data at a clamp voltage of 50 mV reported by Greenstein et al. ([8]; Fig. 8). The restitution time for the RyR channel in rat ventricular myocytes is believed to be at least 25ms [191] and as fast as 150ms [192] indicating the wide range of values reported in the literature. We

demonstrate model-generated RyR refractoriness by changing the duration of the simulated VC pulse and obtain RyR recovery characteristics that are consistent with measured data for Ca^{2+} spark restitution in rat ventricular myocytes reported by Sobie et al. [180]. However, our results on this important phenomena, particularly the onset of tail transients with increasing inter-stimuli interval are preliminary and further modeling investigations would benefit considerably from the availability of additional measured data.

3.5 Conclusion

We have developed a mathematical model of Ca^{2+} dynamics under voltage clamp conditions in the rat ventricular myocyte, which is based solidly on experimental data and includes the most extensive description available of a novel feature, namely the luminal Ca^{2+} sensor in the junctional SR which models the protein-protein interaction between triadin/junctin, calsequestrin and the RyR channel. The luminal sensor imparts the much needed refractoriness to the Ry-sensitive Ca^{2+} release channel. This element is critical in providing realistic fits to cytosolic Ca^{2+} transients and an adequate refilling time for the SR Ca^{2+} stores. Our voltage-clamp simulations demonstrate graded Ca^{2+} transients with sufficient gain, as well as quantification of Ca^{2+} balances for all external and internal Ca^{2+} fluxes. Our model of the dyadic coupling unit (DCU) provides mechanistic explanations of the major input-output relationship for CICR (Fig. 3.10), as well as its modulation by trigger current (clamp voltage). The variety of experiments emulated in this study demonstrates that the model has long-term stability in regulating cytosolic Ca^{2+}, as shown in the 120-sec duration experiments of Negretti et al. (Fig. 3.14) at a pulse repetition rate of 0.33 Hz., and the faster (physiological) paced stimulation at 4Hz shown in Fig. 3.8A. It

also provides biophysically based insights into the molecular mechanisms underlying whole-cell responses to the wide variety of testing approaches used in voltage clamp studies of myocytes that have appeared in the literature over the past two decades (Figures 3.11, 3.12, 3.13 and 3.14). Thus, the model serves as a platform for the predictive modeling of VC investigations in a number of areas. These include new hypotheses with regards to the under-expression of triadin/junctin resulting in a malfunctioning luminal sensor, which could affect long-term calcium stability of the cell (Fig. 3.8B), and/or changes in the refractoriness of the RyR Ca^{2+} channel (Figures 3.7 and 3.15) affecting the integrity of CICR under a variety of conditions. These are fundamental issues that would benefit from a better mechanistic understanding of deranged calcium signalling in the rat ventricluar myocyte. This study is aimed at providing an initial step towards this goal.

Chapter 4

Myocyte Electromechanics

4.1 Background

Cardiac muscle contraction is a result of a transient increase in myoplasmic Ca^{2+} concentration $[Ca^{2+}]_{myo}$. Sarcolemmal membrane depolarization triggers Ca^{2+} influx via dihydropyridine (DHP)-sensitive L-type Ca^{2+} channels. Following diffusion across a small sub-membrane dyadic space, this influx activates ryanodine receptors (RyRs) controlling ryanodine-sensitive Ca^{2+} release channels in the junctional portion of the sarcoplasmic reticulum (jSR). Fabiato and Fabiato [8] named the process calcium-induced calcium release (CICR). Ca^{2+} subsequently diffuses from the dyadic space into the myoplasm. Ultimately, myoplasmic Ca^{2+} concentration $[Ca^{2+}]_{myo}$ is returned to resting levels by combination of: (a) Ca^{2+} buffering in the dyadic space and myoplasm; (b) sequestration of Ca^{2+} by sarcoplasmic/endoplasmic reticulum Ca^{2+}-ATPase (SERCA)-type calcium pumps lining the longitudinal portion of the sarcoplasmic reticulum (LSR); and (c) Ca^{2+} extrusion from the myoplasm by Na^{+}/Ca^{2+} exchangers and Ca^{2+}-ATPase pumps on the sarcolemmal membrane.

Ca^{2+} is an extremely important and highly versatile second messenger in cardiac cells, which plays a crucial role not only in excitation-contraction (E-C) coupling but also in excitation-transcription coupling [48]. Various inter-connected Ca^{2+} signalling pathways help preserve the integrity of the cellular Ca^{2+} system despite any

disturbances (e.g., changes in stimulation frequency or inotropic state). A key role for the dyadic Ca^{2+} release system is the formation of an adequate myoplasmic Ca^{2+} transient that can serve as an input driving signal for the intracellular contractile machinery (the myofilaments). The resultant contractile response is conditioned by a number of additional factors that include the mechanical load; sarcomere equilibrium length; myofilament Ca^{2+} sensitivity; and the temperature. Although it is well-known that the contractile response of a cell is a function of the stimulation frequency (its force-frequency response (FFR)), this study is limited to an investigation at 5 Hz (unless otherwise specified), a physiologically relevant heart rate for a rat ventricular myocyte.

4.2 Testing Protocol

We employ our coupled multiphysics model describing the electrochemical as well as the mechanical subsystems to study cellular contraction emphasizing the various modulatory influences that are at play. We begin with a detailed analysis of different types of twitch response to better understand the influence of various factors such as sarcomere length, peak $[Ca^{2+}]_{myo}$ and the stiffness of the contractile element in cell shortening, followed by a comparative study of these twitch responses. The negative feedback of cellular contraction on the myoplasmic Ca^{2+}-transient [193, 194] is also investigated. We then perform an idealized virtual experiment similar to that carried out in an experimental study [195] to uncover the regulation of cell contraction by Na^{+}/Ca^{2+} exchange, and in the process identifying the role of the SERCA pump in facilitating this effect. We then model the effects of temperature [196] on cardiac contractile response. This is followed by a study identifying the role of myofilament Ca^{2+} sensitivity as a key factor influencing the degree of cell shortening. In particular,

the effect of β-adrenergic agonist isoproterenol, which is known to cause a decrease in myofilament Ca^{2+} sensitivity [55], is investigated. Hence, we have developed an integrated multiphysics model of rat ventricular cell electromechanics and now seek to study its response to various tests prescribed by elements of the virtual protocol above. In doing so, we hope to identify and clarify the role played by key factors involved in modulation of the cell's contractile response.

4.3 Results

From our modeling standpoint, the dyadic coupling unit (DCU) as defined by Krishna et al. [66] is a fundamental element involved in the mechanism of CICR. This previous study described the control features of this unit, as well as its interaction with the SERCA pump and free sarcolemmal pumps and exchangers to achieve a homeostatic regulation of myoplasmic Ca^{2+} concentration. We now extend our voltage clamp studies to address the subject of force generation following CICR, starting with the classical twitch responses below.

4.3.1 Twitch Responses

A twitch response, which is a brief contractile response of a cardiac cell elicited by dynamically changing activator Ca^{2+}, is a commonly used experimental characterization. Following are the three types of recordings commonly used to quantify force generation in isolated cardiac cells: (1) isosarcometric contraction which is experimentally obtained by incorporating feedback sarcomere length (SL) control using laser diffraction techniques [197, 198, 199]; (2) unloaded contraction where the cell is allowed to contract freely; and (3) isometric contraction where overall muscle length is fixed, but sarcomere length is not controlled, allowing considerable internal short-

ening as a result of compliant end connections (series elastic element). All the twitch studies are carried out at 22.5°C [1] to be consistent with the data cited. Under all three loading conditions, the cell is subjected to conditioning train of steady state (100 cycles) voltage clamp pulses at 5 Hz followed by a 0.8 s rest interval (allowing decay to a zero force resting state) which is subsequently followed by a single test twitch for which a transient lasting 1 s is obtained. The voltage clamp protocol used is a 50 ms step pulse to 10 mv from a holding potential of -40 mv. In this study, we report a normalized force with a maximum value of 1 possible under optimal conditions such as high $[Ca^{2+}]_{myo}$, isosarcometric loading (SL = 2.3 μm) and low temperature allowing maximum overlap of thick and thin filaments.

Isosarcometric Contraction

As mentioned above, in isosarcometric contraction, SL is maintained constant via external feedback control. We simulate this type of contraction under two distinct conditions: modulation of developed force by fixed changes in (A) SL, and (B) myoplasmic Ca^{2+} concentration. In case 'A' while SL is fixed at different values, the input Ca^{2+}-transient is kept identical (elicited by the standard 50 ms voltage clamp pulse at 5 Hz). In case 'B' while the level of activator Ca^{2+} is modulated, SL is kept fixed at 2.3 μm.

(A) The steady state force-$[Ca^{2+}]$ (F-Ca) relationship shown in Fig. 4.1A-i exhibits a leftward shift and an increase in developed maximum plateau force as SL is clamped at increasing lengths. This leftward shift results from an increase in myofilament Ca^{2+} sensitivity as SL is increased. Figure 4.1A-ii shows the temporal course of normalized force as SL is changed in steps from 1.8 to 2.3 μm. The waveshape of standard Ca^{2+}-transient is overlaid in dotted lines in this figure. Although an increase

in SL (traces marked + to $*$) does not cause a large variation in the time to peak force (TTP), it does result in an increase in peak force magnitude and twitch duration as the result of an increase in myofilament Ca^{2+} sensitivity. These characteristics show a strong correspondence with measured data from rat ventricular myocytes tested at similar ($\sim$ 22.5 °C) temperatures [198, 167, 200]. The correlation coefficient of the speed of contraction and relaxation has been experimentally observed [201] to be very close (> 0.98). The inset in Fig. 4.1A-ii is a plot of the rate of relaxation (reciprocal of time taken for 50% sarcomere relaxation (RT_{50})) versus rate of contraction (reciprocal of time taken for peak sarcomere contraction (TTP)) for increasing SL. This linear relationship highlights contraction-relaxation coupling, and represents a key intrinsic property of the contractile myofilaments [201]. Figure 4.1A-iii shows the phase plots of normalized force versus the instantaneous Ca^{2+} concentration in the cytosol for increasing SL (traces marked + to $*$) overlayed with two steady state F-Ca relationships corresponding to SL = 1.8 μm (+) and SL = 2.3 μm ($*$). The assessment of dynamic and steady-state Ca^{2+} relationships allows better analysis of the phase-plane loops of force versus $[Ca^{2+}]$. The active twitch curve is related to the steady-state values to determine, at what isochrone the dynamic force-$[Ca^{2+}]$ value equals that obtained in the steady-state relationship. This point of intersection of the steady state F-Ca trace and the corresponding phase plot gives the contraction-relaxation coupling point (CRCP, marked as $\circ$) from initiation of stimulation [75]. Time is implicit on the phase trajectory and at time instants prior to reaching the critical coupling point for a particular trajectory, $[Ca^{2+}]_{myo}$ exceeds the value of Ca^{2+} predicted by the steady state F-Ca relationship. This excess favors continued sarcomere contraction. At later time points beyond the CRCP, the developed force is greater than that predicted by the steady state curve, which favors myofilament relaxation.

(B) Increasing background $[Ca^{2+}]_{myo}$ causes a leftward shift in steady state F-SL relationship as shown in Fig. 4.1B-i. The increase in maximal plateau force with increase in background $[Ca^{2+}]_{myo}$ is observed to be less prominent at higher levels of activator Ca^{2+} in the myoplasm. In Fig. 4.1B-ii the activator Ca^{2+} is varied by modulating the peak of the $[Ca^{2+}]_{myo}$ transient by adjusting the voltage clamp pulse duration (an increase in pulse duration from 5 ms to 50 ms increased peak $[Ca^{2+}]_{myo}$ from 0.5 to 1.1 μM respectively). This protocol allows for the peak of the transient to be changed without a significant change in the duration of the transient (Krishna et al. [66] ; Fig. 11). The traces correspond to increasing peak values from 0.5 ($\bullet$) to 1.1 ($*$) μM. Although similar to case with increasing SL, increasing activator Ca^{2+} results in a relatively non-linear increase in peak force generated. As shown in Fig. 4.1A-i, the steady state F-Ca relationship is characterized by a Hill function as experimentally observed [199]. The time-to-peak force (TTP) remains relatively unaffected by the amount of activator Ca^{2+} causing the twitch response. Inset in Fig. 4.1B-ii shows the dependence of TD_{50} (time taken from 50% activation to 50% relaxation) on peak $[Ca^{2+}]_{myo}$ indicating an increase in twitch duration with increasing levels of activator Ca^{2+}. Figure 4.1B-iii shows the phase plots of normalized force versus the instantaneous Ca^{2+} concentration in the myoplasm for increasing peak $[Ca^{2+}]_{myo}$ (traces marked $\bullet$ to $*$) overlayed with a steady state F-Ca relationships corresponding to SL = 2.3 μm ($*$). The contraction-relaxation coupling point ($\circ$) traverses along the F-Ca relationship to increasing values of $[Ca^{2+}]$ and force with increasing peak $[Ca^{2+}]_{myo}$.

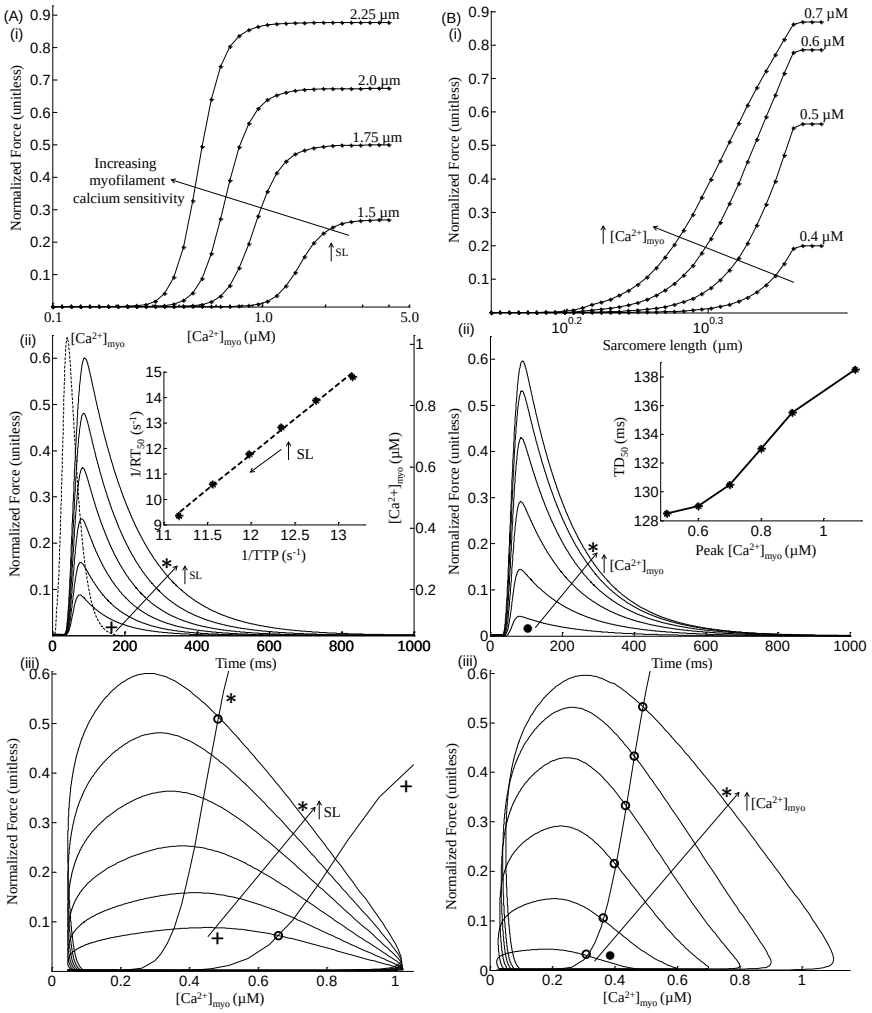

Figure 4.1 : Twitch response - Isosarcometric contraction (A) Modulation of sarcomere length - (i) Steady state F-Ca relationships for increasing SL. (ii) Traces for normalized force with SL varied from 1.8 (+) to 2.3 (∗) μm in increments of 0.1 μm. The Ca^{2+} transient responsible for each of the traces is shown in the overlay. The inset shows the rate of relaxation versus rate of contraction for increasing sarcomere length (reciprocal of RT_{50}, time taken for 50% sarcomere relaxation versus reciprocal of TTP, time taken for peak sarcomere contraction). (iii) Phase plots of normalized force versus instantaneous $[Ca^{2+}]_{myo}$ for increasing SL overlayed with two steady state F-Ca relationships corresponding to SL = 1.8 (+) and 2.3 μm (∗). (B) Modulation of Peak $[Ca^{2+}]_{myo}$ - (i) Steady state F-SL relationships for increasing background $[Ca^{2+}]_{myo}$. (ii) Sarcomere length is held constant at 2.3 μm while the peak $[Ca^{2+}]_{myo}$ transient is scaled down by decreasing the voltage clamp pulse duration. The traces show the contractile response corresponding to myoplasmic Ca^{2+} transients with peak values 1.1(∗), 0.9, 0.8, 0.7, 0.6, 0.5 (•) μM. The inset shows the relationship between TD_{50} (time taken from 50% activation to 50% relaxation) and activator Ca^{2+}. (iii) Phase plots of normalized force versus instantaneous $[Ca^{2+}]_{myo}$ for increasing peak $[Ca^{2+}]_{myo}$ overlayed with a steady state F-Ca relationships corresponding to SL = 2.3 μm (∗). Model generated data corresponds to an idealized rat ventricular myocyte at 22.5°C.

Unloaded Contraction

The protocol for the unloaded case is as follows. The cell is not stretched with preload so that the series elastic element is unattached and is therefore not in play. In the model of Rice et al. ([1]; Fig.1), the contractile element is shunted by elastic and viscous damping elements. In that figure, the nonlinear elastic element is characterized by a cubic force vs SL characteristic centered about an equilibrium point (SL_0=1.9 μm; F=0). In the unloaded case without stimulation, any stored energy in the system is dissipated and SL decays to the equilibrium point on the passive force vs SL characteristic. With electrical activation and subsequent Ca^{2+} release, active force is developed and SL shortening occurs against the aforementioned passive restoring forces. Providing the same sequence of voltage clamp pulses as in Fig. 4.1, an identical sequence of Ca^{2+}-transients is produced to drive the active contractile mechanism. Figure 4.2A is a plot of total developed force (active and passive) as a function of peak $[Ca^{2+}]_{myo}$. This net instantaneous force can become negative when the magnitude of the passive forces exceeds that of the active component (Fig. 4.2A). Thus, an increase in activator Ca^{2+} causes an increase in peak force generated, which translates into enhanced shortening. Corresponding changes in sarcomeric length as shown in Fig. 4.2B indicate that increasing levels of activator Ca^{2+} result in a decrease in time to peak contraction (TTP declined from 156.0 ms ($\bullet$) to 70.5 ms ($*$)) and an increase in the rate of relaxation (RT_{50} computed from time of peak decreased from 183.0 ms ($\bullet$) to 157.5 ms ($*$)).

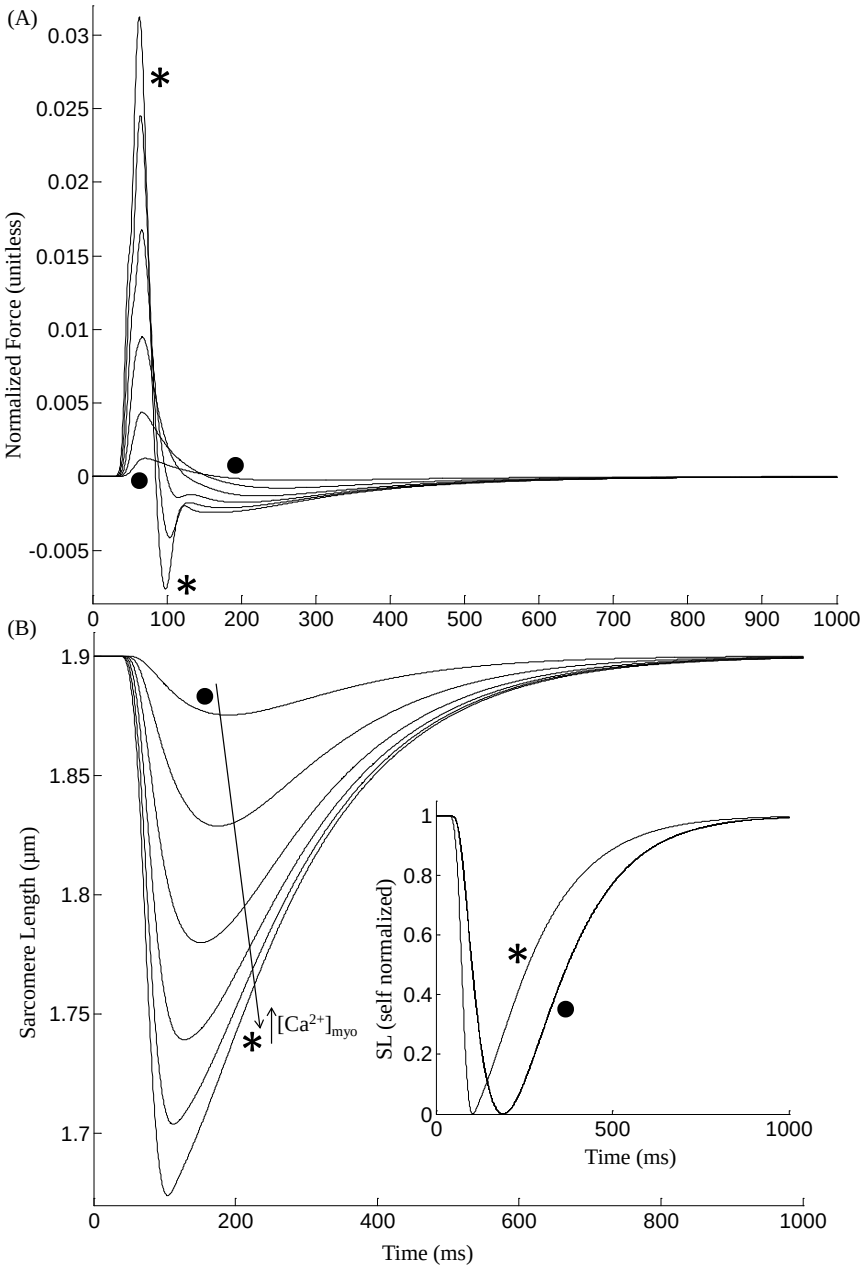

Figure 4.2 : Twitch response - Unloaded contraction. (A) The total muscle force is plotted corresponding to Ca^{2+} transients with peak values 1.1 ($*$), 0.9, 0.8, 0.7, 0.6, 0.5 ($\bullet$) μM as in Fig. 4.1B. (B) Cell shortening twitches as a function of Ca^{2+} activation. The cell is allowed to contract from its equilibrium length of 1.9 μm against the passive elastic and viscous restoring forces in the model of Rice et al. ([1]; Fig.1). Increasing peak translating into increased amount of activator Ca^{2+} causes a decrease in time to peak shortening. The inset shows self-normalized sarcomere length for peak values of 1.1 ($*$) and 0.5 ($\bullet$) μM. Model generated data corresponds to an idealized rat ventricular myocyte at 22.5°C.

Isometric Contraction

A third type of twitch can be simulated where the cell is kept at a fixed total length, allowing it to contract in response to Ca^{2+} release by internal shortening of the sarcomere made possible by a non-contractile series elastic element whose stiffness (KSE value) dictates the end compliance and hence the degree of internal shortening. Increasing KSE values causes an increase in maximal plateau force in steady state F-Ca relationship as shown in Fig. 4.3A. Figure 4.3B shows traces for total force (sum of both passive and active force) during an isometric twitch corresponding to KSE values increased from 1.0 to 50.0 normalized force-μm^{-1}. With an increase in end compliance (decrease in KSE), the degree of internal shortening increases and the total force measured at the cell end decreases, showing a delayed peak and an increase in rate of relaxation (Fig. 4.3B). The delayed peak occurs because the peak force is measured when the series elastic element is at its maximum length, which occurs with greater delay with increasing end compliance. Increasing end compliance decreases twitch duration (Fig. 4.3B) because, as observed experimentally [202] re-lengthening hastens relaxation as a result of an increase in mean distortion of the strongly bound crossbridge states (xXB_PreR, xXB_PostR in Fig. 2.9) which causes a decrease in the forward rotation rate of the crossbridges (Eqn. 22, Rice et al. [1]) and hence a faster force decline. Figure 4.3C shows the phase plots of normalized force versus the instantaneous Ca^{2+} concentration in the myoplasm for increasing KSE values (traces marked $\bullet$ to $*$) overlayed with two steady state F-Ca relationships corresponding to KSE = 1.0 ($\bullet$) and KSE = 50.0 ($*$). The contraction-relaxation coupling point ($\circ$) moves to increasing values of $[Ca^{2+}]$ and force with increasing KSE values with the relative change in $[Ca^{2+}]$ being smaller than force. Figure 4.3D shows the corresponding traces for sarcomere length during the isometric twitch. As

the KSE value is increased from 1 to 50 the decreasing compliance results in a decline in cell shortening accompanied by a decrease in time to peak shortening from 122 ms to 92 ms (Fig. 4.3D).

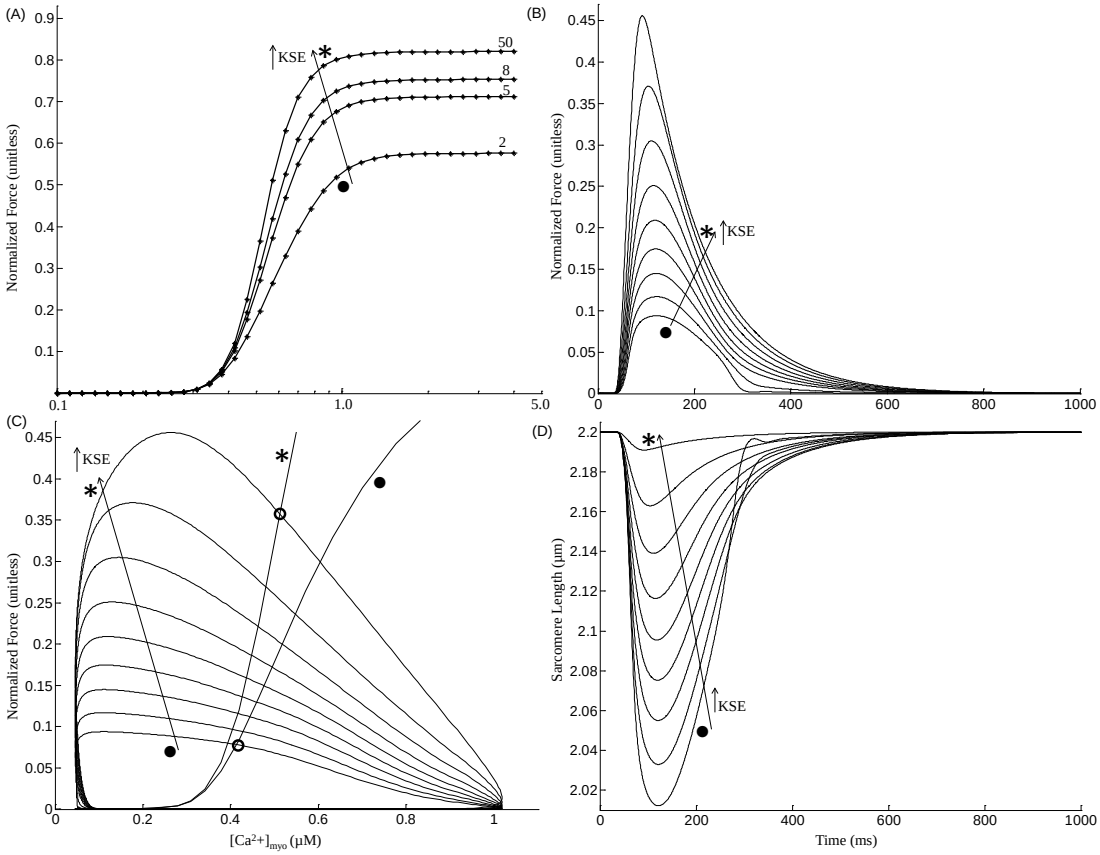

Figure 4.3 : Twitch response - Isometric contraction. The cell is held at a constant total length but the sarcomere is allowed to contract via a series elastic element. (A) Steady state F-Ca relationships for increasing KSE values. (B) Traces for total muscle force during an isometric twitch with KSE values of 1(•), 1.4, 2, 3, 4, 5, 7, 10 and 50 (∗) where units of KSE are normalized force-per-micrometer extension. (C) phase plots of normalized force versus $[Ca^{2+}]_{myo}$ for increasing KSE values (corresponding to panel B) overlayed with two steady state F-Ca relationships corresponding to KSE = 1.0 (•) and 50.0 (∗). (D) Sarcomere length traces showing internal shortening. Model generated data corresponds to an idealized rat ventricular myocyte at 22.5°C.

Figure 4.4 shows the three types of simulated twitch responses studied, compared in their force vs. time plots, as well as in their normalized force vs. $[Ca^{2+}]_{myo}$

phase diagrams. This plotting format aids in drawing a comparison that highlights the unique characteristics of each loading condition. The protocol used here is a steady state 5 Hz stimulation without a rest interval before the test twitch (unlike Figures 4.1, 4.2 and 4.3). Figure 4.4A shows that the isosarcometric case results in maximum force development, whereas the unloaded case records the minimum force for identical sarcomere length and initial conditions. Figure 4.4B shows the phase plots of normalized force versus the instantaneous Ca^{2+} concentration in the cytosol constructed from model-generated data captured at steady state (the last in a train of stimuli comprising 100 cycles at 5 Hz stimulation) from a twitch caused by a $[Ca^{2+}]_{myo}$ transient resulting from a voltage clamp pulse (amplitude -40 mv to 10 mv and a duration of 50 ms). The initial pre-contraction sarcomere length in the isometric case and the sarcomere length clamp in the isosarcometric case are both set to 2.2 μm whereas the equilibrium length in the unloaded case is chosen as 1.9 μm [1].

In the case of an isosarcometric contraction the net force comprises only the active component due to the tension generated by the sarcomere trying to contract. Phase 'a' in Fig. 4.4B-i is indicative of the delay in the contractile response when compared to the $[Ca^{2+}]_{myo}$ transient. However, soon after the $[Ca^{2+}]_{myo}$ reaches its peak (•), the sarcomere begins to contract, resulting in a gradual increase in force, achieving a maximum (■) as seen in phase 'b' of Fig. 4.4B-i. As active force increases, a decline in level of activator Ca^{2+} in the cytosol ultimately causes a recovery to the minimum contractile state (▶), as shown in phase 'c' of Fig. 4.4B-i.

Total force generated by an unloaded cell during contraction against its internal restoring force is a combination of the active component attributed to tension generating action of cycling crossbridges and the passive component attributed to titin

and other cytoskeletal elements. Passive force generated has a negative contribution to the net force for SL values lower than the equilibrium length. Hence, the competition between the active and passive components of force gives the trace in Fig. 4.4B-ii its characteristics. During phase 'a' in Fig. 4.4B-ii, as the Ca^{2+} level in the cytosol increases towards its peak value (•), the sarcomere attains maximum contraction velocity (▼), which is followed by a steep increase in net force as shown in phase 'b' of Fig. 4.4B-ii. However, decreasing sarcomere length increases the negative contribution from the passive component of force resulting in the first transient decline shown in phase 'c' of Fig. 4.4B-ii. The increased Ca^{2+} binding to troponin in response to the rise in activator Ca^{2+} in the cytosol enhances the active component of force, allowing the cell to reach peak net contractile force (■). The fast decline in sarcomere length which causes a rapid increase in the passive component of force results in the second transient decline as shown in phase 'd' of Fig. 4.4B-ii. However, a subsequent decrease in cell shortening soon allows an increase in net force lasting for a short duration (while the SL reaches its minimum (⧫)). The declining Ca^{2+} level in the cytosol, an outcome of SR uptake, then causes a gradual recovery to the resting state (►).

As shown in Fig. 4.4A, for the same activator Ca^{2+}, although the total muscle force generated during isometric contraction exhibits a triphasic response similar to an isosarcometric contraction, its own unique characteristics are a delayed time to peak (an increase from 84.5 ms to 119 ms) and relatively smaller magnitude. As shown in phase 'a' of Fig. 4.4B-iii, the increase in Ca^{2+} concentration is not reflected in a fast mechanical response. After $[Ca^{2+}]_{myo}$ reaches its peak (•), the tension in the sarcomere begins to build up (phase 'b' of Fig. 4.4B-iii) although at a slower rate (compare isometric and isosarcometric traces in Fig. 4.4A), causing a delayed time

to peak (84 ms and 120 ms in isosarcometric and isometric cases, respectively) due to the presence of the series elastic element which facilitates slow internal shortening. The sarcomere achieves peak contraction (⧫) when the total muscle force reaches its maximum (■), following which the cell recovers back to the minimum contractile state (►) as shown in phase 'c', Fig. 4.4B-iii. During isometric contraction (KSE = 2) the afterload (due to the series elastic element) tracks the active component of force generated due to the tension developed in the sarcomere while the passive component of force (attributed to titin and other cytoskeletal elements) is small in magnitude owing to a much smaller degree of sarcomere contraction achieved when compared to the unloaded case (compare trace marked $*$ in Fig. 4.2B and the trace for KSE=2 in Fig. 4.3D).

4.3.2 Effect of Contraction on the $[Ca^{2+}]_{myo}$ Transient

The myoplasmic $[Ca^{2+}]_{myo}$ transient which follows SR release acts as the trigger for myofilament contraction. However, the contracting myofilament also has a feedback effect on the shape of the $[Ca^{2+}]_{myo}$ transient as a result of Ca^{2+} binding to the low affinity regulatory sites on troponin in the myofilament. The Ca^{2+} affinity of this site depends on both the sarcomere length as well as the fraction of strongly-bound crossbridges (Eq. 37, Rice et al. [1]). The protocol used to test these effects is similar to that employed by Janssen and de Tombe [203], wherein the cell is stimulated at 5 Hz for 9 beats under conditions of isometric contraction (KSE=2) followed by a 0.8 s rest interval allowing decay to a zero force resting state. This is followed by the 10th beat for which a transient lasting 1 s is obtained. On the 10th beat, the cell is allowed to sarcometrically shorten as usual (•) or a sarcometric length clamp is imposed at a fixed sarcomere length of 2.2 μm ($*$). At the onset of Ca^{2+}-activation of troponin

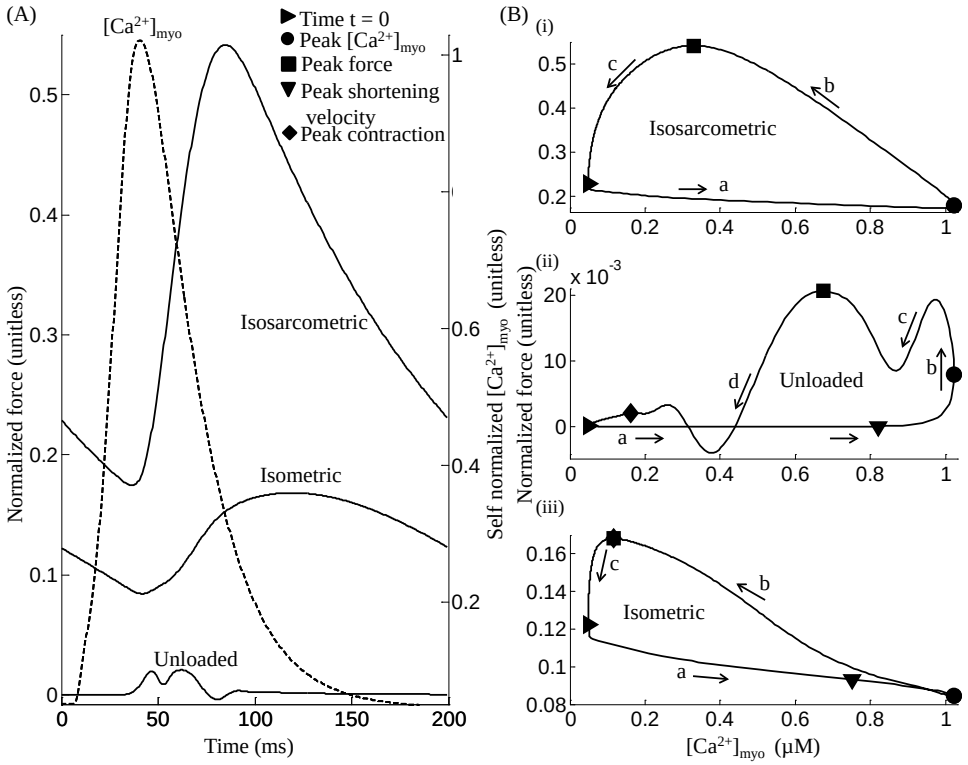

Figure 4.4 : Twitch responses - A comparison between three types of steady state twitch responses from an isolated rat ventricular myocyte viz. isosarcometric, unloaded and isometric (KSE = 2). Fixed SL in the isosarcometric case and the initial pre-contraction SL in the isometric case are chosen as 2.2 μm. Equilibrium SL in the unloaded case is 1.9 μm. (A) Traces for normalized force in each of the three cases with an overlay of normalized $[Ca^{2+}]_{myo}$ transient responsible for the twitch and (B) Phase plots of normalized force versus the instantaneous Ca^{2+} concentration in the cytosol in each of the three cases. Note the overlap of ♦ and ■ in panel iii. Model generated data corresponds to an idealized rat ventricular myocyte at 22.5°C.

on the 10th beat, initial conditions for the two different loading tests (isometric and isosarcometric) are identical. Sarcomere length changes under both loading conditions are shown in Fig. 4.5A. As observed earlier in Figs. 4.4B(i) and (iii) as well as in Fig. 4.5B, isosarcometric conditions generate a larger force than isometric, due to enhanced myofilament Ca^{2+} sensitivity reflected by a decrease in EC_{50} from 0.59 μM (•) to 0.5 μM (∗) (steady state F-Ca relationships shown in the inset in Fig. 4.5B)

and increased Ca^{2+}-binding to troponin. This binding causes a small (<1%) decline in the magnitude of the $[Ca^{2+}]_{myo}$ transient (Fig. 4.5C). Subsequently, as the Ca^{2+}-transient starts to decay, Ca^{2+} dissociates from troponin, slightly decreasing the rate of decline of the Ca^{2+}-transient. When the falling phases of the Ca^{2+}-transients for the two loading conditions are compared, the isosarcometric Ca^{2+}-transient decays more slowly and its curve crosses over the isometric Ca^{2+}-transient. Although Janssen et al. [203] reported an increase in Ca^{2+} transient due to uncontrolled shortening, the crossover was not observed as the noise level was too large. However, the crossover effect has been reported in other studies on rat ventricular trabeculae [193, 194] using long and short sarcomere length twitches producing larger changes in developed force and hence the shape of the $[Ca^{2+}]_{myo}$ transient (>5% change in peak value).

4.3.3 Regulation of Isometric Cell Shortening by Na^+/Ca^{2+} Exchange

During stable, steady-state operation, Ca^{2+} entry into the cytosol via $I_{Ca,L}$ and SR release must exactly balance Ca^{2+} efflux via the sarcolemmal Na^+/Ca^{2+} exchanger (NCX), plasma membrane Ca^{2+}-ATPase pump, and Ca^{2+}-uptake to the SR by the SERCA pump. To study the role of the NCX in isometric SL shortening we develop a virtual experimental protocol loosely patterned after a study on rat ventricular myocytes [195]. In our experiment, isometric contraction is stimulated by voltage clamp pulses at 5 Hz.

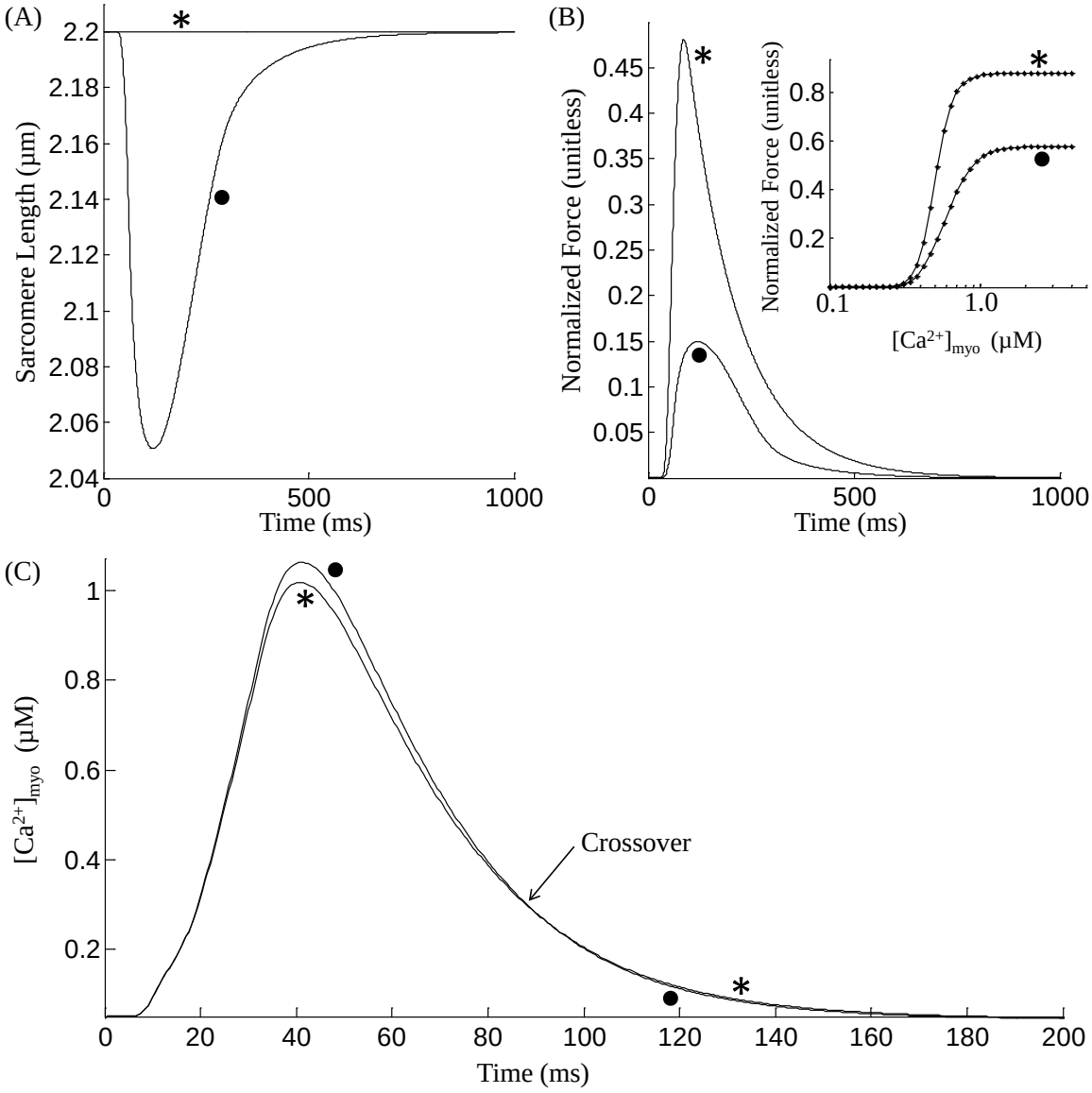

Figure 4.5 : Feedback of internal shortening on myoplasmic $[Ca^{2+}]_{myo}$ transient. The protocol used comprises of 9 beats of isometric contraction followed by a 0.8 s rest interval and beat 10 (shown above) when the cell is allowed to internally shorten (•) or held at a fixed sarcomere length of 2.2 μm ($*$). (A) The sarcomere length in both the cases shows the degree of contraction when the cell is allowed to internally shorten via a series elastic element (KSE = 2). (B) Isosarcometric case shows enhanced force when compared to the isometric case. The inset shows corresponding steady state F-Ca relationships (C) As seen in experimental studies, the isosarcometric case shows a modest decrease in $[Ca^{2+}]_{myo}$ transient. Model generated data corresponds to an idealized rat ventricular myocyte at 22.5°C.

In phase A of the experiment, 30 clamp pulses are applied resulting in regular isometric contractions. This is immediately followed by phase B where the NCX is assumed partially inhibited (achieved in the model by a 25% decrease in maximum Na^+/Ca^{2+} exchange current) by rapid superfusion of a bathing solution containing a NCX inhibitor (e.g. Phe-Arg-Cys-Arg-Ser-Phe-CONH2 (FRCRSFa) or exchanger inhibitory peptide (XIP) which are known [204] to cause selective NCX inhibition). This is followed by phase C where rapid superfusion with normal bathing solution completely removes the inhibitor, thus restoring exchanger activity to initial levels. It is well known that a decrease in NCX activity (Phase B, Fig. 4.6A) results in an increase in SR Ca^{2+} content as a result of the excess Ca^{2+} in the cytosol being resequestered into the SR via the SERCA pump. Figure 4.6B elucidates the relative contribution of the Na^+/Ca^{2+} exchanger and the SERCA pump in Ca^{2+} extrusion from the cytosol, showing an increase in the relative role of SERCA pump as a result of inhibition in NCX activity. As observed experimentally [195] this enhancement in SR Ca^{2+} content results in an increased availability of activator Ca^{2+} following release (Fig. 4.6C) which in turn enables improved cell shortening as seen by an enhancement in peak to peak amplitude of contraction in Fig. 4.6D (Δ increases from 0.0848 μm to 0.0977 μm) and is accompanied by a decrease in mean sarcomere length (Δ_m = 0.0217 μm). A similar study (not shown here) involving a sudden increase in NCX activity instead of a decrease resulted in an opposite (a decrease in SR Ca^{2+} content causing diminished release and hence a decrease in degree of contraction) symmetric response of similar magnitude indicating strong homeostatic control. Myoplasmic Na^+ concentration (17 mM) remains relatively constant throughout and hence is not involved in this indirect control of myofilament contractility. Our virtual experiment only approximates the actual experiment in that we assume the ability to make very

rapid changes in the composition of the bathing medium relative to the time constants involved in the response. However, the model generated responses in steady state can be compared with measured steady state response in the presence/absence of NCX inhibition using selective blocking agents that allow complete post-washout recovery [204].

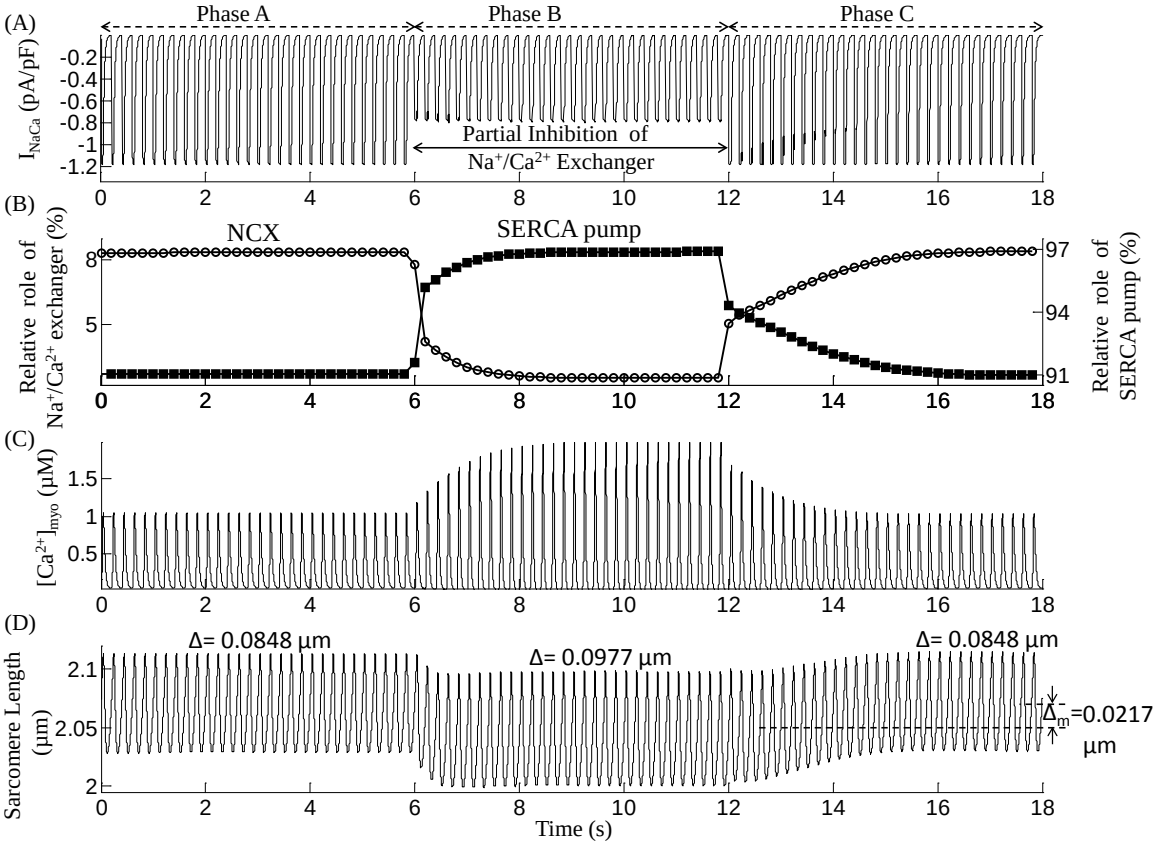

Figure 4.6 : Regulation of isometric cell contraction by Na^+/Ca^{2+} exchange. The protocol used for the isometric contraction is stimulation at 5 Hz comprising of 30 beats when the cell undergoes unperturbed contraction (phase A) followed by 30 beats (phase B) when the Na^+/Ca^{2+} exchanger function is partially inhibited after which the inhibition is relieved allowing the cell to recover to a steady state control during the following 30 beats (phase C). (A) The Na^+/Ca^{2+} exchanger current (I_{NaCa}) showed a rapid transition between the control and inhibited phase and vice versa. (B) Relative role of the Na^+/Ca^{2+} exchanger and the SERCA pump. (C) Myoplasmic Ca^{2+} concentration. (D) Sarcomere length in response to I_{NaCa} inhibition. Model generated data corresponds to an idealized rat ventricular myocyte at 22.5°C.

4.3.4 Effect of Temperature on Contractile Performance

Temperature is known to have a strong effect on the L-type Ca^{2+} current ($I_{Ca,L}$), the Ca^{2+}-transient and the contractile mechanics. One very significant effect of temperature on whole-cell $I_{Ca,L}$ is the pronounced increase in its rate of decline with an increase in temperature [205, 206]. Thus, with an increase from room to body temperature, peak inward trigger current increases but the waveform becomes much narrower. Figure 4.7A shows model-generated $I_{Ca,L}$ waveforms at temperatures between 22°C (+) and 38°C (∗) in steps of 4°C, where one can observe the increase in peak current but also the increased rate of decline in the trigger current waveform with an increase in temperature. Specifically, peak $I_{Ca,L}$ at 22°C was 8.31 pA/pF compared with 15.05 pA/pF at 38°C, whereas time taken for 50% $I_{Ca,L}$ inactivation ($RT_{50,I}$) decreased from 10.75 ms at 22°C to 2.95 ms at 38°C (inset in Fig. 4.7A). These indices are in general agreement with measured voltage clamp data [206, 207] obtained from rat ventricular trabeculae. Although skinned rat ventricular preparations have been used extensively in studies of the cardiac contractile process, data from such preparations violates the assumptions of our whole cell electromechanical model. The integrity of the plasma membrane components and intricate Ca^{2+}-regulatory system are compromised to some degree, regardless of the skinning technique used. Therefore, we have chosen to consider only data from rat ventricular myocytes or ultra-thin rat ventricular trabeculae to help validate the model. The decrease in integrated $I_{Ca,L}$ and faster SR uptake with increasing temperature together cause a decline in peak and duration of the Ca^{2+}-transient as shown in Fig. 4.7B. This agrees with the experimental findings by Janssen et al. ([167]; Fig. 1) on thin rat ventricular trabeculae. $RT_{50,C}$ corresponding to the Ca^{2+}-transient (time taken for 50% decline in $[Ca^{2+}]_{myo}$) decreased from 22.8 ms at 22°C to 18.5 ms at

38°C (inset in Fig. 4.7B). Myofilament Ca^{2+} sensitivity increases with an increase in temperature as a result of a temperature dependent enhancement in crossbridge cycling rate [208, 209, 210]. Traces for the steady state F-Ca relationship in Fig. 4.7C show a temperature dependent increase in myofilament Ca^{2+} sensitivity with no significant change in maximum plateau force. An increase in temperature from 22°C (+) to 38°C (∗) results in a decrease in EC_{50} from 0.55 μM to 0.44 μM (inset in Fig. 4.7C).

As experimentally observed [167], a decrease in peak and duration of the $[Ca^{2+}]_{myo}$-transient with increasing temperature results in a corresponding overall decrease in peak developed contractile force and twitch duration. Our simulations show changes in $I_{Ca,L}$ and $[Ca^{2+}]_{myo}$ in Figs. 4.7A and B, and corresponding changes in developed force in Fig. 4.7D with increasing temperature. As the temperature is increased from 22°C to 30°C, traces for normalized force in Fig. 4.7D show a small increase in peak amplitude despite a decline in the amount of activator Ca^{2+} responsible for contraction due to a temperature dependent increase in myofilament Ca^{2+} sensitivity (Fig. 4.7C). This increase in peak developed force at low, non-physiological temperatures is confirmed by Janssen et al. ([167]; Fig. 1). However, as the temperature is increased further from 30°C to 38°C, further decreases in peak $[Ca^{2+}]_{myo}$ cause strong decreases in peak developed force. Figure 4.7D shows that an increase in temperature was accompanied by a decrease in both time to peak (TTP) as well as $RT_{50,F}$ (time taken for 50% decline in force). The inset in Fig. 4.7D shows the linear relationship [201, 211] between rate of relaxation versus rate of contraction for increasing temperature (reciprocal of $RT_{50,F}$ versus reciprocal of TTP).

Figure 4.7E shows phase plots of normalized force versus instantaneous Ca^{2+} concentration in the myoplasm for increasing temperatures (22°C (+) to 38°C (∗) in

steps of 4°C) overlayed with two steady state F-Ca relationships corresponding to 22°C (+) and 38°C (∗). The contraction-relaxation coupling point (∘) moves to decreasing values of $[Ca^{2+}]$ and force with increasing temperature. Phase-plane analysis of normalized force versus instantaneous Ca^{2+} concentration in the myoplasm reveals that, as the temperature is increased from 22°C to 38°C, the relaxation phase moves to the right towards the corresponding steady-state F-Ca relationship. This suggests that, with increase in temperature there is a departure from cross-bridge kinetics being the rate-limiting factor in cardiac relaxation to a more Ca^{2+}-driven mechanism. As evident from Fig. 4.7D, the inset in Fig. 4.7E shows the temperature dependence of peak force developed indicating a moderate increase at low (< 30°C) temperatures with a strong decline at temperatures above 30°C. Traces for SL shortening in Fig. 4.7F corresponding to $[Ca^{2+}]_{myo}$ transients in panel B, indicate an overall decrease in sarcomere shortening with increasing temperature which agrees with the trend in developed force in panel D. Comparison of insets in Fig. 4.7E and F shows the correlation between peak force developed and the corresponding delta change in SL. The effect of change in temperature on myofilament contractility is a two-stage response with feedback. Firstly, the $[Ca^{2+}]_{myo}$ transient is temperature sensitive owing largely to the temperature dependence of the trigger current $I_{Ca,L}$. Secondly, the cellular contractile machinery is highly temperature sensitive due the strong temperature dependence of rate kinetics involved in the formation of crossbridges. In addition, the process of crossbridge formation is known to have a small feedback effect on the $[Ca^{2+}]_{myo}$ transient as seen in Fig. 4.5. As the temperature is increased from 22°C to 30°C, the temperature sensitivity of crossbridge kinetics predominates the temperature dependence of $[Ca^{2+}]_{myo}$ transient in determining the contractile response. However, for temperatures from 30°C to 38°C the opposite holds true.

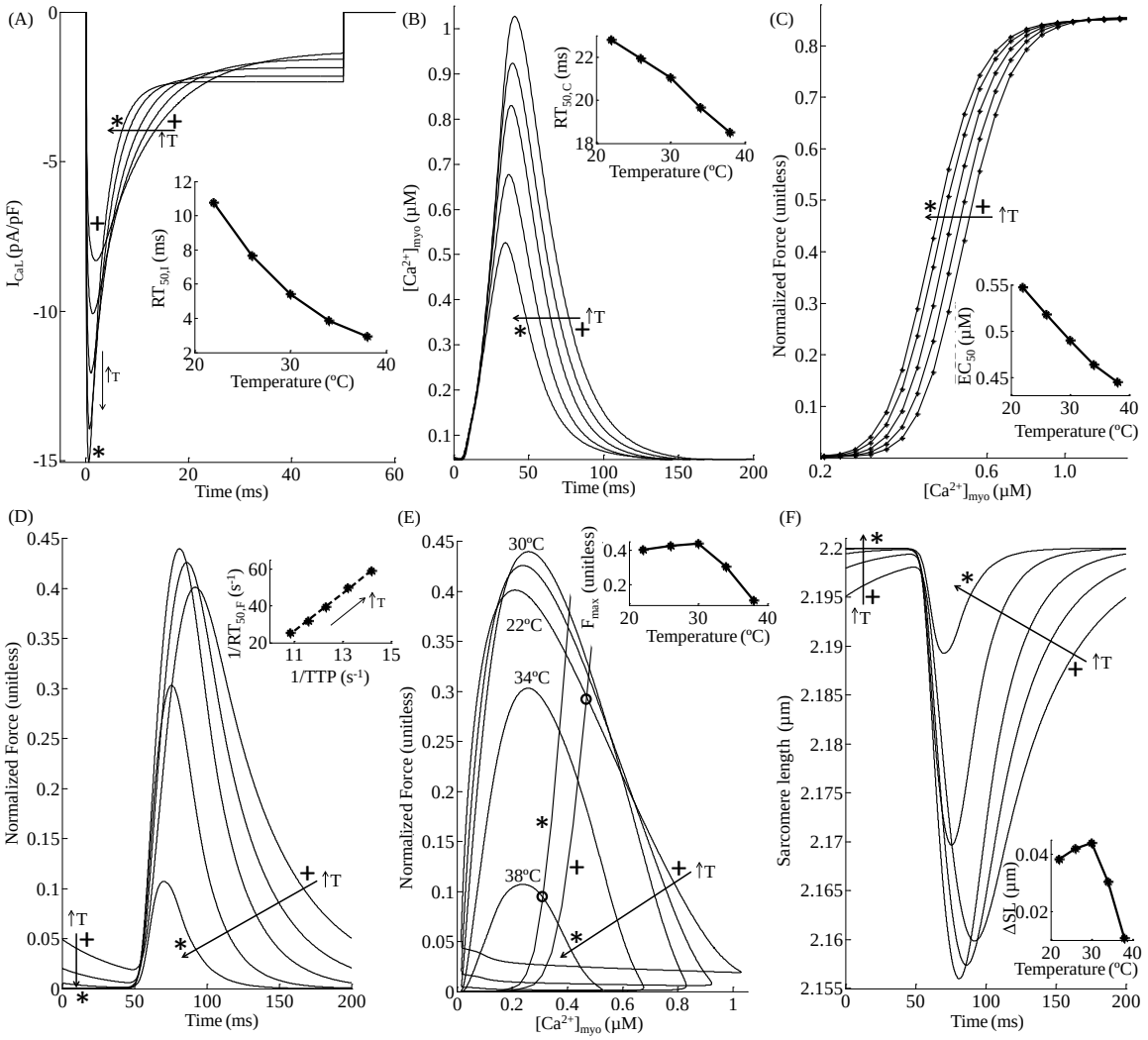

Figure 4.7 : Isometric twitch response (KSE = 10.0) for temperatures ranging from 22°C to 38°C at 5 Hz stimulation. (A) Traces for L-type Ca^{2+} current ($I_{Ca,L}$) showing increasing peak and rate of decline with increase in temperature. The inset shows the temperature dependence of $\mathrm{RT}_{50,I}$, time required for 50% $I_{Ca,L}$ inactivation. (B) Traces for $[Ca^{2+}]_{myo}$ transient for increasing temperatures show a decline in peak. The inset shows the temperature dependence of $\mathrm{RT}_{50,C}$, time required for 50% decline in $[Ca^{2+}]_{myo}$ from its peak value. (C) Steady state F-Ca relationships for increasing temperature. The inset shows the temperature dependence of half maximal effective concentration (EC_{50}). (D) Traces showing temperature dependence of normalized isometric force developed. The inset shows the relationship between rate of relaxation and rate of contraction. (E) Phase plots of normalized force versus instantaneous $[Ca^{2+}]_{myo}$ for increasing temperature overlayed with two steady state F-Ca relationships corresponding to 22°C (+) and 38°C (∗). The inset shows temperature dependence of peak force developed. (F) Sarcomere length corresponding to traces for force developed in panel D.

4.3.5 Role of Myofilament Ca^{2+} Sensitivity

Among various factors influencing the degree of cell shortening achieved in response to myoplasmic $[Ca^{2+}]_{myo}$ transient, the Ca^{2+} affinity of troponin C regulatory site is known to be particularly important. Here, we studied the dependence of isometric force response on myofilament Ca^{2+} sensitivity (MCS). An increase in Ca^{2+} affinity is modeled by a 30% increase in k_{onT} (traces marked ▲ in Fig. 4.8), the rate constant for Ca^{2+}-binding to troponin regulatory site. Similarly, a decrease in MCS is modeled by a corresponding decrease in k_{onT} (traces marked ▼ in Fig. 4.8). The steady state F-Ca relationships in Fig. 4.8A show the gradual rightward shift in response to decreasing MCS as seen experimentally in right ventricular trabeculae from rat in the presence of bupivacaine [212]. A positive/negative change in MCS results in the average $[Ca^{2+}]_{myo}$ required for half-maximal activation to decrease/increase from 0.61 μM in the control case to 0.47 μM and 0.89 μM respectively. However, the Hill coefficient was constant (4.0) showing no change in response to modulation in MCS.

Figure 4.8B shows traces of normalized force captured at steady state in response to a $[Ca^{2+}]_{myo}$ transient (overlaid) in the control case as well as with modified myofilament Ca^{2+} sensitivity. A 30% decrease (from control value) in MCS causes a much larger change in peak isometric force generated than a 30% increase, highlighting the nonlinear response. Figure 4.8B shows that an increase in MCS causes a faster onset of the upstroke in force response and a delay in the start of recovery as a result of enhancement in Ca^{2+} binding to troponin. This delay in recovery manifests in an increase in time to peak from 119.5 ms (•) in the control case to 124 ms (▲). Similarly, a decrease in MCS produces an opposite effect resulting in a decrease in time to peak (112 ms (▼)). The two distinct slopes during the upstroke in force response in Fig. 4.8B are a result of an initial contribution of the strongly bound pre-rotated

state (XB_PreR in Fig. 2.9) followed by the effect of increase in strongly bound post-rotated state (XB_PostR in Fig. 2.9). As shown in the inset in Fig. 4.8B, an increase in MCS causes an increase in TD_{50} (time taken from 50% activation to 50% relaxation).

Phase plots of normalized force versus the instantaneous Ca^{2+} concentration in the cytosol are shown in Fig. 4.8C. As observed experimentally [213], a decrease in myofilament Ca^{2+} sensitivity causes the gradient (units of normalized force/μM) of the trajectory during the relaxation phase of the twitch contraction (marked by thick arrows in Fig. 4.8C) to decrease from 12.4 in the control case to 7.0. A similar but opposite effect was observed in the rate of relaxation with a corresponding increase in MCS. A delayed onset of the upstroke in force response as a result of a decrease in MCS (Fig. 4.8B) causes a distinct loop at high Ca^{2+} concentrations (trace marked ▼ in Fig. 4.8C). The traces for sarcomere length in Fig. 4.8D reflect the changes in force developed, showing an increased degree of shortening with an enhancement in MCS. Peak shortening velocity also increases with an increase in myofilament Ca^{2+} sensitivity as shown in Fig. 4.8E.

Effect of Isoproterenol: The β-adrenergic agonist isoproterenol (ISO) is known to cause a decrease in myofilament Ca^{2+} sensitivity as a result of PKA-mediated phosphorylation of troponin I at Ser23/Ser24 [55, 166]. However, the increase in amplitude of myoplasmic Ca^{2+} transient more than compensates for the decrease in Ca^{2+} sensitivity in order to facilitate the inotropic effect of β-adrenergic stimulation.

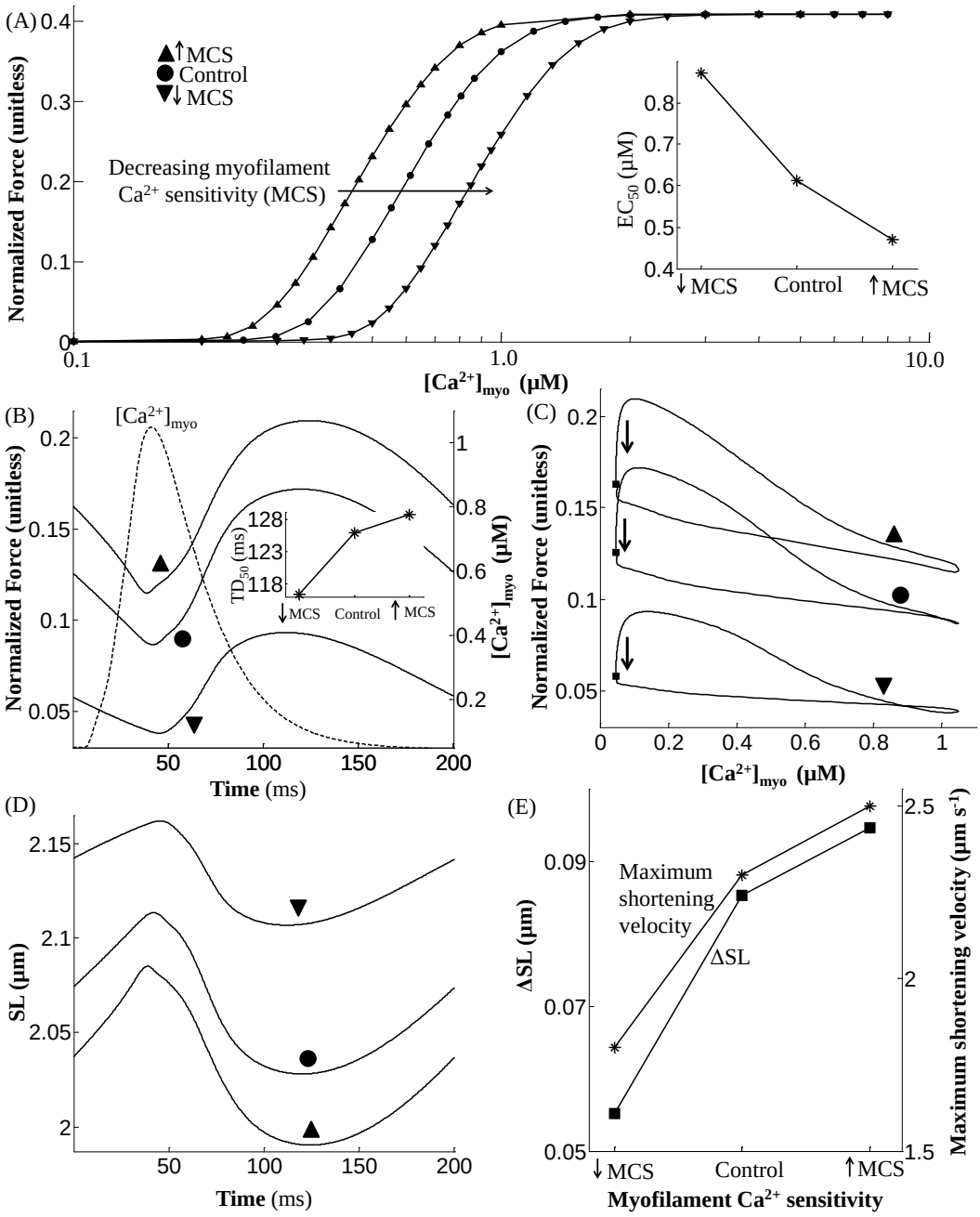

Figure 4.8 : Dependence of isometric contraction on myofilament Ca^{2+} sensitivity (MCS). (A) The steady state normalized force versus $[Ca^{2+}]_{myo}$ relationship shows a rightward shift with decreasing myofilament Ca^{2+} sensitivity. (B) Traces for normalized force recorded at steady state with an overlay of the $[Ca^{2+}]_{myo}$ transient. The inset shows MCS dependent changes in TD_{50} (time taken from 50% activation to 50% relaxation). (C) Phase plots of normalized force versus the instantaneous Ca^{2+} concentration in the cytosol. (D) Traces for sarcomere length indicating increased shortening with temperature. (E) Degree of sarcomere shortening and peak shortening velocity as a function of MCS. Model generated data corresponds to an idealized rat ventricular myocyte at 22.5°C driven by standard 50 ms voltage pulses at a repetition frequency of 5 Hz.

Here, we adopt a 1 Hz stimulation protocol used by Roof et al. ([214]; Fig. 1) to study the effect of 1 μM isoproterenol on isometric contraction and compare it with the effect of increasing extracellular Ca^{2+} concentration ($[Ca^{2+}]_o$) from 1 mM (control) to 3 mM. As shown in Fig. 4.9A, administration of 1 μM isoproterenol or an increase in $[Ca^{2+}]_o$ to 3 mM causes a substantial (3-fold) enhancement in peak myoplasmic $[Ca^{2+}]_{myo}$ as observed experimentally ([214]; Fig. 1). The isoproterenol-dependent effect is a result of PKA mediated dose-dependent increase (23%) in peak $I_{Ca,L}$ current together with an increase (17%) in the maximal uptake rate of the SERCA pump when compared to the control case (Appendix C.1, Eqs. C.1,C.2 & C.64-C.66). In the presence of isoproterenol, the significant increase in peak $[Ca^{2+}]_{myo}$ causes an increase in the strength of isometric tension developed (Fig. 4.9B) despite a decrease in myofilament Ca^{2+} sensitivity. Increase in $[Ca^{2+}]_o$ to 3 mM causes a similar effect of increasing isometric tension due to an increase in activator Ca^{2+} in the cytosol. The increase in peak $[Ca^{2+}]_{myo}$ is a result of an increase in SR Ca^{2+} content due to enhanced Ca^{2+} entry via $I_{Ca,L}$ assisted by impaired Na^+/Ca^{2+} exchange due to elevated $[Ca^{2+}]_o$. However, compared to β-adrenergic stimulation, the lack of a decrease in MCS results in a moderately larger developed force. Figure 4.9C shows the phase plots of normalized force versus the instantaneous Ca^{2+} concentration in the cytosol. As expected, either the presence of isoproterenol or an increase in $[Ca^{2+}]_o$ causes rightward extension (due to increase in peak $[Ca^{2+}]_{myo}$) of the phase plot and increases the area enclosed by it due to elevated myoplasmic Ca^{2+} level combined with an increase in tension developed. In the presence of isoproterenol, the increase in isometric tension developed occurs despite a decrease in myofilament Ca^{2+} sensitivity (Fig. 4.9C) which manifests as an increase (0.65 μM to 0.85 μM) in EC_{50}, the average $[Ca^{2+}]_{myo}$ at 50% of maximal developed force.

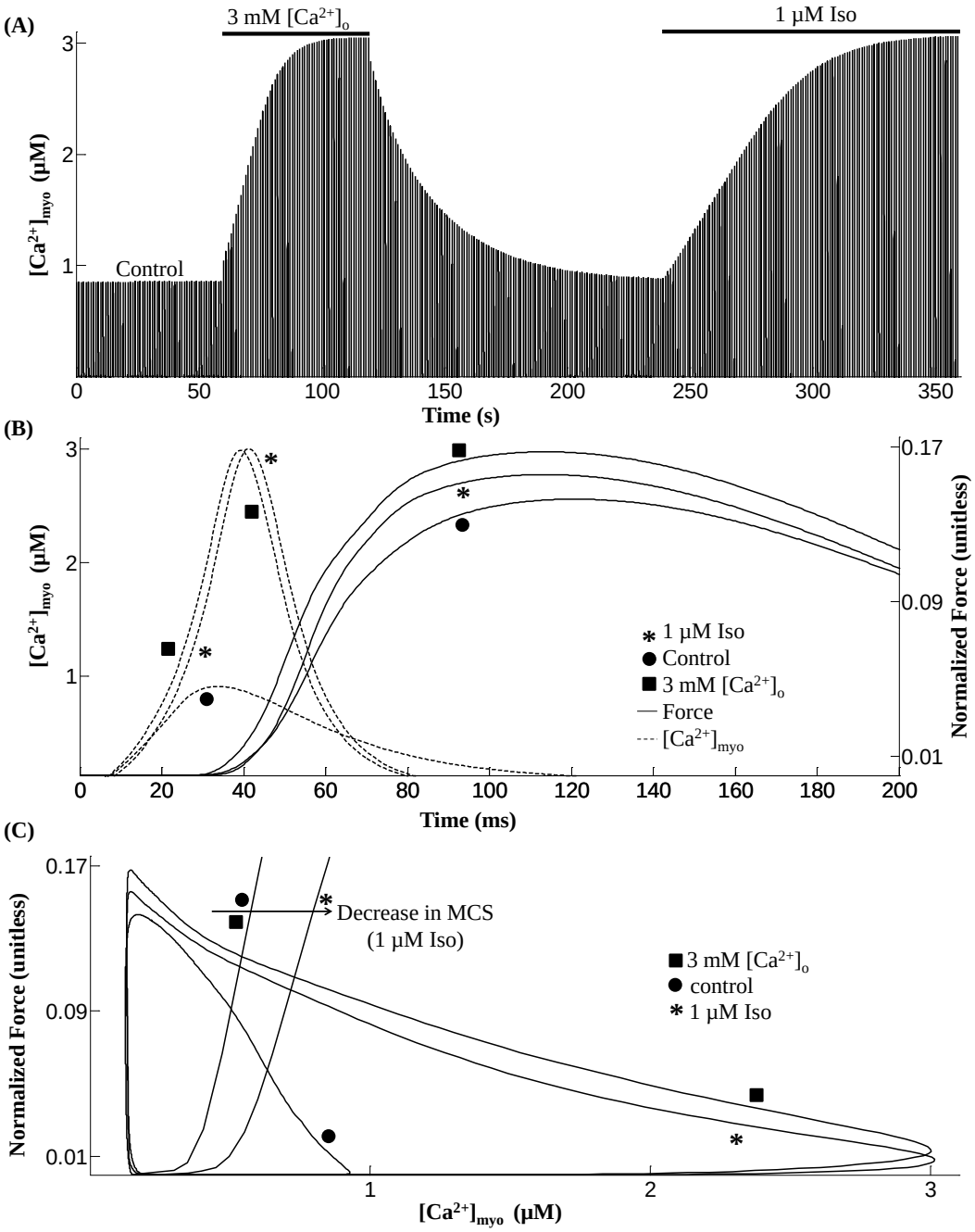

Figure 4.9 : Role of isoproterenol and $[Ca^{2+}]_o$. (A) Time record of $[Ca^{2+}]_{myo}$ transient in the control case as well as with 3 mM $[Ca^{2+}]_o$ and 1 μM ISO. (B) Traces for normalized force recorded at steady state with an overlay of $[Ca^{2+}]_{myo}$ transient. (C) Phase plots of normalized force versus the instantaneous Ca^{2+} concentration in the cytosol with an overlay of traces showing normalized steady state force versus $[Ca^{2+}]_{myo}$ relationship. Model generated data corresponds to an idealized rat ventricular myocyte at 22.5°C.

4.4 Discussion

Myofilament dynamics have been captured by various representations ranging from the highly simplified models to complex empirical [50, 51] and biophysical models [1]. While simplified models tend to use an explicit parabolic tension profile [52], the empirical models use predefined expressions to specify the average force developed by the cross bridges, based on experimental observations of isolated muscle contraction under different loading conditions. On the contrary, biophysical models of cardiac myofilament dynamics include descriptions of cross-bridge cycling and their elastic properties. An extensive review of various myofilament models in the literature is given by Trayanova and Rice [53]. We have developed a composite multiphysics model of excitation-contraction coupling in the rat ventricular myocyte based on a mechanistic electrochemical model of calcium-induced calcium-release (CICR) [66] and a detailed mechanochemical model of cooperative activation and crossbridge cycling [1]. After integrating these component models, the resultant multiphysics model of cardiac electromechanics is used to examine the mechanisms regulating myofilament contractility in an isolated rat ventricular myocyte under a voltage clamp protocol.

In particular, we have studied the role of different modulatory factors in influencing the various types of twitch response (isosarcometric, unloaded and isometric) elicited by an isolated rat ventricular myocyte. The dependence of isosarcometric contraction on the amount of activator Ca^{2+} available in the myoplasm to trigger contraction and the sarcomere length which modulates myofilament Ca^{2+} sensitivity is demonstrated (Fig. 4.1). Unloaded cell contraction is investigated to understand the influence of $[Ca^{2+}]_{myo}$ transient on the degree of sarcomere contraction achieved by an unrestrained cell highlighting the enhanced shortening velocity and rate of recovery with increasing peak $[Ca^{2+}]_{myo}$ (shorter time to peak and faster rate of re-

laxation in the inset in Fig. 4.2B). In agreement with Rice et al. [1] we demonstrate that in isometric contraction (Fig. 4.3), there can be significant internal shortening of the sarcomere as the result of compliant end connections (low KSE values).

Ca^{2+} released as a result of CICR is known to act as an actuator, triggering myofilament contraction by binding to the low affinity regulatory sites on troponin C which act as the sensor, the Ca^{2+} affinity of which is a function of dynamically changing sarcomere length as well as the fraction of strongly bound crossbridges. This hence facilitates not only a feedforward but also a moderate feedback interaction between the $[Ca^{2+}]_{myo}$ transient and the myofilament contractile mechanism. This feedback effect is seen in Fig. 4.5C where the presence of isometric contraction results in a small decrease in peak Ca^{2+} transient, a result of the Ca^{2+} buffering action of troponin.

Although it is well known that myoplasmic Ca^{2+} concentration has a direct influence on beat to beat cell shortening, other indirect modulatory influences exist. Of particular interest is the indirect coupling of the cellular plasma membrane with the myofilament contractile mechanism. A decrease in Na^{+}/Ca^{2+} exchanger function in extruding Ca^{2+} from the cytosol results in an increased relative role for the SERCA pump, augmenting SR Ca^{2+} content. This in turn results in enhanced release increasing the availability of post-release activator Ca^{2+} in the cytosol, thus translating into greater degree of contraction (Fig. 4.6). This completes a control loop that allows modulation of NCX activity to force a readjustment in myofilament contractility.

Experimental conditions such as temperature strongly influence cardiac myofilament contractility. An increase in temperature results in an increase in sensitivity of the myofilaments to myoplasmic Ca^{2+} [196]. As the temperature is increased from 22°C to 30°C, increasing myofilament Ca^{2+} sensitivity (Fig. 4.7C) causes a moderate

increase in peak force despite a decline in peak $[Ca^{2+}]_{myo}$. However, a further increase to body temperature results in a steep decline in force developed (Fig. 4.7D). Hence, an increase in temperature from 22°C to 38°C which results in a decline in peak $[Ca^{2+}]_{myo}$ [167], causes an overall decrease in force developed. This translates into an overall decrease in the degree of cell shortening with increasing temperature (Fig. 4.7F). This temperature dependent behavior is not captured by the model proposed by Rice et al. [1] where an increase in temperature causes an increase in peak force developed as a result of the large Q10 values used (Qf_{app}, Qh_f, Qh_b and Qg_{xb}, Table 1, [1]).

Modulation of myofilament Ca^{2+} sensitivity (MCS) as a result of a change in Troponin I (TnI) phosphorylation by PKA has been implicated in heart failure [215]. Here we study the role of MCS in modulating myofilament contractile response (Fig. 4.8) an aspect overlooked in recent modeling studies including Rice et al. [1]. In particular, we model the effect of isoproterenol, a β-adrenergic agonist, which is known to cause a decline in myofilament Ca^{2+} sensitivity as a result of protein kinase A (PKA) mediated phosphorylation of troponin I at Ser23/Ser24 [55, 75]. Such a decline in Ca^{2+} sensitivity aids myofilament relaxation in the presence of increased levels of activator Ca^{2+}. Figure 4.9 shows that an increase in amplitude of the myoplasmic Ca^{2+} transient (a cumulative effect of enhancement in trigger current and increase in uptake rate of the SERCA pump) is more than adequate to compensate for the decrease in Ca^{2+} sensitivity, thus facilitating the desired effect of β-adrenergic stimulation, namely an increase in contractile force generated.

4.4.1 Model Limitations

1. Our model of a rat ventricular myocyte is limited to Ca^{2+} related channels, exchanger and pumps ($I_{Ca,L}$, I_{NaCa}, I_{PMCA}, I_{ryr} and SERCA pump), while lacking exclusive Na^+ or K^+ related channels and transporters (described in Krishna et al. [66]). In our voltage clamp protocol, external solution in the bath is modeled as normal Tyrode with Cs^+ substituted for K^+. We have represented I_{NaCs} in our model (described in Krishna et al. [66]) by the expression for Na^+/K^+ pump formulated by Lindblad et al. [144] replacing K^+ ion concentrations with the Cs^+ ion concentration. While ensuring whole cell Na^+ ion balance, the peak Na^+/Cs^+ pump current is modified to be one-sixth to account for the decreased potency of the cation Cs^+ in activating the pump. The voltage-dependence of I_{NaCs} is adopted from the data on Na^+/K^+ pump from Hansen et al. [165]. The role of mitochondrial Ca^{2+} uniporter is not modeled in this study due to its negligible ($< 1\%$) role in Ca^{2+} transport from the cytosol [216]. This model is aimed at mimicking voltage clamp conditions where channels other than calcium are blocked, and it cannot be used to study any action potential-induced Ca^{2+} transient-frequency relationship. However, its focus on the Ca^{2+} dynamics allows one to comprehend more clearly the important role of Ca^{2+} signalling pathways and feedback control systems in maintaining whole cell homeostasis over a prolonged period of time.

2. The cooperative activation of the thin filament and the strain-dependent transitions of the crossbridge cycle have been approximately modeled as non-spatial, state-variables. However, this simplification is valid as these transitions are inherently local phenomena and the model reproduces a wide range of steady

state and dynamic responses in cardiac muscle [1]. Although a CaM-dependent pathway is reported [168] to be responsible in modulation of myofibrillar contractility implying a possible CaM mediated role for Ca-dependent kinases or phosphatases in regulating myofilament contractility (particularly in frequency dependent acceleration of relaxation), further studies are required to clarify the molecular mechanisms involved.

3. The temperature dependence of passive force attributed to titin and other cytoskeletal elements is not modeled in this study and the assumption of constant stiffness for the series elastic element (KSE) does not account for temperature dependent effects. This is an area where the model can be expanded but additional measured data on the temperature sensitivity of these elements is necessary. Regardless, our model provides reasonable approximations to the temperature dependence of developed force in intact thin rat ventricular trabeculae [167].

4.5 Conclusion

We have developed a composite mathematical model for cardiac electromechanics which includes a detailed description of Ca^{2+} dynamics under voltage clamp conditions in the rat ventricular myocyte, based on experimental data [66, 1]. We have investigated the role of different factors including the myoplasmic $[Ca^{2+}]_{myo}$ transient and the sarcomeric length in influencing various types of twitch responses obtained under different loading conditions (including isosarcometric, isometric and unloaded conditions). Various control loops influencing cell shortening have been explored. In particular, the bidirectional interaction of the Ca^{2+} transient with the myofilament

contractile mechanism and the importance of indirect SR mediated interaction of the sarcolemma with the contractile machinery is highlighted by showing the regulation of isometric contraction by the degree of NCX activity. The effect of temperature on cell shortening is investigated identifying the differential sensitivity of the $[Ca^{2+}]_{myo}$ transient and the myofilament contractile mechanism. The important role of myofilament Ca^{2+} sensitivity in force generation is studied with particular emphasis on the effect of β-adrenergic stimulation on cardiac contractile response. In agreement with Janssen [211], we also demonstrate a key linear relationship between the rate of contraction and relaxation, which is shown here to be intrinsically coupled over the full range of physiological perturbations (including temperature, sarcomeric length, activator Ca^{2+}, and isoproterenol; e.g. see insets in Figs. 4.7D, 4.1A-ii).

This study demonstrates that the model has long-term stability in regulating myoplasmic Ca^{2+}, as shown in the 18-sec duration experiments at a physiological rate of stimulation (conditioning train of voltage clamp pulses at 5 Hz) shown in Fig. 4.6. This long term Ca^{2+} balance under physiological conditions is crucial in facilitating implementation of this model in large scale simulations such as frequency dependent studies analyzing cellular force-frequency response. Our study also provides mechanistic insights into whole-cell responses to a wide variety of testing approaches used in studies of cardiac myofilament contractility that have appeared in the literature over the past two decades (Figures 4.1-4.8). Thus, the model serves as a platform for the predictive modeling of VC investigations of cardiac electromechanics pertaining to the rat ventricular myocyte in a number of areas. These are fundamental issues that would benefit from a better mechanistic understanding of the cardiac contractile mechanism in the rat ventricluar myocyte. This study is aimed at providing an initial step towards this goal.

Chapter 5

Force-Frequency Response

5.1 Background

Cardiac muscle contraction is a result of a transient increase in intracellular Ca^{2+} concentration $[Ca^{2+}]_{myo}$. Sarcolemmal (SL) membrane depolarization triggers Ca^{2+} influx via the dihydropyridine (DHP)-sensitive L-type Ca^{2+} channels. Following diffusion across a small sub-membrane dyadic space, this influx activates ryanodine receptors (RyRs) controlling ryanodine-sensitive Ca^{2+} release channels in the junctional portion of the sarcoplasmic reticulum (jSR). Fabiato and Fabiato [8] named the process calcium-induced calcium release (CICR). Ca^{2+} subsequently diffuses from the dyadic space into the myoplasm. Ultimately, intracellular Ca^{2+} concentration $[Ca^{2+}]_{myo}$ is returned to resting levels by combination of: (a) Ca^{2+} buffering in the dyadic space and myoplasm; (b) sequestration of Ca^{2+} by sarcoplasmic/endoplasmic reticulum Ca^{2+}-ATPase (SERCA)-type calcium pumps lining the longitudinal portion of the sarcoplasmic reticulum (LSR); and (c) Ca^{2+} extrusion from the myoplasm by Na^{+}/Ca^{2+} exchangers and Ca^{2+}-ATPase pumps on the sarcolemmal membrane.

Ca^{2+} is an extremely important and highly versatile second messenger in cardiac cells, which plays a crucial role not only in excitation-contraction (E-C) coupling but also in excitation-transcription coupling [48]. Various inter-connected Ca^{2+} signalling pathways help preserve the integrity of the cellular Ca^{2+} system despite any changes

in pacing frequency. Specifically, Ca^{2+} triggers the CaM-mediated rate-dependent effects of CaMKII and CaN on the characteristics of the apposed dihydropyridine (DHP) and ryanodine-sensitive Ca^{2+} channels in the dyad, whose interaction forms the basis for CICR. The proteins CaMKII and CaN not only influence the release mechanism but also affect the SERCA pump either directly or indirectly via phospholamban (PLB), thus modulating the Ca^{2+} uptake process [148, 149, 150, 151]. It is also known that β-adrenergic stimulation of the cardiac cell, mediated by the second messenger cAMP, modulates the frequency dependence of the peak force generated by the myofilaments, the force-frequency response (FFR). These protein-mediated and second messenger pathways help maintain Ca^{2+} homeostasis over a wide range of stimulation frequencies.

Cardiac contractile function is closely coupled with heart rate (Bowditch effect [217]). Although positive [218], almost flat [219] and negative [220, 221] peak FFR have been reported in the literature, it is clear from in-vitro studies involving stimulation in the physiological range of frequencies [222, 223] that rat ventricle exhibits a positive peak FFR. The issue of force-frequency relationship requires broadened investigation into the various underlying cellular and molecular mechanisms. We propose that mathematical modeling would be a useful tool in helping to sort out this complex issue.

5.2 Results

From our modeling standpoint, the dyadic coupling unit (DCU) as defined by Krishna et al [66] is a fundamental element involved in the mechanism of CICR. These previous studies have described the control features of this unit, as well as its interaction with the SERCA pump and free sarcolemmal pumps and exchangers to

achieve a homeostatic regulation of myoplasmic Ca^{2+} concentration. We now extend our voltage clamp studies to address the subject of frequency-dependent characteristics of CICR and begin with the study of frequency dependence of the DCU, one of the most important components of the model. All the frequency-dependent behavior discussed here is at steady state unless otherwise specified. The first task is to examine the frequency dependence of the $I_{Ca,L}$ trigger current, followed by the RyR Ca^{2+} channel, highlighting the rate-dependent CaM-mediated signalling involved. This analysis is followed by examining the SR Ca^{2+} content and the various factors controlling it in a rate-dependent manner. A quantitative study of the overall cellular Ca^{2+} balance is performed to highlight its rate-dependent feature. Emphasis is placed on relative roles played by the longitudinal sarcoplasmic reticulum (LSR) membrane SERCA pump and the plasma membrane Na^{+}/Ca^{2+} exchanger, as two principal Ca^{2+} transport routes in the maintenance of Ca^{2+} homeostasis. We finally examine the myoplasmic Ca^{2+} transient as a function of frequency with a particular interest in the rate dependence of the force-frequency response (FFR) generated by the coupled electromechanical model. This is subsequently followed by an investigation of the rate-dependent influence of cAMP-mediated β-adrenergic stimulation on the cardiac contractile response.

5.2.1 L-type Ca^{2+} Current ($I_{Ca,L}$)

An increase in stimulation frequency from 0.5 Hz to 8 Hz, results in a frequency-dependent monotonic increase in the peak trigger current (inset in Fig. 5.1A and Fig. 5.1B) while slowing down the rate of decline after it reaches its maximum (note the traces corresponding to 0.5 Hz to 8 Hz in Fig. 5.1A). The most critical mechanism involved in frequency encoding of the $I_{Ca,L}$ channel activity is the rate-dependent

change in the average level of activated-CaMKII (Fig. 5.1C), which is known to assist CaM-mediated Ca^{2+}-dependent facilitation (CDF). As stimulation frequency is increased from 0.5 Hz to 8 Hz, the increase in peak $I_{Ca,L}$(Fig. 5.1B) closely tracks the increase in the average level of activated-CaMKII. However, beyond 8 Hz a decrease in peak is observed (Fig. 5.1B) despite a further increase in CaMKII (Fig. 5.1C). This occurs as a result of incomplete channel recovery at high ($>$ 8Hz) stimulation rates, which results in a decline in peak channel open probability (Fig. 5.1D). At low (0.5 Hz $\leq$ f $\leq$ 4.0 Hz) stimulation rates, an increase in activated CaN (85% to 97%) is also known to enhance $I_{Ca,L}$ channel activity, whereas at higher ($>$ 4 Hz) rates, the lack of a substantial rate-dependent increase in its average level (Fig. 5.1C) minimizes its role in Ca^{2+}-dependent facilitation. The maximum value attained by the open probability of the DHP-sensitive Ca^{2+} channel (Fig. 5.1D) reflects the trend shown by the peak value of the trigger current over the entire range of stimulation frequencies investigated (0.5 to 12.0 Hz) investigated. At frequencies less than 8 Hz, the upstroke velocity of $I_{Ca,L}$ current can be seen to increase with an increase in frequency, but above 8 Hz it begins to decline (Fig. 5.1E) due to insufficient time for full channel recovery. It is important to note that the model predicts a frequency-dependent modulation in peak $I_{Ca,L}$ current of less than 20% over the entire frequency range (0.5 Hz to 12.0 Hz). This small modulation of peak current (Fig. 5.1B) is far less than the percentile changes in CaMKII activation (50%, Fig. 5.1C), due to the insufficient time for channel recovery at high ($>$ 4 Hz) stimulation rates.

5.2.2 RyR Ca^{2+} Release

Fig. 5.2A shows a phase plot of RyR open probability (P_o) versus $[Ca^{2+}]_{RyR}$ constructed from model-generated data corresponding to different stimulation rates with

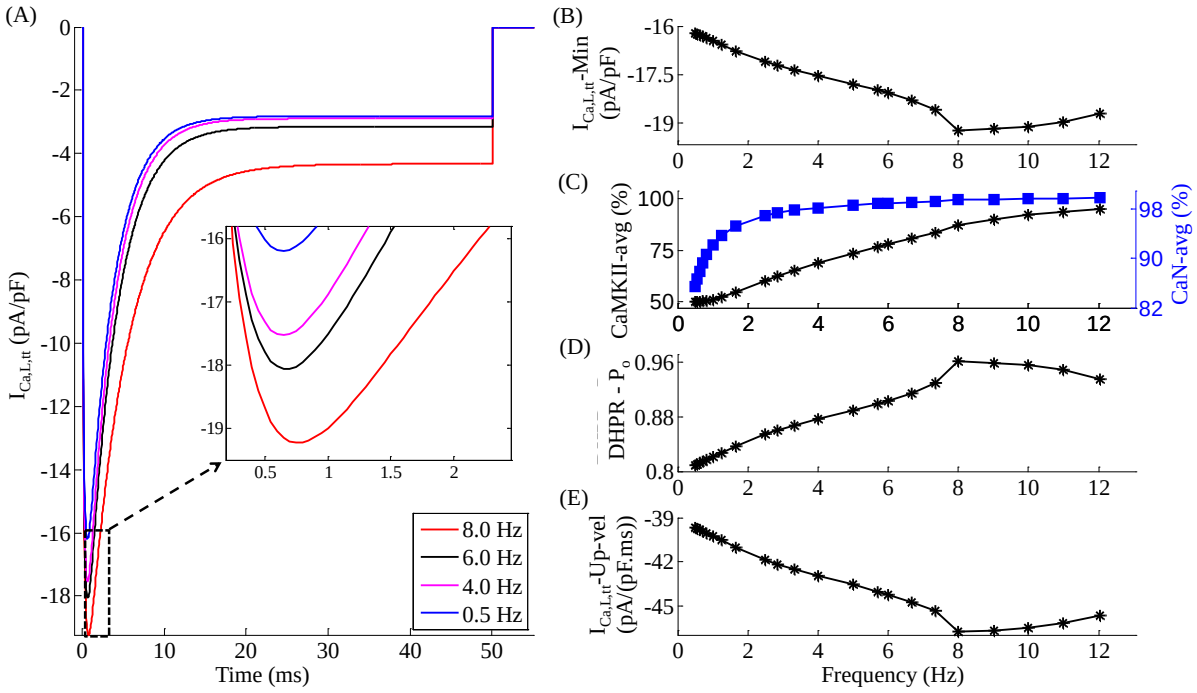

Figure 5.1 : Frequency-dependent characteristics of the DHP-sensitive Ca^{2+} channel $I_{Ca,L}$, which forms the trigger current. Voltage clamp protocol used is a 50 ms step pulse to 10 mv from a holding potential of -40 mv. (A) $I_{Ca,L}$ at different frequencies of stimulation ranging from 0.5 Hz to 8.0 Hz. Inset gives an expanded view of the rate-dependent modulation of $I_{Ca,L}$ over the range of frequencies investigated (B) Dependence of peak $I_{Ca,L}$ current on frequency of stimulation (C) Frequency-dependent increase in average levels of activated auxiliary proteins CaMKII and CaN in the dyad (D) Frequency-dependent modulation of peak open probability of the DHP-sensitive Ca^{2+} channel. (E) Rate-dependent changes in $I_{Ca,L}$ upstroke velocity.

the inset showing the peak open probability attained by each of the phase loops. As the stimulation frequency is increased from 0.5 Hz to 4 Hz, a marginal increase ($< 1\%$) in peak RyR open probability occurs (inset in Fig. 5.2A) as a result of the factors: (a) a frequency-dependent CaMKII mediated (Fig. 5.2B) $I_{Ca,L}$ facilitation (Fig. 5.1A); (b) a moderate increase in SR Ca^{2+} content (despite a relatively constant maximal SERCA uptake rate), due to increased trigger current and the subsequent increase in $[Ca^{2+}]_{myo}$ combined with an increase in $[Na^{+}]_{myo}$ (30% in Fig. 5.2B) which impedes

Ca^{2+} extrusion via the NCX; and (c) a direct CaMKII-mediated enhancement in RyR release. As the stimulation frequency is increased from 4 Hz to 8 Hz, despite a moderate increase in both the trigger current and SR Ca^{2+} content, a small decrease in RyR open probability occurs as a result of an increase in post-release $[Ca^{2+}]_{jSR}$ (Fig. 5.2C), which forces an incomplete luminal sensor-based RyR recovery (as described in Krishna et al [66]). Beyond 8.0 Hz, the peak RyR open probability decreases due to two mechanisms: (a) a small parallel decrease in the trigger current (Fig. 5.1B) indicating a close coupling enforced by a stable CICR, and (b) insufficient time for full channel recovery, accompanied by a falling pre-release diastolic jSR Ca^{2+} level (Fig. 5.2C). Both the declining trigger current and the declining $[Ca^{2+}]_{jSR}$ result in a strong decline in $[Ca^{2+}]_{RyR}$. The decrease in $[Ca^{2+}]_{RyR}$ at high (> 8 Hz) frequencies can be seen in Fig. 5.2A, where the open probability loop for 10 Hz is enclosed within that of 8 Hz. The frequency dependence of the area enclosed by the loops (which indicates the amount of SR Ca^{2+} released into the dyad) mirrors that of the peak RyR open probability. The SR Ca^{2+} release from the Ry-sensitive receptor exhibits strong frequency-dependent behavior as shown in Fig. 5.2D. Instantaneous RyR flux is obtained by multiplying the open probability by the concentration gradient across the channel. The rate dependence of the peak instantaneous RyR flux (Fig. 5.2D, E) is a result of two factors: (a) the frequency dependence of peak RyR open probability (Fig 5.2A), which indicates the degree of recruitment of RyR release channels; and (b) the pre-release SR Ca^{2+} content (Fig. 5.2C), which establishes the initial concentration gradient across the release channel. Figure 5.2D also shows the gradation in the time required for RyR recovery.

The frequency dependence of RyR release activation (Fig. 5.2F), shares its characteristics with the peak RyR open probability (Fig. 5.2A). Besides increasing trigger

current, RyR release is also facilitated by increasing levels of activated-CaMKII (Fig. 5.2E) and increasing SR Ca^{2+} content(Fig. 5.2C). The frequency-dependent modulation of RyR inactivation rate (Fig. 5.2F) mimics the rate dependence of minimum SR Ca^{2+} levels reached after release (Fig. 5.2C), mediated via the luminal sensor. With increasing stimulation frequency (0.5 Hz $\leq$ f $\leq$ 8.0 Hz), despite decreasing time available for uptake, increasing pre-release SR Ca^{2+} content is achieved only by increased rate of SR filling. This increased rate of SR filling translates into a faster decline in inhibition via the luminal sensor (a RyR inactivation mechanism described in Krishna et al [66]). Hence, the rate of inactivation decreases as the frequency is increased from 0.5 Hz to 8.0 Hz (Fig. 5.2F) owing to increasing SR Ca^{2+} content in this range of frequencies. With increase in frequency, the rate-dependent increase in the level of activated-CaMKII in the dyadic space also causes an increased CaMKII-mediated up-regulation of the ryanodine receptor [118, 121, 119, 110, 111, 112, 113]. This CaMKII mediated up-regulation delays the onset of declining SR Ca^{2+} content-driven (8.0 Hz $\leq$ f $\leq$ 12.0 Hz) increase in the rate of RyR channel inactivation.

The RyR channel experiences a frequency-dependent modulation by both the trigger current and the amount of activated-CaMKII on its dyadic side. On its luminal side, it experiences modulation by the luminal sensor (as described in Krishna et al [66]) controlling refractoriness, and the SR Ca^{2+} content providing the drive for Ca^{2+} through the channel.

5.2.3 SR Ca^{2+} Content

The frequency dependence of pre-release Ca^{2+} level in the SR is a result of several factors namely: (a) available $[Ca^{2+}]_{myo}$ for sequestration; (b) the rate-dependent behavior of the SERCA pump; (c) the frequency dependence of the release characteristics

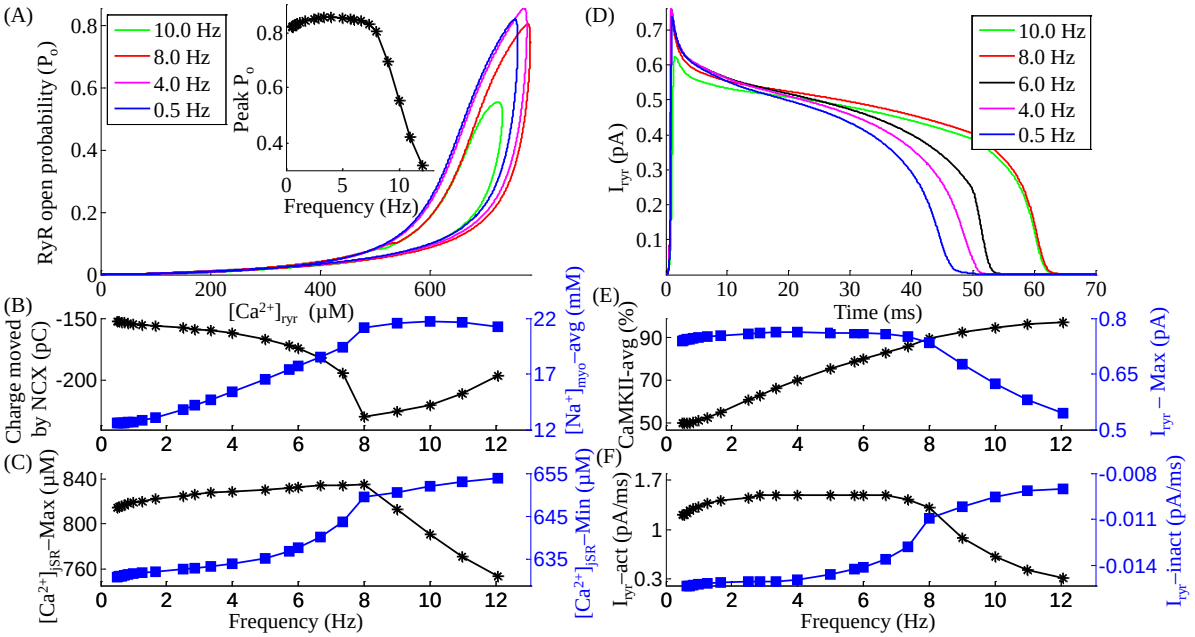

Figure 5.2 : Frequency-dependent characteristics of the SR Ca^{2+} release channel I_{ryr}. Voltage clamp protocol used is a 50 ms step pulse to 10 mv from a holding potential of -40 mv. (A) RyR open probability vs $[Ca^{2+}]_{ryr}$ for increasing frequency of stimulation (0.5 Hz to 10.0 Hz). The inset shows the frequency-dependent modulation of peak RyR open probability. (B) Frequency dependence of average charge transported by NCX and average $[Na^{+}]_{myo}$ in the myoplasm. (C) Rate dependence of pre-release maximum and post-release minimum SR Ca^{2+} level. (D) Traces for RyR release for the corresponding frequencies of stimulation in panel A. (E) Dependence of average level of activated-CaMKII and peak I_{ryr} current on frequency of stimulation. (F) Frequency-dependent changes in average I_{ryr} activation and inactivation rates. The legend for traces in panel A is shared by panel D.

of Ry-sensitive Ca^{2+} channel; and (d) the cumulative transmembrane Ca^{2+} transport via $I_{Ca,L}$ and NCX. The combined effect of these factors results in the biphasic relationship (inset in Fig. 5.3A) between free Ca^{2+} content in the SR and the frequency of stimulation. As the frequency is increased from 0.5 Hz to 8.0 Hz, the SR Ca^{2+} content increases due to the following frequency-dependent, active CaMKII-mediated effects: (a) enhancement of maximal uptake rate of the SERCA pump due to increase in PLB phosphorylation (Fig. 5.3B) assisted by increasing levels of activated-CaMKII

(Fig. 5.3C); (b) decrease in the half-activation constant for the forward (myoplasm to SR) operation of the SERCA pump (Fig. 5.3D) translating into increased Ca^{2+} sensitivity of the pump for uptake; and (c) increase in half-activation constant for the backward (SR to myoplasm) operation of the SERCA pump (Fig. 5.3D), reducing tendency for back-flow via the SERCA pump. The increase in SR Ca^{2+} content is also facilitated by a CaMKII mediated enhancement in $I_{Ca,L}$ as well as inhibition of Ca^{2+} extrusion via NCX due to increasing $[Na^{+}]_{myo}$. As the stimulation frequency is gradually increased further from 8.0 Hz to 12.0 Hz, a steep decrease in SR Ca^{2+} content is observed (inset in Fig. 5.3A). This frequency-dependent decrease in pre-release SR Ca^{2+} content at very high ($>$ 8.0 Hz) stimulation frequencies is a result of the following: (a) a decrease in maximal uptake rate of the SERCA pump (Fig. 5.3B) along with a significant decrease in time available for resequestration of cytosolic Ca^{2+}; (b) a decrease in Ca^{2+} entry into the cell via the trigger current $I_{Ca,L}$ (Fig. 5.1B); and (c) relatively constant intracellular $[Na^{+}]_{myo}$ (Fig. 5.2B). Between stimulation frequencies 0.5 Hz and 8.0 Hz, the characteristics of the post-release SR Ca^{2+} level tracks the pre-release peak SR Ca^{2+} content. However, beyond 8.0 Hz, a declining SR Ca^{2+} content causes increasing inhibition on RyR release via the luminal sensor [66], resulting in a gradual increase in post-release SR Ca^{2+} level.

The frequency encoding involved in the uptake mechanism via the SERCA pump is strongly regulated by two key proteins, PLB and activated-CaMKII. The rate-dependent decrease in the level of unphosphorylated phospholamban (PLB) (Fig. 5.3B) capable of inhibiting the SERCA pump is a result of increasing levels of activated-CaMKII (Fig. 5.3C). It is important to note that phosphorylation of PLB is sensitive to small changes in activated-CaMKII [77]. Our results show that activated-CaMKII (Fig. 5.3C) has a prominent role in rate-dependent modulation

of the SERCA pump despite its low level (three orders of magnitude compared to activated CaN (note the 10^{-5} on left ordinate in Fig. 5.3C)) in the myoplasm [48]. Our results show that activated CaN (Fig. 5.3C) has minimal role in rate-dependent inhibition of the SERCA pump. However, over-expression of CaN in failing heart is known to significantly compromise SERCA activity [153]. At a given frequency of stimulation, an increase in trigger current forces a gradual increase in SR Ca^{2+} uptake which in turn results in a corresponding increase in RyR release, which translates into an elevated cytosolic Ca^{2+} level and subsequently an increased activated-CaMKII level. This causes an increase in SR Ca^{2+} uptake rate via phosphorylation of PLB, thus completing a positive feedback loop. Hence, the peak $I_{Ca,L}$ trigger current sets the peak SR Ca^{2+} content if the SERCA pump is not operating in saturation. Thus the frequency dependence of the maximal rate of uptake by the SERCA pump (Fig. 5.3B) shares its characteristics with peak $I_{Ca,L}$ current (Fig. 5.1B) linked together by activated-CaMKII (Fig. 5.3C). It is important to note that rate-dependent enhancement in SERCA activty by CaMKII significantly overrides the inhibitory influence of CaN in a non-failing heart [153]. Figure 5.3B also shows the underlying rate-dependent decline in unphosphorylated PLB responsible for rate-dependent increase in SR uptake.

Although marginally ($< 1\%$ change over 0.5 Hz $\leq$ f $\leq$ 12.0 Hz) frequency-dependent, the SERCA pump has a primary role in resequestration of myoplasmic Ca^{2+} when compared with the combined influence of Na^{+}/Ca^{2+} exchange (I_{NaCa}) as well as Ca^{2+} transport via the plasma membrane Ca^{2+} ATPase pump,(I_{PMCA}). As the frequency of stimulation is increased from 0.5 Hz to 4.0 Hz, increasing activated-CaMKII-dependent enhancement in SERCA activity assisted by a decrease in Ca^{2+} extrusion via NCX due to increasing $[Na^{+}]_{myo}$ (Fig. 5.2B) result in a marginal in-

crease in the relative role of SERCA pump as shown in Fig. 5.3E. However, as frequency is further increased, declining SERCA-mediated uptake activity due to a decrease in CaMKII-mediated SERCA enhancement, as well as reduced time available for uptake results in a small negative slope to the frequency dependence of the relative role of SERCA pump (Fig. 5.3E).

5.2.4 Myoplasmic Ca^{2+} Transient $[Ca^{2+}]_{myo}$

Figure 5.4A shows the traces of $[Ca^{2+}]_{myo}$ at increasing frequencies showing an increase in the peak myoplasmic Ca^{2+} transient during systole with increasing stimulation frequency in the range 0.5 Hz to 8.0 Hz. A 'primary phase' negative peak FFR (a decrease in peak contractile force with increase in stimulation frequency observed at low (< 1.0 Hz) stimulation rates) reported in studies on rat ventricular myocytes [224, 225, 218, 219] could be a result of low unphysiological temperatures employed in those studies.

The inset in Fig. 5.4A shows that the peak rate of rise (R_{rise}) and decay (R_{decay}) of the $[Ca^{2+}]_{myo}$ transient increases with the frequency of stimulation from 0.5 Hz to 8.0 Hz. The increase in rate of rise is a result of an increase in peak trigger current $I_{Ca,L}$ (Fig. 5.1B) and SR Ca^{2+} content (inset in Fig. 5.3A) while the increase in rate of decay is a result of CaMKII-mediated acceleration of relaxation (Fig. 5.3C) due to a rate-dependent enhancement in uptake by the SERCA pump. An opposite effect is observed in the rate of rise and decay of the $[Ca^{2+}]_{myo}$ transient beyond a stimulation rate of 8.0 Hz due to declining peak trigger current and reduced CaMKII activity. As shown in Fig. 5.4B, increasing stimulation rate from 0.5 Hz to 8.0 Hz results in a steep increase in peak $[Ca^{2+}]_{myo}$ (maximum), which parallels a strong increase in pre-release diastolic $[Ca^{2+}]_{jSR}$ (Fig. 5.3A). This increase in $[Ca^{2+}]_{jSR}$ is mirrored by a

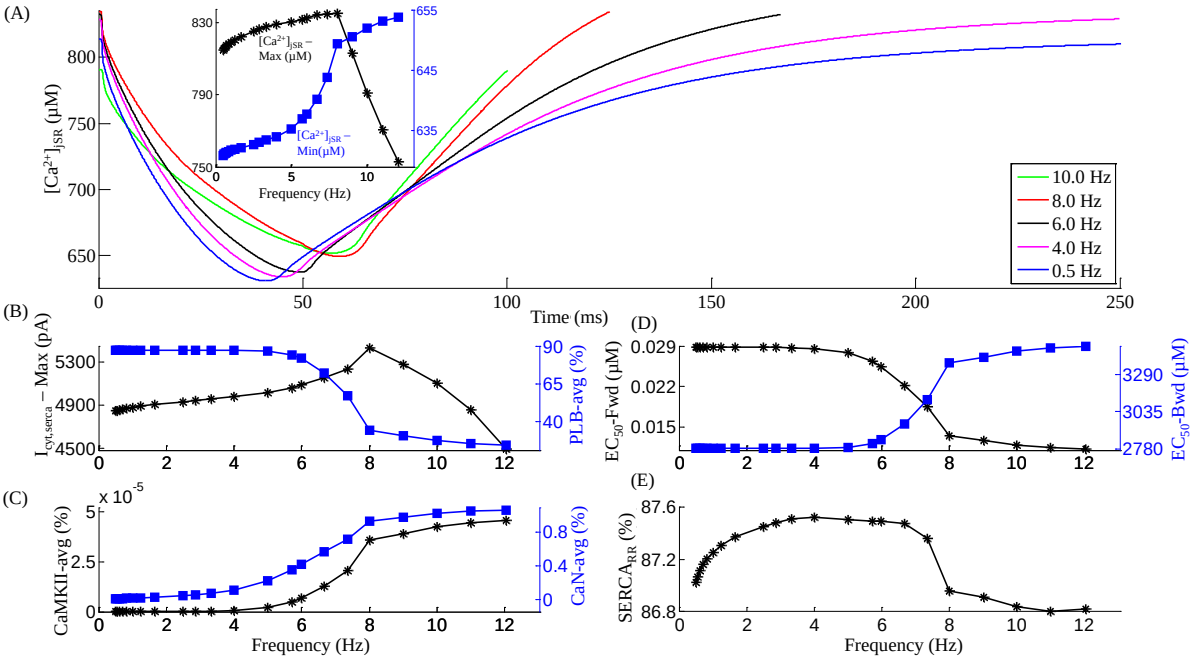

Figure 5.3 : Mechanisms underlying the frequency-dependent modulation in SR Ca^{2+} content. Voltage clamp protocol used is a 50 ms step pulse to 10 mv from a holding potential of -40 mv. (A) $[Ca^{2+}]_{jSR}$ traces indicating rate-dependent changes in SR filling. The inset shows the frequency dependence of the maximum and minimum SR Ca^{2+} concentration. (B) frequency dependence of the maximal pumping rate of SERCA and the average level of phosphorylated PLB. (C) Frequency-dependent increase in average levels of activated auxiliary proteins CaMKII and CaN in the myoplasm. (D) Frequency dependence of the half-activation constant for the forward and backward flow via the SERCA pump. (E) Rate dependence of the relative role of the SERCA pump (when compared to the Na^{+}/Ca^{2+} exchanger (I_{NaCa})and the plasma membrane Ca^{2+} ATPase pump (I_{PMCA}).

corresponding increase in pre-release minimum value attained by $[Ca^{2+}]_{myo}$ during diastole (Fig. 5.4B). As the stimulation frequency is increased beyond 8.0 Hz, although the SERCA activity is saturated [222], the declining SR Ca^{2+} content (inset in Fig. 5.3A) aids in the decrease of peak $[Ca^{2+}]_{myo}$ by compromising SR release. However, a lack of sufficient time for uptake continues to manifest in increasing pre-release diastolic $[Ca^{2+}]_{myo}$ (Fig. 5.4B) at these rates. Our study suggests that a decrease in

pH_i causing a decrease in myofilament Ca^{2+} sensitivity [226] is not required to cause the 'secondary phase' negative peak FFR (a decrease in peak contractile force with increase in stimulation frequency observed at high (> 8.0 Hz) stimulation rates). We attribute this phase which involves a decrease in force response, to the declining peak $[Ca^{2+}]_{myo}$ as seen in Fig. 5.4B. The rate-dependence of peak $[Ca^{2+}]_{myo}$ for increasing stimulation frequencies (0.5 Hz $\leq$ f $\leq$ 12.0 Hz) is comparable to that reported by Kentish et al. (Fig. 1, [227]) in rat ventricular trabeculae. Figure 5.4C shows the frequency-dependent changes in gain calculated as the ratio of peak Ca^{2+} transient in the presence of CICR to the peak calcium transient in its absence, contributed by the trigger calcium alone [28]. The EC coupling gain increases with the frequency of stimulation from 0.5 Hz to 8.0 Hz, due to rate dependent CaMKII-mediated increase in uptake rate of the SERCA pump (Fig. 5.3B), which decreases the peak $[Ca^{2+}]_{myo}$ in the absence of CICR and increases peak $[Ca^{2+}]_{myo}$ in its presence (due to increase in SR content (inset in Fig. 5.3A)). Beyond a stimulation frequency of 8.0 Hz, the rapid decrease in SR content causes a steep decline in EC coupling gain.

5.2.5 Positive Force-Frequency Relationship

Changing the stimulation rate has a very prominent effect on cardiac muscle contraction by way of affecting the amplitude and time course of the intracellular Ca^{2+} transient (Figs. 5.4 and 5.5A). Here, we simulate a positive peak force-frequency response elicited using a voltage clamp stimulation protocol. Figure 5.5B shows the traces for the isometric contractile force generated for increasing stimulation frequencies. As stimulation frequency increases from 0.5 Hz to 8.0 Hz, peak contractile force increases (Figs. 5.5B and C) mirroring an increase in peak $[Ca^{2+}]_{myo}$. As seen in Figs. 5.1B and 5.3B, this is mainly a result of CaMKII-dependent upregulation of

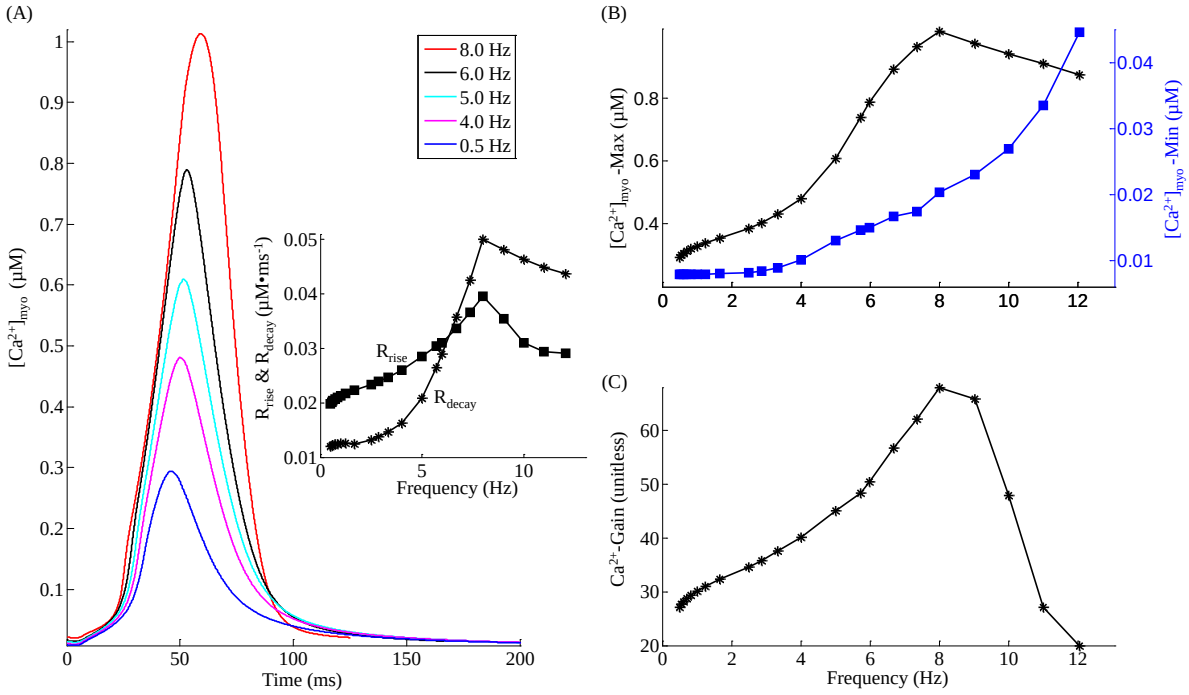

Figure 5.4 : Frequency-dependent modulation of myoplasmic Ca^{2+} transient. Voltage clamp protocol used is a 50 ms step pulse to 10 mv from a holding potential of -40 mv. (A) $[Ca^{2+}]_{myo}$ traces showing rate-dependent effects on systolic Ca^{2+} concentration in the myoplasm for increasing stimulation frequencies from 0.5 Hz to 8.0 Hz. The inset shows the change in the maximum rate of rise and decay of the $[Ca^{2+}]_{myo}$ transient with stimulation frequency. (B) frequency dependence of the maximum and minimum myoplasmic Ca^{2+} concentration. (C) bi-phasic rate dependence of EC coupling gain.

$I_{Ca,L}$ and SERCA activity which translates into a frequency-dependent increase in SR Ca^{2+} content, and thereby SR Ca^{2+} release. As reported in the literature [1], the non-linear sigmoidal steady state Force-Ca^{2+} relationship (overlayed in Fig. 5.5D) causes a non-linear response in peak force developed for a corresponding change in peak $[Ca^{2+}]_{myo}$. As shown in Fig. 5.5D the contraction-relaxation coupling point (CRCP) moves to larger values of force and Ca^{2+} concentration with increase in rate of stimulation. The peak contractile force is attained at a physiological rate of 8.0 Hz, beyond which the gradual decline in peak $I_{Ca,L}$ current (Fig. 5.1B), which forces a

corresponding decrease in SR Ca^{2+} content (Fig. 5.3A), and hence RyR release (Fig. 5.2E), causes a marginal decline in peak contractile force generated. The frequency at which peak contractile force is generated is temperature-dependent as reported by Layland et al. [222] and shifts to the right on the frequency axis as the temperature increases. The peak force frequency response obtained mimics the experimentally observed frequency dependence (Fig. 1, [227]). The minimum value of contractile force per cycle (end-diastolic) increases with increasing rate of stimulation as a result of the combination of factors: (a) increasing myoplasmic Ca^{2+} levels due to rate-dependent increase in SR release (Fig 5.4); and (b) decreasing time available for resequestering released Ca^{2+} from the myoplasm. The frequency dependence of the force response translates into a reciprocal rate dependent characteristic of the sarcomere length as shown in Figures 5.5E and F.

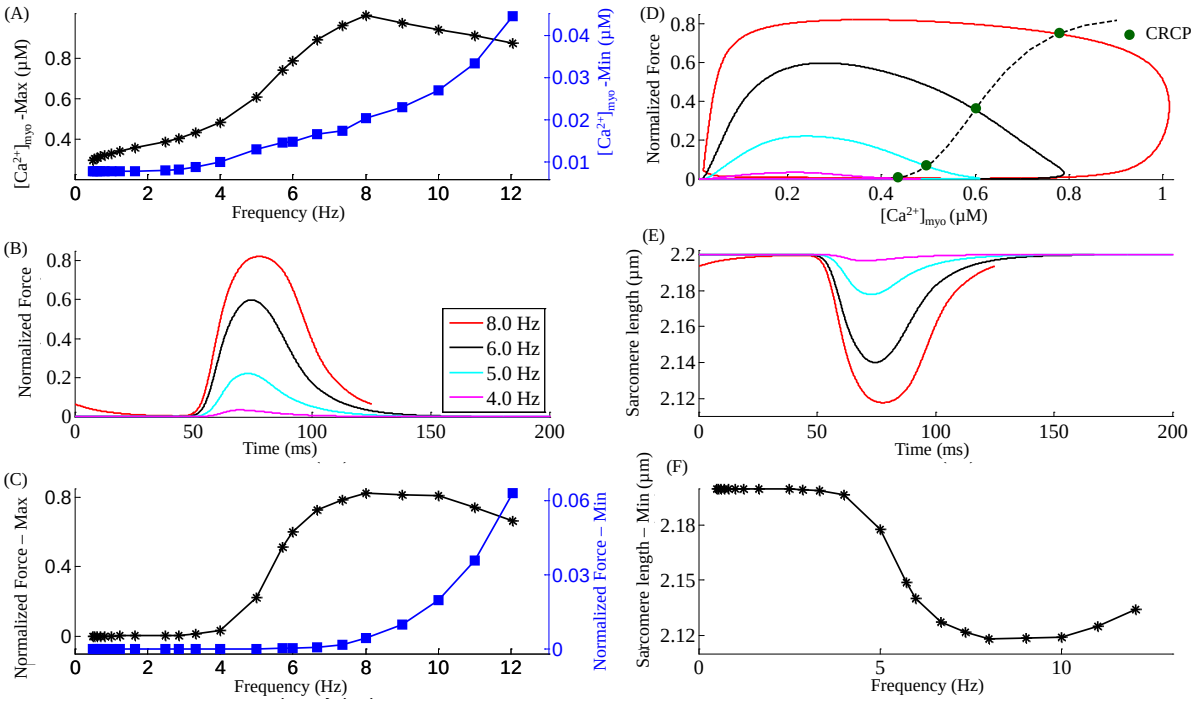

Figure 5.5 : Rate-dependent changes in myoplasmic Ca^{2+} concentration, the corresponding contractile force generated and the resulting sarcomere length. Voltage clamp protocol used is a 50 ms step pulse to 10 mv from a holding potential of -40 mv. (A) Frequency dependence of the maximum and minimum myoplasmic Ca^{2+} concentration (B) Traces for normalized isometric force developed at stimulations rates of 4, 5, 6, and 8 Hz. (C) Traces for sarcomere contraction corresponding to isometric force in panel B. (D) Phase loops for normalized isometric force vs $[Ca^{2+}]_{myo}$ for increasing frequency of stimulation (4.0 Hz to 8.0 Hz) corresponding to panel B. (E) Rate Dependence of the maximum and minimum normalized force generated. (F) Frequency dependence of minimum sarcomere length achieved at peak contraction. The legend for traces in panel B is shared by panel D and E.

5.2.6 Effect of Maximal β-Adrenergic Stimulation

β-adrenergic stimulation bears a very crucial physiological relevance in normal functioning of the heart. We have investigated the effect of β-adrenergic stimulation on $[Ca^{2+}]_{myo}$ under voltage clamp conditions. The degree of CaMKII mediated $I_{Ca,L}$ facilitation is kept identical to the control case discussed earlier. Besides a moderate CaMKII-mediated [228, 77] enhancement in $I_{Ca,L}$, we observe that increase in stim-

ulation frequency causes a strong β-adrenergic stimulation-dependent facilitation in $I_{Ca,L}$, resulting in an enhanced positive slope in the FFR as the stimulation frequency is increased. These results tend to agree with studies that show that increased cAMP levels reverse the abnormalities in the FFR that are found in end-stage heart failure [229], and that moderate stimulation by isoproterenol partly reverses the negative FFR found in NYHA (New York Heart Association) class IV (severe) type heart failure and preserves the positive FFR in nonfailing myocardium [230]. It is important to note that variations in experimental protocol could result in undesirable artifacts owing to the time-sensitive nature of the effects of cAMP [231]. Here, we show that the presence of maximal β-adrenergic stimulation results in a stronger positive FFR (frequency dependence of peak contractile force generated) at physiological stimulation frequencies.

At low ($<$ 2.5 Hz) stimulation frequencies β-adrenergic stimulation plays no role in altering intracellular Ca^{2+} dynamics. However, in the presence of maximal β-adrenergic stimulation (elevated levels of cAMP), an increase in stimulation rate ($>$ 2.5 Hz) causes increased up-regulation of $I_{Ca,L}$ [232, 233, 234]. The model predicts (Fig. 5.6A) that as the frequency of stimulation is increased in steps, peak $I_{Ca,L}$ magnitude increases at a regular rate, before declining at high stimulation frequencies ($>$ 8.0 Hz) as a result of incomplete channel recovery. As shown in Fig. 5.6B, as the frequency is increased from 2.5 Hz to 8.0 Hz, the peak SR Ca^{2+} content increases due to two mechanisms, namely cAMP-dependent enhancement of both trigger current and a rate-dependent increase in uptake by the SERCA pump as a result of a stronger decline in the average level of unphosphorylated PLB, which stimulates the uptake. It is important to note that although the increase in peak $[Ca^{2+}]_{myo}$ (traces in Fig. 5.6C) causes a strong CaM-mediated CaMKII-dependent up-regulation of the

SERCA pump due to an increase in PLB phosphorylation, cAMP-mediated phosphorylation of PLB causes further enhancement of the uptake mechanism. An increase in stimulation rate beyond 8.0 Hz, causes a decrease in SR Ca^{2+} content due to insufficient time for SR recovery along with a saturated operation of the SERCA pump. The presence of β-adrenergic stimulation significantly alters the relationship between the peak force response and the frequency of stimulation. As shown in the traces for force response in Fig. 5.7A, besides an increase in peak force generated (a result of increased peak $[Ca^{2+}]_{myo}$ (Figs. 5.6C and 5.7B)), β-adrenergic stimulation causes an increase in contraction and relaxation rate. This cAMP-mediated increase in the rate of sarcomere contraction and relaxation is a combined result of increasing rate of rise and decline of the Ca^{2+}-transient and a cAMP-mediated enhancement in rate kinetics governing cross-bridge formation. The inset in Fig. 5.7A is a plot of the maximum rate of relaxation (R_{relax}) versus maximum rate of contraction (R_{act}) for increasing stimulation frequency with and without β-adrenergic stimulation (shows significant overlap). This linear relationship highlights contraction-relaxation coupling, and represents a key intrinsic property of the contractile myofilaments [201]. As shown in Fig. 5.7B, although β-adrenergic stimulation further assists (due to the upregulation of $I_{Ca,L}$ and SERCA pump) a CaMKII-mediated rate-dependent increase in peak $[Ca^{2+}]_{myo}$, CaMKII is the key factor responsible for this behavior (a 2-fold increase in peak $[Ca^{2+}]_{myo}$ from 4 Hz to 8 Hz both in the presence/absence of cAMP-mediated effects). In the presence of β-adrenergic stimulation, Fig. 5.7C shows an enhancement in peak force generated and a decrease in minimum force as a result of a parallel trend in the peak systolic and end-diastolic levels of $[Ca^{2+}]_{myo}$ (Fig. 5.7B) supported by faster cross-bridge kinetics. The delta increment in force due to β-adrenergic stimulation (compared to the control case) is maximum at the stimula-

tion rate of 5 Hz (Fig. 5.7C) and decreases both above and below this frequency. The cAMP-mediated effect on the dependence of maximum sarcomere contraction (Fig. 5.7D) on stimulation frequency mirrors that of the peak force response (Fig. 5.7C) showing an opposite trend.

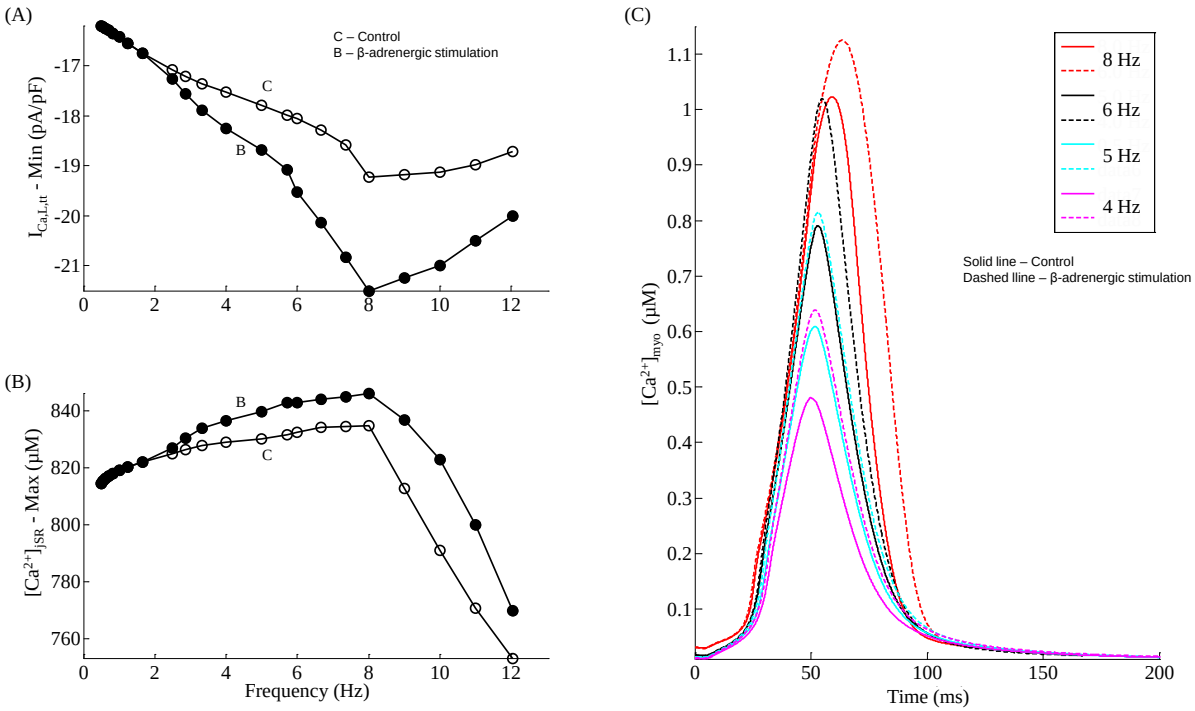

Figure 5.6 : A comparison between cAMP-mediated maximal β-adrenergic stimulation and basal condition. Voltage clamp protocol used is a 50 ms step pulse to 10 mv from a holding potential of -40 mv. (A) Rate dependence of peak $I_{Ca,L}$ current. (B) Frequency dependence of the maximum pre-release SR Ca^{2+} concentration. (C) $[Ca^{2+}]_{myo}$ traces showing rate-dependent effects on systolic Ca^{2+} concentration in the myoplasm for increasing stimulation frequencies from 4.0 Hz to 8.0 Hz.

5.3 Discussion

In this study, we have examined the role of two key mechanisms: (a) CaMKII-mediated upregulation; and (b) frequency-dependent cAMP-mediated β-adrenergic

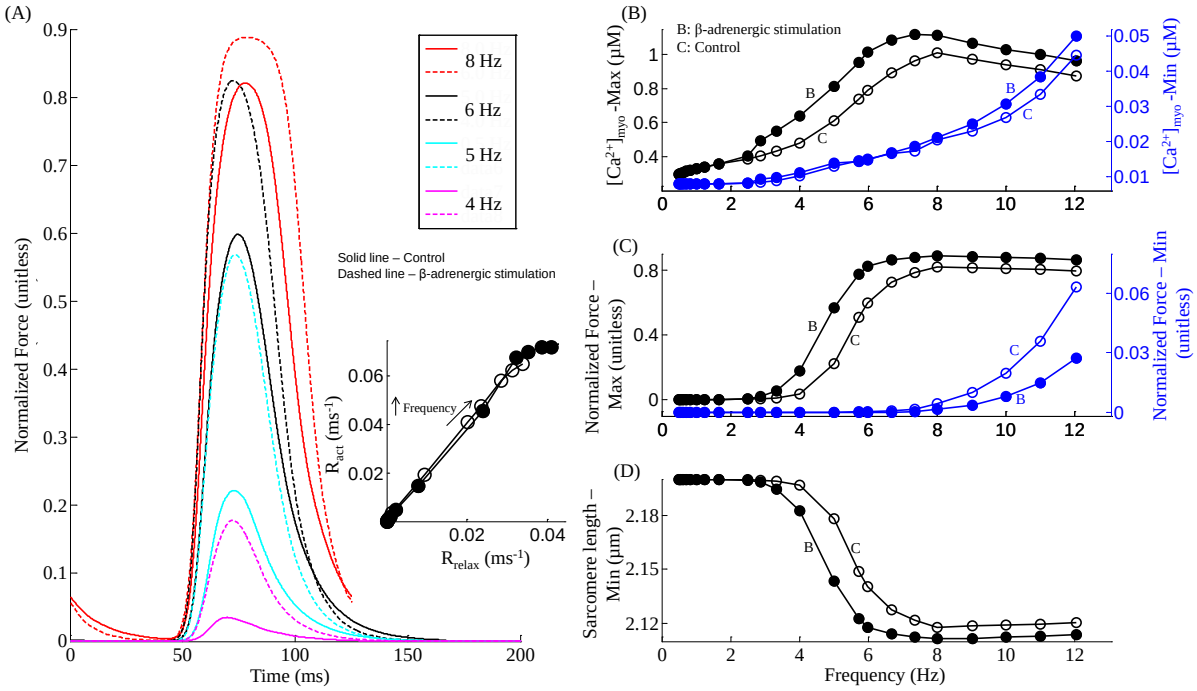

Figure 5.7 : A comparison between cAMP-mediated maximal β-adrenergic stimulation and basal condition. Voltage clamp protocol used is a 50 ms step pulse to 10 mv from a holding potential of -40 mv. (A) Traces for normalized isometric force developed for increasing stimulation frequencies from 4.0 Hz to 8.0 Hz. The inset shows a plot of the maximum rate of relaxation (R_{relax}) versus maximum rate of contraction (R_{act}) for increasing stimulation frequency. (B) The frequency dependence of the maximum and minimum myoplasmic Ca^{2+} concentration. (C) Rate Dependence of the maximum and minimum normalized force generated. (D) Frequency dependence of minimum sarcomere length achieved at peak contraction.

stimulation on Ca^{2+} cycling and their effect on the force-frequency response. In particular, we have modeled their two crucial signalling mechanisms: the rate-dependent upregulation of the DHP-sensitive $I_{Ca,L}$ channel [232, 78, 235, 236] and SERCA pump activity [237, 238], which our study suggests are the key factors responsible for the characteristics of FFR in rat ventricular myocytes. These two signalling pathways mediate $I_{Ca,L}$ enhancement bringing an extra supply of trigger current into the dyad to both enhance CICR and assist in a rate-dependent build up in pre-release diastolic

SR Ca^{2+} concentration. This frequency-dependent increase in SR Ca^{2+} content is strongly assisted by a β-adrenergic stimulation-dependent cAMP-mediated increase in PLB phosphorylation, which relieves the inhibition exerted on the SERCA pump. This is especially important in the light of decreasing time for Ca^{2+} uptake with increasing stimulation rate.

We have systematically analyzed the important role of Ca^{2+}-dependent CaM-mediated function of CaMKII and CaN as rate sensors. CaMKII is known to regulate EC coupling [110, 119] and has substrates in both the dyadic domain ($I_{Ca,L}$ and I_{ryr}) [89, 119] as well as the myoplasm (phospholamban) [46], and immunoprecipitates with the $I_{Ca,L}$ channel [89] and RyR [239]. Our study confirms that activated-CaMKII causes rate-dependent acceleration of relaxation [148] both by direct phosphorylation of the SERCA pump as well as phosphorylation of PLB resulting in a decreased inhibition of the SERCA pump. Although the time course of the indirect effect of CaMKII via PLB phosphorylation is reported to be delayed with regard to frequency-dependent acceleration of relaxation [240], the direct phosphorylation of the SERCA pump by activated-CaMKII could cause an immediate increase in maximal pumping rate [149, 77]. Despite poor sensitivity of CaMKII to myoplasmic Ca^{2+} signals due to its relatively low affinity for CaM and an inadequate supply of myoplasmic Ca^{2+}-CaM complex (compared to the dyad), activated-CaMKII in the cytosol plays an important role in the enhancement of uptake via the SERCA pump except at high (> 8 Hz, inset in Fig. 5.3A) stimulation frequencies. Here, the rapid decrease in time available for uptake results in gradually declining pre-release SR Ca^{2+} content. CaMKII has a more critical role in the dyadic cleft where we show [48] substantial CaMKII activity owing to large local Ca^{2+} concentration and CaM enrichment. It is reported that frequency-dependent CaMKII activity contributes to $I_{Ca,L}$ channel facilitation [87]

and assists a positive force-frequency relationship [47]. Our study shows that CaMKII causes a significant enhancement of $I_{Ca,L}$ even under basal conditions (absence of β-adrenergic stimulation) as the stimulation frequency is increased to 8.0 Hz (Fig. 5.1B), beyond which incomplete recovery begins to cause a decline in peak $I_{Ca,L}$. A rate-dependent increase in SR Ca^{2+} content can be achieved only when the CaMKII-mediated (Fig.5.1C) increase in trigger current (Fig.5.1B) is supported by an increase in uptake via the SERCA pump by activated-CaMKII in the myoplasm (Fig. 5.3C) which enhances PLB phosphorylation. CaMKII fails to sustain a positive FFR at very high ($>$ 8.0 Hz) stimulation frequencies due to incomplete channel recovery causing a decline in trigger current and subsequently SR Ca^{2+} content. Data from atrial myocytes [241] show that myoplasmic CaN is also found to be responsive to increased pacing frequency.

Although CaN is also involved in $I_{Ca,L}$ enhancement in the dyad at low ($<$ 2.0 Hz) stimulation frequencies, at high stimulation rates ($>$ 2.0 Hz), the large Ca^{2+} signals along with very slow dissociation of the Ca_4CaM-CaN complex force it to be constitutively active, limiting its modulatory role. The presence of β-adrenergic stimulation, which also supports a sustained frequency-dependent increase in $I_{Ca,L}$ (Fig. 5.6A) and SERCA activity (Fig. 5.6B) results in enhanced contractile response (Fig. 5.7A and C).

Here, we have integrated an electro-mechanical model with our electrophysiological model of a rat ventricular myocyte [66] to describe isometric contractile force generated by myofibrils and investigate its rate-dependent characteristics. Our model for the cardiac contractile mechanism is derived from the description of cooperative activation and cross-bridge cycling given by Rice et al [1]. However, we have incorporated a rate-dependent cAMP mediated enhancement in cross-bridge kinetics which

is shown to be responsible for sustaining linear contraction-relaxation coupling (inset in Fig. 5.7A) at increasing frequencies. It is important to note that the presence of CaMKII-mediated $I_{Ca,L}$ enhancement or β-adrenergic stimulation results in physiologically relevant rate-dependent increase in peak cardiac contractile force (positive FFR).

5.3.1 Model Limitations

(a) This model of a rat ventricular myocyte is limited to Ca^{2+} related channel, exchanger and pumps ($I_{Ca,L}$, I_{NaCa}, I_{PMCA}, I_{ryr} and SERCA pump), while lacking exclusive Na^{+} or K^{+} related channels and transporters. Hence, it is aimed at mimicking voltage clamp conditions where channels other than calcium are blocked, and it cannot be used to study any action potential-induced Ca^{2+} transient-frequency relationship. However, its focus on the Ca^{2+} dynamics alone allows one to comprehend more clearly the important role of various Ca^{2+}-dependent regulatory proteins such as CaMKII, CaN, PLB and cAMP in affecting multiple targets and thus generating a cell's response to a change in the frequency of stimulation.

(b) It is known that CaMKII alters the function of numerous ion channels and Ca^{2+} regulatory targets in a rate-dependent fashion. However, disparate findings exist on its modulation of targets such as the SERCA [242, 243] and RyR channel [118, 122, 110]. Although our model aligns with rate-dependent CaN-mediated inhibition of the SERCA pump, its role in modulating SERCA activity is controversial due to conflicting findings [153, 152]. Similarly, the effect of β-adrenergic stimulation via cAMP particularly, its dose-dependent influence on L-Type Ca^{2+}

channels both in terms of modifying the single channel behavior such as Ca^{2+} ion permeability (channel conductance) as well as overall channel recruitment characteristics (open probability) is not clearly understood. While cAMP has been shown to increase channel open probability [98, 99], increased levels of cAMP also result in increased phosphorylation of L-type Ca^{2+} channels, causing an increased permeability to Ca^{2+} ions [100, 101, 99]. Although we have modeled enhancement in $I_{Ca,L}$ due to beta-adrenergic stimulation solely by a rate-dependent cAMP-mediated increase in channel conductance, the relative contribution of these factors to cAMP-dependent $I_{Ca,L}$ enhancement has to be examined further. A detailed investigation is required to clarify the nature of these interactions. We hope that this study would help motivate more pointed experimental investigation of frequency-dependent CaMKII, CaN and cAMP effects on FFR in rat ventricular myocytes.

(c) The effect of β-adrenergic stimulation on cardiac Na^{+}/Ca^{2+} exchange has been controversial. Perchenet et al [244] report an enhancement in Na^{+}/Ca^{2+} exchange by the β-adrenergic/PKA-mediated phosphorylation of the exchanger protein. However, a cAMP-mediated enhancement in NCX activity would impede rate dependent increase in SR Ca^{2+} content. We base our model for the Na^{+}/Ca^{2+} exchanger on a more recent study by Lin et al [245] which supports the view that β-adrenergic stimulation does not upregulate Na^{+}/Ca^{2+} exchange current.

(d) The cooperative activation of the thin filament and the strain-dependent transitions of the cross-bridge cycle have been approximately modeled as non-spatial, state-variables. However, this simplification is valid as these transitions are in-

herently local phenomena and the model reproduces a wide range of steady state and dynamic responses in cardiac muscle [1].

5.4 Conclusion

Using a mathematical model of an isolated rat ventricular myocyte in a voltage clamp setting, we have systematically examined the issue of rate-dependence in the proper functioning of the dyadic coupling unit, the regulation of SERCA function to provide adequate SR Ca^{2+} content, the peak amplitude of the myoplasmic Ca^{2+} transient and the complex interaction of all these factors. Given the complexity of these interacting systems, computer modeling gives an insight into the relative roles of different Ca^{2+} transport mechanisms. Our simulations explain the Ca^{2+}-dependent, CaM-mediated, rate sensitive effects of CaMKII and CaN on various intracellular targets. We also investigate a significant, frequency-dependent, cAMP-mediated effect of β-adrenergic stimulation and its modulatory influence on the $I_{Ca,L}$ channel as well as the SERCA pump. Rate-dependent CaMKII mediated $I_{Ca,L}$ facilitation as well as cAMP-dependent upregulation of intracellular targets could play a vital role in reversing the negative FFR found in failing hearts. However, further studies are required to develop a clear understanding of the relative role of CaMKII and cAMP in the rate-dependent up-regulation of various intra-cellular targets especially the DHP-sensitive $I_{Ca,L}$ channel. This would help in assigning rate-dependent weights to these signalling pathways. One could use KN-93 and autocamtide-2 related inhibitory peptide [246] for a study to delineate these effects. Our coupled electro-physiological and electro-mechanical model also sheds light on the rate dependence of the cardiac contractile mechanism. In particular, our model accounts for cAMP-dependent modulation of the rate kinetics governing cross-bridge formation. In agreement with Janssen [211],

we also demonstrate a key linear relationship between the rate of contraction and relaxation, which is shown here to be intrinsically coupled over the full range of physiological frequencies both in the absence/presence of β-adrenergic stimulation. This study provides mechanistic, biophysically based explanations for the rate-dependent Ca^{2+} signalling underlying the force-frequency response in rat ventricular myocytes, generating useful and testable hypotheses.

Chapter 6

Conclusion

We have developed a composite multiphysics model of a rat ventricular myocyte which includes a detailed description of Ca^{2+} dynamics under voltage clamp conditions and cardiac electromechanics, based on experimental data [66, 1]. Here, we summarize the significant contributions and discuss the implications of this study.

- Our mathematical model includes the most extensive description available of a novel feature, namely the luminal Ca^{2+} sensor in the junctional SR which describes the protein-protein interaction between triadin/junctin, calsequestrin and the RyR channel. The luminal sensor imparts the much needed refractoriness to the Ry-sensitive Ca^{2+} release channel. This element is critical in providing realistic fits to cytosolic Ca^{2+} transients and an adequate refilling time for the SR Ca^{2+} stores. Our voltage-clamp simulations demonstrate graded Ca^{2+} transients with sufficient gain, as well as quantification of Ca^{2+} balances for all external and internal Ca^{2+} fluxes. Our model of the dyadic coupling unit (DCU) provides mechanistic explanations of the major input-output relationship for CICR, as well as its modulation by trigger current (clamp voltage). The variety of experiments emulated in this study demonstrates that the model has long-term stability in regulating cytosolic Ca^{2+}. It also provides biophysically based insights into regulatory mechanisms underlying whole-cell responses to Ca^{2+} perturbation. The model helps generate a new hypotheses with regards to the under-expression of triadin/junctin resulting in a malfunctioning luminal sensor, which could affect long-term Ca^{2+} stability of the cell, and/or changes

in the refractoriness of the RyR Ca^{2+} channel affecting the integrity of CICR under a variety of conditions.

• We have investigated the role of different factors including the myoplasmic $[Ca^{2+}]_{myo}$ transient and the sarcomeric length in influencing various types of twitch responses obtained under different loading conditions (including isosarcometric, isometric and unloaded conditions). Various control loops influencing cell shortening have been explored. In particular, the bidirectional interaction of the Ca^{2+} transient with the myofilament contractile mechanism and the importance of indirect SR mediated interaction of the sarcolemma with the contractile machinery is highlighted by showing the regulation of isometric contraction by the degree of NCX activity. The effect of temperature on cell shortening is investigated identifying the differential sensitivity of the $[Ca^{2+}]_{myo}$ transient and the myofilament contractile mechanism. The important role of myofilament Ca^{2+} sensitivity in force generation is studied with particular emphasis on the effect of β-adrenergic stimulation on cardiac contractile response. In agreement with Janssen [211], we also demonstrate a key linear relationship between the rate of contraction and relaxation, which is shown here to be intrinsically coupled over the full range of physiological perturbations (including temperature, sarcomeric length, activator Ca^{2+}, and isoproterenol).

• We have systematically examined the issue of rate-dependence in the proper functioning of the dyadic coupling unit, the regulation of SERCA function to provide adequate SR Ca^{2+} content, the peak amplitude of the myoplasmic Ca^{2+} transient and the complex interaction of all these factors. Our simulations explain the Ca^{2+}-dependent, CaM-mediated, rate sensitive effects of CaMKII and CaN on various intracellular targets. We also investigate a significant, frequency-dependent, cAMP-mediated effect of β-adrenergic stimulation and its modulatory influence on the $I_{Ca,L}$

channel as well as the SERCA pump. Rate-dependent CaMKII mediated $I_{Ca,L}$ facilitation as well as cAMP-dependent upregulation of intracellular targets could play a vital role in reversing the negative FFR found in failing hearts. Our coupled electro-physiological and electro-mechanical model also sheds light on the rate dependence of the cardiac contractile mechanism. In particular, our model accounts for cAMP-dependent modulation of the rate kinetics governing cross-bridge formation. We demonstrate contraction-relaxation coupling over the full range of physiological frequencies both in the absence/presence of β-adrenergic stimulation. This study provides mechanistic, biophysically based explanation for the rate-dependent Ca^{2+} signalling underlying the force-frequency response in rat ventricular myocytes.

Future Work: Exciting venues exist for advancing this study. Few of the directions with immediate clinical relevance are listed here:

1. Inclusion of the description of Na^+ and K^+ related channels and transporters in the model along with their neurohumoral regulation would enable producing a realistic cardiac action potential (preliminary modeling results shown in Fig. 6.1) and the subsequent CICR and myofilament contraction. Such a model could be used to investigate a wide variety of cardiac pathogenesis.

2. Integrating mitochondrial energetics into models of cardiomyocyte function is the natural step forward to understand heart physiology and pathophysiology. When combined with a model of the AP, a comprehensive formulation of mitochondrial energetics, could help develop a better understanding of the three major conditions leading to acute ischemia: elevated $[K^+]_o$, acidosis and anoxia. It could also provide valuable insight into arrhythmias arising from Ca^{2+} overload during ischemia and reperfusion-induced arrhythmias.

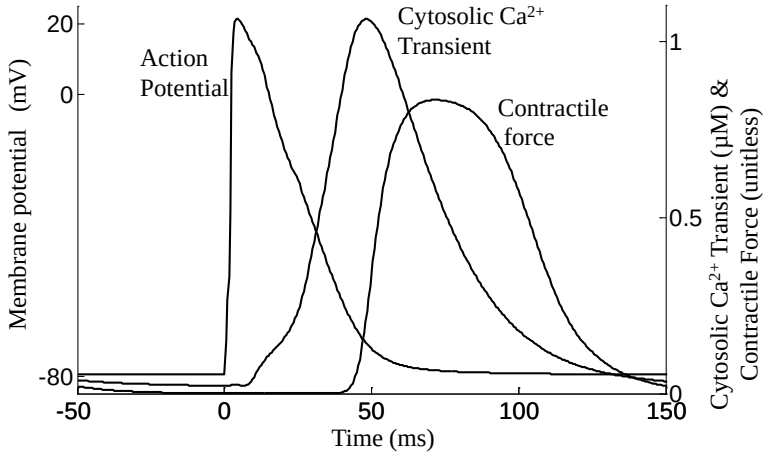

Figure 6.1 : Model generated traces of an action potential from a rat ventricular myocyte and a corresponding cytosolic Ca^{2+} transient and the isometric force developed.

3. Muscle contraction is not completely understood. There are several proteins that influence muscle contraction whose role is not clear yet. For example, molecules such as titin, an unusually long protein spanning sarcomeres in vertebrates which appears to bind to actin is not well characterized. In addition, there have been reports of muscle cells that behave in ways that do not match our current understanding of them. For example, some myocytes exhibit plasticity and generate force for long periods, a poorly understood phenomenon sometimes called "catch-tension" or force hysteresis [247]. Modeling could provide valuable insights into these phenomena effecting tension development.

Studying these and other aspects of cardiac myocytes are exciting avenues for biologists and computational scientists alike. Ultimately, this research can help us better understand and treat cardiac disorders.

Appendix A

Abbreviations

Abbreviations

APD = Action potential duration;

ATP = Adenosine triphosphate;

$[Ca^{2+}]$= calcium ion concentration;

$[Ca^{2+}]_{dhp}$ = Ca^{2+} concentration at the mouth of the DHP-sensitive $I_{Ca,L}$ channel;

$[Ca^{2+}]_{dyad}$ = spatial Ca^{2+} concentration in the dyad;

$[Ca^{2+}]_{jSR}$ = luminal Ca^{2+} concentration in the jSR;

$[Ca^{2+}]_{LSR}$ = Ca^{2+} concentration in the LSR;

$[Ca^{2+}]_{myo}$ = cytosolic Ca^{2+} concentration;

$[Ca^{2+}]_{serca}$ = Ca^{2+} concentration buffered by the SERCA protein;

$[Ca^{2+}]_{o}$ = extracellular Ca^{2+} concentration;

$[Ca^{2+}]_{ryr}$ = Ca^{2+} concentration at the "mouth" of the RyR channel on the dyadic side;

CaCM = Ca^{2+} bound calmodulin;

CaF3 = Ca^{2+} bound to the buffer Fluo3;

CaM = calmodulin;

CaMKII = Ca^{2+}/calmodulin-dependent protein kinase II;

$CaMKII_{act}$ = activated Ca^{2+}/calmodulin-dependent protein kinase II;

CaN = calcineurin;

CaN_{act} = activated calcineurin;

CDF = calcium dependent facilitation;

CDI = calcium dependent inactivation;

CF = caffeine;

CICR = calcium-induced calcium-release;

CRCP = contraction-relaxation coupling point;

CS = calsequestrin;

$[Cs^+]_{myo}$ = Cs^+ concentration in the cytosol;

$[Cs^+]_{dyad}$ = Cs^+ concentration in the dyadic space;

DCU = dyadic coupling unit;

DHP = dihydropyridine;

DHPR = dihydropyridine receptor;

E-C = excitation-contraction;

ECC = excitation-contraction coupling;

EC_{50} = half maximal effective concentration;

EC_{50}^{bwd} = affinity of backward Ca^{2+} flux from LSR to cytosol;

EC_{50}^{fwd} = affinity of forward Ca^{2+} flux from cytosol to LSR;

F-Ca = force versus Ca^{2+};

FFR = force frequency response;

FRCRSFa = Phe-Arg-Cys-Arg-Ser-Phe-CONH2;

F-SL = force versus sarcomere length;

$I_{Ca,L}$ = L-type Ca^{2+} current;

$I_{Ca,L,SL}$ = sarcolemmal component of the $I_{Ca,L}$ channel current;

$I_{Ca,L,TT}$ = $I_{Ca,L}$ channel facing the dyadic space;

I_{Cs} = cesium current through the $I_{Ca,L}$ channel;

$I_{cyt,serca} = Ca^{2+}$ uptake current directed from the cytosol to the SERCA;

I_{Na} = sodium current through the $I_{Ca,L}$ channel;

$I_{Na,b}$ = background sodium current;

I_{NaCa} = sodium calcium exchanger current;

$I_{NaCa,SL}$ = sarcolemmal component of the I_{NaCa} exchanger current;

$I_{NaCa,TT} = I_{NaCa}$ exchanger facing the dyadic space;

I_{NaCs} = sodium cesium pump current;

I_{PMCA} = plasma membrane Ca^{2+} ATPase pump current;

$I_{ryr} = Ca^{2+}$ current due to CICR from an individual jSR;

$I_{serca,sr} = Ca^{2+}$ uptake current directed from the SERCA to the LSR;

ISO = Isoproterenol;

$I_{tr} = Ca^{2+}$ current due to concentration gradient driven Ca^{2+} transport from LSR to jSR;

jSR = junctional portion of the sarcoplasmic reticulum;

k_d = dissociation constant;

k_{mp} = half saturation constant for the sarcolemmal Ca^{2+} pump;

KSE = stiffness coefficient of the non-contractile series elastic element;

LCC = L-type DHP-sensitive Ca^{2+} channel;

L-type = long lasting type;

LSR = longitudinal portion of the sarcoplasmic reticulum;

MCS = myofilament Ca^{2+} sensitivity;

μm = micro meter;

μM = micro molar;

mM = milli molar;

mV = milli volt;

$[Na^+]_{dyad}$ = Na^+ concentration in the dyadic space;

$[Na^+]_{myo}$ = Na^+ concentration in the cytosol;

NCX = Na^+/Ca^{2+} exchanger;

nM = nano molar;

NO = Nitric oxide;

O_c = fractional occupancy of calmodulin by Ca^{2+} in the cytosol;

O_{calse} = fractional occupancy of calsequestrin by Ca^{2+} in the jSR;

ODE = ordinary differential equation;

O_{tc} = fractional occupancy of troponin-Ca sites by Ca^{2+} in the cytosol;

O_{tmgc} = fractional ocupancy of troponin-Mg sites by Ca^{2+} in the cytosol;

O_{tmgmg} = fractional occupancy of troponin-Mg sites by Mg^{2+} in the cytosol;

pA/pF = pico amps per pico farad;

pC = pico coulomb;

P_o = Open probability;

PKA = protein kinase A;

PLB = phospholamban;

PLB_{dp} = Unphosphorylated phospholamban;

PLB_p = phosphorylated phospholamban;

PSR = phospholamban to SERCA ratio;

RT_{50} = time required for 50% sarcomere relaxation;

$RT_{50,C}$ = time required for 50% decline in Ca^{2+}-transient;

$RT_{50,F}$ = time required for 50% decline in force response;

$RT_{50,I}$ = time required for 50% $I_{Ca,L}$ inactivation;

Ry = ryanodine;

RyR = ryanodine receptor;

SERCA = sarcoplasmic reticulum Ca^{2+} ATPase;

SL = sarcomere length;

SR = sarcoplasmic reticulum;

Tc = Ca^{2+}-specific troponin binding site;

TD_{50} = time taken from 50% activation to 50% relaxation;

TnC = Troponin C;

TnI = Troponin I;

TnI_u = fraction of unphosphorylated Troponin I;

TTP = time required to attain peak value;

T-tubule = transverse tubules;

TT = transverse tubules;

VC = voltage clamp;

VDI = voltage dependent inactivation; XIP = Exchanger inhibitory peptide;

Appendix B

Tables

Table B.1 : Surface area of various plasma membranes in the cell

Variable	Description	Value
$A_{Ext.SL}$	Surface area of external SL	11.4×10^3 μm^2
A_{TT}	Surface area of T-tubule	5.52×10^3 μm^2
A_{TotSL}	Surface area of total SL (including external SL and T-tubule)	16.9×10^3 μm^2 (*)
$A_{JunctExt.SL}$	Surface area of junctional external SL	0.846×10^3 μm^2
$A_{JunctTT}$	Surface area of junctional T-tubule	2.54×10^3 μm^2
$A_{TotJunct}$	Surface area of total junctional plasma membrane	3.39×10^3 μm^2
$A_{JunctSR}$	Surface area of junctional SR	6.99×10^3 μm^2
A_{LongSR}	Surface area of longitudinal SR	36.8×10^3 μm^2
A_{TotSR}	Surface area of total SR	43.8×10^3 μm^2

*Electrical capacitance of the cell membrane = 169 pF (using 1 $\mu F/cm^2$). All the above parameters are derived from Bers [55].

Table B.2 : Parameters used to model ion transport across the sarcolemmal membrane

Parameter	Definition	Value	References
F	Faraday's constant	96485 $coul \cdot mol^{-1}$	—
R	Ideal gas constant	8314 $mJ \cdot mol^{-1} \cdot K^{-1}$	—
T	Absolute temperature	290 K	Measured
$[Ca^{2+}]_o$	Extracellular Ca^{2+} concentration	1.0 mM	Measured
$[Na^{+}]_o$	Extracellular Na^{+} concentration	140.0 mM	Measured
$[Cs^{+}]_o$	Extracellular Cs^{+} concentration	3.0 mM	Measured
Z_{Na}, Z_{Cs}	Valence of Na^{+} and Cs^{+} ions	1.0	—
Z_{Ca}, Z_{Ba}	Valence of Ca^{2+} and Ba^{2+} ions	2.0	—
P_{Ca}	Permeability of L-Type calcium channel to Ca^{2+}	6.7367×10^{-9} $\mu L \cdot s^{-1}$	[86]*
P_{Na}	Permeability of L-Type calcium channel to Na^{+}	8.0355×10^{-11} $\mu L \cdot s^{-1}$	[86]*
P_{Cs}	Permeability of L-Type calcium channel to Cs^{+}	6.2088×10^{-11} $\mu L \cdot s^{-1}$	[86]*
K_{mAllo}	Dissociation constant for allosteric Ca^{2+} activation	125×10^{-6} mM	[156]*
K_{mCao}	Dissociation constant for extracellular Ca^{2+}	1.14 mM	[156]*
K_{mCai}	Dissociation constant for intracellular Ca^{2+}	0.0036 mM	[248]*
K_{mNao}	Dissociation constant for extracellular Na^{+}	87.5 mM	[155]*
K_{mNai}	Dissociation constant for intracellular Na^{+}	12.3 mM	[156]*
V_{max}	Maximum Na^{+}/Ca^{+} exchange current	776.2392 pA	[156]‡
k_{mpca}	Half saturation constant for the SL Ca^{2+} pump	0.5 μM	[86]*
$\overline{I}_{PMCA}$	Maximum sarcolemmal Ca^{2+} pump current	1.15 pA	[86]*
k_{mcs}	Dissociation constant for extracellular Cs^{+}	1.5×10^{3} μM	[165, 163, 159,
k_{mna}	Dissociation constant for intracellular Na^{+}	2.14×10^{5} μM	[165, 163, 159,
$\overline{I}_{NaCs}$	Maximum Na^{+}/Cs^{+} pump current	147.3 pA	[165, 163, 159,
G_{Nab}	Maximum background Na^{+} current conductance	0.00141 nS	[86]*
R_a	Mean access resistance of the tubular system	20.0 $k\Omega$	[249]*

Parameters used to model the transmembrane currents $I_{Ca,L}$, I_{NaCa}, I_{PMCA}, I_{NaCs} and the background sodium current $I_{Na,b}$. Adopted (*) or estimated (‡) from the cited sources.

Table B.3 : Parameters used to model intracellular ion transport

Parameter	Definition	Value	References
k_{12}^{PLB}	rate of PLB_{dp} phosphorylation	6800 s^{-1}	[147]*
k_{21}^{PLB}	rate of PLB_{p} dephosphorylation	1000 s^{-1}	[147]*
$K_{cyt,serca}$	Maximal binding/release rate of Ca^{2+} from cytosol to SERCA	6250 s^{-1}	[147]*
$K_{serca,sr}$	Maximal binding/release rate of Ca^{2+} from SERCA to LSR	6.25 s^{-1}	[147]*
$SERCA_{tot}$	Total amount of SERCA	47.0 μM	[147]*
PSR	Phospholamban to SERCA ratio	1.0	[147]*
PKA_{act}	Relative regulatory activity of PKA	0.1	[147]†
τ_{tr}	Time const. for transfer of Ca^{2+} from LSR to jSR	7.0×10^{-3} s	[86]‡
τ_{Na}	Time const. for transfer of Na^{+} from dyad to myoplasm	1.0×10^{-3} s	[86]‡
τ_{Cs}	Time const. for transfer of Cs^{+} from dyad to myoplasm	6.0×10^{-3} s	[86]‡
P_{ryr}	Permeability of the RyR channel	1.714×10^{-7} $\mu L \cdot s^{-1}$	[83, 84, 38]‡
D_{Ca}	Diffusion constant for Ca^{2+} in the dyadic space	100.0 $\mu m^2 s^{-1}$	[250]*
N_h	Density of high-affinity Ca^{2+} binding sites	200.0 μM	[250]‡
N_l	Density of low-affinity Ca^{2+} binding sites	16.0 μM	[250]‡
K_l	Half-saturation value of low-affinity Ca^{2+} binding site	1100.0 μM	[250]*
K_h	Half-saturation value of high-affinity Ca^{2+} binding site	13.0 μM	[250]*
$[Mg^{2+}]_{myo}$	Intracellular Mg^{2+} concentration	634 μM	[251]*
$[fluo3]_{tot}$	total concentration of indicator dye	100.0 μM	Measured
k_{fluo3}^{+}	association rate of Ca^{2+} binding to dye fluo-3	80 $\mu M^{-1} \cdot s^{-1}$	[252]*
k_{fluo3}^{-}	dissociation rate of Ca^{2+} binding to dye fluo-3	90 s^{-1}	[252]*

Parameters used to model the intracellular ion transport $I_{cyt,serca}$, $I_{serca.sr}$, I_{tr}, I_{RyR}, and Ca^{2+} diffusion/buffering. Adopted (*), derived (†) or estimated (‡) from the cited sources.

Table B.4 : Parameters used to model sub-cellular morphology

Parameter	Definition	Value	References
N_{dyad}	Number of dyadic units	10000	[33]‡
V_{myo}	Myoplasmic volume	5.3581×10^{-2} nL	[55]†
V_{LSR}	Longitudinal SR volume	1.1776×10^{-3} nL	[55]*
$\sum_{Ndyad} V_{jSR}$	Total junctional SR volume	1.104×10^{-4} nL	[55]*
Δr	Step size in the 'r' direction	10 nm	Numerical solution†
d	Diameter of the cylindrical cleft space in the 'r' direction	400 nm	[250, 33, 253, 188, 31]‡
Δz	Step size in the 'z' direction	0.76 nm	Numerical solution†
h	Length of the cylindrical cleft space in the 'z' direction	15.2 nm	[250, 33, 253, 188, 31]‡
V_{cleft}	Volume of a unit dyadic space	1.91×10^{-9} nL	—

Adopted (*), derived (†) or estimated (‡) from the cited sources.

Table B.5 : Initial Conditions

State variable	Definition	Initial Value
$[Ca^{2+}]_{myo}$	Ca^{2+} concentration in the myoplasm	$8.1027 \times 10^{-5}\ mM$
$[Ca^{2+}]_{jSR}$	Ca^{2+} concentration in jSR	$1.2677\ mM$
$[Ca^{2+}]_{LSR}$	Ca^{2+} concentration in LSR	$1.3346\ mM$
$[Na^{+}]_{myo}$	Na^{+} concentration in myoplasm	$16.746\ mM$
$[Na^{+}]_{dyad}$	Na^{+} concentration in dyadic space	$16.321\ mM$
$[Cs^{+}]_{myo}$	Cs^{+} concentration in myoplasm	$140.2154\ mM$
$[Cs^{+}]_{dyad}$	Cs^{+} concentration in dyadic space	$140.2157\ mM$
O_c	Fractional occupancy of Calmodulin by Ca^{2+}	0.033091
O_{tc}	Fractional occupancy of Troponin by Ca^{2+}	0.016049
O_{tmgc}	Fractional occupancy of Troponin by Mg^{2+} and Ca^{2+}	0.321764
O_{tmgmg}	Fractional occupancy of Troponin by Mg^{2+}	0.598385
$[CaF3]$	Concentration of Fluo3-Ca^{2+} complex	$21.88721\ \mu M$
$C1_{ryr}$	Closed (resting) state of RyR channel	0.9990953
$O2_{ryr}$	Open (activated) state of RyR channel	1.03668×10^{-9}
$C3_{ryr}$	Inactivated state of RyR channel	9.38711×10^{-13}
$C1_{dhpr}$	Closed (resting) state of DHPR sensitive Ca^{2+} channel	0.1673614
$O2_{dhpr}$	Open (activated) state of DHPR sensitive Ca^{2+} channel	1.499173×10^{-3}
$O3_{dhpr}$	Open (activated) state of DHPR sensitive Ca^{2+} channel	3.300291×10^{-3}
$C4_{dhpr}$	Closed (resting) state of DHPR sensitive Ca^{2+} channel	7.478058×10^{-8}
$C6_{dhpr}$	Closed (resting) state of DHPR sensitive Ca^{2+} channel	7.478058×10^{-8}
$A1_{ls}$	Fraction of Tr/J bound to RyR	0.6709816
$I2_{ls}$	Fraction of Tr/J bound to RyR and Calsequestrin	0.155258
$I3_{ls}$	Fraction of Tr/J bound only to Calsequestrin	0.0623695
$B6_{ls}$	Fraction Calsequestrin bound to Ca^{2+}	0.619346

Table B.6 : Initial Conditions (Contd.)

State variable	Definition	Initial Value
$[Ca^{2+}]_{serca}$	Ca bound to the serca protein	$36.0637 \times 10^{-5} \mu M$
$S2_{dhpr}$	Fraction of IQ Motif bound to Ca_4CaM	6.816729×10^{-2}
PLB_{dp}	Fraction of unphosphorylated Phospholamban	7.684160×10^{-2}
Ca_2CaM	2 Ca^{2+} ions bound to C-terminus of CaM	34.56529
Ca_4CaM	4 Ca^{2+} ions bound to C & N terminus of CaM	8.635052×10^{-2}
$CaMB$	Buffered CaM	7.563836×10^{-2}
Ca_2CaMB	Buffered Ca_2CaM	2.035086
Ca_4CaMB	Buffered Ca_4CaM	1.288455×10^{-6}
P_1	Fraction of inactive dephosphorylated CaMKII in Ca_2CaM bound state	5.527608×10^{-1}
P_3	Fraction of active dephosphorylated CaMKII in Ca_4CaM bound state	3.661260×10^{-1}
P_6	Fraction of active Thr^{287}-autophosphorylated but CaM autonomous CaMKII	1.314410×10^{-3}
P_5	Fraction of active Thr^{287}-autophosphorylated but Ca2CaM bound CaMKII	6.277911×10^{-7}
P_4	Fraction of active Thr^{287}-autophosphorylated but Ca4CaM trapped CaMKII	9.121920×10^{-8}
Ca_4CaN	CaN bound to 4 Ca^{2+} ions	$2.606246 \times 10^{-4} \mu M$
$CaMCaN$	CaN bound to CaM	$4.348535 \times 10^{-3} \mu M$
$Ca_2CaMCaN$	CaN bound to 2 Ca^{2+} ions and CaM	$1.419613 \times 10^{-1} \mu M$
$Ca_4CaMCaN$	CaN bound to 4 Ca^{2+} ions and CaM	$3.473412 \mu M$
$[Ca^{2+}]_{dyad}$	Ca^{2+} concentration in the dyadic space	$9.012 \times 10^{-5}\ mM$

Table B.7 : Parameters used in the luminal sensor model

Rate Constant	Value	Rate Constant	Value
k_{12}^{ls}	88.16	k_{23}^{ls}	57.9
k_{21}^{ls}	4.1	k_{32}^{ls}	2.42
k_{14}^{ls}	0.5	k_{35}^{ls}	150.3
k_{41}^{ls}	85.7	k_{53}^{ls}	25.5
k_{42}^{ls}	2.98	k_{52}^{ls}	88.16
k_{43}^{ls}	25.5	k_{56}^{ls}	1.2
k_{34}^{ls}	150.3	k_{65}^{ls}	401.7

Table B.8 : Rate constants used to model Ca/CaM binding and CaM buffering

Rate Constant	Value	Rate Constant	Value
k_{02}^{CM}	$4.8387^{\ddagger}$	k_{42B}^{CM}	k_{42}^{CM}
k_{20}^{CM}	10.0^{*}	k_{0Bon}^{CM}	$3.5 \times 10^{-4\ddagger}$
k_{24}^{CM}	$3.4722^{\ddagger}$	k_{0Boff}^{CM}	$1.4 \times 10^{-6\ddagger}$
k_{42}^{CM}	500.0^{*}	k_{2Bon}^{CM}	k_{0Bon}^{CM}
k_{02B}^{CM}	k_{02}^{CM}	k_{2Boff}^{CM}	k_{0Boff}^{CM}
k_{20B}^{CM}	$k_{20}^{CM}/100$	k_{4Bon}^{CM}	k_{0Bon}^{CM}
k_{24B}^{CM}	k_{24}^{CM}	k_{4Boff}^{CM}	k_{0Boff}^{CM}

All the above parameters are adopted (*) or estimated (‡) from Saucerman et. al. [48]

Table B.9 : Rate constants used to model Ca/CaM/CaMKII interactions

Rate Constant	Value	Rate Constant	Value
k_{PP1}	1.72	k_{32}^{CK}	2.2
k_{mPP1}	11.5	k_{45}^{CK}	3.35×10^{-3}
k_{21}^{CK}	65.67164	k_{54}^{CK}	3.4722
k_{12}^{CK}	328.3582	k_{46}^{CK}	2.2×10^{-3}
k_{13}^{CK}	3.4722	k_{64}^{CK}	65.67164
k_{31}^{CK}	3.35	k_{56}^{CK}	328.3582
k_{23}^{CK}	65.67164	k_{65}^{CK}	65.67164

All the above parameters are adopted from Saucerman et. al. [48]

Table B.10 : Rate constants used to model Ca/CaM/CaN interactions

Rate Constant	Value	Rate Constant	Value
k_{Caon}^{CN}	2.0	k_{0on}^{CN}	46.0
k_{Caoff}^{CN}	1.0	k_{0off}^{CN}	537.966
k_{02}^{CN}	4.8387	k_{2on}^{CN}	46.0
k_{20}^{CN}	0.0606	k_{2off}^{CN}	3.2604
k_{24}^{CN}	3.4722	k_{4on}^{CN}	46.0
k_{42}^{CN}	0.199362	k_{4off}^{CN}	1.3×10^{-3}

All the above parameters are adopted from Saucerman et. al. [48]

Table B.11 : Q_{10} values

Parameter description	Q_{10} value	References
Rate constants modulating $I_{Ca,L}$ channel kinetics	2.4	[254, 255]
Maximum uptake rate of the SERCA pump	1.415	[256]
Maximum Na^+/Ca^+ exchange current (V_{max})	1.77	[256]
Maximum plasma membrane Ca^{2+}-ATPase pump current ($\overline{I}_{PMCA}$)	4.3	[256]

Q_{10} values in the electromechanical model were adopted from Rice et al.[1] with Qf_{app}, Qh_f, Qh_b and Qg_{xb} decreased to 2.25 to reproduce temperature dependence of peak force developed [167].

Table B.12 : Frequency dependence of intracellular cAMP concentration

Stimulation frequency (Hz)	Intracellular cAMP concentration (μM)
0.50 - 1.67	2.67^{δ}
2.50	3.00
2.86	3.19
3.33	3.45
4.00	3.85
5.00	4.67
5.71	5.58
6.67	18.06
8.00	24.58
10.00	27.03
12.00	29.17

Intracellular cAMP concentration corresponding to maximal β-adrenergic stimulation (based on Eqn. 2, Demir et al [78])

Appendix C

Complete set of equations used in the model

C.1 Equations for currents in the model

C.1.1 L-Type Ca^{2+} current

Ca^{2+} current through the DHP-sensitive $I_{Ca,L}$ channel

$$I_{Ca,L} = R_{Ca,L} F_{cAMP,Ical} \left(O2_{dhpr} + O3_{dhpr}\right) P_{Ca} Z_{Ca}^2 \frac{F^2 V}{RT} \times \left(\frac{[Ca^{2+}]_{dhp} e^{\frac{2FV}{RT}} - 341.0[Ca^{2+}]_o}{e^{\frac{2FV}{RT}} - 1} \right) \tag{C.1}$$

$$F_{cAMP,Ical} = 1.094 - 0.163 \times exp(-0.219 \times [cAMP]) \tag{C.2}$$

Na^{+} current through the DHP-sensitive $I_{Ca,L}$ channel

$$I_{Na} = \frac{1.056 \times e^{\left(\frac{\nu - 21.73}{21.23841}\right)}}{1.056 \times e^{\left(\frac{\nu - 21.73}{21.23841}\right)} + [Ca_o^{2+}]} P_{Na} Z_{Na}^2 \frac{F^2 V}{RT} \times \left(\frac{0.75[Na^{+}]_{dhp} e^{\frac{FV}{RT}} - 0.75[Na^{+}]_o}{e^{\frac{FV}{RT}} - 1} \right) \tag{C.3}$$

Cs^{+} current through the DHP-sensitive $I_{Ca,L}$ channel

$$I_{Cs} = \frac{1.056 \times e^{\left(\frac{\nu-21.73}{21.23841}\right)}}{1.056 \times e^{\left(\frac{\nu-21.73}{21.23841}\right)} + [Ca_o^{2+}]} P_{Cs} Z_{Cs}^2 \frac{F^2 V}{RT} \times \left(\frac{0.75[Cs^+]_{dhp} e^{\frac{FV}{RT}} - 0.75[Cs^+]_o}{e^{\frac{FV}{k_{Cs}RT}} - 1} \right) \tag{C.4}$$

where $k_{Cs} = 0.5$ and $[Ca^{2+}]_{dhp}$, $[Na^+]_{dhp}$, $[Cs^+]_{dhp}$ are Concentrations at the mouth of the DHP-sensitive Ca^{2+} channel.

The corresponding unitary currents $i_{Ca,L}$, i_{Na}, i_{Cs} are obtained by dividing the above net channel currents by the number of dyadic units, N_{dyad}.

Gating scheme for the 2-state Markovian model used to allow Ca^{2+} mediated interaction of the DHP-sensitive $I_{Ca,L}$ channel and calmodilin:

$$S1_{dhpr} = 1 - S2_{dhpr} \tag{C.5}$$

$$\frac{dS2_{dhpr}}{dt} = ks_{12}^{dhpr} S1_{dhpr} - ks_{21}^{dhpr} S2_{dhpr} \tag{C.6}$$

Expressions for the rate constants:

$$ks_{12}^{dhpr} = 4.0 \times e^{\left(\frac{[Ca_4CaM]_{dhp}-100.0}{90.0}\right)} \tag{C.7}$$

$$ks_{21}^{dhpr} = 18.0 \tag{C.8}$$

Gating scheme for the 6-state Markovian model for the DHP-sensitive L-type Ca^{2+} release channel:

$$\begin{aligned} C5_{dhpr} =& 1 - (C1_{dhpr} + O2_{dhpr} + O3_{dhpr}) \\ & - (C4_{dhpr}) \end{aligned} \tag{C.9}$$

$$\begin{aligned} \frac{dC1_{dhpr}}{dt} =& k_{21}^{dhpr} O2_{dhpr} + k_{51}^{dhpr} C5_{dhpr} \\ & - \left(k_{12}^{dhpr} + k_{15}^{dhpr}\right) C5_{dhpr} \end{aligned} \tag{C.10}$$

$$\begin{aligned} \frac{dO2_{dhpr}}{dt} =& k_{12}^{dhpr} C1_{dhpr} + k_{42}^{dhpr} C4_{dhpr} \\ & + k_{32}^{dhpr} O3_{dhpr} + k_{52}^{dhpr} C5_{dhpr} \\ & - \left(k_{21}^{dhpr} + k_{23}^{dhpr}\right) O2_{dhpr} \\ & - \left(k_{24}^{dhpr} + k_{25}^{dhpr}\right) O2_{dhpr} \end{aligned} \tag{C.11}$$

$$\frac{dO3_{dhpr}}{dt} = k_{23}^{dhpr} O2_{dhpr} - k_{32}^{dhpr} O3_{dhpr} \tag{C.12}$$

$$\begin{aligned} \frac{dC4_{dhpr}}{dt} =& k_{54}^{dhpr} C5_{dhpr} + k_{24}^{dhpr} O2_{dhpr} \\ & - \left(k_{45}^{dhpr} + k_{42}^{dhpr}\right) C4_{dhpr} \end{aligned} \tag{C.13}$$

$$\frac{dC6_{dhpr}}{dt} = k_{36}^{dhpr} O3_{dhpr} - k_{63}^{dhpr} C6_{dhpr} \tag{C.14}$$

The open state $O3_{dhpr}$ accounts for the increased tail current produced as the result of a large depolarization.

Expressions for rate constants:

$$k_{42}^{dhpr} = 1000.0 \tag{C.15}$$

$$k_{45}^{dhpr} = 600000.0 \tag{C.16}$$

$$k_{54}^{dhpr} = \frac{k_{45}^{dhpr} k_{52}^{dhpr} k_{24}^{dhpr}}{k_{42}^{dhpr} k_{25}^{dhpr}} \tag{C.17}$$

$$k_{15}^{dhpr} = \frac{k_{51}^{dhpr} k_{12}^{dhpr} k_{25}^{dhpr}}{k_{52}^{dhpr} k_{21}^{dhpr}} \tag{C.18}$$

Case 1: With CICR (control)

$$k_{12}^{dhpr} = \left(300.3808 - \frac{301.0817}{1+e^{\left(\frac{\nu-13.5918}{8.85}\right)}}\right) \tag{C.19}$$

$$k_{21}^{dhpr} = \left(3359.8754 + \frac{966.95}{1+e^{\left(\frac{\nu-1.66}{1.4585}\right)}}\right) \tag{C.20}$$

$$\xi = 550 + CaMKII_{act} \times \tag{C.21}$$

$$\left(1.348 + \frac{CaMKII_{act}^{3.22}}{3.135\times10^{6} - 0.755\times CaMKII_{act}^{3.22}}\right) + CaN_{act} \tag{C.22}$$

$$k_{24}^{dhpr} = \left(\frac{336160 \times S2_{dhpr}}{\xi}\right) \tag{C.23}$$

$$k_{25}^{dhpr} = \left(\frac{5939.4 + \frac{306806.8}{1+e^{\left(\frac{\nu+1.8716}{1.3072}\right)}}}{\xi}\right) \tag{C.24}$$

$$k_{52}^{dhpr} = \left(0.02925 + \frac{0.48961}{1+e^{\left(\frac{\nu+12.2249}{0.974}\right)}}\right) \tag{C.25}$$

$$k_{23}^{dhpr} = \left(1352 - \frac{1350}{1+e^{\left(\frac{\nu}{1.8}\right)}} + \frac{1700}{1+e^{(\nu+5)}}\right) \tag{C.26}$$

$$k_{32}^{dhpr} = \left(1030.0575 - \frac{713.1966}{1+e^{(\nu-5.0)}}\right) \tag{C.27}$$

$$k_{51}^{dhpr} = \frac{383.5435}{1+e^{-\left(\frac{\nu-8.3702}{7.047}\right)}} + \frac{0.16725}{1+e^{-\left(\frac{\nu-31.8252}{0.01075}\right)}} + \frac{378.7085}{1+e^{\left(\frac{\nu-7.8953}{6.7691}\right)}} - 373.015 \tag{C.28}$$

$$k_{36}^{dhpr} = \left(100 - \frac{100.0}{1+e^{\left(\frac{\nu-41.0}{1.0}\right)}}\right) \tag{C.29}$$

$$k_{63}^{dhpr} = \left(\frac{600.0}{1+e^{\left(\frac{\nu-41.0}{1.0}\right)}}\right) \tag{C.30}$$

Case 2: With Ryanodine applied (no RyR release)

$$k_{12}^{dhpr} = \left(30392.87 - \frac{30394.73}{1+e^{\left(\frac{\nu-183.5975}{28.5662}\right)}}\right) \tag{C.31}$$

$$k_{21}^{dhpr} = \left(3568.74658 + \frac{21921.25344}{1+e^{\left(\frac{\nu+24.9838}{0.7372}\right)}}\right) \tag{C.32}$$

$$\xi = 550 + 6 \times CaMKII_{act} \tag{C.33}$$

$$+CaN_{act}$$

$$k_{24}^{dhpr} = \left(\frac{336160 \times S2_{dhpr}}{\xi}\right) \tag{C.34}$$

$$k_{25}^{dhpr} = \frac{0.0893 + \frac{26.3268}{1+e^{\left(\frac{\nu+15.0}{1.0}\right)}}}{\xi} \tag{C.35}$$

$$+\frac{\frac{32.6642}{1+e^{-\left(\frac{\nu-14.4897}{0.3131}\right)}} + \frac{63.808}{1+e^{\left(\frac{\nu-27.411}{0.0854}\right)}}}{\xi} \tag{C.36}$$

$$k_{52}^{dhpr} = 2.69 + \frac{0.74152}{1+e^{\left(\frac{\nu+27.945}{1.46976}\right)}} - \frac{2.43098}{1+e^{\left(\frac{\nu-40.25}{0.4034}\right)}} \tag{C.37}$$

$$k_{23}^{dhpr} = 1908 - \frac{2687.3087}{1+e^{\left(\frac{\nu+15.0}{0.9998}\right)}} + \frac{879.543}{1+e^{\left(\frac{\nu-11.1635}{0.3238}\right)}} \tag{C.38}$$

$$k_{32}^{dhpr} = 145107.50934 - \frac{150299.048}{1+e^{\left(\frac{\nu-1037.5224}{312.91482}\right)}} + \frac{5537.7875}{1+e^{\left(\frac{\nu-9.4649}{0.2893}\right)}} \tag{C.39}$$

$$k_{51}^{dhpr} = \frac{27.651}{1+e^{-\left(\frac{\nu-59.48}{4.444}\right)}} + \frac{11.488}{1+e^{-\left(\frac{\nu+15.1148}{0.9423}\right)}} - \frac{16.3777}{1+e^{-\left(\frac{\nu+15.01}{0.6351}\right)}} + 5.3384 \tag{C.40}$$

$$k_{36}^{dhpr} = \left(100 - \frac{100.0}{1+e^{\left(\frac{\nu-41.0}{1.0}\right)}}\right) \tag{C.41}$$

$$k_{63}^{dhpr} = \left(\frac{600.0}{1+e^{\left(\frac{\nu-41.0}{1.0}\right)}}\right) \tag{C.42}$$

Case 3: With Ca^{2+} substituted with Ba^{2+}

$$k_{12}^{dhpr} = 3028.7604 - \frac{6279.833}{1+e^{\left(\frac{\nu-58.1484}{9.5348}\right)}} + \frac{3259.706}{1+e^{\left(\frac{\nu-40.2856}{0.2272}\right)}} \tag{C.43}$$

$$k_{21}^{dhpr} = \frac{26296.0826}{1+e^{\left(\frac{\nu+17.40398}{0.22797}\right)}} + \frac{4718.8152}{1+e^{-\left(\frac{\nu+1.4892}{4.9581}\right)}} + \frac{1544.9745}{1+e^{-\left(\frac{\nu-132.7305}{3.6234}\right)}} - 808.0319 \tag{C.44}$$

$$k_{24}^{dhpr} = (0.0) \tag{C.45}$$

$$k_{25}^{dhpr} = -5883.3476 + \frac{5973.3014}{1+e^{\left(\frac{\nu-41.4221}{0.5703}\right)}} + \frac{528.171}{1+e^{-\left(\frac{\nu-20.4274}{0.187}\right)}} \tag{C.46}$$

$$k_{52}^{dhpr} = 175.78742 - \frac{174.7872}{1+e^{\left(\frac{\nu-32.3072}{4.4783}\right)}} - \frac{229.8479}{1+e^{-\left(\frac{\nu-36.9508}{5.4521}\right)}} \tag{C.47}$$

$$k_{23}^{dhpr} = \frac{2601.9597}{1+e^{\left(\frac{\nu-19.882}{0.4459}\right)}} - \frac{2647.5114}{1+e^{\left(\frac{\nu+15.6872}{2.1947}\right)}} - \frac{2501.6394}{1+e^{\left(\frac{\nu-39.8404}{0.3926}\right)}} + 2647.2042 \tag{C.48}$$

$$k_{32}^{dhpr} = \frac{1683.7686}{1+e^{-\left(\frac{\nu-20.0452}{0.40326}\right)}} + \frac{2161.9699}{1+e^{\left(\frac{\nu-360.2862}{1879.441}\right)}} - \frac{5926.5225}{1+e^{-\left(\frac{\nu+1.7842}{13.43183}\right)}} + 4129.8882 \tag{C.49}$$

$$k_{51}^{dhpr} = \frac{11.1993}{1+e^{-\left(\frac{\nu-35.2478}{0.2466}\right)}} + \frac{36.2341}{1+e^{-\left(\frac{\nu+23.9615}{15.8653}\right)}} - \frac{12.163}{1+e^{-\left(\frac{\nu-27.1529}{0.9455}\right)}} + 37.7673 \tag{C.50}$$

$$k_{36}^{dhpr} = \left(100 - \frac{100.0}{1+e^{\left(\frac{\nu-41.0}{1.0}\right)}}\right) \tag{C.51}$$

$$k_{63}^{dhpr} = \left(\frac{600.0}{1+e^{\left(\frac{\nu-41.0}{1.0}\right)}}\right) \tag{C.52}$$

C.1.2 Uptake of Ca^{2+} from the cytosol into the LSR

Ca^{2+} fluxes from cytosol to SERCA and SERCA to LSR

$$\begin{aligned} J_{cyt,serca} &= k_{cyt,serca} \times [Ca^{2+}]^2_{myo} \times SERCA_{tot} \\ &\quad -k_{cyt,serca} \times [Ca^{2+}]^2_{myo} \times [Ca^{2+}]_{serca} \\ &\quad -k_{serca,cyt} \times [Ca^{2+}]_{serca} \end{aligned} \tag{C.53}$$

$$\begin{aligned} J_{serca,sr} &= k_{sr,serca} \times [Ca^{2+}]^2_{LSR} \times [Ca^{2+}]_{serca} \\ &\quad -k_{sr,serca} \times [Ca^{2+}]^2_{LSR} \times SERCA_{tot} \\ &\quad +k_{cyt,sr} \times [Ca^{2+}]_{myo} \end{aligned} \tag{C.54}$$

$$I_{cyt,serca} = J_{cyt,serca} \times 2FV_{serca} \tag{C.55}$$

$$I_{serca,sr} = J_{serca,sr} \times 2FV_{serca} \tag{C.56}$$

Differential equation for Ca^{2+} buffered by the SERCA protein:

$$\frac{d[Ca^{2+}]_{serca}}{dt} = J_{cyt,serca} - J_{serca,sr} \tag{C.57}$$

Expressions for the rate constants for Ca^{2+} binding to/release from SERCA:

$$k_{cyt,serca} = K_{cyt,serca}\left(1.07 + 5500 \times CaMKII_{act}\right) \tag{C.58}$$

$$k_{cyt,serca} = K_{cyt,serca}\left(EC_{50}^{fwd}\right)^2 \tag{C.59}$$

$$k_{serca,sr} = K_{serca,sr}\left(1.07 + 5500 \times CaMKII_{act}\right) \tag{C.60}$$

$$k_{sr,serca} = \frac{K_{serca,sr}}{\left(EC_{50}^{bwd}\right)^2} \tag{C.61}$$

Affinities for the forward and backward Ca^{2+} fluxes:

$$\begin{aligned} EC_{50}^{fwd} &= 0.015(1 + PSR \times PLB_{dp}) \\ &\quad \times \left(\frac{1.027}{1 + 5500 \times CaMKII_{act}}\right) \end{aligned} \tag{C.62}$$

$$EC_{50}^{bwd} = 1250 - 1110 \times PSR \times PLB_{dp} \tag{C.63}$$

Differential equation for phospholamban

$$\begin{aligned} \frac{dPLB_{dp}}{dt} =& k_{12}^{PLB}(1 + (CaN_{act} \times 10^{-4})^2)PLB_p \\ &- k_{21}^{PLB}(1 + (CaMKII_{act} \times 10^5)^2 + F_{cAMP,SERCA}^2)PLB_{dp} \end{aligned} \tag{C.64}$$

$$F_{cAMP,SERCA} = 0.1094 - 0.0163 \times exp(-0.219 \times [cAMP]) \tag{C.65}$$

$$PLB_p = 1 - PLB_{dp} \tag{C.66}$$

C.1.3 Ca^{2+} pump in SL

$$I_{PMCA} = \overline{I_{PMCA}}\left(\frac{[Ca^{2+}]_{myo}}{kmpca + [Ca^{2+}]_{myo}}\right) \tag{C.67}$$

C.1.4 Na^{+}/Ca^{2+} exchanger

$$I_{NaCa} = \frac{NUM1 \times (NUM2 - NUM3)}{\wp\left(1 + 0.27e^{\frac{-0.65FV}{RT}}\right)} \tag{C.68}$$

$$
\begin{aligned}
NUM1 &= R_{NaCa}\left(\frac{V_{\max}}{1+\left(\frac{K_{mAllo}}{[Ca^{2+}]_{NaCa}}\right)^2}\right) && \text{(C.69)}\\
NUM2 &= e^{\frac{0.35FV}{RT}}([Na^+]_{NaCa})^3[Ca^{2+}]_o && \text{(C.70)}\\
NUM3 &= e^{\frac{0.65FV}{RT}}([Na^+]_o)^3[Ca^{2+}]_{NaCa} && \text{(C.71)}
\end{aligned}
$$

$$
\begin{aligned}
\wp =& K_{mCao}([Na^+]_{NaCa})^3 + K^3_{mNao}[Ca^{2+}]_{NaCa}\\
&+ K^3_{mNai}[Ca^{2+}]\left(1+\frac{[Ca^{2+}]_{NaCa}}{K_{mCai}}\right)\\
&+ K_{mCai}([Na^+]_o)^3\left(1+\left(\frac{[Na^+]_{NaCa}}{K_{mNai}}\right)^3\right) && \text{(C.72)}\\
&+ ([Na^+]_{NaCa})^3[Ca^{2+}]_o\\
&+ ([Na^+]_o)^3[Ca^{2+}]_{NaCa}
\end{aligned}
$$

where $[Ca^{2+}]_{NaCa}$, $[Na^+]_{NaCa}$ are Concentrations at the mouth of the NaCa-exchanger. The corresponding unitary current i_{NaCa} is obtained by dividing the above net channel current I_{NaCa} by the number of dyadic units N_{dyad}.

C.1.5 $\mathbf{Na^+/Cs^+}$ pump

$$
\begin{aligned}
I_{NaCs} &= R_{NaCs}\overline{I_{NaCs}}\left(\frac{[Cs^+]_o}{[Cs^+]_o+kmcs}\right)\\
&\quad\times\left(\frac{100\,([Na^+]_{myo})^{1.5}}{([Na^+]_{myo})^{1.5}+kmna^{1.5}}\right)\\
&\quad\times\left(\frac{0.65558}{0.18445+e^{-\left(\frac{\nu+53.353}{15.58}\right)}}\right) && \text{(C.73)}
\end{aligned}
$$

The corresponding unitary current i_{NaCs} is obtained by dividing the above net channel current I_{NaCs} by the number of dyadic units N_{dyad}.

C.1.6 Background Na^+ current

$$I_{Na,b} = G_{Nab}\left(\nu - \frac{RT}{F}\ln\left(\frac{[Na^+]_o}{[Na^+]_{myo}}\right)\right) \tag{C.74}$$

C.1.7 Ca^{2+} transfer from LSR to a single jSR

$$i_{tr} = \left(\frac{[Ca^{2+}]_{LSR} - [Ca^{2+}]_{jSR}}{\tau_{tr}}\right) 2FV_{jSR} \tag{C.75}$$

C.1.8 Ca^{2+} release from a unit jSR into a single DCU

$$i_{ryr} = J_{ryr} \times \left(2F \times \pi\Delta_r^2\Delta_z\right) \tag{C.76}$$

where,

$$J_{ryr} = \frac{O2_{ryr}\left([Ca^{2+}]_{jSR} - [Ca^{2+}]_{ryr}\right)P_{ryr}}{\pi\Delta_r^2\Delta_z} \tag{C.77}$$

Gating scheme for the 4-state Markovian model for the RyR-sensitive SR Ca^{2+} release channel:

$$C4_{ryr} = 1 - (C1_{ryr} + O2_{ryr} + C3_{ryr}) \tag{C.78}$$

$$\begin{aligned}\frac{dC1_{ryr}}{dt} =& k_{41}^{ryr}C4_{ryr} + k_{21}^{ryr}O2_{ryr} \\ & - \left(k_{12}^{ryr} + k_{14}^{ryr}\right)C1_{ryr}\end{aligned} \tag{C.79}$$

$$\begin{aligned}\frac{dO2_{ryr}}{dt} =& k_{12}^{ryr}C1_{ryr} + k_{32}^{ryr}C3_{ryr} \\ & - \left(k_{21}^{ryr} + k_{23}^{ryr}\right)O2_{ryr}\end{aligned} \tag{C.80}$$

$$\begin{aligned}\frac{dC3_{ryr}}{dt} =& k_{23}^{ryr}O2_{ryr} + k_{43}^{ryr}C4_{ryr} \\ & - \left(k_{34}^{ryr} + k_{32}^{ryr}\right)C3_{ryr}\end{aligned} \tag{C.81}$$

$$k_{12}^{ryr} = [Ca^{2+}]_{ryr}^2 \left(0.05 - \frac{3.7465 \times 10^{-2}}{1 + e^{\frac{[Ca^{2+}]_{ryr} - 2052.7}{5.983}}} \right) var + \left(\frac{CaMKII_{act}}{12000} \right) \tag{C.82}$$

$$k_{21}^{ryr} = \left(698.56 - \frac{618.56}{1 + e^{\frac{[Ca^{2+}]_{ryr} - 2052.9}{4.35}}} \right) \times \left(1 + \frac{6.0}{[Ca^{2+}]_{ryr}} \right) \frac{1}{var} \tag{C.83}$$

$$k_{14}^{ryr} = 8.748 \times 10^{-2} [Ca^{2+}]_{ryr} var \tag{C.84}$$

$$k_{41}^{ryr} = \left(\frac{2.0}{var} \right) + \frac{CaMKII_{act}}{12000} \tag{C.85}$$

$$k_{43}^{ryr} = k_{12}^{ryr}; \;\; k_{34}^{ryr} = k_{21}^{ryr}; \tag{C.86}$$

$$k_{23}^{ryr} = k_{14}^{ryr}; \;\; k_{32}^{ryr} = k_{41}^{ryr}; \tag{C.87}$$

$$var = \left[10.0 \times e^{\frac{A1_{ls} - 0.7013}{0.03}} \right]^2 \tag{C.88}$$

where $[Ca^{2+}]_{ryr}$ is the Ca^{2+} concentration at the mouth of the RyR channel on the dyadic side. In the presence of caffeine (CF, concentration in μM):

$$O2_{ryr} = \left(\frac{-0.522}{1 + e^{\frac{[CF] - 410}{264.9}}} \right) + 0.503 \tag{C.89}$$

Gating scheme for the 6-state Markovian model for the Luminal Calcium sensor.

$$I4_{ls} = 1 - (A1_{ls} + I2_{ls} + I3_{ls}) \tag{C.90}$$

$$B5_{ls} = 1 - (I2_{ls} + I3_{ls} + B6_{ls}) \tag{C.91}$$

$$\frac{dA1_{ls}}{dt} = k_{41}^{ls} I4_{ls} + k_{21}^{ls} I2_{ls} - \left(k_{12}^{ls} B5_{ls} + k_{14}^{ls} \right) A1_{ls} \tag{C.92}$$

$$\begin{aligned}\frac{dI2_{ls}}{dt} =& k_{12}^{ls} B5_{ls} A1_{ls} + k_{42}^{ls} B5_{ls} I4_{ls} + k_{32}^{ls} I3_{ls} \\ & - \left(k_{21}^{ls} + k_{24}^{ls} + k_{23}^{ls} + k_{25}^{ls}\right) I2_{ls}\end{aligned} \tag{C.93}$$

$$\frac{dI3_{ls}}{dt} = k_{43}^{ls} B5_{ls} I4_{ls} + k_{23}^{ls} I2_{ls} - \left(k_{34}^{ls} + k_{32}^{ls}\right) I3_{ls} \tag{C.94}$$

$$\frac{dB6_{ls}}{dt} = k_{56}^{ls} [Ca^{2+}]_{jSR} B5_{ls} - k_{65}^{ls} B6_{ls} \tag{C.95}$$

$A1_{ls}$ Fractional occupancy of RyR by Triadin/Junctin

$I2_{ls}$ Fractional occupancy of RyR by Triadin/Junctin and Calsequestrin

$I3_{ls}$ Fractional occupancy of Triadin/Junctin by Calsequestrin

$I4_{ls}$ Free Triadin/Junctin, B5ls - Free Calsequestrin

$B6_{ls}$ Fractional Occupancy of Calsequestrin by Calcium

C.1.9 Ca^{2+} dependent CaM mediated activation of CaMKII and CaN

Ca^{2+} binding to CaM and CaM buffering

$$\begin{aligned}CaM =& CaM_{tot} - Ca_2CaM - Ca_4CaM - CaMB \\ & - Ca_2CaMB - Ca_4CaMB - CaMCaN \\ & - Ca_2CaMCaN - Ca_4CaMCaN \\ & - CaMKII_{tot} \left(P_1 + P_3 + P_5 + P_4\right)\end{aligned} \tag{C.96}$$

$$B = B_{tot} - (CaMB + Ca_2CaMB + Ca_4CaMB) \tag{C.97}$$

$$R02 = k_{02}^{CM} \left[Ca^{2+}\right]^2 \times CaM - k_{02}^{CM} \times Ca_2CaM \tag{C.98}$$

$$R24 = k_{24}^{CM} \left[Ca^{2+}\right]^2 \times Ca_2CaM - k_{42}^{CM} \times Ca_4CaM \tag{C.99}$$

$$R02B = k_{02B}^{CM} \left[Ca^{2+}\right]^2 \times CaMB - k_{20B}^{CM} \times Ca_2CaMB \tag{C.100}$$

$$\begin{aligned} R24B =& k_{24B}^{CM} \left[Ca^{2+}\right]^2 \times Ca_2CaMB \\ & - k_{42B}^{CM} \times Ca_4CaMB \end{aligned} \tag{C.101}$$

$$R0B = k_{0Bon}^{CM} \times CaM \times B - k_{0Boff}^{CM} \times Ca_2CaMB \tag{C.102}$$

$$R2B = k_{2Bon}^{CM} \times Ca_2CaM \times B - k_{2Boff}^{CM} \times Ca_2CaMB \tag{C.103}$$

$$R4B = k_{4Bon}^{CM} \times Ca_4CaM \times B - k_{4Boff}^{CM} \times Ca_4CaMB \tag{C.104}$$

$$\begin{aligned} \frac{dCa_2CaM}{dt} =& R02 - R24 - R2B - R2CaN \\ & + CaMKII_{tot} \times (RCK_{56} - RCK_{21}) \end{aligned} \tag{C.105}$$

$$\begin{aligned}\frac{dCa_4CaM}{dt} =& R24 - R4CaN - R4B \\ & - CaMKII_{tot} \times (RCK_{46} - RCK_{23})\end{aligned} \tag{C.106}$$

$$\begin{aligned}\frac{dCa_4CaM}{dt} =& R24 - R4CaN - R4B \\ & - CaMKII_{tot} \times (RCK_{46} - RCK_{23})\end{aligned} \tag{C.107}$$

$$\frac{dCaMB}{dt} = R0B - R02B \tag{C.108}$$

$$\frac{dCa_2CaMB}{dt} = R02B + R2B - R24B \tag{C.109}$$

$$\frac{dCa_4CaMB}{dt} = R24B - R4B \tag{C.110}$$

CaMKII activation:

$$P_2 = 1 - P_3 - P_1 - P_4 - P_5 - P_6 \tag{C.111}$$

$$T = P_3 + P_4 + P_5 + P_6 \tag{C.112}$$

$$\begin{aligned}k_{34}^{CK} =& 0.055 \times T + 0.0074 \times T^2 \\ & + 0.015 \times T^3\end{aligned} \tag{C.113}$$

$$\begin{aligned}RCK_{34} =& k_{34}^{CK} \times P_3 \\ & - \left(\frac{K_{PP1} \times PP1_{tot} \times P_4}{k_{mpp1} + (CaMKII_{tot} \times P_4)} \right)\end{aligned} \tag{C.114}$$

$$
\begin{aligned}
RCK_{21} &= k_{21}^{CK} \times Ca_2CaM \times P_2 \\
&\quad -k_{12}^{CK} \times P_1 && \text{(C.115)} \\
RCK_{13} &= k_{13}^{CK} \times \left[Ca^{2+}\right]^2 \times P_1 \\
&\quad -k_{32}^{CK} \times P_3 && \text{(C.116)} \\
RCK_{23} &= k_{23}^{CK} \times Ca_4CaM \times P_2 \\
&\quad -k_{32}^{CK} \times P_3 && \text{(C.117)} \\
RCK_{45} &= k_{45}^{CK} \times P_4 \\
&\quad -k_{54}^{CK} \times \left[Ca^{2+}\right]^2 \times P_5 && \text{(C.118)} \\
RCK_{46} &= k_{46}^{CK} \times P_4 \\
&\quad -k_{64}^{CK} \times Ca_4CaM \times P_6 && \text{(C.119)} \\
RCK_{56} &= k_{56}^{CK} \times P_5 \\
&\quad -k_{65}^{CK} \times Ca_2CaM \times P_6 && \text{(C.120)} \\
RCK_{51} &= \frac{k_{PP1} \times PP1_{tot} \times P_5}{k_{mPP1} + (CaMKII_{tot} \times P_5)} && \text{(C.121)} \\
RCK_{62} &= \frac{k_{PP1} \times PP1_{tot} \times P_6}{k_{mPP1} + (CaMKII_{tot} \times P_6)} && \text{(C.122)}
\end{aligned}
$$

$$\frac{dP_1}{dt} = RCK_{21} + RCK_{51} - RCK_{13} \tag{C.123}$$
$$\frac{dP_3}{dt} = RCK_{23} + RCK_{13} - RCK_{34} \tag{C.124}$$
$$\frac{dP_4}{dt} = RCK_{34} - RCK_{46} - RCK_{45} \tag{C.125}$$
$$\frac{dP_5}{dt} = RCK_{45} - RCK_{56} - RCK_{51} \tag{C.126}$$
$$\frac{dP_6}{dt} = RCK_{46} - RCK_{56} - RCK_{62} \tag{C.127}$$

$$CaMKII_{act} = 100 \times (P_3 + P_4 + P_5 + P_6) \tag{C.128}$$

CaN activation:

$$\begin{aligned} Ca_2CaN =& CaN_{tot} - Ca_4CaN - CaMCaN \\ & - Ca_2CaMCaN - Ca_4CaMCaN \end{aligned} \tag{C.129}$$

$$\begin{aligned} RCN_{Ca4} =& k_{Caon}^{CN} \times \left[Ca^{2+}\right]^2 \times Ca_2CaN \\ & - k_{Caoff}^{CN} \times Ca_4CaN \end{aligned} \tag{C.130}$$

$$\begin{aligned} RCN_{02} =& k_{02}^{CN} \times \left[Ca^{2+}\right]^2 \times CaMCaN \\ & - k_{20}^{CN} \times Ca_2CaMCaN \end{aligned} \tag{C.131}$$

$$\begin{aligned} RCN_{24} =& k_{24}^{CN} \times \left[Ca^{2+}\right]^2 \times Ca_2CaMCaN \\ & - k_{42}^{CN} \times Ca_4CaMCaN \end{aligned} \tag{C.132}$$

$$\begin{aligned} RCN_0 =& k_{0on}^{CN} \times CaM \times Ca_4CaN \\ & - k_{0off}^{CN} \times CaMCaN \end{aligned} \tag{C.133}$$

$$\begin{aligned} RCN_2 =& k_{2on}^{CN} \times Ca_2CaM \times Ca_4CaN \\ & - k_{2off}^{CN} \times Ca_2CaMCaN \end{aligned} \tag{C.134}$$

$$\begin{aligned} RCN_4 =& k_{4on}^{CN} \times Ca_4CaM \times Ca_4CaN \\ & - k_{4off}^{CN} \times Ca_4CaMCaN \end{aligned} \tag{C.135}$$

$$\frac{dCa_4CaN}{dt} = RCN_{Ca4} - RCN_0 - RCN_2 - RCN_4 \tag{C.136}$$

$$\frac{dCaMCaN}{dt} = RCN_0 - RCN_{02} \tag{C.137}$$

$$\frac{dCa_2CaMCaN}{dt} = RCN_2 + RCN_{02} - RCN_{24} \tag{C.138}$$

$$\frac{dCa_4CaMCaN}{dt} = RCN_4 + RCN_{24} \tag{C.139}$$

$$\begin{aligned} CaN_{act} =& 100(Ca_4CaMCaN + 0.1Ca_2CaMCaN) \\ &+ 10Ca_4CaMCaN + 0.1CaMCaN \\ &+ 0.1Ca_4CaN \end{aligned} \tag{C.140}$$

C.2 Differential equations for buffers used in the model

Fluorescent indicator dye

$$\begin{aligned} \frac{d[CaF3]}{dt} =& k^+_{fluo3}[Ca^{2+}_{myo}]\left([fluo3]_{tot} - [CaF3]\right) \\ &- k^-_{fluo3}[CaF3] \end{aligned} \tag{C.141}$$

Intracellular Ca^{2+} buffering:

calmodulin (bulkmyoplasm):

$$\frac{dO_c}{dt} = 200[Ca^{2+}]_{myo}\left(1 - O_c\right) - 476.0 \times O_c \tag{C.142}$$

Troponin

(Fractional occupancy of troponin-Ca complex by Ca^{2+}):

$$\frac{dO_tc}{dt} = 78.4[Ca^{2+}]_{myo}\left(1 - O_{tc}\right) - 392.0 \times O_{tc} \tag{C.143}$$

(Fractional occupancy of troponin-Mg complex by Ca^{2+}):

$$\begin{aligned} \frac{dO_c}{dt} =& 200[Ca^{2+}]_{myo}\left(1 - O_{tmgc} - O_{tmgmg}\right) \\ &- 6.6 \times O_{tmgc} \end{aligned} \tag{C.144}$$

(Fractional occupancy of troponin-Mg complex by Mg^{2+}):

$$\begin{aligned}\frac{dO_{tmgmg}}{dt} =& 2.0[Mg^{2+}]_{myo}\,(1 - O_{tmgc} - O_{tmgmg}) \\ & - 666.0 \times O_{tmgmg}\end{aligned} \tag{C.145}$$

C.3 Differential equations for ion concentrations used in the model

C.3.1 Intracellular Ca^{2+} concentration:

1. *Ca^{2+} concentration in the cytosol*

$$\begin{aligned}\frac{d[Ca^{2+}]_{myo}}{dt} =& \frac{I_{dyad} - I_{PMCA} - I_{Ca,L,SL}}{2FV_{myo}} \\ & + \frac{-I_{cyt,serca} + 2I_{NaCa,SL}}{2FV_{myo}} \\ & - \frac{dO}{dt} - \frac{dCaF1}{dt}\end{aligned} \tag{C.146}$$

where I_{dyad} is the net integrated Ca^{2+} flux diffusing out of all the dyadic units into the cytosol.

$$\frac{dO}{dt} = 3.2\frac{dO_{TC}}{dt} + 6.4\frac{dO_{TMgC}}{dt} + 1.8\frac{dO_c}{dt} \tag{C.147}$$

2. *Ca^{2+} concentration in the jSR*

$$\frac{d[Ca^{2+}]_{jSR}}{dt} = \frac{i_{tr} - i_{ryr}}{2FV_{jSR}} - 31000\frac{dB6_{ls}}{dt} \tag{C.148}$$

3. *Ca^{2+} concentration in the LSR*

$$\frac{d[Ca^{2+}]_{LSR}}{dt} = \frac{I_{cyt,serca} - N_{dyad} i_{tr}}{2FV_{LSR}} \tag{C.149}$$

4. *Diffusion equation for Calcium in the dyadic space*

$$\begin{aligned}\frac{\partial[Ca^{2+}]_{dyad}}{\partial t} =& D_{Ca}\nabla^2[Ca^{2+}]_{dyad} + J_{ryr} \\ &+ J_{dhpr} + J_{NaCa} + J_{bnd}\end{aligned} \tag{C.150}$$

$$J_{dhpr} = \left(\frac{i_{Ca,L,TT}}{N_{dyad}}\right)\left(\frac{5.1821 \times 10^3}{\pi\Delta_r^2\Delta_z}\right) \tag{C.151}$$

$$J_{NaCa,TT} = \left(\frac{i_{NaCa,TT}}{N_{dyad}}\right)\left(\frac{2 \times 5.1821 \times 10^3}{\pi\Delta_r^2\Delta_z}\right) \tag{C.152}$$

$$\begin{aligned}J_{bnd} =& \left(\frac{N_h K_h}{(K_h + [Ca^{2+}]_{dyad})^2}\right) \\ &\times \left(\frac{N_l K_l}{(K_l + [Ca^{2+}]_{dyad})^2}\right)\frac{\partial[Ca^{2+}]_{dyad}}{\partial t}\end{aligned} \tag{C.153}$$

C.3.2 Intracellular Na^+ concentration:

1. *Na^+ concentration in the cytosol*

$$\begin{aligned}\frac{d[Na^+]_{myo}}{dt} =& N_{dyad}\left[\frac{[Na^+]_{dyad} - [Na^+]_{myo}}{\tau_{Na}}\right] \\ &- \left[\frac{I_{Na,b} + 3I_{NaCa,SL}}{F \times V_{myo}}\right] \\ &+ \left[\frac{3I_{NaCs,SL}}{F \times V_{myo}}\right]\end{aligned} \tag{C.154}$$

2. *Na^+ concentration in the dyadic space*

$$\begin{aligned}\frac{d[Na^+]_{dyad}}{dt} =& \left(\frac{[Na^+]_{myo} - [Na^+]_{dyad}}{\tau_{Na}}\right) \\ &- \left(\frac{3i_{NaCa,TT} + 3i_{NaCs,TT}}{F \times V_{cleft}}\right)\end{aligned} \tag{C.155}$$

C.3.3 Intracellular Cs^+ concentration:

1. *Cs^+ concentration in the cytosol*

$$\begin{aligned}\frac{d[Cs^+]_{myo}}{dt} =& N_{dyad}\left(\frac{[Cs^+]_{dyad} - [Cs^+]_{myo}}{\tau_{Cs}}\right) \\ &+ \left(\frac{2I_{NaCs,SL}}{F \times V_{myo}}\right)\end{aligned} \tag{C.156}$$

2. *Cs^+ concentration in the dyadic space*

$$\begin{aligned}\frac{d[Cs^+]_{dyad}}{dt} =& \left(\frac{[Cs^+]_{myo} - [Cs^+]_{dyad}}{\tau_{Cs}}\right) \\ &+ \left(\frac{2i_{NaCs,TT}}{F \times V_{cleft}}\right)\end{aligned} \tag{C.157}$$

C.4 Equations governing electro-mechanics modified (from Rice et al. [1]) in the model

Regulatory Ca^{2+}-binding to troponin

$$\begin{aligned}\frac{dCaTrop_H}{dt} =& k_{onT}TnI_u[Ca^{2+}]_{myo}(1 - CaTrop_H) \\ &- k_{offHT}CaTrop_H\end{aligned} \tag{C.158}$$

$$\begin{aligned}\frac{dCaTrop_L}{dt} =& k_{onT} TnI_u [Ca^{2+}]_{myo} (1 - CaTrop_L) \\ & - k_{offLT} CaTrop_L\end{aligned} \tag{C.159}$$

k_{onT} = 22.22 $\mu M^{-1} s^{-1}$; k_{offHT} = 17.36 s^{-1}; k_{offLT} = 173.61 s^{-1}; (Rice et al. [1]).

$$\frac{dTnI_p}{dt} = k_{onTI} \Delta_{PKA} TnI_u - k_{offTI} TnI_p \tag{C.160}$$

k_{onTI} = 698.69 s^{-1} ; k_{offTI} = 80.0 s^{-1}; (estimated from Roof et al. [214]).

$$TnI_u = 1 - TnI_p \tag{C.161}$$

$$\Delta_{PKA} = \frac{0.3 \times [cAMP]}{[cAMP] + 12.1} \tag{C.162}$$

$$fappT_{new} = fappT^{\ddagger} \times F_{cAMP,Force} \tag{C.163}$$

$$hfT_{new} = hfT^{\ddagger} \times F_{cAMP,Force} \tag{C.164}$$

$$hbT_{new} = hbT^{\ddagger} \times F_{cAMP,Force} \tag{C.165}$$

$$gxbT_{new} = gxbT^{\ddagger} \times F_{cAMP,Force} \tag{C.166}$$

$$F_{cAMP,Force} = 1.873 - 1.4 \times exp(-0.192 \times [cAMP]) \tag{C.167}$$

‡- Rate constants governing cross-bridge kinetics described in Rice et al [1].

Bibliography

[1] J. J. Rice, F. Wang, D. M. Bers, and P. P. de Tombe, "Approximate model of cooperative activation and crossbridge cycling in cardiac muscle using ordinary differential equations," *Biophys J*, vol. 95, no. 5, pp. 2368–2390, 2008.

[2] B. Katz, *Nerve, Muscle and Synapse*. New York: McGraw Hill, 1966.

[3] D. Noble, *The Initiation of the Heart Beat*. New York: Oxford University Press, 1979.

[4] B. Hille, *Ion channels of excitable membranes*. Sunderland, MA: Sinauer Associates, 3rd ed., 2001.

[5] M. R. Flax and W. H. Holmes, "Goldman-hodgkin-katz cochlear hair cell models - a foundation for nonlinear cochlear mechanics," in *INTERSPEECH'08*, pp. 683–686, 2008.

[6] O. P. Hamill, A. Marty, E. Neher, B. Sakmann, and F. J. Sigworth, "Improved patch-clamp techniques for high-resolution current recording from cells and cell-free membrane patches," *Pfulgers Arch-Eur J Physiol*, vol. 391, no. 2, pp. 85–100, 1981.

[7] T. Powell, "Methods for the isolation and preparation of single adult myocytes," in *Biology of Isolated Cardiac Myocytes* (W. A. Clark, R. S. Decker, and T. K. Borg, eds.), pp. 9–13, Amsterdam: Elsevier, 1988.

[8] A. Fabiato and F. Fabiato, "Contractions induced by a calcium-triggered release of calcium from the sarcoplasmic reticulum of single skinned cardiac cells," *J Physiol*, vol. 249, pp. 469–495, 1975.

[9] D. J. Beuckelmann and W. G. Wier, "Mechanism of release of calcium from sarcoplasmic reticulum of guinea-pig cardiac cells," *J Physiol (Lond)*, vol. 405, pp. 233–235, 1988.

[10] A. F. Huxley and R. Niedergerke, "Structural changes in muscle during contraction: Interference microscopy of living muscle fibres," *Nature*, vol. 173, pp. 971–973, 1954.

[11] H. E. Huxley and J. Hanson, "Changes in the cross-striations of muscle during contraction and stretch and their structural interpretation," *Nature*, vol. 173, pp. 973–976, 1954.

[12] W. Lehman, R. Craig, and P. Vibert, "Ca(2+)-induced tropomyosin movement in limulus thin filaments revealed by three-dimensional reconstruction," *Nature*, vol. 368, no. 6466, pp. 65–67, 1994.

[13] A. L. Hodgkin and A. F. Huxley, "A quantitative description of membrane current and its application to conduction and excitation in nerve," *J Physiol*, vol. 117, pp. 500–544, 1952.

[14] P. G. Hoel, S. C. Port, and C. J. Stone, *Introduction to stochastic processes*. Boston, MA: Houghton Mifflin, 1972.

[15] C. E. Clancy and Y. Rudy, "Cellular consequences of herg mutations in the long qt syndrome: precursors to sudden cardiac death," *Cardiovasc Res*, vol. 50, pp. 301–313, 2001.

[16] T. Brennan, M. Fink, and B. Rodriguez, "Multiscale modelling of drug-induced effects on cardiac electrophysiological activity," *Eur J Pharm Sci*, vol. 36, pp. 62–77, 2009.

[17] E. Grandi, J. L. Puglisi, S. Wagner, L. S. Maier, S. Severi, and D. M. Bers, "Simulation of ca-calmodulin-dependent protein kinase ii on rabbit ventricular myocyte ion currents and action potentials," *Biophys J*, vol. 93, pp. 3835–3847, 2007.

[18] D. DiFrancesco and D. Noble, "A model of cardiac electrical activity incorporating ionic pumps and concentration changes," *Philos Trans R Soc Lond B Biol Sci*, vol. 307, pp. 353–398, 1985.

[19] C. H. Luo and Y. Rudy, "A dynamic model of the cardiac ventricular action potential: I. simulations of ionic currents and concentration changes," *Circ Res*, vol. 74, pp. 1071–1096, 1994.

[20] T. R. Shannon, K. S. Ginsburg, and D. M. Bers, "Reverse mode of the sarcoplasmic reticulum ca pump limits sarcoplasmic reticulum ca uptake in permeabilized and voltage-clamped myocytes," *Ann N Y Acad Sci*, vol. 853, pp. 350–352, 1998.

[21] R. L. Winslow, J. Rice, S. Jafri, E. Marban, and B. ORourke, "Mechanisms of altered excitationcontraction coupling in canine tachycardia-induced heart failure, ii: model studies," *Circ Res*, vol. 84, pp. 571–586, 1999.

[22] J. L. Puglisi and D. M. Bers, "Labheart: an interactive computer model of rabbit ventricular myocyte ion channels and ca transport," *Am J Physiol Cell Physiol*, vol. 281, pp. C2049–C2060, 2001.

[23] T. R. Shannon, F. Wang, J. Puglisi, C. Weber, and D. M. Bers, "A mathematical treatment of integrated ca dynamics within the ventricular myocyte," *Biophys J*, vol. 87, no. 5, pp. 3351–3371, 2004.

[24] E. Grandi, F. S. Pasqualini, and D. M. Bers, "A novel computational model of the human ventricular action potential and ca transient," *J Mol Cell Cardiol*, vol. 48, pp. 112–121, 2010.

[25] N. P. Smith and E. J. Crampin, "Development of models of active ion transport for whole-cell modelling: cardiac sodium-potassium pump as a case study," *Prog Biophys Mol Biol*, vol. 85, pp. 387–405, 2004.

[26] K. Tran, N. P. Smith, D. S. Loiselle, and E. J. Crampin, "A thermodynamic model of the cardiac sarcoplasmic/endoplasmic ca(2+) (serca) pump," *Biophys J*, vol. 96, pp. 2029–2042, 2009.

[27] T. M. Kang and D. W. Hilgemann, "Multiple transport modes of the cardiac na+/ca2+ exchanger," *Nature*, vol. 427, pp. 544–548, 2004.

[28] M. D. Stern, "Theory of excitation-contraction coupling in cardiac muscle," *Biophys J*, vol. 63, pp. 497–517, 1992.

[29] D. W. Hilgemann and D. Noble, "Excitation-contraction coupling and extracellular calcium transients in rabbit atrium: reconstruction of basic cellular mechanisms," *Proc R Soc Lond B*, vol. 230, pp. 163–205, 1987.

[30] G. Isenberg, "Cardiac excitation-contraction coupling: from global to microscopic models," in *Physiology and Pathophysiology of the Heart* (N. Sperelakis, ed.), pp. 289–307, Kluwer Academic, 1995.

[31] M. D. Stern, L. S. Song, H. Cheng, J. S. K. Sham, H. T. Yang, K. R. Boheler, and E. Rios, "Local control models of cardiac excitation-contraction coupling," *J Gen Physiol*, vol. 113, pp. 469–489, 1999.

[32] J. J. Rice, S. Jafri, and R. L. Winslow, "Modeling gain and gradedness of ca^{2+} release in the functional unit of the cardiac diadic space," *Biophys J*, vol. 77, pp. 1871–1884, 1999.

[33] J. L. Greenstein and R. L. Winslow, "An integrative model of the cardiac ventricular myocyte incorporating local control of ca^{2+} release," *Biophys J*, vol. 83, pp. 2918–2945, 2002.

[34] R. L. Winslow, A. Tanskanen, M. Chen, and J. L. Greenstein, "Multiscale modeling of calcium signaling in the cardiac dyad," *Ann NY Acad Sci*, vol. 1080, pp. 362–375, 2006.

[35] R. Hinch, J. L. Greenstein, A. J. Tanskanen, L. Xu, and R. L. Winslow, "A simplified local control model of calcium-induced calcium release in cardiac ventricular myocytes," *Biophys J*, vol. 87, no. 6, pp. 3723–3736, 2004.

[36] J. L. Greenstein, R. Hinch, and R. L. Winslow, "Mechanisms of excitation-contraction coupling in an integrative model of the cardiac ventricular myocyte," *Biophys J*, vol. 90, pp. 77–91, 2006.

[37] R. Hinch, J. L. Greenstein, and R. L. Winslow, "Multi-scale models of local control of calcium induced calcium release," *Prog Biophys Mol Biol*, vol. 90, pp. 136–150, 2006.

[38] S. Q. Wang, L. S. Song, E. G. Lakatta, and H. Cheng, "ca^{2+} signalling between

single l-type ca^{2+} channels and ryanodine receptors in heart cells," *Nature*, vol. 410, pp. 592–596, 2001.

[39] A. V. Zima, E. Picht, D. M. Bers, and L. A. Blatter, "Termination of cardiac ca^{2+} sparks: role of intra-sr [ca^{2+}], release flux, and intra-sr ca^{2+} diffusion," *Circ Res*, vol. 103, pp. 105–115, 2008.

[40] Y. Shiferaw, M. A. Watanabe, A. Garfinkel, J. N. Weiss, and A. Karma, "Model of intracellular calcium cycling in ventricular myocytes," *Biophys J*, vol. 85, pp. 3666–3686, 2003.

[41] D. Terentyev, S. Viatchenko-Karpinski, S. Vedamoorthyrao, S. Oduru, I. Gyorke, S. C. Williams, and S. Gyorke, "protein protein interactions between triadin and calsequestrin are involved in modulation of sarcoplasmic reticulum calcium release in cardiac myocytes," *J Physiol*, vol. 583, pp. 71–80, 2007.

[42] J. L. Greenstein, A. J. Tanskanen, and R. L. Winslow, "Modeling the actions of beta-adrenergic signaling on excitationcontraction coupling processes," *Ann N Y Acad Sci*, vol. 1015, pp. 16–27, 2004.

[43] J. J. Saucerman, L. L. Brunton, A. P. Michailova, and A. D. McCulloch, "Modeling beta-adrenergic control of cardiac myocyte contractility in silico," *J Biol Chem*, vol. 278, pp. 47997–48003, 2003.

[44] G. M. Faber and Y. Rudy, "Action potential and contractility changes in [na(+)](i) overloaded cardiac myocytes: a simulation study," *Biophys J*, vol. 78, pp. 2392–2404, 2000.

[45] R. C. Ahrens-Nicklas, C. E. Clancy, and D. J. Christini, "Reevaluating the

efficacy of β-adrenergic agonists and antagonists in long qt-3 syndrome through computational modelling," *Cardiovasc Res*, vol. 82, pp. 439–447, 2009.

[46] L. S. Maier and D. M. Bers, "Role of ca^{2+}/calmodulin-dependent protein kinase (camk) in excitation-contraction coupling in the heart," *Cardiovasc Res*, vol. 73, pp. 631–640, 2007.

[47] T. J. Hund and Y. Rudy, "Rate dependence and regulation of action potential and calcium transient in a canine cardiac ventricular cell model," *Circulation*, vol. 110, pp. 3168–3174, 2004.

[48] J. J. Saucerman and D. M. Bers, "Calmodulin mediates differential sensitivity of camkii and calcineurin to local ca^{2+} in cardiac myocytes," *Biophysical Journal*, vol. 95, pp. 4597–4612, 2008.

[49] Y. L. Hashambhoy, R. L. Winslow, and J. L. Greenstein, "Camkii-induced shift in modal gating explains l-type ca^{2+} current facilitation: a modeling study," *Biophys J*, vol. 96, no. 5, pp. 1770–1785, 2009.

[50] P. J. Hunter, A. D. McCulloch, and H. E. ter Keurs, "Modelling the mechanical properties of cardiac muscle," *Prog Biophys Mol Biol*, vol. 69, pp. 289–331, 1998.

[51] O. Solovyova, L. Katsnelson, S. Guriev, L. Nikitina, Y. Protsenko, S. Routkevitch, and V. Markhasin, "Mechanical inhomogeneity of myocardium studied in parallel and serial cardiac muscle duplexes: experiments and models," *Chaos, Solitons and Fractals*, vol. 13, pp. 1685–1711, 2002.

[52] R. C. Kerckhoffs, P. H. Bovendeerd, J. C. Kotte, F. W. Prinzen, K. Smits, and T. Arts, "Homogeneity of cardiac contraction despite physiological asynchrony of depolarization: a model study," *Ann Biomed Eng*, vol. 31, pp. 536–547, 2003.

[53] N. A. Trayanova and J. J. Rice, "Cardiac electromechanical models: from cell to organ," *Front Physiol*, vol. 2, no. 43, 2011.

[54] J. J. Rice and P. P. de Tombe, "Approaches to modeling crossbridges and calcium-dependent activation in cardiac muscle," *Prog Biophys Mol Biol*, vol. 85, pp. 179–195, 2004.

[55] D. M. Bers, *Excitation-Contraction Coupling and Cardiac Contractile Force*. Dordrecht: Kluwer Academic, 2nd ed., 2001.

[56] Y. E. Earm and D. Noble, "A model of the single atrial cell: relation between calcium current and calcium release," *Proc R Soc Lond B Biol Sci*, vol. 240, pp. 83–96, 1990.

[57] D. Noble, A. Varghese, P. Kohl, and P. Noble, "Improved guinea-pig ventricular cell model incorporating a diadic space, ikr and iks, and length- and tension-dependent processes," *Can J Cardiol*, vol. 14, pp. 123–134, 1998.

[58] S. A. Niederer, P. J. Hunter, and N. P. Smith, "A quantitative analysis of cardiac myocyte relaxation: a simulation study," *Biophys J*, vol. 90, pp. 1697–1722, 2006.

[59] S. A. Niederer and N. P. Smith, "A mathematical model of the slow force response to stretch in rat ventricular myocytes," *Biophys J*, vol. 92, pp. 4030–4044, 2007.

[60] S. V. Pandit, R. B. Clark, W. R. Giles, and S. S. Demir, "A mathematical model of action potential heterogeneity in adult rat left ventricular myocytes," *Biophys J*, vol. 81, pp. 3029–3051, 2001.

[61] J. J. Rice, R. L. Winslow, and W. C. Hunter, "Comparison of putative cooperative mechanisms in cardiac muscle: length dependence and dynamic responses," *Am J Physiol*, vol. 276, pp. H1734–H1754, 1999.

[62] J. J. Rice, S. Jafri, and R. L. Winslow, "Cardiac ca^{2+} dynamics: the roles of ryanodine receptor adaptation and sarcoplasmic reticulum load," *Biophys J*, vol. 74, pp. 1149–1168, 1998.

[63] S. G. Campbell, S. N. Flaim, C. H. Leem, and A. D. McCulloch, "Mechanisms of transmurally varying myocyte electromechanics in an integrated computational model," *Phil Trans A Math Phys Eng Sci*, vol. 366, pp. 3361–3380, 2008.

[64] K. Tran, N. P. Smith, D. S. Loiselle, and E. J. Crampin, "A metabolite-sensitive, thermodynamically constrained model of cardiac cross-bridge cycling: implications for force development during ischemia," *Biophys J*, vol. 98, pp. 267–276, 2010.

[65] J. C. Butcher, *The Numerical Analysis of Ordinary Differential Equations: Runge-Kutta and General Linear Methods*. Chichester: John Wiley and Sons, 1987.

[66] A. Krishna, L. Sun, M. Valderrábano, P. T. Palade, and J. W. J. Clark, "Modeling cicr in rat ventricular myocytes: Voltage clamp studies," *Theoretical Biology and Medical Modelling*, vol. 6, pp. 199–222, 2010.

[67] M. Naraghi and E. Neher, "Linearized buffered Ca^{2+} diffusion in microdomains and its implications for calculation of $[Ca^{2+}]$ at the mouth of a calcium channel," *J Neurosci*, vol. 17, pp. 6961–6973, 1997.

[68] S. M. Simon and R. R. Llinás, "Compartmentalization of the submembrane calcium activity during calcium influx and its significance in transmitter release," *Biophys J*, vol. 48, pp. 485–498, 1985.

[69] N. Shirokova, J. Garcia, G. Pizarro, and E. Rios, "Ca^{2+} release from the sarcoplasmic reticulum compared in amphibian and mammalian skeletal muscle," *J Gen Physiol*, vol. 107, pp. 1–18, 1996.

[70] J. Crank, *The mathematics of diffusion.* Oxford, London: Clarendon Press, 2nd ed., 1975.

[71] G. D. Smith, J. E. Keizer, M. D. Stern, W. J. Lederer, and H. Cheng, "A simple numerical model of calcium spark formation and detection in cardiac myocytes," *Biophys J*, vol. 75, pp. 15–32, 1998.

[72] D. W. Marquardt, "An algorithm for least-squares estimation of nonlinear parameters," *J Soc Ind Appl Math*, vol. 11, pp. 431–441, 1963.

[73] H. T. Lau, "Overdetermined nonlinear systems," in *A Numerical Library in C for Scientists and Engineers*, pp. 354–358, 2000 Corporate Blvd. N.W., Boca Raton, Florida 33431: CRC Press, 1st ed., 1995.

[74] E. Marban and R. W. Tsien, "Enhancement of calcium current during digitalis inotropy in mammalian heart: positive feed-back regulation by intracellular calcium?," *J Physiol*, vol. 329, pp. 589–614, 1982.

[75] K. D. Varian, S. Raman, and P. M. Janssen, "Measurement of myofilament calcium sensitivity at physiological temperature in intact cardiac trabeculae," *Am J Physiol Heart Circ Physiol*, vol. 290, no. 5, pp. H2092–2097, 2006.

[76] A. Persechini and P. M. Stemmer, "Calmodulin is a limiting factor in the cell," *Trends Cardiovasc Med*, vol. 12, pp. 32–37, 2002.

[77] E. Picht, J. DeSantiago, S. Huke, M. A. Kaetzel, J. R. Dedman, and D. M. Bers, "Camkii inhibition targeted to the sarcoplasmic reticulum inhibits frequency-dependent acceleration of relaxation and ca^{2+} current facilitation," *J Mol Cell Cardiol*, vol. 42, pp. 196–205, 2007.

[78] S. S. Demir, J. W. Clark, and W. R. Giles, "Parasympathetic modulation of sinoatrial node pacemaker activity in rabbit heart: a unifying model," *Am J Physiol*, vol. 276, pp. 2221–2244, 1999.

[79] J. Yang, J. W. Clark, R. M. Bryan, and C. S. Robertson, "Mathematical modeling of the nitric oxide/cgmp pathway in the vascular smooth muscle cell," *Am J Physiol Heart Circ Physiol*, vol. 289, no. 2, pp. 886–897, 2005.

[80] S. D. Prabhu, A. Azimi, and T. Frosto, "Nitric oxide effects on myocardial function and force-interval relations: regulation of twitch duration," *J Mol Cell Cardiol*, vol. 31, no. 12, pp. 2077–2085, 1999.

[81] S. Despa, F. Brette, C. H. Orchard, and D. M. Bers, "Na/ca exchange and na/k-atpase function are equally concentrated in transverse tubules of rat ventricular myocytes," *Biophys J*, vol. 85, pp. 3388–3396, 2003.

[82] M. Kawai, M. Hussain, and C. H. Orchard, "Excitation-contraction coupling in rat ventricular myocytes after formamide-induced detubulation," *Am J Physiol*, vol. 277, pp. 603–609, 1999.

[83] H. Cheng, W. J. Lederer, and M. B. Cannell, "Calcium sparks: elementary

events underlying excitation-contraction coupling in heart muscle," *Science*, vol. 262, pp. 740–744, 1993.

[84] L. A. Blatter, J. Hüser, and E. Riós, "Sarcoplasmic reticulum ca^{2+} release flux underlying ca^{2+} sparks in cardiac muscle," *Proc Natl Acad Sci USA*, vol. 94, pp. 4176–4181, 1997.

[85] M. E. Diaz, S. C. O'Neill, and D. A. Eisner, "Sarcoplasmic reticulum calcium content fluctuation is the key to cardiac alternans," *Circulation Research*, vol. 94, pp. 650–656, 2004.

[86] L. Sun, J. S. Fan, J. W. Clark, and P. T. Palade, "A model of the l-type ca^{2+} channel in rat ventricular myocytes: ion selectivity and inactivation mechanisms," *J Physiol (Lond)*, vol. 529, pp. 139–158, 2000.

[87] W. Yuan and D. M. Bers, "Ca-dependent facilitation of cardiac ca current is due to ca-calmodulin-dpenedent protein kinase," *American Journal of Physiology*, vol. 267, pp. H082–H993, 1994.

[88] D. M. Bers and E. Grandi, "Calcium/calmodulin-dependent kinase ii regulation of cardiac ion channels," *J Cardiovasc Pharmacol*, vol. 54, pp. 180–187, 2009.

[89] A. Hudmon, H. Schulman, J. Kim, M. Maltez, R. W. Tsien, and G. S. Pitt, "Camkii tethers to l-type ca^{2+} channels, establishing a local and dedicated integrator of ca^{2+} signals for facilitation," *Journal of Cell Biology*, vol. 171, pp. 537–547, 2005.

[90] S. Tandan, Y. Wang, T. T. Wang, N. Jiang, D. D. Hall, J. W. Hell, X. Luo, B. A. Rothermel, and J. A. Hill, "Physical and functional interaction between

calcineurin and the cardiac l-type ca^{2+} channel," *Circ Res*, vol. 105, pp. 51–60, 2009.

[91] S. Tandan, Y. Wang, T. T. Wang, N. Jiang, D. D. Hall, J. W. Hell, X. Luo, B. A. Rothermel, and J. A. Hill, "Physical and functional interaction between calcineurin and the cardiac l-type ca^{2+} channel," *Circulation Research*, vol. 105, pp. 51–60, 2009.

[92] L. V. Hryshko and D. M. Bers, "Ca current facilitation during postrest recovery depends on ca entry," *American Journal of Physiology*, vol. 259, pp. 951–961, 1990.

[93] V. J. Schouten and M. Morad, "Regulation of ca^{2+} current in frog ventricular myocytes by the holding potential, c-amp and frequency," *Pflügers Arch*, vol. 415, pp. 1–11, 1989.

[94] M. X. Mori, M. G. Erickson, and D. T. Yue, "Functional stoichiometry and local enrichment of calmodulin interacting with ca^{2+} channels," *Science*, vol. 304, pp. 394–395, 2004.

[95] G. S. Pitt, R. D. Zühlke, A. Hudmon, H. Schulman, H. Reuter, and R. W. Tsien, "Molecular basis of calmodulin tethering and ca^{2+}-dependent inactivation of l-type ca^{2+} channels," *The Journal of Biological Chemistry*, vol. 276, no. 33, pp. 30794–30802, 2001.

[96] N. M. Soldatov, "ca^{2+} channel moving tail: link between ca^{2+}-induced inactivation and ca^{2+} signal transduction," *TRENDS in Pharmacological Sciences*, vol. 24, no. 4, pp. 167–171, 2003.

[97] N. M. Soldatov, "ca^{2+} channel moving tail: link between ca^{2+}- induced inactivation and ca^{2+} signal transduction," *TRENDS in pharmacological Sciences*, vol. 24, no. 4, pp. 167–171, 2003.

[98] D. T. Yue, S. Herzig, and E. Marban, "β-adrenergic stimulation of calcium channels occurs by potentiation of high-activity gating modes," *Proc Natl Acad Sci*, vol. 87, pp. 753–757, 1990.

[99] G. Klein, F. Schröder, D. Vogler, A. Schaefer, A. Haverich, B. Schieffer, T. Korte, and H. Drexler, "Increased open probability of single cardiac l-type calcium channels in patients with chronic atrial fibrillation. role of phosphatase 2a," *Cardiovascular Res*, vol. 59, pp. 37–45, 2003.

[100] S. D. Salhanick and M. W. Shannon, "Management of calcium channel antagonist overdose," *Drug Saf*, vol. 26, pp. 65–79, 2003.

[101] R. E. Klabunde, "Cellular structure and function," in *Cardiovascular Physiology Concepts*, pp. 41–58, 351 West Camden St., Baltimore, MD 21201: Lippincott Williams & Wilkins, 1st ed., 2004.

[102] J. A. Post, G. A. Langer, J. A. Op den Kamp, and A. J. Verkleij, "Phospholipid asymmetry in cardiac sarcolemma. analysis of intact cells and 'gas-dissected' membranes," *Biochem Biophys Acta*, vol. 943, no. 2, pp. 256–266, 1988.

[103] J. A. Post and G. A. Langer, "Sarcolemmal calcium binding sites in heart: I. molecular origin in "gas-dissected" sarcolemma," *J Membr Biol*, vol. 129, no. 1, pp. 49–57, 1992.

[104] T. Cens, M. Rousset, J. P. Leyris, P. Fesquet, and P. Charnet, "Voltage- and

calcium-dependent inactivation in high voltage-gated ca^{2+} channels," *Prog Biophys Mol Biol*, vol. 90, pp. 104–117, 2006.

[105] J. Keizer and L. Levine, "Ryanodine receptor adaptation and ca^{2+}-induced ca^{2+} release-dependent ca^{2+} oscillations," *Biophys J*, vol. 71, pp. 3477–3487, 1996.

[106] S. Gyorke and M. Fill, "Ryanodine receptor adaptation: control mechanism of ca^{2+}-induced ca2+ release in heart," *Science*, vol. 263, pp. 986–988, 1993.

[107] A. Zahradnikova and I. Zahradnik, "A minimal gating model for the cardiac calcium release channel," *Biophys J*, vol. 71, pp. 2996–3012, 1996.

[108] J. Keizer and G. D. Smith, "Spark-to-wave transitions: salutatory transmission of calcium wave in cardiac myocytes," *Biophys Chem*, vol. 72, pp. 87–100, 1998.

[109] M. D. Stern, G. Pizarro, and E. Rios, "Local control model of excitation-contraction coupling in skeletal muscle," *J Gen Physiol*, vol. 110, pp. 415–440, 1997.

[110] L. Li, H. Satoh, K. S. Ginsburg, and D. M. Bers, "The effect of ca^{2+}-calmodulin-dependent protein kinase ii on cardiac excitation-contraction coupling in ferret ventricular myocytes," *Journal of Physiology*, vol. 501, pp. 17–32, 1997.

[111] L. S. Maier, T. Zhang, L. Chen, J. DeSantiago, J. H. Brown, and D. M. Bers, "Transgenic camkiiδc overexpression uniquely alters cardiac myocyte ca^{2+} handling: reduced sr ca^{2+} load and activated sr ca^{2+} release," *Circulation Research*, vol. 92, pp. 904–911, 2003.

[112] S. Currie, C. M. Loughrey, M. A. Craig, and G. L. Smith, "Calcium/calmodulin-dependent protein kinase iidelta associates with the ryanodine receptor complex

and regulates channel function in rabbit heart," *Biochemical Journal*, vol. 377, pp. 357–366, 2004.

[113] T. Guo, T. Zhang, R. Mestril, and D. M. Bers, "ca^{2+}/calmodulin-dependent protein kinase ii phosphorylation of ryanodine receptor does affect calcium sparks in mouse ventricular myocytes," *Circulation Research*, vol. 99, pp. 398–406, 2006.

[114] V. Lukyanenko, T. F. Wiesner, and S. Gyorke, "Termination of ca^{2+} release during ca^{2+} sparks in rat ventricular myocytes," *J Physiol (Lond)*, vol. 507, pp. 667–677, 1998.

[115] W. G. Wier, T. M. Egan, R. Lopez-Lopez, and C. W. Balke, "Local control of excitation-contraction coupling in rat heart cells," *J Physiol (Lond)*, vol. 474, pp. 463–471, 1994.

[116] R. Zucchi and S. Ronca-Testoni, "The sarcoplasmic reticulum ca^{2+} channel/ryanodine receptor: modulation by endogenous effectors, drugs and disease states," *Pharmacol Rev*, vol. 49, no. 1, pp. 1–51, 1997.

[117] D. M. Balshaw, L. Xu, N. Yamaguchi, D. A. Pasek, and G. Meissner, "Calmodulin binding and inhibition of cardiac muscle calcium release channel (ryanodine receptor)," *Journal of Biological Chemistry*, vol. 276, pp. 20144–20153, 2001.

[118] D. R. Witcher, R. J. Kovacs, H. Schulman, D. C. Cefali, and L. R. Jones, "Unique phosphorylation site on the cardiac ryanodine receptor regulates calcium channel activity," *The Journal of Biological Chemistry*, vol. 266, no. 17, pp. 11144–11152, 1991.

[119] X. H. Wehrens, S. E. Lehnart, S. R. Reiken, and A. R. Marks, "ca^{2+}/calmodulin-dependent protein kinase ii phosphorylation regulates the cardiac ryanodine receptor," *Circulation Research*, vol. 94, no. 6, pp. 61–70, 2004.

[120] P. Rodriguez, M. S. Bhogal, and J. Colyer, "Stoichiometric phosphorylation of cardiac ryanodine receptor on serine 2809 by calmodulin-dependent kinase ii and protein kinase a," *Journal of Biological chemistry*, vol. 278, pp. 38593–38600, 2003.

[121] J. Hain, H. Onoue, M. Mayrleitner, S. Fleischer, and H. Schindler, "Phosphorylation modulates the function of the calcium release channel of sarcoplasmic reticulum from cardiac muscle," *The Journal of Biological Chemistry*, vol. 270, no. 5, pp. 2074–2081, 1995.

[122] A. J. Lokuta, T. B. Rogers, W. J. Lederer, and H. H. Valdivia, "Modulation of cardiac ryanodine receptors of swine and rabbit by a phosphorylation-dephosphorylation mechanism," *Journal of Physiology*, vol. 487, pp. 609–622, 1995.

[123] D. Yang, W. Z. Zhu, B. Xiao, D. X. Brochet, S. R. Chen, E. G. Lakatta, R. P. Xiao, and H. Cheng, "ca^{2+}/calmodulin kinase ii-dependent phosphorylation of ryanodine receptors suppresses ca^{2+} sparks and ca^{2+} waves in cardiac myocytes," *Circulation Research*, vol. 100, no. 3, pp. 399–407, 2007.

[124] A. Bandyopadhyay, D. W. Shin, J. O. Ahn, and D. H. Kim, "Calcineurin regulates ryanodine receptor/ca^{2+}-release channels in rat heart," *Biochem J*, vol. 352, pp. 61–70, 2000.

[125] L. Zhang, J. Kelley, G. Schmeisser, Y. M. Kobayashi, and L. R. Jones, "Complex formation between junctin, triadin, calsequestrin, and the ryanodine receptor. proteins of the cardiac junctional sarcoplasmic reticulum membrane," *J Biol Chem*, vol. 33, pp. 233–247, 1997.

[126] C. Franzini-Armstrong, "Ryanodine receptors of striated muscles: a complex channel capable of multiple interactions," *Physiol Rev*, vol. 77, pp. 699–729, 1997.

[127] D. M. Bers, "Macromolecular complexes regulating cardiac ryanodine receptor function," *J Mol Cell Cardiol*, vol. 37, pp. 417–429, 2004.

[128] G. Meissner, "Ryanodine receptor/ca^{2+} release channels and their regulation by endogenous effectors," *Annu Rev Physiol*, vol. 56, pp. 485–508, 1994.

[129] M. Fill and J. A. Copello, "Ryanodine receptor calcium release channels," *Physiol Rev*, vol. 82, pp. 893–922, 2002.

[130] R. D. Mitchell, H. K. Simmerman, and L. R. Jones, "ca^{2+} binding effects on protein conformation and protein interactions of canine cardiac calsequestrin," *J Biol Chem*, vol. 263, pp. 1376–1381, 1988.

[131] N. A. Beard, D. R. Laver, and A. F. Dulhunty, "Calsequestrin and the calcium release channel of skeletal and cardiac muscle," *Prog Biophys Mol Biol*, vol. 85, pp. 33–69, 2004.

[132] L. R. Jones, L. Zhang, K. Sanborn, A. O. Jorgensen, and J. Kelley, "Purification, primary structure, and immunological characterization of the 26-kda calsequestrin binding protein (junctin) from cardiac junctional sarcoplasmic reticulum," *J Biol Chem*, vol. 270, pp. 30787–30796, 1995.

[133] Y. M. Kobayashi and L. R. Jones, "Identification of triadin 1 as the predominant triadin isoform expressed in mammalian myocardium," *J Biol Chem*, vol. 274, pp. 28660–28668, 1999.

[134] Y. M. Kobayashi, B. A. Alseikhan, and L. R. Jones, "Localization and characterization of the calsequestrin-binding domain of triadin 1. evidence for a charged beta-strand in mediating the protein-protein interaction," *J Biol Chem*, vol. 275, pp. 17639–17646, 2000.

[135] N. Ikemoto, M. Ronjat, L. G. Meszaros, and M. Koshita, "Postulated role of calsequestrin in the regulation of calcium release from sarcoplasmic reticulum," *Biochemistry*, vol. 28, pp. 6764–6771, 1989.

[136] I. Gyorke, N. Hester, L. R. Jones, and S. Gyorke, "The role of calsequestrin, triadin, and junctin in conferring cardiac ryanodine receptor responsiveness to luminal calcium," *Biophys J*, vol. 86, pp. 2121–2128, 2004.

[137] B. C. Knollmann, N. Chopra, T. Hlaing, B. Akin, T. Yang, K. Ettensohn, B. E. Knollmann, K. D. Horton, N. J. Weissman, I. Holinstat, W. Zhang, D. M. Roden, L. R. Jones, C. Franzini-Armstrong, and K. Pfeifer, "Casq2 deletion causes sarcoplasmic reticulum volume increase, premature ca^{2+} release, and catecholaminergic polymorphic ventricular tachycardia," *J Clin Invest*, vol. 116, pp. 2510–2520, 2006.

[138] P. Lauger, "Conformational transitions of ionic channels," in *Single-Channel Recording* (B. Sakmann, ed.), pp. 177–189, New York: Plenum Press, 1983.

[139] A. Finkelstein and C. S. Peskin, "Some unexpected consequences of a simple physical mechanism of voltage-dependent gating in biological membranes,"

Biophys J, vol. 46, pp. 549–558, 1984.

[140] J. S. K. Sham, L. Cleemann, and M. Morad, "Functional coupling of ca^{2+} channels and ryanodine receptors in cardiac myocytes," *Proc Natl Acad Sci*, vol. 92, pp. 121–125, 1995.

[141] S. L. Adachi-Akahane, Cleemann and M. M, "Cross-signaling between l-type ca^{2+} channels and ryanodine receptors in rat ventricular myocytes," *J Gen Physiol*, vol. 108, pp. 435–454, 1996.

[142] J. D. Potter and H. G. Zott, "The role of actin in modulating ca^{2+} binding to troponin," *Biophys J*, vol. 37, p. 43A, 1982.

[143] M. B. Cannell and D. Allen, "Model of calcium movements during activation in the sarcomere of frog skeletal muscle," *Biophys J*, vol. 45, pp. 913–925, 1984.

[144] D. S. Lindblad, C. R. Murphey, J. W. Clark, and W. R. Giles, "A model of the action potential and underlying membrane currents in a rabbit atrial cell," *Am J Physiol-Heart Circ Physiol*, vol. 271, pp. H1666–H1696, 1996.

[145] T. R. Shannon, K. S. Ginsburg, and D. M. Bers, "Potentiation of fractional sarcoplasmic reticulum calcium release by total and free intra-sarcoplasmic reticulum calcium concentration," *Biophys J*, vol. 78, pp. 334–343, 2000.

[146] J. Lytton, M. Westlin, S. E. Burk, G. E. Shull, and D. H. MacLennan, "Functional comparisons between isoforms of the sarcoplasmic or endoplasmic reticulum family of calcium pumps," *J Biol Chem*, vol. 267, pp. 14483–14489, 1992.

[147] J. T. Koivumäki, J. Takalo, T. Korhonen, P. Tavi, and M. Weckström, "Modelling sarcoplasmic reticulum calcium atpase and its regulation in cardiac my-

ocytes," *Phil Trans R Soc A*, vol. 367, pp. 2181–2202, 2009.

[148] R. A. Bassani, A. Mattiazzi, and D. M. Bers, "Camkii is responsible for activity-dependent acceleration of relaxation in rat ventricular myocytes," *American J Physiol*, vol. 268, pp. 703–712, 1995.

[149] A. Xu, C. Hawkins, and N. Narayanan, "Phosphorylation and activation of the ca^{2+}-pumping atpase of cardiac sarcoplasmic reticulum by ca^{2+}/calmodulin-dependent protein kinase," *J Biol Chem*, vol. 268, no. 12, pp. 8394–8397, 1993.

[150] B. M. Wolska, "Calcineurin and cardiac function: is more or less better for the heart?," *American Journal of Physiology Heart Circulation Physiology*, vol. 297, pp. H1576–H1577, 2009.

[151] P. J. Schaeffer, J. Desantiago, J. Yang, T. P. Flagg, A. Kovacs, C. J. Weinheimer, M. Courtois, T. C. Leone, C. G. Nichols, D. M. Bers, and D. P. Kelly, "Impaired contractile function and calcium handling in hearts of cardiac-specific calcineurin b1-deficient mice," *American J Physiol Heart Circ Physiol*, vol. 297, pp. 1263–1273, 2009.

[152] G. Chu, A. N. Carr, K. B. Young, J. W. Lester, A. Yatani, A. Sanbe, M. C. Colbert, S. M. Schwartz, K. F. Frank, P. D. Lampe, J. Robbins, J. D. Molkentin, and E. G. Kranias, "Enhanced myocyte contractility and ca^{2+} handling in a calcineurin transgenic model of heart failure," *Cardiovasc Res*, vol. 54, no. 1, pp. 105–116, 2002.

[153] G. M*ü*nch, B. B*ö*lck, P. Karczewski, and R. H. Schwinger, "Evidence for calcineurin-mediated regulation of serca 2a activity in human myocardium," *J Mol Cell Cardiol*, vol. 34, no. 3, pp. 321–334, 2002.

[154] P. Caroni, M. Zurini, A. Clark, and E. Carafoli, "Further characterization and reconstitution of the purified ca-pumping atpase of heart sarcolemma," *J Biol Chem*, vol. 258, pp. 7305–7310, 1983.

[155] J. Kimura, S. Miyamae, and A. Noma, "Identification of sodium-calcium exchange current in single ventricular cells of guinea-pig ventricular cells," *J Physiol (Lond)*, vol. 384, pp. 199–222, 1987.

[156] C. R. Weber, K. S. Ginsburg, K. D. Philipson, T. R. Shannon, and D. M. Bers, "Allosteric regulation of na/ca exchange current by cytosolic ca in intact cardiac myocytes," *J Gen Physiol*, vol. 117, no. 2, pp. 119–131, 2001.

[157] J. H. B. Bridge, J. R. Smolley, and K. W. Spitzer, "The relationship between charge movements associated i_{Ca} and i_{Na-Ca} in cardiac myocytes," *Science*, vol. 248, pp. 376–378, 1990.

[158] C. L. Overend, D. A. Eisner, and S. C. O'Neill, "The effect of tetracaine on spontaneous ca^{2+} release and sarcoplasmic reticulum calcium content in rat ventricular myocytes," *J Physiol*, vol. 502, no. 3, pp. 471–479, 1997.

[159] H. G. Glitsch, "Electrophysiology of the sodium-potassium-atpase in cardiac cells," *Physiol Rev*, vol. 81, no. 4, pp. 1791–1826, 2001.

[160] H. P. Rang and J. M. Ritchie, "On the electrogenic sodium pump in mammalian non-myelinated nerve fibres and its activation by various external cations," *J Physiol*, vol. 196, no. 1, pp. 183–221, 1968.

[161] N. Akaike, "Activation of electrogenic sodium pump in mammalian skeletal muscle by external cations," *Pflügers Arch*, vol. 355, no. 4, pp. 281–290, 1975.

[162] T. Akera, R. H. Gubitz, T. M. Brody, and T. Tobin, "Effects of monovalent cations on (na^+ + k^+)-atpase in rat brain slices," *Eur J Pharmacol*, vol. 55, no. 3, pp. 281–292, 1979.

[163] D. A. Eisner and W. J. Lederer, "The role of the sodium pump in the effects of potassium-depleted solutions on mammalian cardiac muscle," *J Physiol*, vol. 294, pp. 279–301, 1979.

[164] Y. Kasamaki, A. C. Guo, L. M. Shuba, T. Ogura, and T. F. McDonald, "Sodium-pump potentials and currents in guinea-pig ventricular muscles and myocytes," *Can J Physiol Pharmacol*, vol. 77, no. 5, pp. 339–349, 1999.

[165] P. S. Hansen, K. A. Buhagiar, B. Y. Kong, R. J. Clarke, D. F. Gray, and H. H. Rasmussen, "Dependence of na^+-k^+ pump current-voltage relationship on intracellular na^+, k^+, and cs^+ in rabbit cardiac myocytes," *Am J Physiol Cell Physiol*, vol. 283, no. 5, pp. C1511–C1521, 2002.

[166] A. E. Messer, A. M. Jacques, and S. B. Marston, "Troponin phosphorylation and regulatory function in human heart muscle: dephosphorylation of Ser23/24 on troponin I could account for the contractile defect in end-stage heart failure," *J Mol Cell Cardiol*, vol. 42, pp. 247–259, 2007.

[167] P. M. Janssen, L. B. Stull, and E. Marbán, "Myofilament properties comprise the rate-limiting step for cardiac relaxation at body temperature in the rat," *Am J Physiol Heart Circ Physiol*, vol. 282, pp. H499–H507, 2002.

[168] N. Suematsu, S. Satoh, Y. Ueda, and N. Makino, "Effects of calmodulin and okadaic acid on myofibrillar ca^{2+} sensitivity in cardiac myocytes," *Basic Res Cardiol*, vol. 97, no. 2, pp. 137–144, 2002.

[169] J. S. Fan and P. Palade, "One calcium ion may suffice to open the tetrameric cardiac ryanodine receptor in rat ventricular myocytes," *J Physiol (Lond)*, vol. 516, pp. 769–780, 1999.

[170] Y. Wang, S. Tandan, J. Cheng, C. Yang, L. Nguyen, J. Sugianto, J. L. Johnstone, Y. Sun, and J. A. Hill, "ca^{2+}/calmodulin-dependent protein kinase ii-dependent remodeling of ca^{2+} current in pressure overload heart failure," *J Biol Chem*, vol. 283, no. 37, pp. 25524–25532, 2008.

[171] K. S. Lee, E. Marban, and R. W. Tsien, "Inactivation of calcium channels in mammalian heart cells: joint dependence on membrane potential and intracellular calcium," *Journal of Physiology*, vol. 364, pp. 395–411, 1985.

[172] A. A. Sher, R. Hinch, P. J. Noble, D. J. Gavaghan, and D. Noble, "Functional significance of na^{+}/ca^{2+} exchangers co-localization with ryanodine receptors," *Ann N Y Acad Sci*, vol. 1099, pp. 215–220, 2007.

[173] R. Mejia-Alvarez, C. Kettlun, E. Rios, M. Stern, and M. Fill, "Unitary ca^{2+} current through cardiac ryanodine receptor channels under quasiphysiological ionic conditions," *J Gen Physiol*, vol. 113, pp. 177–186, 1999.

[174] M. B. Cannel, J. R. Berlin, and W. J. Lederer, "Effect of membrane potential changes on the calcium transient in single rat cardiac muscle cells," *Science*, vol. 238, pp. 1419–1423, 1987.

[175] L. Cleemann and M. Morad, "Role of ca^{2+} channel in cardiac excitation-contraction coupling in the rat: evidence from ca^{2+} transients and contraction," *J Physiol*, vol. 432, pp. 283–312, 1991.

[176] M. B. Cannell, H. Cheng, and W. J. Lederer, "The control of calcium release in heart muscle," *Science*, vol. 268, pp. 1045–1050, 1995.

[177] L. S. Song, S. Q. Wang, R. P. Xiao, H. Spurgeon, E. G. Lakatta, and H. Cheng, "β-adrenergic stimulation synchronizes intracellular ca^{2+} release during excitation-contraction coupling in cardiac myocytes," *Circ Res*, vol. 88, pp. 794–801, 2001.

[178] J. Altamirano and D. M. Bers, "Voltage dependence of cardiac excitation-contraction coupling: unitary ca^{2+} current amplitude and open channel probability," *Circ Res*, vol. 101, no. 6, pp. 590–597, 2007.

[179] E. Picht, J. DeSantiago, L. A. Blatter, and D. M. Bers, "Cardiac alternans do not rely on diastolic sarcoplasmic reticulum calcium content fluctuations," *Circ Res*, vol. 99, pp. 740–748, 2006.

[180] E. A. Sobie, L. S. Song, and W. J. Lederer, "Local recovery of ca^{2+} release in rat ventricular myocytes," *J Physiol*, vol. 565, pp. 441–447, 2005.

[181] D. A. Eisner, L. A. Venetucci, and A. W. Trafford, "Life, sudden death and intracellular calcium," *Circulation Research*, vol. 99, pp. 223–224, 2006.

[182] M. E. Diaz, A. W. Trafford, S. C. O'Neill, and D. A. Eisner, "Measurement of sarcoplasmic reticulum ca^{2+} content and sarcolemmal ca^{2+} fluxes in isolated rat ventricular myocytes during spontaneous ca^{2+} release," *J Physiol (Lond)*, vol. 501, pp. 3–16, 1997.

[183] A. W. Trafford, G. C. Sibbring, M. E. Diaz, and D. A. Eisner, "The effects of low concentrations of caffeine on spontaneous ca release in isolated rat ventricular myocytes," *Cell Calcium*, vol. 28, no. 4, pp. 269–276, 2000.

[184] M. E. Diaz, H. K. Graham, S. C. O'Neill, A. W. Trafford, and D. A. Eisner, "The control of sarcoplasmic reticulum ca content in cardiac muscle," *Cell Calcium*, vol. 38, pp. 391–396, 2005.

[185] N. Negretti, A. Varro, and D. A. Eisner, "Estimate of net calcium fluxes and sarcoplasmic reticulum calcium content during systole in rat ventricular myocytes," *J Physiol (Lond)*, vol. 486, pp. 581–591, 1995.

[186] L. Barcenas-Ruiz and W. G. Wier, "Voltage dependence of intracellular $[ca^{2+}]_i$ transients in guinea pig ventricular myocytes," *Circ Res*, vol. 61, pp. 148–154, 1987.

[187] A. Fleig and R. Penner, "Silent calcium channels generate excessive tail currents and facilitation of calcium currents in rat skeletal myoballs," *J Physiol*, vol. 494.1, pp. 141–153, 1996.

[188] D. M. Bers, D. A. Eisner, and H. H. Valdivia, "Sarcoplasmic reticulum ca^{2+} and heart failure: roles of diastolic leak and ca^{2+} transport," *Circ Res*, vol. 93, pp. 487–490, 2003.

[189] X. H. Sun, F. Protasi, M. Takahashi, H. Takeshima, D. G. Ferguson, and C. Franzini-Armstrong, "Molecular architecture of membranes involved in excitation-contraction coupling of cardiac muscle," *J Cell Biology*, vol. 129, no. 4, pp. 659–667, 1995.

[190] C. Franzini-Armstrong, F. , Protasi, and V. Ramesh, "Shape, size, and distribution of ca^{2+} release units and couplons in skeletal and cardiac muscles," *Biophys J*, vol. 77, pp. 1528–1539, 1999.

[191] H. Tanaka, T. Sekine, T. Kawanishi, R. Nakamura, and K. Shigenobu, "Intrasarcomere ca^{2+} gradients and their spatio-temporal relation to ca^{2+} sparks in rat cardiomyocytes," *J Physiol*, vol. 508, pp. 145–152, 1998.

[192] H. Cheng, M. R. Lederer, W. J. Lederer, and M. B. Cannell, "Calcium sparks and $[ca^{2+}]_i$ waves in cardiac myocytes," *American Journal of Physiology*, vol. 270, no. 1.1, pp. 148–159, 1996.

[193] P. H. Backx and H. E. Ter Keurs, "Fluorescent properties of rat cardiac trabeculae microinjected with fura-2 salt," *Am J Physiol*, vol. 264, pp. H1098–H1110, 1993.

[194] J. C. Kentish and A. Wrzosek, "Changes in force and cytosolic Ca^{2+} concentration after length changes in isolated rat ventricular trabeculae," *J Physiol*, vol. 506, pp. 431–444, 1998.

[195] R. A. Bouchard, R. B. Clark, and W. R. Giles, "Regulation of unloaded cell shortening by sarcolemmal sodium-calcium exchange in isolated rat ventricular myocytes," *J Physiol*, vol. 469, pp. 583–599, 1993.

[196] S. M. Harrison and D. M. Bers, "Temperature dependence of myofilament Ca sensitivity of rat, guinea pig, and frog ventricular muscle," *Am J Physiol*, vol. 258, no. 2.1, pp. C274–C281, 1990.

[197] J. C. Kentish, H. E. ter Keurs, L. Ricciardi, J. J. Bucx, and M. I. Noble, "Comparison between the sarcomere length-force relations of intact and skinned trabeculae from rat right ventricle. influence of calcium concentrations on these relations," *Circulation Research*, vol. 58, pp. 755–768, 1986.

[198] P. M. Janssen and W. C. Hunter, "Force, not sarcomere length, correlates with prolongation of isosarcometric contraction," *Am J Physiol*, vol. 269, pp. H676–H685, 1995.

[199] D. P. Dobesh, J. P. Konhilas, and P. P. de Tombe, "Cooperative activation in cardiac muscle: impact of sarcomere length," *Am J Physiol Heart Circ Physiol*, vol. 282, pp. H1055–H1062, 2002.

[200] P. P. de Tombe and W. C. Little, "Inotropic effects of ejection are myocardial properties," *Am J Physiol*, vol. 266, pp. H1202–H1213, 1994.

[201] P. M. Janssen, "Kinetics of cardiac muscle contraction and relaxation are linked and determined by properties of the cardiac sarcomere," *Am J Physiol Heart Circ Physiol*, vol. 299, pp. H1092–H1099, 2010.

[202] S. U. Sys and D. L. Brutsaert, "Determinants of force decline during relaxation in isolated cardiac muscle," *Am J Physiol*, vol. 257, no. 5.2, pp. H1490–H1497, 1989.

[203] P. M. Janssen and P. P. de Tombe, "Uncontrolled sarcomere shortening increases intracellular Ca^{2+} transient in rat cardiac trabeculae," *Am J Physiol*, vol. 272, pp. H1892–H1897, 1997.

[204] Q. H. Han, D. M. Wu, J. Y. Lu, and B. W. Wu, "Inhibition of Na^{+}/Ca^{2+} exchange by hexapeptide frcrsfa in rat ventricular myocytes," *Acta Pharmacol Sin*, vol. 23, no. 6, pp. 529–533, 2002.

[205] A. Cavalié, T. F. McDonald, D. Pelzer, and W. Trautwein, "Temperature-induced transitory and steady-state changes in the calcium current of guinea pig ventricular myocytes," *Pflugers Arch*, vol. 405, no. 3, pp. 294–296, 1985.

[206] S. O. McMorn, S. M. Harrison, and M. R. Boyett, "The effect of temperature on the rate-dependent decrease of the rat ventricular calcium current," *Exp Physiol*, vol. 83, pp. 49–63, 1998.

[207] K. W. Linz and R. Meyer, "Profile and kinetics of l-type calcium current during the cardiac ventricular action potential compared in guinea-pigs, rats and rabbits," *Pflugers Arch*, vol. 439, pp. 588–599, 2000.

[208] S. M. Harrison and D. M. Bers, "Influence of temperature on the calcium sensitivity of the myofilaments of skinned ventricular muscle from the rabbit," *J Gen Physiol*, vol. 93, pp. 411–428, 1989.

[209] P. P. de Tombe and G. J. M. Stienen, "The rate of tension redevelopment in rat cardiac muscle: Influence of temperature and contractile activation level," *Circulation*, vol. 96, pp. 517–518, 1997.

[210] P. P. de Tombe and G. J. M. Stienen, "Impact of temperature on cross-bridge cycling kinetics in rat myocardium," *J Physiol*, vol. 584, pp. 591–600, 2007.

[211] P. M. Janssen, "Myocardial contraction-relaxation coupling," *Am J Physiol Heart Circ Physiol*, vol. 299, pp. H1741–H1749, 2010.

[212] Y. Mio, N. Fukuda, Y. Kusakari, Y. Tanifuji, and S. Kurihara, "Bupivacaine attenuates contractility by decreasing sensitivity of myofilaments to Ca^{2+} in rat ventricular muscle," *Anesthesiology*, vol. 97, no. 5, pp. 1168–1177, 2002.

[213] F. C. Howarth and M. A. Qureshi, "Myofilament sensitivity to Ca^{2+} in ventricular myocytes from the goto-kakizaki diabetic rat," *Mol Cell Biochem*, vol. 315, pp. 69–74, 2008.

[214] S. R. Roof, T. R. Shannon, P. M. Janssen, and M. T. Ziolo, "Effects of increased systolic Ca^{2+} and phospholamban phosphorylation during β-adrenergic stimulation on Ca^{2+} transient kinetics in cardiac myocytes," *Am J Physiol Heart Circ Physiol*, vol. 301, pp. H1570–H1578, 2011.

[215] A. E. Messer, C. E. Gallon, W. J. McKenna, C. G. Dos Remedios, and S. B. Marston, "The use of phosphate-affinity SDS-PAGE to measure the cardiac troponin I phosphorylation site distribution in human heart muscle," *Proteomics Clin Appl*, vol. 12, pp. 1371–1382, 2009.

[216] D. M. Bers, "Calcium fluxes involved in control of cardiac myocyte contraction," *Circ Res*, vol. 87, pp. 275–281, 2000.

[217] H. P. Bowditch, "Ueber die eigenth*ü*mlichkeiten der reizbarkeit, welche die muskelfasern des herzens zeigen," *Arb Physiol Anst Leipzig*, vol. 6, pp. 139–176, 1871.

[218] V. J. Schouten and H. E. ter Keurs, "Role of ica and na^{+}/ca^{2+} exchange in the force-frequency relationship of rat heart muscle," *J Mol Cell Cardiol*, vol. 23, no. 9, pp. 1039–1050, 1991.

[219] M. Vornanen, "Force-frequency relationship, contraction duration and recirculating fraction of calcium in postnatally developing rat heart ventricles: correlation with heart rate," *Acta Physiol Scand*, vol. 145, no. 4, pp. 311–321, 1992.

[220] P. Jouannot and P. Y. Hatt, "Rat myocardial mechanics during pressure-induced hypertrophy development and reversal," *Am J Physiol*, vol. 229, no. 2, pp. 355–364, 1975.

[221] L. S. Maier, D. M. Bers, and B. Pieske, "Differences in ca^{2+}-handling and sarcoplasmic reticulum ca^{2+}-content in isolated rat and rabbit myocardium," *J Mol Cell Cardiol*, vol. 32, no. 12, pp. 2249–2258, 2000.

[222] J. Layland and J. C. Kentish, "Positive force- and $[ca^{2+}]_i$-frequency relationships in rat ventricular trabeculae at physiological frequencies," *Am J Physiol*, vol. 276, pp. H9–H18, 1999.

[223] M. M. Monasky and P. M. Janssen, "The positive force-frequency relationship is maintained in absence of sarcoplasmic reticulum function in rabbit, but not in rat myocardium," *J Comp Physiol B*, vol. 179, no. 4, pp. 469–479, 2009.

[224] K. Mubagwa, W. Lin, K. Sipido, S. Bosteels, and W. Flameng, "Monensin-induced reversal of positive force-frequency relationship in cardiac muscle: role of intracellular sodium in rest-dependent potentiation of contraction," *J Mol Cell Cardiol*, vol. 29, no. 3, pp. 977–989, 1997.

[225] C. H. Orchard and E. G. Lakatta, "Intracellular calcium transients and developed tension in rat heart muscle: a mechanism for the negative interval strength relationship," *J Gen Physiol*, vol. 86, pp. 637–651, 1985.

[226] I. Morii, Y. Kihara, T. Konishi, T. Inubushi, and S. Sasayama, "Mechanism of the negative force-frequency relationship in physiologically intact rat ventricular myocardium–studies by intracellular ca^{2+} monitor with indo-1 and by 31p-nuclear magnetic resonance spectroscopy," *Jpn Circ J*, vol. 60, no. 8, pp. 593–603, 1996.

[227] J. Layland and J. C. Kentish, "Positive force- and $[ca^{2+}]_i$-frequency relationships in rat ventricular trabeculae at physiological frequencies," *Am J Physiol*,

vol. 276, pp. H9–H18, 1999.

[228] J. Guo and H. J. Duff, "Calmodulin kinase ii accelerates l-type ca^{2+} current recovery from inactivation and compensates for the direct inhibitory effect of $[ca^{2+}]_i$ in rat ventricular myocytes," *J Physiol*, vol. 574, pp. 509–518, 2006.

[229] P. J. Phillips, J. K. Gwathmey, M. D. Feldman, F. J. Schoen, W. Grossman, and J. P. Morgan, "Post-extrasystolic potentiation and the force-frequency relationship: differential augmentation of myocardial contractility in working myocardium from patients with end-stage heart failure," *J Mol Cell Cardiol*, vol. 22, pp. 99–110, 1990.

[230] R. H. Schwinger, M. Böhm, J. Müller-Ehmsen, R. Uhlmann, U. Schmidt, A. Stäblein, P. Überfuhr, E. Kreuzer, B. Reichart, H. J. Eissner, and et al., "Effect of inotropic stimulation on the negative force-frequency relationship in the failing human heart," *J Mol Cell Cardiol*, vol. 23, no. 9, pp. 1039–1050, 1993.

[231] J. Giesen, M. Sondermann, E. Juengling, and H. Kammermeier, "Time dependent partial loss of the effects of isoproterenol on function and energy metabolism of isolated rat hearts," *Basic Res Cardiol*, vol. 75, pp. 515–525, 1980.

[232] S. Lemaire, C. Piot, F. Leclercq, V. Leuranguer, J. Nargeot, and S. Richard, "Heart rate as a determinant of l-type ca^{2+} channel activity: mechanisms and implication in force-frequency relation," *Basic Res Cardiol*, vol. 93, pp. 51–59, 1998.

[233] S. J. Liu, W. Zhou, and R. H. Kennedy, "Suppression of beta-adrenergic responsiveness of l-type ca^{2+} current by il-1 beta in rat ventricular myocytes," *Am J Physiol-Heart Circ Physiol*, vol. 276, pp. H141–H148, 1996.

[234] F. Tiaho, C. Piot, J. Nargeot, and S. Richard, "Regulation of the frequency-dependent facilitation of l-type ca2+ currents in rat ventricular myocytes," *J Physiol*, vol. 477, pp. 237–251, 1994.

[235] N. Delpech, H. Soustre, and D. Potreau, "Antagonism of beta-adrenergic stimulation of l-type ca2+ current by endothelin in guinea-pig atrial cells," *Eur J Pharmacol*, vol. 285, pp. 217–220, 1995.

[236] Z. Nagyk*á*ldi, D. Kem, R. Lazzara, and B. Szab*ó*, "The coupling of canine ventricular myocyte beta2-adrenoceptors to l-type calcium current," *Acta Pharm Hung*, vol. 69, pp. 247–257, 1999.

[237] R. H. Schwinger, G. M*ü*nch, B. B*ö*lck, P. Karczewski, E. G. Krause, and E. Erdmann, "Reduced ca^{2+}-sensitivity of serca 2a in failing human myocardium due to reduced serin-16 phospholamban phosphorylation," *J Mol Cell Cardiol*, vol. 31, no. 3, pp. 479–491, 1999.

[238] B. Ait-Mamar, M. Cailleret, C. Rucker-Martin, A. Bouabdallah, G. Candiani, C. Adamy, P. Duvaldestin, F. Pecker, N. Defer, and C. Pavoine, "The cytosolic phospholipase a2 pathway, a safeguard of beta2-adrenergic cardiac effects in rat," *J Biol Chem*, vol. 280, pp. 18881–18890, 2005.

[239] T. Zhang, L. S. Maier, N. D. Dalton, S. Miyamoto, J. J. Ross, D. M. Bers, and J. H. Brown, "The δc isoform of camkii is activated in cardiac hypertrophy and

induces dilated cardiomyopathy and heart failure," *Circ Res*, vol. 92, pp. 912–919, 2003.

[240] S. Huke and D. M. Bers, "Temporal dissociation of frequency-dependent acceleration of relaxation and protein phosphorylation by camkii," *J Mol Cell Cardiol*, vol. 42, no. 3, pp. 590–599, 2007.

[241] P. Tavi, S. Pikkarainen, J. Ronkainen, P. Niemelä, M. Ilves, M. Weckström, O. Vuolteenaho, J. Bruton, H. Westerblad, and H. Ruskoaho, "Pacing-induced calcineurin activation controls cardiac ca^{2+} signalling and gene expression," *J Physiol*, vol. 554, pp. 309–320, 2004.

[242] T. Toyofuku, K. Curotto Kurzydlowski, N. Narayanan, and D. H. MacLennan, "Identification of ser38 as the site in cardiac sarcoplasmic reticulum ca^{2+}-atpase that is phosphorylated by ca^{2+}/calmodulin-dependent protein kinase," *J Biol Chem*, vol. 269, no. 42, pp. 26492–29496, 1994.

[243] A. Odermatt, K. Kurzydlowski, and D. H. MacLennan, "The v_{max} of the ca^{2+}-atpase of cardiac sarcoplasmic reticulum (serca2a) is not altered by ca^{2+}/calmodulin-dependent phosphorylation or by interaction with phospholamban," *J Biol Chem*, vol. 271, no. 24, pp. 14206–14213, 1996.

[244] L. Perchenet, A. K. Hinde, K. C. Patel, J. C. Hancox, and A. J. Levi, "Stimulation of na/ca exchange by the beta-adrenergic/protein kinase a pathway in guinea-pig ventricular myocytes at 37 degrees c," *Pflugers Arch*, vol. 439, pp. 822–828, 2000.

[245] X. Lin, H. Jo, Y. Sakakibara, K. Tambara, B. Kim, M. Komeda, and S. Matsuoka, "Beta-adrenergic stimulation does not activate na^{+}/ca^{2+} exchange cur-

rent in guinea pig, mouse, and rat ventricular myocytes," *Am J Physiol Cell Physiol*, vol. 290, pp. C601–C608, 2006.

[246] J. DeSantiago, L. S. Maier, and D. M. Bers, "Frequency-dependent acceleration of relaxation in the heart depends on camkii, but not phospholamban," *J Mol Cell Cardiol*, vol. 34, no. 8, pp. 975–984, 2002.

[247] G. Hoyle, "Comparative aspects of muscle," *Annual Review of Physiology*, vol. 31, pp. 43–82, 1969.

[248] D. W. Hilgemann, A. Collins, and D. P. Cash, "Cardiac na^{+}-ca^{2+} exchange system in giant membrane patches," *Annu NY Acad Sci*, vol. 639, pp. 127–139, 1991.

[249] M. Pásek, J. Simurda, and G. Christé, "The functional role of cardiac t-tubules explored in a model of rat ventricular myocytes," *Philos Transact A Math Phys Eng Sci*, vol. 364, no. 1842, pp. 1187–1206, 2006.

[250] G. A. Langer and A. Peskoff, "Calcium concentration and movement in the diadic cleft space of the cardiac ventricular cell," *Biophys J*, vol. 70, pp. 1169–1182, 1996.

[251] H. Y. Li and G. A. Quamme, "Effect of ph on intracellular free mg^{2+} in isolated adult rat cardiomyocytes," *Biochim Biophys Acta*, vol. 1222, no. 2, pp. 164–170, 1994.

[252] A. B. Harkins, N. Kurebayashi, and S. M. Baylor, "Resting myoplasmic free calcium in frog skeletal muscle fibers estimated with fluo-3," *Biophys J*, vol. 65, no. 2, pp. 865–881, 1993.

[253] E. A. Sobie, K. W. Dilly, J. Dos Santos Cruz, W. J. Lederer, and M. S. Jafri, "Termination of cardiac ca^{2+} sparks: an investigative mathematical model of calcium-induced calcium release," *Biophys J*, vol. 83, pp. 59–78, 2002.

[254] J. C. Herve, K. Yamaoka, V. W. Twist, T. Powell, J. C. Ellory, and L. C. Wang, "Temperature dependence of electrophysiological properties of guinea pig and ground squirrel myocytes," *Am J Physiol*, vol. 263, no. 1.2, pp. R177–R184, 1992.

[255] M. R. Mitchell, T. Powell, D. A. Terrar, and V. W. Twist, "The effects of ryanodine, egta and low-sodium on action potentials in rat and guinea pig ventricular myocytes: evidence for two inward currents during the plateau," *Br J Pharmacol*, vol. 81, pp. 543–550, 1984.

[256] U. Mackiewicz and B. Lewartowski, "Temperature dependent contribution of Ca^{2+} transporters to relaxation in cardiac myocytes: important role of sarcolemmal Ca^{2+}-atpase," *J Physiol Pharmacol*, vol. 57, no. 1, pp. 3–15, 2006.